Biological and Medical Physics, Biomedical Engineering

Andrew Rubin
Galina Riznichenko

Mathematical Biophysics

Springer

BIOLOGICAL AND MEDICAL PHYSICS, BIOMEDICAL ENGINEERING

The fields of biological and medical physics and biomedical engineering are broad, multidisciplinary and dynamic. They lie at the crossroads of frontier research in physics, biology, chemistry, and medicine. The Biological and Medical Physics, Biomedical Engineering Series is intended to be comprehensive, covering a broad range of topics important to the study of the physical, chemical and biological sciences. Its goal is to provide scientists and engineers with textbooks, monographs, and reference works to address the growing need for information.

Books in the series emphasize established and emergent areas of science including molecular, membrane, and mathematical biophysics; photosynthetic energy harvesting and conversion; information processing; physical principles of genetics; sensory communications; automata networks, neural networks, and cellular automata. Equally important will be coverage of applied aspects of biological and medical physics and biomedical engineering such as molecular electronic components and devices, biosensors, medicine, imaging, physical principles of renewable energy production, advanced prostheses, and environmental control and engineering.

Editor-in-Chief:

Elias Greenbaum, Oak Ridge National Laboratory, Oak Ridge, Tennessee, USA

Editorial Board:

Masuo Aizawa, Department of Bioengineering, Tokyo Institute of Technology, Yokohama, Japan

Olaf S. Andersen, Department of Physiology, Biophysics & Molecular Medicine, Cornell University, New York, USA

Robert H. Austin, Department of Physics, Princeton University, Princeton, New Jersey, USA

James Barber, Department of Biochemistry, Imperial College of Science, Technology and Medicine, London, England

Howard C. Berg, Department of Molecular and Cellular Biology, Harvard University, Cambridge, Massachusetts, USA

Victor Bloomfield, Department of Biochemistry, University of Minnesota, St. Paul, Minnesota, USA

Robert Callender, Department of Biochemistry, Albert Einstein College of Medicine, Bronx, New York, USA

Britton Chance, Department of Biochemistry/ Biophysics, University of Pennsylvania, Philadelphia, Pennsylvania, USA

Steven Chu, Lawrence Berkeley National Laboratory, Berkeley, California, USA

Louis J. DeFelice, Department of Pharmacology, Vanderbilt University, Nashville, Tennessee, USA

Johann Deisenhofer, Howard Hughes Medical Institute, The University of Texas, Dallas, Texas, USA

George Feher, Department of Physics, University of California, San Diego, La Jolla, California, USA

Hans Frauenfelder, Los Alamos National Laboratory, Los Alamos, New Mexico, USA

Ivar Giaever, Rensselaer Polytechnic Institute, Troy, NewYork, USA

Sol M. Gruner, Cornell University, Ithaca, New York, USA

Judith Herzfeld, Department of Chemistry, Brandeis University,Waltham, Massachusetts, USA

Mark S. Humayun, Doheny Eye Institute, Los Angeles, California, USA

Pierre Joliot, Institute de Biologie Physico-Chimique, Fondation Edmond de Rothschild, Paris, France

Lajos Keszthelyi, Institute of Biophysics, Hungarian Academy of Sciences, Szeged, Hungary

Robert S. Knox, Department of Physics and Astronomy, University of Rochester, Rochester, New York, USA

Aaron Lewis, Department of Applied Physics, Hebrew University, Jerusalem, Israel

Stuart M. Lindsay, Department of Physics and Astronomy, Arizona State University, Tempe, Arizona, USA

David Mauzerall, Rockefeller University, New York, New York, USA

Eugenie V. Mielczarek, Department of Physics and Astronomy, George Mason University, Fairfax, Virginia, USA

Markolf Niemz, Medical Faculty Mannheim, University of Heidelberg, Mannheim, Germany

V. Adrian Parsegian, Physical Science Laboratory, National Institutes of Health, Bethesda, Maryland, USA

Linda S. Powers, University of Arizona, Tucson, Arizona, USA

Earl W. Prohofsky, Department of Physics, Purdue University,West Lafayette, Indiana, USA

Andrew Rubin, Department of Biophysics, Moscow State University, Moscow, Russia

Michael Seibert, National Renewable Energy Laboratory, Golden, Colorado, USA

David Thomas, Department of Biochemistry, University of Minnesota Medical School, Minneapolis, Minnesota, USA

For further volumes:

http://www.springer.com/series/3740

Andrew Rubin • Galina Riznichenko

Mathematical Biophysics

Springer

Andrew Rubin
Department of Biophysics
Lomonosov Moscow State University
Moscow, Russia

Galina Riznichenko
Department of Biophysics
Lomonosov Moscow State University
Moscow, Russia

ISBN 978-1-4614-8701-2 ISBN 978-1-4614-8702-9 (eBook)
DOI 10.1007/978-1-4614-8702-9
Springer New York Heidelberg Dordrecht London

Library of Congress Control Number: 2013951223

© Springer Science+Business Media New York 2014
This work is subject to copyright. All rights are reserved by the Publisher, whether the whole or part of the material is concerned, specifically the rights of translation, reprinting, reuse of illustrations, recitation, broadcasting, reproduction on microfilms or in any other physical way, and transmission or information storage and retrieval, electronic adaptation, computer software, or by similar or dissimilar methodology now known or hereafter developed. Exempted from this legal reservation are brief excerpts in connection with reviews or scholarly analysis or material supplied specifically for the purpose of being entered and executed on a computer system, for exclusive use by the purchaser of the work. Duplication of this publication or parts thereof is permitted only under the provisions of the Copyright Law of the Publisher's location, in its current version, and permission for use must always be obtained from Springer. Permissions for use may be obtained through RightsLink at the Copyright Clearance Center. Violations are liable to prosecution under the respective Copyright Law.
The use of general descriptive names, registered names, trademarks, service marks, etc. in this publication does not imply, even in the absence of a specific statement, that such names are exempt from the relevant protective laws and regulations and therefore free for general use.
While the advice and information in this book are believed to be true and accurate at the date of publication, neither the authors nor the editors nor the publisher can accept any legal responsibility for any errors or omissions that may be made. The publisher makes no warranty, express or implied, with respect to the material contained herein.

Printed on acid-free paper

Springer is part of Springer Science+Business Media (www.springer.com)

Preface

In contemporary biophysics, mathematical and computer models based on experimental data are widely used to understand system dynamics and regulation mechanisms and to determine corresponding control parameters. The relevant literature encompasses tens of thousands of papers and books devoted to models of processes in living systems at different levels of organization—from the structural molecular level (e.g., Schlyck, Molecular modeling and simulation, 2010) up to the physiological level (e.g., Keener and Sneyd, Mathematical Physiology, two volumes, 2011). A bona fide encyclopedia on modeling living systems at various levels of organization is presented by James Murray in *Mathematical biology* (2002).

The present book offers concise descriptions of the basic models used for the simulation of biological processes. These models from the classic and contemporary literature on mathematical modeling employ different mathematical apparatus with respect to both the experimentally investigated biological processes and certain types of dynamic interactions between system constituents. On the basis of classic ecological models, these interactions follow mechanisms of free collisions, diffusion of reagents, intramacromolecular complex redox interactions, and the effects of external factors (electric fields) on reaction rate constants.

With the advent of supercomputers the goals of simulation were no longer limited by the general characteristics of system dynamics as was the case in the early stages of modeling using the qualitative theory of differential equations. Combined with a detailed knowledge of the structure and metabolism of cells, mathematical modeling has become a powerful tool for studying the nature of cell processes. By analyzing mathematical models, it is now possible to reveal the dynamic behavior and regulating mechanisms of separate metabolites to determine the corresponding parameters. The success of mathematical simulation depends strongly on both an accurate understanding of intrasystem interactions and the proper choice of mathematical apparatus.

We present several examples of real biological systems to illustrate how mathematical simulation can be applied when different mechanisms of interaction

between a large number of constituent elements proceed simultaneously in a system. These model descriptions are based on data in the literature as well as on our own experimental and theoretical studies.

Mathematical Modeling of Living Systems

Mathematical models formalize our knowledge of living system dynamics and the kinetics of major metabolic processes. Basic models consist of one, two, or three equations and allow us to perform a qualitative analysis and to describe the principal regulatory mechanisms of biological processes. They can demonstrate the existence of several stable stationary states in system, oscillations, quasi-stochastic regimes, traveling pulses and waves, and the generation of structures arising from space heterogeneity. The nonlinearity of these models is their most important fundamental property and is inherent to biological objects as open systems far from thermodynamic equilibrium. This principle applies to different models of, for example, cell growth, species interactions, lotic cultures of microorganisms, genetic triggers, intracellular calcium oscillations, glycolysis, and nerve conductivity. Identification of these models based on experimental data allows us to characterize real processes in living systems and to determine their parameters. Thus, these models have considerable heuristic value.

A good example is a model of the primary processes of photosynthesis. With the use of computers, imitational models have been developed where the behavior of complex systems is described on the basis of data on the relevant structural elements and the regulation of their interactions. The imitational models are constructed at all levels of biological organization starting from biomacromolecules and proceeding to the cellular and subcellular levels, then to the level of organs, organisms, populations and communities, ecosystems, and, finally, to the level of the biosphere as a whole system. The degree of mathematization in biophysics depends on the available experimental data and on the facilities for mathematical analysis of the processes under examination.

The future development of mathematical modeling in biophysics rests in many respects upon the use of information technologies, which can combine our knowledge in the form of both mathematical objects and visual images. The resulting models present complex mechanisms of the regulation operating in living systems that may be difficult to formalize verbally.

Processes proceeding at the subcellular level (nano level) are organized via fundamental physical interactions between biological macromolecules like proteins, lipids, DNA, and small chemical molecules (e.g., H_2O, K^+, Na^+, Cl^- and other ions) within cell structures such as cell membranes and subcellular organelles.

Mathematical biophysics, combined with modern experimental techniques, constitutes a powerful instrument for understanding how physical laws operate in complex biological systems. Cell processes such as electron transport in

photosynthetic and mitochondrial membranes and selective ion transport across biological membranes illustrate this approach.

However, mathematical simulation also presents a considerable challenge in living systems. Unlike physics, where mathematics is a generally accepted inherent instrument of analysis, mathematical models in biology and biophysics must correspond to actual, observed biological phenomena. The term *model* itself emphasizes that certain qualitative and quantitative characteristics of the processes in a living system are presented in abstract, idealized forms, expressed mathematically, and thus differ from the qualitative description of the system usually accepted in biology.

To analyze processes where biomacromolecules are involved, the approaches of physics, quantum mechanics, and thermodynamics are often employed. Mathematical modeling of intramolecular interactions between atoms and structural fragments of such molecules and their interactions with the aqueous environment and small compounds takes into account the unique structure of biomacromolecules (proteins, lipids, polynucleotides), which contain several thousand atoms, and is thus possible only with the use of powerful computer facilities.

Another large class of models of biochemical reactions, including enzyme reactions, have been well developed and thoroughly analyzed using mostly ordinary differential equations (ODEs). Through analytical and numerical analysis of these models, conditions for the generation of qualitatively new regimes such as multi-steady-state, self-oscillation, and quasistochastic regimes arising in the chains of metabolic reactions have been identified. This class also includes models of processes in active media, where local elements participate in biochemical reactions via diffusion and transport in space.

In cellular biophysics, these models describe processes in biological membranes, subcellular organelles (chloroplasts, mitochondria), and nerve pulse propagation. Since the 1990s, the theory of metabolic control has been actively developed and aimed at the examination of and search for maximally controllable stages in complex metabolic cycles of intracellular reactions.

Historically, the mathematical biophysics of complex systems was the first subdiscipline to emerge. It includes the models associated with systemic mechanisms that determine the behavior of complex systems. These are the models of population dynamics, which became an original "mathematical testing ground" for mathematical biology and biophysics. The basic models of population dynamics provided the basis for other models in cellular biology, microbiology, immunity, epidemiology, mathematical genetics, theory of evolution, and other areas. Simulation of multicomponent biological systems also revealed the dynamic regulatory mechanisms of cardiac activity, hematopoiesis, digestive tract, morphogenesis, production processes in plants, aquatic and terrestrial ecosystems, and finally processes in the biosphere.

Usually there are two approaches to modeling complex biological systems. Following the integrated and phenomenological approach, the system characteristics (variables) are revealed (for example, the total number of classes) and qualitative properties of their behavior in time are considered (the stability of a stationary

state, presence of oscillations, spatial heterogeneity). This approach is historically the oldest one and was developed in the dynamic theory of populations.

Another approach implies a detailed consideration of a system's elements and their interactions and the construction of an imitational model where parameters have clear physical and biological meanings. Such a model does not allow one to obtain a direct analytical solution, but if parts of the system are sufficiently investigated experimentally, then the model can quantitatively forecast the system's behavior under various external conditions. Due to the enormous capabilities of modern information technologies, such models can provide knowledge about the system in distributed databases and simulate thousands of processes in great detail.

In phenomenological models, the property of *self-reproduction* is often expressed in equations by autocatalytic terms responsible for exponential growth under unlimited conditions. This term, in a mathematical sense, is necessary for the instability of a stationary state in local systems (the necessary condition for the emergence of oscillatory and quasistochastic regimes) and for the instability of a homogeneous stationary state in spatially distributed systems (the condition of spatially inhomogeneous distribution and autowave regimes). Transport processes play an important role in the development of complex spatiotemporal regimes, whether chaotic (diffusion) or directed by exterior forces (gravity, electromagnetic fields) or cellular structural elements (motion of cytoplasm in cells under the action of microfilaments).

Living systems have a complex *spatial structure*. Living cells and their organelles have membranes, and any living organism contains an enormous number of membranes whose total area reaches tens of hectares. It is natural, then, that the medium inside the living system cannot be considered homogeneous. The emergence of such a spatial structure and the laws of its formation represent one of the main problems in modern biology and biophysics. The nonlinearity of spatial distribution and transfer processes stipulates the patterns of stationary structures (spots on the skin of various shapes, periodic dissipative structures) and the types of autowave behavior (e.g., moving fronts, traveling waves, leading centers, spiral waves).

The mathematical theory of morphogenesis is one of the approaches aimed at solving this problem. Spatial heterogeneity is usually described by means of compartmental models or partial differential equations. New computer approaches allow us to simulate the processes in the complex interior of living cells. The specific processes in photosynthetic membranes will be considered in Part IV of this book.

Membranes separate reaction volumes in a living cell and separate biotic and abiotic media. They play a key role in metabolic selectivity, allowing flows of inorganic ions and organic molecules to proceed or preventing them. Thus, in the membranes of chloroplasts, the primary photosynthetic process of the accumulation of light energy in the form of macroergic chemical compounds occurs. The key stages of the breathing process occur in the membranes of mitochondria; the membranes of nerve cells determine their capability to conduct nerve impulses.

Mathematical models of the processes in biological membranes comprise a significant portion of mathematical biophysics. Existing models are mostly presented by systems of differential equations. However, it is obvious that continuous models cannot describe in detail the processes in discrete and structured systems such as living systems. As the computational, graphical, and intellectual capabilities of computers develop, the role of imitational models based on the discrete mathematics in mathematical biophysics increases.

As a rule, imitational models of complex living systems take into account all available information about a given object. Imitational models are employed to describe objects at different levels of organization of living matter: from biomacromolecules to ecosystems. In the latter case, the models must include blocks describing both living and "inert" components. Models of molecular dynamics are a classic example of imitational models—they include coordinates and moments of all atoms that constitute a biomacromolecule. The interactions of these biomacromolecules in turn are governed by prescribed laws. Patterns of life systems simulated by a computer allows one to follow the manifestation of physical laws in the functioning of the simplest biological objects—biomacromolecules and their environment. Similar models, in which the elements (bricks) are not atoms but groups of atoms (coarse-grain models), are employed in modern methods of the computer modeling of biotechnological catalysts and therapeutics that act upon certain active groups of membranes of microorganisms and viruses or perform some other directed actions.

Imitational models were created to describe the physiological processes that occur in vitally important organs such as nerve tissue, heart, brain, digestive tract, and blood vessels. These models are used to simulate "scripts," courses of development of processes that occur normally and in various pathologies, and to examine the effect of various exterior impacts on these processes, including directed therapies.

We would like to thank all our colleagues, collaborators, and students whose results are presented in this book: Anna Abaturova, Natalia Belyaeva, Dmitry Chernavskii, Eugene Grachev, Olga Knjazeva, Ilia Kovalenko, Anastasia Lavrova, Stefan Muller, Tatjana Plyusnina, Andrei Polezhaev, Yury Romanovsky, Natalja Stepanova, Lada Tjorlova, Dmitry Ustinin, Ludmila Yakushevich, and others.

Special thanks to Sergei Khrushchev and Alexandra Diakonova for their assistance in preparing the manuscript of this book for publication.

Moscow, Russia — Andrew Rubin
Moscow, Russia — Galina Riznichenko

Contents

Part I Basic Models in Mathematical Biophysics

1 Growth and Catalysis Models 3
Unlimited Growth, Exponential Growth, Self-Catalysis (Autocatalysis) 3
Limited Growth: Verhulst Equation 4
Constraints with Respect to Substrate: Models of Monod and Michaelis–Menten 6
Competition, Selection 8
Jacob and Monod Trigger System 10
Classic Lotka and Volterra Models 11
Models of Species Interactions 13
Models of Enzyme Catalysis 16
Model of a Continuous Microorganism Culture 17
Age-Structured Populations 19
Leslie Matrices 22
Continuous Models of Age Structure 23

2 Oscillations, Rhythms, and Chaos in Biological Systems 25
Oscillations in Glycolysis 25
Intracellular Calcium Oscillations 27
Deterministic Chaos 28
Chaos in Community of Three Species 31
Periodic Supply of Substrate in System of Glycolysis 32

3 Spatiotemporal Self-Organization of Biological Systems 35
Waves of Life 36
Autowaves and Dissipative Structures 39
Basic Brusselator Model 40
Localized Dissipative Structures 43
Belousov–Zhabotinsky Reaction 43

4 Model of Impact of a Weak Electric Field on Nonlinear System of Transmembrane Ion Transport 55
Transmembrane Ion Transport Model 56
Bistable Model 60
Auto-oscillating System 63

Part II Models of Complex Systems

5 Oscillations and Periodic Space Structures of pH and Electric Potential Along the Cell Membrane of Algae *Chara corallina* 69
Kinetic Model of Proton ATPase (Pump) 70
Equation Describing Dynamics of Proton Concentration in Vicinity of Cell 72
Equation for Potential Dynamics 73
Oscillations in Local System 75
pH Patterns Along Cellular Membrane 75
Dependence of Processes on Light Intensity: Hysteresis 76
Scheme of Interactions of Photosynthesis and Ion Fluxes Leading to Nonlinear Dynamics 79

6 Models of Morphogenesis 83
Turing Instability 83
Morphogenetic Field 90
Model of a Distributed Trigger 91
Animal Coat Markings 95
Models of Amoeba Aggregation. The Role of Chemotaxis 99

7 Autowave Processes, Nerve Pulse Propagation, and Heart Activity 103
Experiments and Model of Hodgkin and Huxley 105
Reduced FitzHugh–Nagumo Model 107
Excited Element of Local System 107
Running Pulses 109
Detailed Models of Cardiomyocytes 111
Axiomatic Models of Excited Medium: Autowave Processes and Cardiac Arrhythmia 111

8 Nonlinear Models of DNA Dynamics 117
Hierarchy of Structural and Dynamic Models 121
Linear DNA Theory 123
Simple Linear Model of an Elastic Bar 123
Nonlinear Models of DNA Mobility: Mechanical Analog 126
Mathematical Model Simulating Single DNA Base's Nonlinear Oscillations 130
Physical Analogs of Real DNA Sequences 133
Long-Range Effects 135
Nonlinear Mechanisms of Transcription Regulation 137

Part III Kinetic Models of Photosynthetic Processes

9 Models of Photosynthetic Electron Transport: Electron Transfer in a Multienzyme Complex 141
Organization of Processes in Photosynthetic Membrane 142
Kinetic Description of Redox Reactions in Solution 146
Modeling Electron Transfer in a Multienzyme Complex 148
Electron Transfer in a Two-Component Complex 148
Electron Transfer in an *n*-Carrier Complex 150
Electron Transport via Mobile Carriers 152
Electron Transport in an Isolated Photosynthetic Reaction Center 153

10 Kinetic Model of Interaction of Two Photosystems 157
Types of Regulation of Photosynthetic Processes 157
Model of PSI and PSII Interaction 158
Subsystem PSII 159
Scheme of PSII States 160
Charge Separation 161
Submodel of PSI 163
Description of Mobile Carrier Redox Evolution 165
Relationships Between Total Concentrations of Electron Carriers 166
Modeling of Electron Transport Chain of Wild-Type and Mutant *Arabidopsis thaliana* 167

11 Detailed Model of Electron Transfer in PSII 171
Fluorescence as an Indicator of the State of the Photosystem 171
Scheme of PSII States 173
Equations Describing Processes in PSII 175
Dependence of Rate Constants on Thylakoid Transmembrane Electric Potential 177
Energy Loss Processes 178
Experiment 178
Description of Events in PSII Electron Transport System After a Short Light Flash 180

12 Generalized Kinetic Model of Primary Photosynthetic Processes 187
Model Structure 187
Photosystem II Complex 188
Cytochrome b_6f Complex 190
Photosystem I Complex 192
Mobile Carriers in Kinetic Model 193
Role of Transmembrane Electric Potential 194

Transmembrane Ion Transfer and $\Delta\mu_{H^+}$ Generation 194
Buffer Properties of Lumen and Stroma 195
Parameter Values 196
Simulation of Fluorescence Transients at Different Light Intensities 197
Role of Different States of Photosystem II in Fluorescence Induction 198
Simulation of $\Delta\Psi$ Kinetics 200

Part IV Direct Multiparticle Models of Processes in Subcellular Systems

13 Method of Direct Multiparticle Simulation of Protein Interactions 205
Restricted Diffusion of Mobile Electron Carriers in Photosynthetic Membrane 206
Direct Model Environment 207
Brownian Dynamics of Mobile Carriers 208
Simulation of Cyclic Electron Transport Around Photosystem I 210

14 Modeling of Protein Complex Formation in Solution with Diffusion and Electrostatic Interactions 213
Steps of Redox Protein Interactions 213
Model of Protein–Protein Interaction in Solution 214
Protein Diffusion. Approximation with Ellipsoids of Revolution 215
Simulation of Geometric Shape of Proteins and Their Collisions 217
Electrostatic Interactions 219
Simulation of Complex Formation 223
Docking Rate Constant Dependence on Ionic Strength of Solution 224
Comparative Analysis of Interaction of Pc with Cyt f and PSI Reaction Centers in Higher Plants and Cyanobacteria. Role of Electrostatics 226

15 Modeling of Protein Interactions in Photosynthetic Membrane . . . 231
Interaction of Pc with Cyt f in Thylakoid Lumen 232
Modeling of Pc–PSI Interaction Considering Membrane Surface Charge and Multienzyme Complexes Embedded in Membrane 233
Modeling of Pc Interaction with Cyt f and PSI considering Membrane surface charge and Mulienzyme complexes Embedded in Membrane 235

16 Spatiotemporal Evolution of Electrochemical Potential $\Delta\mu_{H+}$ in Photosynthetic Membrane 241
Modeling of Proton Transfer 241
Model of Proton Release into Lumen 243
Model of Lateral Diffusion of Protons 244
Proton Flow Through ATP–Synthase and ATP Synthesis 245
Computer Simulation of Proton Gradient Evolution and ATP Creation 245

Conclusion 249

References 251

Index 269

Part I
Basic Models in Mathematical Biophysics

Chapter 1
Growth and Catalysis Models

In mathematical biophysics, as in any science, there are simple models that lend themselves to analytic examination and possess properties that allow a whole spectrum of natural phenomena to be described. Such models are called basic. For example, in physics, a harmonic oscillator (a ball, a material point, on a spring without friction) is one such basic model.

First, with a basic model the essence of analyzed processes is examined in detail mathematically, and then, by analogy, the phenomena that occur in much more complex real systems can be understood.

Many biologically dynamic properties such as the existence of two or more stationary regimes, self-oscillating regimes (biorhythms), spatial nonhomogeneities, and quasistochasticity can be demonstrated using comparatively simple nonlinear dynamic models, which play the role of basic models in mathematical biophysics.

Unlimited Growth, Exponential Growth, Self-Catalysis (Autocatalysis)

The rate of growth is proportional to the population numbers, regardless of whether it is a population of rabbits or cells. This is one of the fundamental assumptions underlying all models of growth. For many single-cell organisms or for cells in tissues, proliferation means simple division, that is, the number of cells doubles in a certain time interval, which is called the characteristic division time. Proliferation of plant and animal cells follows more complicated laws; however, in the simplest model, one may assume that the proliferation rate of species is proportional to their numbers.

This can be written mathematically in the form of a differential equation that is linear with respect to variable x characterizing the numbers (concentration) of individuals in a population:

A. Rubin and G. Riznichenko, *Mathematical Biophysics*, Biological and Medical Physics, Biomedical Engineering, DOI 10.1007/978-1-4614-8702-9_1,

© Springer Science+Business Media New York 2014

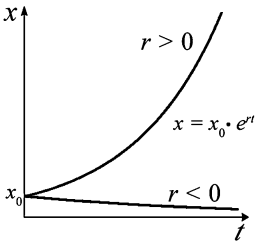


Fig. 1.1 Exponential growth dynamics according to (1.1) and (1.2)

$$\frac{dx}{dt} = rx. \tag{1.1}$$

Here r can be, in a general case, a function of both numbers and time or depend on other exterior and interior parameters.

The law (1.1) was formulated by Thomas Robert Malthus (1766–1834) in his book *An Essay on the Principle of Population* (1798). Equation (1.1) shows that if the proportionality coefficient $r = \text{const}$, $r > 0$ (as Malthus assumed), then the numbers grow exponentially and without limits, and if $r < 0$, then the population numbers drop exponentially (Fig 1.1) according to the formula

$$x = x_0 e^{rt}, \quad x_0 = x \ \ (t = 0). \tag{1.2}$$

For most populations limiting factors exist, and population growth terminates due to a variety of reasons. Human population is not an exception: over historical time, its numbers have increased faster than exponentially, but in recent decades its development has demonstrated a tendency toward limited growth. The investigations performed by Malthus greatly influenced both economists and biologists. In particular, Charles Darwin analyzed Malthus's theory in detail in his diaries. Darwin believed the struggle for existence between organisms was one of the causes of failure of Malthus's law in nature.

The law of exponential growth is valid at a certain growth stage for cell populations in tissue, or for algae or bacteria in a culture. In modeling, a mathematical expression that describes a population's increase in size is referred to as an autocatalytic term (catalysis means modification of the reaction rate, usually its increase, with the help of substances that do not participate in the reaction), and *autocatalysis* means "self-acceleration" of a reaction.

Limited Growth: Verhulst Equation

The Verhulst model (1838) is a basic model that describes limited growth:

$$\frac{dx}{dt} = rx\left(1 - \frac{x}{K}\right). \tag{1.3}$$

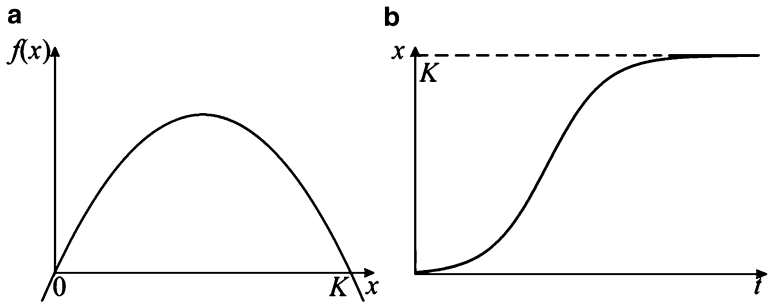


Fig. 1.2 Limited growth: (**a**) dependence of growth rate on numbers; (**b**) time dependence of numbers for logistic equation

Parameter K is called the population capacity and is expressed in units of numbers (concentration); depending on a system's properties, it is determined by a number of different factors. Among the latter are the limitations of the amount of the substrate consumed by microorganisms, the area available for cell populations in tissue, food, or refuge for superior animals. Diagrams of the dependence of the right-hand side of (1.3) on the numbers x and changes of population numbers in time are presented in Fig. 1.2a, b.

Examination of a discrete analog of (1.3) in the second half of the twentieth century revealed its new and wonderful properties. Consider the population numbers at sequential times, which corresponds to a real procedure of assessing population numbers (or cells). The dependence of the numbers at a time step $n + 1$ on the numbers at the preceding step n can be written as

$$x_{n+1} = rx_n(1 - x_n). \tag{1.4}$$

The behavior of the variable x_n in time depending on the parameter r can be characterized not only by limited growth, as it was in the continuous model (1.3), but it can also become oscillating or quasistochastic, as is shown on the right in Fig. 1.3. The gradient of the curve $F(N)$ at the origin, which corresponds to the parameter of intrinsic growth rate r, increases from top to bottom. The curves representing the dependence of the numbers at a given time $(t + 1)$ on the numbers at the preceding time t are depicted on the left in Fig. 1.3; this rate increases at small numbers and, at higher numbers, decreases and then vanishes. The type of the dynamics of the population growth curve depends on the growth rate at small r numbers, i.e., it is determined by the derivative (the tangent of the inclination angle of this curve) at zero. For small r ($r < 2$), the population numbers approach stable equilibrium. When the diagram on the left becomes steeper, stable equilibrium transforms into stable cycles. As the numbers increase, the cycle length increases, and every 2, 4, 8, …, 2^n generations the values of the numbers repeat. At the value $r > 2.570$, chaotization of solutions happens. At r sufficiently large, the population dynamics demonstrate chaotic spikes (outbursts of the numbers). Equations of this type describe the number dynamics of seasonally multiplying insects with nonoverlapping generations.

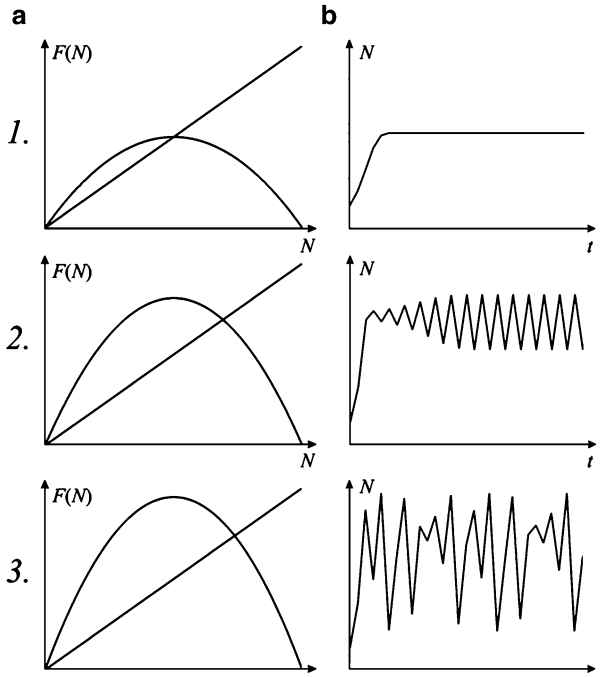


Fig. 1.3 (**a**) Dependence of numbers at subsequent step on numbers at preceding step. (**b**) Behavior of numbers at different values of parameter r for discrete model of logistic growth (1.4): (1) limited growth, (2) oscillations, (3) chaos

The discrete description proved to be useful for systems of a different nature. The presentation of the dynamic behavior of the system on the plane $[x_t, x_{t+T}]$ allows one to determine whether the observed system is oscillatory or quasistochastic. For example, such a representation of cardiogram data made it possible to establish that normal systoles of the human heart are of an irregular nature, while during breast pangs or in a preinfarct state, the systolic rhythm becomes strictly regular. Such a "rigid" mode is a defensive reaction of an organism in a stress situation that evolved as a response to danger.

Constraints with Respect to Substrate: Models of Monod and Michaelis–Menten

Shortage of food is one of the limiting growth factors (in microbiological language, *substrate limitation*). It is well known from biological studies that under conditions of substrate limitation, the growth rate increases proportionally to the substrate concentration and in the abundance of substrate becomes constant and is determined by the genetic capabilities of the population. For a certain period the

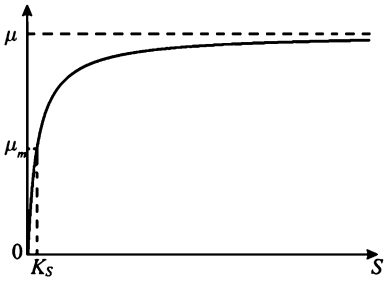


Fig. 1.4 Dependence of growth rate constant on substrate concentration (1.5)

population numbers increase exponentially until the growth rate becomes limited by some other factors. The dependence of the growth rate r in (1.1) on the substrate can be presented in the form as shown in Fig. 1.4:

$$r(S) = \frac{\mu_s S}{K_S + S}. \tag{1.5}$$

Here, K_S is a constant equal to the substrate concentration at half the growth rate of its maximum value, and μ_s is the maximal growth rate equal to r in (1.2). Equation (1.5) was written for the first time by the outstanding French biochemist Jacques Monod (1942, 1950), who, in collaboration with Francoise Jacob, developed a concept of gene regulation. According to their theory, a structural gene (the one from which mRNA is synthesized) is controlled by a regulator gene (promotor), which affects a region of the structural gene called the operator (Monod and Jacob 1961). They called this set of DNA regions the *operon*. This mechanism proved to be operating in bacteria, and both scholars (along with Andre L'vov) were awarded the Nobel Prize in Physiology or Medicine in 1965. Jacques Monod was also a philosopher of science and an exceptional writer. In his famous book *Chance and Necessity* (Monod 1971) he expressed his thoughts on the accidental origins of life on Earth and evolution, and also on the role of humans and their responsibility for the processes that occur on Earth.

The form of the Monod model (1.5) strongly resembles the Michaelis–Menten equation (1913), which describes the dependence of the rate of an enzymatic reaction on the substrate concentration when the total number of enzyme molecules is constant and much less than the number of substrate molecules:

$$\mu(S) = \frac{\mu_0 S}{K_m + S}. \tag{1.6}$$

Here, K_m is the Michaelis constant, one of the most important parameters of enzyme reactions. It can be determined experimentally as the substrate concentration at half of the maximal reaction rate. The Michaelis–Menten law is derived on the basis of chemical kinetics equations and describes the rate of formation of a product according to the scheme

$$E + S \Leftrightarrow [ES] \Leftrightarrow E + P$$

It can be argued that empirical Monod formula has close resemblance with the Michaelis–Menten formula because the enzymatic reactions underlie the vital activity and growth rates of microorganisms.

Competition, Selection

In biological systems constituents interact with each other at all levels, whether in interactions of macromolecules in biochemical reactions or interactions of species in populations. Such interactions can lead to a certain set of states at subcellular, cellular, and organism levels. The kinetics of the processes in the corresponding structures is described by mathematical models, which as a rule are comprised of equations for the probabilities of the states generated in a system.

In the case of random interaction, the rate is determined by the concentration of interacting components and by their mobility (diffusion). These are the concepts that are accepted in basic models of species interaction. The monograph by Vito Volterra *Mathematical Theory of the Struggle for Existence* (1931), where mathematical models of species interaction were considered, became a classical work (Scudo 1971; Israel 1988). In that book, the characteristics of biological objects and their interactions are presented in mathematical form and then examined as mathematical objects.

Vito Volterra (1860–1940) acquired worldwide renown from his results in the field of integral equations and functional analysis. Besides pure mathematics, he was interested in the application of mathematical methods in biology, physics, and social sciences. During his years in the Italian air force, he was seriously engaged in research on military engineering and technology (problems of ballistics, bombing, and echo sounding). His personality combined scientific talent with the temperament of an active politician; he was a principled opponent of fascism. He was the only Italian senator to vote against the transfer of power to Mussolini. During the years of fascist dictatorship in Italy, Volterra was working in France. Mussolini, who wanted to bring the world famous scholar over to his side, offered Volterra various high positions in fascist Italy but always received a firm refusal. Because of his antifascist position Volterra rejected the position of chair of the department of mathematics at the University of Rome and membership in Italian academic societies.

Volterra became seriously interested in the dynamics of populations in 1924 following discussions with a young zoologist named Umberto D'Ancona, the future husband of his daughter Louisa. D'Ancona, while examining the statistics of fish markets in Adriatic, established a curious fact: when in the years of the First World War (and immediately after) fishing intensity dropped sharply, the relative portion of predator fish in catches increased. This effect was predicted by a predator–prey model proposed by Volterra (1924).

Volterra assumed, by analogy with statistical physics, that interaction strength is proportional to the probability of encounter (collision probability for molecules), that is, to the product of concentrations. These and other assumptions made it

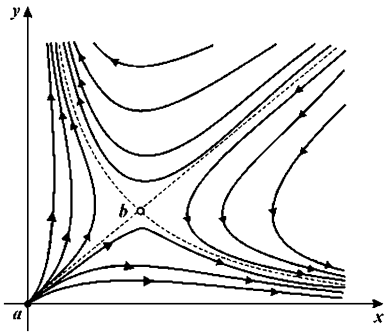


Fig. 1.5 Phase portrait of system (1.7), which describes selection of one of two equal species in the absence of constraints to growth. (**a**) Origin—unstable node. (**b**) Saddle

possible to construct a mathematical theory of the interactions between populations on the same trophic level (competition, symbiosis) or on different trophic levels (predator–prey, parasite–host).

The simplest of these models—the model of selection on the basis of competitive relations—considers competitive interactions of any kind: optical isomers (L and D amino acids), competing cells, species, and populations. Its modifications can be applied to describe competition in economy. Let us consider two absolutely identical antagonist (meaning if they encounter each other one suppresses the other) species with the same proliferation rate. A model of their interaction can be written as (Chernavskii 1986, 2000; Romanovsky et al. 2004) (Fig. 1.5)

$$\begin{aligned} \frac{dx}{dt} &= ax - bxy, \\ \frac{dy}{dt} &= ay - bxy. \end{aligned} \tag{1.7}$$

According to this model, a state in which only one of the two species exists is unstable: one of the interacting species inevitably dies out, while the other proliferates infinitely. The introduction of a limit to substrate (1.5) or intrapopulational competition ($-x^2$) makes it possible to construct models in which one of the species survives and reaches certain stable numbers. Such models describe Gause's principle—a competition principle well known in experimental ecology—according to which only one species survives in every ecological niche.

In cases where species possess different intrinsic growth rates, the coefficients of the autocatalytic terms are different, and the system's phase pattern becomes asymmetrical. Various ratios of parameters in such a system give rise to two possibilities: the survival of one of the two species with the extinction of the other (if the mutual suppression is more intense than self-regulation of their numbers) and the coexistence of both species (when mutual suppression is less pronounced than the self-limitation of each species).

Jacob and Monod Trigger System

The Jacob–Monod model of the alternative synthesis of two enzymes presented in Fig. 1.6a is another classic model of bistable systems. A regulator gene in each scheme synthesizes an inactive repressor. This repressor combines with the product of the opposite system of enzyme synthesis and forms an active complex. The active complex reversibly reacts with a structural portion of the gene called the operon and blocks synthesis of mRNA. Thus the product of the second system P_2 becomes a corepressor of the first system. The same is true of the second gene, so P_1 is a corepressor of the second system. One, two, or more molecules can participate in the corepression process. Obviously, under such interactions the second system will be blocked by the intense activity of the first system and vice versa. Models of this system were proposed and thoroughly examined by Goodwin (1984) and Chernavskii (Romanovsky et al. 1975, 2004). After relevant simplifications, equations describing the synthesis of the products P_1 and P_2 take the following form:

$$\begin{aligned} \frac{dP_1}{dt} &= \frac{A_1}{B_1 + P_2^m} - q_1 P_1, \\ \frac{dP_2}{dt} &= \frac{A_2}{B_2 + P_1^m} - q_2 P_2. \end{aligned} \tag{1.8}$$

Here, P_1 and P_2 are concentrations of the products, and A_1, A_2, B_1, and B_2 depend on the parameters of the systems. The power index m shows how many molecules of the active repressor (complexes of the product molecules with molecules of the inactive repressor, which is assumed to be in abundance) combine with the operon to block mRNA synthesis. A phase diagram of the system (the trajectories of a system under different initial conditions on the coordinate plane, where the system variables are marked on the axes) at $m = 2$ and certain relations between

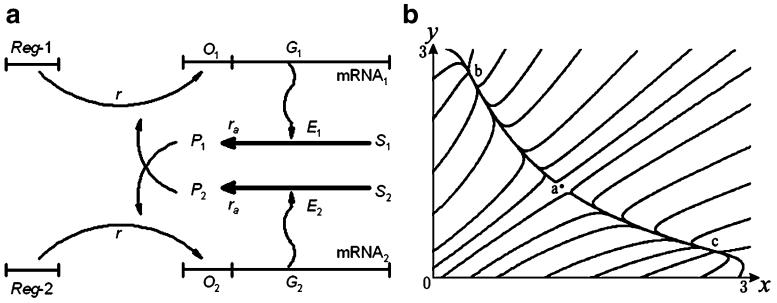


Fig. 1.6 (**a**) Jacob–Monod scheme for synthesis of two enzymes. (**b**) Phase portrait of trigger system (1.8). **a**, **c** Stable nodes. **b** Saddle (unstable point). Parameter values: $A_1 = A_2 = 3$; $B_1 = B_2 = 1$; $q_1 = q_2 = 1$; $m = 2$

the remaining variables are shown in Fig. 1.6b. Jacob–Monod scheme for synthesis of two enzymes has a trigger character, like the system of two competing species. The similarity suggests that the competition of species, enzymes, and states underlies the system's ability to switch between two possibilities. The ability of a trigger to switch from one stationary state to another is an important property of models of cellular cycles, differentiation, and others.

The system can be "tossed" over the separatrix in two ways: forcibly, by adding a sufficient amount of the substance of which there was less in the initial state, or parametrically, by changing the character of the phase portrait so that the initial stable state of the system becomes unstable (the transition through the saddle–node bifurcation). Thus the system acquires only one stable steady state. This type of regulation was proposed in models of cell cycles. Moreover, the change in the system parameters can be conditioned by a genetic program, as in the case of the cell cycle in the process of cell growth.

Classic Lotka and Volterra Models

The simplest nonlinear Lotka and Volterra models made it possible for the first time to demonstrate the existence of oscillations in energetically rich systems due to the specificity of interactions between their constituents. An equation formulated by Lotka in 1925 in the book *Elements of Physical Biology* (Lotka 1925) describes a system of the following chemical reactions:

$$\rightarrow \mathrm{A} \xrightarrow{k_0} \mathrm{X} \xrightarrow{k_1} \underset{\leftarrow}{\mathrm{Y}} \xrightarrow{k_2} \mathrm{B}$$

In a medium, substance A is in abundance. Molecules of A in turn convert into molecules of X (zero-order reaction) at a constant rate (rate constant k_0). Substance X can convert into substance Y, and the rate of this reaction increases with the concentration of substance Y (second-order reaction). This is shown by the reverse arrow over the symbol Y in the scheme. In turn, molecules of Y decompose irreversibly, and as a result, substance B forms (first-order reaction). The system of equations describing this reaction has the form

$$\begin{aligned} \frac{dx}{dt} &= k_0 - k_1 xy, \\ \frac{dy}{dt} &= k_1 xy - k_2 y, \\ \frac{dB}{dt} &= k_2 y. \end{aligned} \tag{1.9}$$

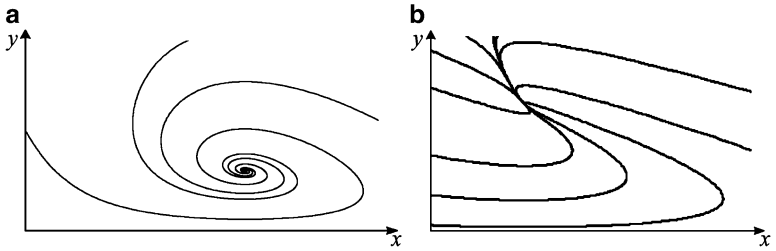


Fig. 1.7 Lotka model of chemical reactions. (**a**) Phase portrait of system for parameter values corresponding to damped oscillations—stable spiral; values of parameters: $k_0 = 2,\ k_1 = 2,\ k_2 = 4$. (**b**) Stable node; values of parameters: $k_0 = 2,\ k_1 = 10,\ k_2 = 2$

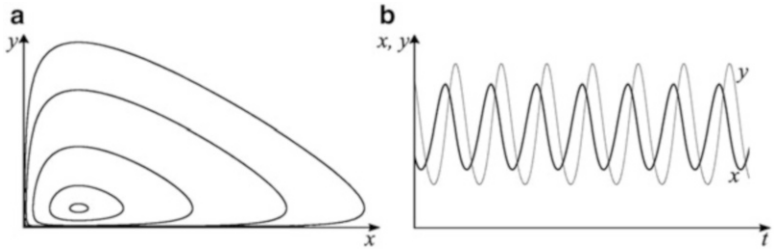


Fig. 1.8 Volterra predator–prey model describing continuous oscillations of numbers. (**a**) Phase portrait. (**b**) Time dependence of numbers of predators and prey. Values of parameters: $a = 1;\ b = 0.5;\ c = 1;\ d = 2$

Here, x, y, and B are concentrations of chemical components. The first two equations of the system are independent of B; therefore, they can be considered separately. In this system, at certain values of the parameters, damped oscillations are possible (Fig. 1.7a).

The classic Volterra equation describing predator–prey interactions of species is a basic model of continuous oscillations. As in the models of competition (1.8), interaction between species is described according to the principles of chemical kinetics: the decrease in prey numbers (x) and the gain in predator numbers (y) are believed to be proportional to their product:

$$\begin{aligned} \frac{dx}{dt} &= ax - bxy, \\ \frac{dy}{dt} &= cxy - dy. \end{aligned} \tag{1.10}$$

A phase portrait of this system is presented in Fig. 1.8. The numbers of prey (x) and predators (y) are marked on the axes. It can be seen that the numbers of predators and prey oscillate in antiphase. The simplest Volterra model (1.10) has an essential drawback: the oscillation characteristics of its variables vary with the fluctuations of the system parameters and variables.

Models of Species Interactions

In the middle of the twentieth century, thanks to the rapid development of computing facilities, it became possible to solve and examine rather complex systems of nonlinear equations. As a result, population dynamics simulations developed extensively. The problem was to search for general criteria to establish models that could describe the main features of the behavior of population dynamics and, in particular, stable oscillations.

These studies proceeded in two directions. The first direction considered only the qualitative properties of the functions of model systems, such as positivity, monotony, and larger–smaller relations (Kolmogorov 1972; Rosenzweig and MacArthur 1963; Pielou 1969, 1977; MacArthur 1970; Nisbet and Gurney 1982). Followers of the second direction developed models where interactions of species were described as close as possible to real systems, and the results were comparable to observed or experimental data.

Kolmogorov's work of 1935, revised in 1972, (Kolmorov 1972) can serve as an example of the qualitative direction. He considered a generalized model of interactions between biological species, a predator–prey or parasite–host scheme. The model is presented as a system of two equations of the general type

$$\begin{aligned} \frac{dx}{dt} &= k_1(x)x - L\big(x\big)y, \\ \frac{dy}{dt} &= k_2(x)y. \end{aligned} \tag{1.11}$$

In this model, the following assumptions are made:

1. Predators do not interact with each other, i.e., the proliferation coefficient of predators k_2 and the number of prey L consumed by one predator in a unit of time do not depend on y.
2. The increment in the number of prey in the presence of predators is equal to the increment in the absence of predators minus the number of prey consumed by predators. The functions $k_1(x)$, $k_2(x)$, and $L(x)$ are continuous and defined on the positive semiaxes $x, y \geq 0$.
3. $dk_1/dx < 0$. This means that the proliferation coefficient of prey in the absence of predators monotonously decreases with an increase in prey numbers, which reflects the limitation of food and other resources.
4. $dk_2/dx < 0$, $k_2(0) < 0 < k_2(\infty)$. The proliferation coefficient of predators decreases monotonously with prey numbers, going from negative values (when there is nothing to eat) to positive values.
5. The number of prey consumed by one predator in a unit of time $L(x) > 0$ for $N > 0$; $L(0) = 0$.
6. Possible patterns of phase diagrams of system (1.11) are presented in Fig. 1.9.

Steady states (two or three) have the following coordinates:

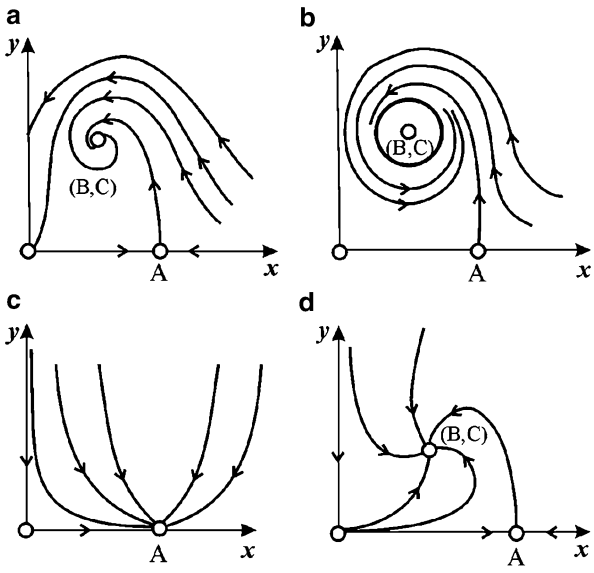


Fig. 1.9 Phase patterns of Kolmogorov system (1.11) describing two species interaction at different ratios of parameter values (Kolmogoroff 1972). See description in text

1. $\overline{x}_1 = 0, \quad \overline{y}_1 = 0$
2. $\overline{x}_2 = A, \quad \overline{y}_2 = 0$

Value A can be found using the equation $k_1(A) = 0$.

3. $\overline{x}_3 = B, \quad \overline{y}_3 = C$

Values B and C can be defined from the equations

$$k_2(B) = 0; \quad k_1(B)B - L(B)C = 0.$$

Let us consider the stability type of the steady states. The point $\overline{x}_1 = 0$, $\overline{y}_1 = 0$ is a saddle at all parameter values (Fig. 1.9a–d).

The point $\overline{x}_2 = A$, $\overline{y}_2 = 0$ is a saddle if $B < A$ (Fig. 1.9a, b, d) and a stable node if $B > A$. This case, which corresponds to the death of a predator and the survival of prey, is presented in Fig. 1.9c.

The point $\overline{x}_3 = B$, $\overline{y}_3 = C$ is a spiral (Fig. 1.9a) or a node (Fig. 1.9d), and its stability depends on the parameter value σ:

$$\sigma^2 = -k_1(B) - k_1(B)B + L(B)C.$$

If $\sigma > 0$, then the point is stable; if $\sigma < 0$, then the point is unstable, and limit cycles can exist around it (Fig 1.9b).

An analysis of model (1.11) and its special cases, for example, the Rosenzweig model (1969), leads to the conclusion that regular oscillations in the system take

place if the number of predators is limited by the presence of prey. If the prey number is limited by the presence or absence of the resources they need, or the predator number is bounded not by the prey number but by some other factor, then damped oscillations occur. Damped oscillations also happen when there is a refuge for prey that makes them inaccessible to predators.

In the second direction, various modifications of the Volterra model were considered, including sequentially various additional factors in the original system (Holling 1959; MacArthur 1970; Rosenzweig and MacArthur 1963; Rosenzweig 1969; Bazykin 1985, 1998; Petrovskii and Malchow 1999; Ginzbourg and Colivan 2004; Riznichenko and Rubin 2004).

Modification of the Volterra model with regard to substrate limitations in the Monod form (1.5) and a description of the self-limitation of the numbers [as in (1.3)] led to a model examined by Bazykin in his book *Nonlinear Dynamics of Interacting Populations* (1998):

$$\begin{aligned} \frac{dx}{dt} &= Ax - \frac{Bxy}{1+px} - Ex^2, \\ \frac{dy}{dt} &= -Cy + \frac{Dxy}{1+px} - My^2. \end{aligned} \tag{1.12}$$

System (1.12) combines the properties of the basic equations (1.1), (1.3), (1.5), and (1.10). At small numbers and in the absence of predators, prey (x) will proliferate according to the exponential law (1.1); predators (y) in the absence of prey will also exponentially die out. If there are many individuals of one or the other kind, then, according to the basic model (1.3), the factor of Verhulst's system works (the term $-Ex^2$ in the first equation and the term $-My^2$ in the second one). The strength of the interaction between species is assumed to be proportional to the product of their numbers [as in model (1.10)] and is described in the Monod form [model (1.5)]; prey species play the role of substrate, and predator species play the role of microorganisms. The model allows for a description of complex types of behavior of interacting species, for example, the presence of two stable steady states, dumped oscillations of the numbers, and self-oscillations.

Computing facilities have made it possible to apply the results obtained with models (1.11) and (1.12) to analyses of specific populations, in particular, to resolve issues of, for example, efficient fisheries and hunting, and to develop biological methods of insect pest control.

A special problem is the development of criteria to evaluate the proximity of a system to a dangerous boundary. The crossing of this boundary causes the system either to cease to exist or to transform qualitatively into another state. In these cases, the population dynamics change dramatically, for example, a population either transitions from monotonous growth to sharp oscillations of its numbers or simply dies out. Such boundaries are referred to as *bifurcational* ones. Analysis of model properties shows that very slow restoration of the numbers after the impact of an unfavorable factor is one of the indicators of the closeness of a population to a

dangerous boundary. A change in the form of oscillations of predator and prey numbers is also an indicator of nearness to a dangerous boundary. If almost harmonic oscillations become relaxational, that is, the characteristic times of changes in numbers start to very more and more significantly increasing in time, this can result in the loss of system stability or in the extinction of one or both species.

Models of Enzyme Catalysis

It is known that enzymes are highly specialized catalysts that accelerate biochemical reactions by hundreds of thousands of times. All enzymatic transformations start with the bonding of substrate molecules in an active center of the enzyme and finish with the breaking of these bonds. A hypothesis on the formation of a substrate–enzyme complex was first suggested by Brown in 1902. Trying to qualitatively explain the phenomenon of amylase reaction saturation by substrates, Henri (1902, 1903) suggested that the reaction of enzyme–substrate complex formation is in equilibrium and derived an equation for the initial reaction rate:

$$\mu(S) = \frac{\mu_0 S}{K_\mathrm{M} + S}.$$

Michaelis and Menten in 1913 and later Briggs and Haldane in 1925 arrived at similar equations assuming a quasistationary character of the enzyme–substrate complex formation. In 1943 Chance experimentally confirmed the formation of such a complex using spectrophotometric methods and traced changes in its concentration in the course of a reaction catalyzed by the enzyme peroxidase. In 1930, Haldane extended theoretical concepts on the enzyme–substrate complex to the two-substrate case and reversible reactions and postulated the existence of different intermediate enzyme–substrate, enzyme–product, and enzyme–inhibitor complexes. To date, a large number of such complexes has been examined.

Inclusion of an inhibitor in a system, in particular when the substrate molecules play the role of an inhibitor and form both active and inactive complexes with the enzyme, leads to a more complicated and nonlinear expression for the reaction rate:

$$\mu(S) = \frac{\mu_\mathrm{m} S}{K_\mathrm{m} + S + AS^2}.$$

This type of nonlinearity highlights the important properties of enzyme systems: a multiplicity of steady states, the oscillatory character of changes in variables, and quasistochastic regimes. An analysis of kinetic features of various types of enzyme reactions using phase plane and parametric space representations is given in detail in Ivanitskii et al. (1978) and Murray (2002).

Model of a Continuous Microorganism Culture

Microbial populations are a good subject on which to experimentally verify the concepts and results of both ecological and evolutionary dynamic analysis. Microorganisms are mostly one-cellular organisms; they possess a high surface-to-volume ratio and, therefore, a high intensity of mass–energy exchange with the environment, and they have high proliferation rates. Usually, in mathematical descriptions of microbial populations, ODEs are used. Such an approach is more justified for microbiological systems compared to land and water higher organisms. In laboratory experiments in vitro, more than 10^{10} individual organisms are usually considered. In a large industrial cultivator, approximately 10^{16}–10^{17} yeast cells can live simultaneously. A deviation of the numbers from average values caused by random factors is proportional to $1/\sqrt{N}$, where N is the population numbers. Thus for numerous populations one can construct a model in terms of average numbers or concentrations. The relative homogeneity of microorganism cultures in cultivator medium is another factor that allows spatial effects to be disregarded.

In microbiology an empirical approach to the construction of models is commonly used. Of all the factors that affect cell growth, a limiting one is usually chosen, and then a dependence of the growth rate on its concentration is found empirically. Generally, the kinetics of cell concentration in a homogeneous culture is described by the equation

$$\frac{dx}{dt} = x(\mu - v), \tag{1.13}$$

where x is the cell concentration in a cultivator; μ is a function describing the proliferation of a population, which may depend on cell concentration x, substrate concentration, usually denoted by S, temperature, the pH of the medium, or other factors; and v is the rate of elution.

To keep culture in a region of unlimited growth, external regulators are required. In the case of growth limited by an external factor, for example, by the shortage of a substrate, the stable working regime of a cultivator is attained by self-regulation. This takes place in natural lotic systems and, in the most frequently used type of continuous cultivators, a hemostate, in which the dilution rate or flow velocity for a culture is set. Monod (1950) and Herbert (Herbert et al. 1956; Herbert, 1958) were the first to develop the hemostate theory, which has been continuously refined since then. In modern models, the structural nonhomogeneity of biomass, age-related nonhomogeneity, and other details of cultivation are taken into account.

Under conditions of continuous mixing it is possible to assume that the total cultivator medium is uniformly filled and that cell and substrate concentrations are the same at every point of a cultivator. Then the behavior of these concentrations over time can be described by a system of ODEs:

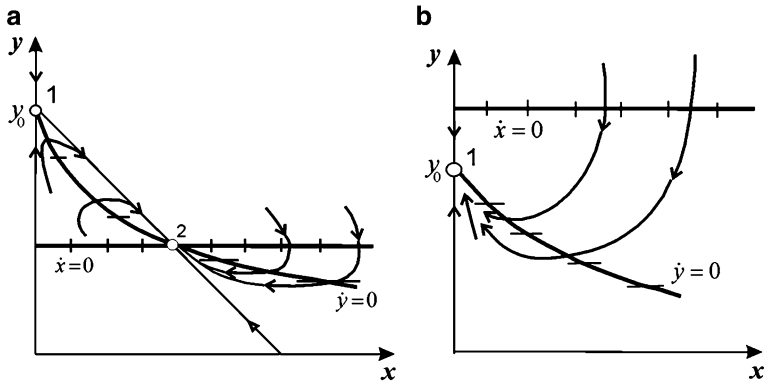


Fig. 1.10 Phase patterns for two cases: (**a**) operative mode; (**b**) washout regime. Phase diagrams for system (1.14); parameter values: $\alpha = 1$; $\mu_m = 1$; $K_m = 1$; $S_0 = 1$. The dilution velocity determines the regime: (**a**) $D = 0.2$—operative regime; (**b**): $D = 1$—washout regime

$$\begin{aligned} &\text{(a)} \quad \frac{dx}{dt} = \mu(S)x - Dx, \\ &\text{(b)} \quad \frac{dS}{dt} = DS_0 - \alpha\mu(S)x - DS, \\ &\text{(c)} \quad \mu(S) = \frac{\mu_m S}{K_m + S}. \end{aligned} \tag{1.14}$$

Here, S is the substrate concentration, x is the cell concentration in a cultivator, S_0 is the concentration of a substrate loaded into the cultivator, D is the flow (dilution) velocity of the culture, and α is the biomass yield indicating what fraction of the consumed substrate contributes to biomass increase. The meanings of other terms on the right-hand sides of the equations are as follows: $\mu(S)x$ is the biomass increment taking into account the consumed substrate, $-Dx$ is the outflow of biomass from a cultivator, $-\alpha\mu(S)x$ is the amount of substrate consumed by the cultured cells, DS_0 is the inflow of a substrate into a cultivator, and $-DS$ is the outflow of the nonutilized substrate from the cultivator. The growth rate of the biomass is assumed to be dependent only on the substrate concentration according to the Monod formula (1.5).

System (1.14) has two steady states:

1. $\overline{x}_1 = 0, \quad \overline{S}_1 = S_0$
2. $\overline{x}_2 = \alpha S_0\left(1 - \frac{D}{\mu_m - D}\right), \quad \overline{S}_2 = K_m \frac{D}{\mu_m - D}$

Their stability depends on the value D—the dilution velocity of the culture. If D is greater than the value $D_0 = \frac{\mu_m S_0}{K_m + S_0}$, called the *washout velocity*, then steady state (1) is stable, the substrate concentration in the cultivator is equal to the initial substrate concentration S_0, and the biomass concentration is equal to zero because at such a rapid dilution microorganisms do not have enough time to multiply in the cultivator.

If $D < D_0$, then steady state (2) is stable. Corresponding phase diagrams are presented in Fig. 1.10.

The considered model is simplified and requires some additional assumptions to describe real processes. For example, at high concentrations, a substrate can act as an inhibitor, and then the formula for the growth rate should be written as

$$\mu(S) = \frac{\mu_{\mathrm{m}} S}{K_{\mathrm{m}} + S + AS^2}. \tag{1.15}$$

In a system with such a dependence of the growth rate on the substrate, trigger regimes are possible, i.e., the presence of two stable steady states and the dependence of the steady concentrations of substrate and biomass on the initial conditions (on volume of yeast and on initial biomass concentration).

The growth rate of biomass can also be influenced by the concentration of products of metabolism in the surrounding cell medium. Then to the two equations describing the dynamics of biomass concentrations in continuous cultivation processes a third equation must be added describing the dynamics of metabolism product concentrations:

$$\mu(S) = \frac{\mu_{\mathrm{m}} S}{(K_{\mathrm{m}} + S)(K_P + P)}. \tag{1.16}$$

Formula (1.16) is known as the Monod–Jerusalemskii formula (Murray 2002; Romanovsky et al. 2004).

In biotechnology, to calculate the optimal cultivation regimes formulas are used that take into account other peculiarities of the metabolism of microorganisms themselves and of the conditions of their cultivation.

Age-Structured Populations

The homogeneity of cells in a microbial population is always relative. For example, age structure plays an important role in growth processes. Only cells of a certain age (or certain size) are capable of dividing, i.e., of increasing their numbers. The age heterogeneity of a population can be a cause of complex, nonmonotonic dynamics of its numbers.

The simplest two-age model of a cell population was proposed by Stepanova in 1985 (Romanovsky et al. 2004). A population is divided into two groups of cells: young and old. Cells of the first group grow intensively, but they are not physiologically mature and are incapable of dividing. Members of the second group are capable of dividing, and the fission process can be delayed with the help of inhibitors. Equations for the numbers of young (N_1) and old (N_2) cells have the form

$$\begin{aligned} \frac{dN_1}{dt} &= \frac{2}{T_2} N_2 - \frac{1}{T_1} N_1 - DN_1, \\ \frac{dN_2}{dt} &= \frac{2}{T_1} N_1 - \frac{1}{T_2} N_2 - DN_2. \end{aligned} \tag{1.17}$$

Here, T_1 is the average maturation time of a young cell, T_2 is the average reproduction period of an old cell, and D is the flow velocity. Multiplier 2 in the first equation reflects the fact that an old cell divides, forming two young cells. The assumption that old cells can secrete an inhibitor makes it possible to describe oscillatory regimes in a system.

Without substrate limitation on the duration of the first phase, T_1, is constant, and the duration of the second phase, T_2, depends on the mutual influence of cells via the metabolites excreted into the medium. If the rate of their excretion and dissociation is much greater than the rate of cell division, then the metabolite concentration can be considered proportional to the number of cells excreting these metabolites.

Let the concentration of an inhibiting metabolite be I. Its effect on the growth rate can be written in the form

$$T_2^{-1} = \omega = \omega_0 \left[1 + \left(\frac{I}{k_1} \right)^n \right]^{-1}.$$

Here ω_0 is the growth rate in the absence of inhibitor; I is the exponent n order of inhibition, and k_1 is the rate constant of inhibition.

Three cases were considered:

1. Only young cells excrete inhibitors.
2. Only old cells excrete inhibitors.
3. Both young and old cells excrete inhibitors.

Analysis of the model showed that the assumption about inhibition by old cells makes it possible to describe oscillations in a system. In terms of the model, it means that the growth rate depends on the number N_2:

$$\omega = \omega_0 \left[1 + \left(\frac{N_2}{N_1} \right)^n \right]^{-1}.$$

Let us introduce dimensionless variables and parameters:

$$x = \frac{N_1}{N_0}, \quad y = \frac{N_2}{N_0}, \quad t' = \frac{t}{T_1}, \quad \sigma = \omega_0 T_1, \quad \delta = D T_1.$$

In dimensionless form the system becomes

$$\begin{aligned} \frac{dx}{dt} &= -\frac{2\sigma y}{1 + y^n} - (\delta + 1)x, \\ \frac{dy}{dt} &= x - \delta y - \frac{\sigma y}{1 + y^n}. \end{aligned} \tag{1.18}$$

The prime on the time variable is omitted.

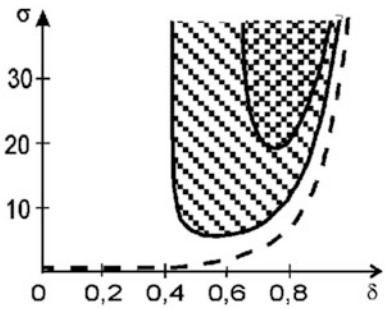


Fig. 1.11 Parametric domains of instability for nonzero steady state for $n = 2$ (*double grid*) and $n = 3$ (*simple grid*) (Stepanova from: Romanovsky et al. 2004)

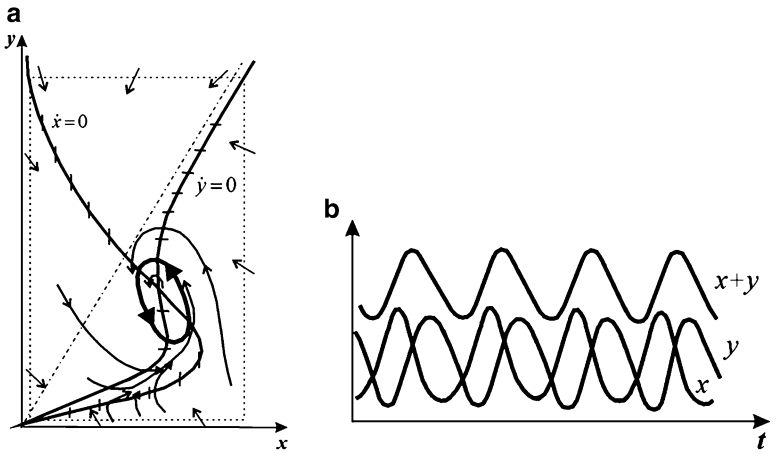


Fig. 1.12 Dynamics of variables of system (1.18) in instability domain. (**a**) Phase diagram; *bold curve* limit cycle. (**b**) Time dependence of variables (Stepanova from: Romanovsky et al. 2004)

Besides the trivial steady state (0,0) the system has one additional steady state:

$$\overline{x} = 2\sigma\overline{y}\,\frac{1}{1-\delta}, \quad \overline{y} = \frac{(1-\delta)\sigma}{(1+\delta)\sigma} - 1.$$

The type of stability of this steady state can be different depending on the system parameters. The width of the instability domain depends on the order n of inhibition: the greater n is, the wider the instability domain is. Instability domains on the parameter plane (σ, δ) for the second $(n = 2)$ and third $(n = 3)$ order of inhibition are presented in Fig. 1.11.

A phase portrait in the instability domain includes a limit cycle (Fig. 1.12a). The dynamics of the variables are presented in Fig. 1.12b.

Leslie Matrices

A detailed description of the population age structure leads to a class of *matrix models*, first proposed by Leslie (1945, 1948). It is assumed that a population contains n age groups, and those with the numbers $k, k+1, \ldots, k+p$ bear offspring. Proliferation occurs at certain times, $t_1, t_2, \ldots, t_n$. Therefore, at the initial moment t_0, the population is characterized by the column vector

$$\mathbf{X}(t_0) = \begin{vmatrix} x_1(t_0) \\ x_2(t_0) \\ \vdots \\ x_n(t_0) \end{vmatrix}.$$

The vector $\mathbf{X}(t_1)$, which characterizes the population at the next time moment, for example next year, is related to vector $\mathbf{X}(t_0)$ through the transfer matrix $\mathbf{L}$ and can be presented as follows:

$$\mathbf{X}(t_1) = \begin{vmatrix} x_1(t_1) \\ x_2(t_2) \\ \vdots \\ x_n(t_n) \end{vmatrix} = \begin{vmatrix} \sum_{i=k}^{k+p} \alpha_i x_i(t_0) \\ \beta_1 x_1(t_0) \\ \vdots \\ \beta_{n-1} x_{n-1}(t_0) \end{vmatrix}. \tag{1.19}$$

Let us explain the meaning of the right-hand-side vector. The offspring of all the reproductive groups that appear in one unit of time joins group 1. This means that the first component of the vector is

$$x_1(t_1) = \sum_{i=k}^{k+p} \alpha_i x_i(t_0) = \alpha_k x_k(t_0) + \alpha_{k+1} x_{k+1}(t_0) + \cdots + \alpha_{k+p} x_{k+p}(t_0). \tag{1.20}$$

The second component is obtained through the transfer of individuals that were in the first group at the moment t_0 into the second group and also takes into account a coefficient describing the death of a fraction of these individuals:

$$\beta_1 x_1(t_0), \quad 0 < \beta_n < 1.$$

The third group and all remaining components are obtained similarly. All individuals who were in the last age group at the moment t_0 die out at the moment t_1. Therefore, the last component of the vector $\mathbf{X}(t_1)$ is composed only of individuals that have passed from the preceding group:

$$x_n(t) = \beta_{n-1} x_{n-1}(t), \quad 0 < \beta_n < 1.$$

Coefficients α and β are the rates of birth and survival, respectively. In the Leslie models, they are constant; in more complicated models, they can be represented by functions depending on time, substrate concentration, and population size.

The vector $\mathbf{X}(t_1)$ is obtained by multiplying the vector $\mathbf{X}(t_0)$ by the matrix $\mathbf{L}$:

$$\mathbf{X}(t_1) = \mathbf{L}\mathbf{X}(t_0). \tag{1.21}$$

Matrix $\mathbf{L}$ has the form

$$\mathbf{L} = \begin{vmatrix} 0 & 0 & 0 & \alpha_k & \alpha_{k=1} & \alpha_{k=p} & 0 & 0 \\ \beta_1 & 0 & 0 & 0 & 0 & 0 & 0 & 0 \\ 0 & \beta_2 & 0 & 0 & 0 & 0 & 0 & 0 \\ & & & & & & & \\ 0 & 0 & & & & & 0 & 0 \\ 0 & 0 & & & & & \beta_{n-1} & 0 \end{vmatrix}. \tag{1.22}$$

The diagonal consists of zeros, survival coefficients β are below the diagonal elements, and terms that characterize the number of individuals born in corresponding groups are in the first row. All the remaining elements of the matrix are equal to zero. Thus, if the structure of matrix $\mathbf{L}$ and the initial population state [the column vector $\mathbf{X}(t_0)$] are known, then it is possible to predict the state of the population at any arbitrary moment:

$$\begin{aligned} &\mathbf{X}(t_1) = \mathbf{L}\mathbf{X}(t_0), \\ &\mathbf{X}(t_2) = \mathbf{L}\mathbf{X}(t_1) = \mathbf{L}\mathbf{L}\mathbf{X}(t_0) = \mathbf{L}^2\mathbf{X}(t_0), \\ &\mathbf{X}(t_k) = \mathbf{L}\mathbf{X}(t_{k-1}) = \mathbf{L}^k\mathbf{X}(t_0). \end{aligned} \tag{1.23}$$

The principal eigenvalue of matrix $\mathbf{L}$ yields the rate at which the population proliferates when its age structure becomes stable.

Continuous Models of Age Structure

Continuous models deal with a continuous function of the age distribution among organisms rather than with the numbers of individual age groups. An equation for the distribution function density was suggested by MacKendrick in 1926 and was "rediscovered" by von Foerster in 1959 and bears the name of the latter. The equation represents a differential form of the conservation law for numbers of individuals. There are two independent variables in this equation: t, time, and τ, age, which is counted from the moment of birth; $n(t, \tau)d\tau$ is the number of individuals whose age is in the interval $[\tau, \tau + d\tau]$. The total number of individuals

of all ages at time t is determined by the integral $N(t) = \int_0^\infty n(t,\tau)d\tau$. The Foerster equation has the form

$$\frac{\partial n(t,\tau)}{\partial \tau} + \frac{\partial n(t,\tau)}{\partial \tau} = -[D(t) + \omega(t,\tau)n(t,\tau)]. \tag{1.24}$$

The initial condition is $n(0, \tau) = g(\tau)$.

There is derivative dn/dt on the left-hand side of (1.24), and it is taken into account that $d\tau/dt = 1$; the terms on the right-hand side describe processes that lead to changes in the numbers of cells of a certain age. A decrease in cell numbers can be caused by various factors, such as death and migration; for a lotic culture all these causes can be regarded as negligible compared to the flow of cells through a cultivator. Flow velocity, $D(t)$, is independent of cell ages but can depend on time. The term $-\omega(t, \tau)u(t, \tau)$ describes a decrease in the number of cells of a given age during fission into daughter cells at a rate ω. An increase in the numbers resulting from proliferation occurs at zero age and is a part of the boundary condition at $\tau = 0$:

$$n(t,0) = k\int_0^\infty n\left(t,\tau'\right)W\left(t,\tau'\right)d\tau'. \tag{1.25}$$

Here k is the offspring numbers in a single multiplication act, $W(t, \tau')d\tau'$ is the probability of proliferation of a parent in the age interval $[\tau',\tau' + d\tau']$, which is equal to the intrinsic proliferation rate

$$W(t,\tau)d\tau = \omega(t,\tau)dt, \qquad \omega = W\frac{d\tau}{dt} = W. \tag{1.26}$$

If parents remain in a population after proliferation (yeast), then $W(t, \tau)$ is the density of the absolute probability of fission at age τ (fission age distribution function). If cells drop out of their age group after fission (algae, bacteria), then $W(t, \tau)$ is the density of the conditional probability of fission at age τ if a cell has reached this age without fission.

There are models that describe the distribution of cells with respect to size and mass. They are easier to correlate with experimental data because there are experimental methods for determining the sizes of cells. Methods of micromeasurements are being actively developed that also allow one to measure other parameters of individual cells (e.g., photosynthetic activity, chlorophyll content in algae, intracellular pH). Methods of lotic microfluorimetry make it possible to register the spectral characteristics of hundreds and thousands of microorganisms and construct the corresponding distributions of characteristics of individual organisms. Information about the evolution of these distributions presents new possibilities for estimating the state of microorganism populations, for example, the state of plankton populations in the oceans, microorganisms in soil, and blood cells.

Chapter 2
Oscillations, Rhythms, and Chaos in Biological Systems

Periodic change in various characteristics is common in biological systems. The period of these variations can be associated with periodic changes in conditions on Earth, such as the seasons of the year and alternation of day and night. However, many periodic processes have frequency not related explicitly to the external geospace cycles. These are the so-called biological clocks: oscillations of biomacromolecules' concentrations, biochemical oscillations, rhythms of breathing, heart contractions, and periodic changes in body temperature, all the way up to population waves.

Regular periodic changes in quantities represent one of the types of stationary (time-independent) regimes of system behavior. Regimes that are established in time and then remain unchanged are called attracting regimes or *attractors*. If oscillations in a system have constant period and amplitude, settle independently of initial conditions, and are supported due to properties of the system itself rather than because of periodic forcing, then such a system is called a *self-oscillating system*. On the phase plane, the attracting regime of self-oscillations has a closed isolated phase trajectory, the *limit cycle*. Continuous oscillations in such systems are stable since deviations from a stationary oscillatory regime die out. A class of self-oscillatory biological systems includes oscillating metabolic systems, periodic photosynthesis processes, variations in calcium concentrations within cells, oscillations in cardiac muscle, and variations in the numbers of animals in populations and communities.

Oscillations in Glycolysis

Glycolysis is a classic example of an oscillatory biochemical reaction. In a glycolytic process, glucose and other sugars decompose, and the compounds, containing six molecules of carbon, turn into tricarbon acids that include three carbon molecules. Due to the excess of free energy in the glycolytic process, two ATP molecules form per molecule of the six-carbon sugar. The main role in the

A. Rubin and G. Riznichenko, *Mathematical Biophysics*, Biological and Medical Physics, Biomedical Engineering, DOI 10.1007/978-1-4614-8702-9_2,

© Springer Science+Business Media New York 2014

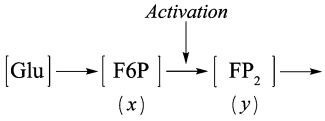


Fig. 2.1 Reaction scheme of first steps of glycolysis

generation of observed concentration oscillations of the reaction components fructose-6-phosphate, fructose-1,6-bisphosphate, and reduced nicotinamide adenine dinucleotide (NADH) belongs to the key enzyme of the glycolytic path, phosphofructokinase (PPK). A reaction scheme of the first steps of glycolysis is presented in Fig. 2.1.

In this scheme, [Glu] is glucose, [F6P] is fructose-6-phosphate, substrate of the key reaction, and [FP_2] is fructose-1,6-bisphosphate, a product of this reaction and a substrate in the next step. Both reactions are catalyzed by enzymes. In dimensionless coordinates, the system of equations that governs the reactions can be written as (Dynnik and Sel'kov 1975; Sel'kov et al. 1979; Ivanitskii et al. 1978)

$$\begin{aligned}\frac{dx}{dt} &= k - \chi \frac{x}{(K_{mx}+x)} \frac{y}{(K_{my}+y)},\\ \frac{dy}{dt} &= \chi \frac{x}{(K_{mx}+x)} \frac{y}{(K_{my}+y)} - q \frac{y}{(K'_{my}+y)}.\end{aligned} \tag{2.1}$$

Here, the dependencies of the reaction rates on variables are written in the Michaelis–Menten (Monod) form, as in (1.6).

If the conditions $K_{mx} \gg x$, $K_{my} \gg y$ are satisfied, then we can introduce dimensionless variables:

$$t' = \frac{t\chi k K'_{my}}{K_{mx} K_{my}(q-k)}, \quad x' = \frac{x\chi K'_{my}}{K_{mx} K_{my}(q-k)}, \quad y' = y\frac{q-k}{kK'_{my}}.$$

Omitting the primes, the dimensionless system becomes

$$\begin{aligned}\frac{dx}{dt} &= 1 - xy,\\ \frac{dy}{dt} &= \alpha y\left(x - \frac{1+r}{1+ry}\right),\end{aligned} \tag{2.2}$$

where

$$\alpha = \frac{(q-k)^2 K_{mx} K_{my}}{(K'_{my})^2 k\chi}, \quad r = \frac{k}{q-k}.$$

The kinetics and phase patterns of system (2.2) with different parameter values are presented in Fig. 2.2.

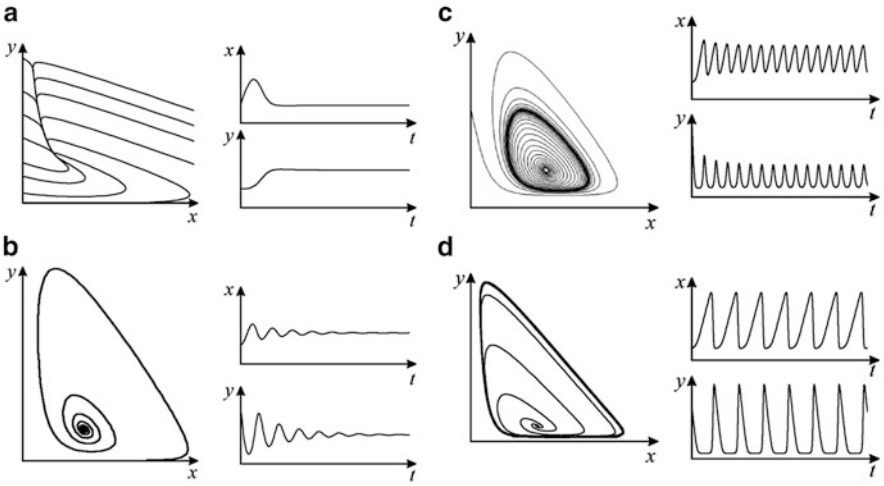


Fig. 2.2 Model of glycolysis (2.1). *Left*: system phase patterns; *right*: kinetics of concentrations; x corresponds to fructose-6-phosphate, y to fructose bisphosphate. (**a**) Oscillationless process, $\alpha = 0.25$; $r = 1$. (**b**) Damping oscillations, $\alpha = 0.25$, $r = 0.2$. (**c**) Quasiharmonic oscillations, $\alpha = 6$, $r = 0.24$. (**d**) Relaxation oscillations: $\alpha = 8$, $r = 0.5$

Oscillatory reactions in the glycolysis system were first predicted with a mathematical model (Higgins 1964, 1967) and were later registered experimentally in a laboratory by differential spectrophotometry.

Intracellular Calcium Oscillations

In many types of living cells, oscillations of intracellular calcium concentration are observed; their period can vary from 0.5 to 10 min. The simplest scheme of the processes that lead to calcium concentration oscillations is presented in Fig. 2.3. These oscillations were first observed by Endo et al. (1970) in skeletal muscle cells, by Fabiato and Fabiato (1975) in the sarcoplasmatic reticulum of an ox heart, and later by many other researchers.

A scheme and model of these processes were proposed and described by Dupont and Goldbeter (1989, 1994). The following processes were considered: influx and outflow of calcium through the cell membrane (velocities v_1 and v_2, respectively), messenger-activated release of calcium from pool (velocity v_3), active transport of cytosolic calcium into pool (v_4), release of calcium from pool activated by cytosolic calcium (v_5), and leakage of calcium from pool into cytosol (v_6). The reduced model consists of two differential equations:

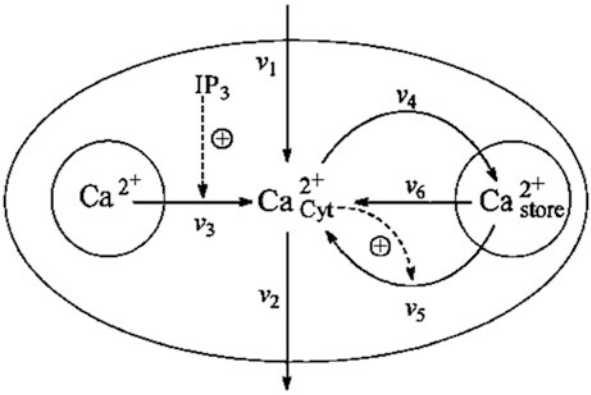


Fig. 2.3 Scheme of processes that lead to intracellular oscillations of calcium concentration (Dupont and Goldbeter 1992). Here, IP_3 is a messenger molecule stimulating the oscillations

$$\begin{aligned} \frac{dS_1}{dt} &= v_1 - v_2 + v_3 - v_4 + v_5 + v_6, \\ \frac{dS_2}{dt} &= v_4 - v_5 - v_6. \end{aligned} \tag{2.3}$$

Here S_1 is the calcium concentration in the cytosol, and S_2 is the calcium concentration in the messenger-sensitive pool. Expressions for the velocities were first proposed by Somogyi and Stuckin (1991):

$$v_2 = k_2 S_1; \quad v_4 = k_4 S_1; \quad v_5 = \frac{k_5 S_2 S_1^{nH}}{K_{0.5}^{nH} + S_1^{nH}}; \quad v_6 = k_6 S_2. \tag{2.4}$$

The model predicts oscillations of calcium concentration in time that closely resemble experimental observations. Figure 2.4 shows the kinetics of Ca^{2+} concentrations in cytosol (a) and a phase diagram of the system (b).

In Fig. 2.5 we see the kinetics of Ca^{2+} oscillations in cytosol and in the store (Fig. 2.3) according to model [(2.3), (2.4)]. The oscillations have a relaxation character and are far from harmonic.

At the greater value of calcium influx the shape of oscillations becomes more similar to a harmonic (Fig. 2.6).

Deterministic Chaos

Chaotic behavior is often observed in living systems. At first this behavior was attributed to unknown random internal and external factors and the complexity of the system in question. But in the second half of the twentieth century, it became clear that quasistochastic behavior of variables is possible in an autonomous ODE system of the third and higher order and even in one difference equation or in an

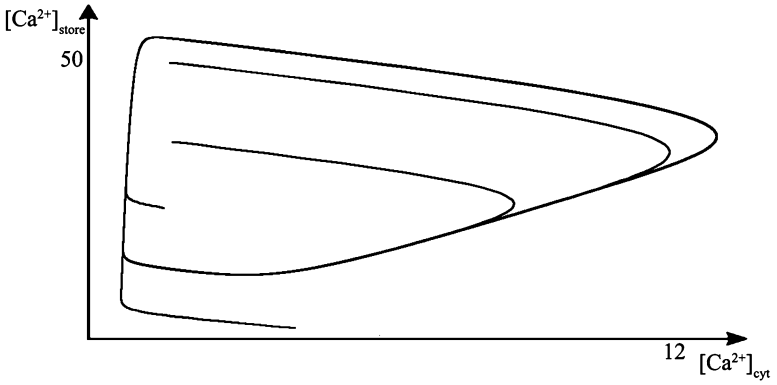


Fig. 2.4 Phase diagram of system; parameter values: $k_2 = 1$; $k_4 = 2$; $k_5 = 1$; $k_6 = 0.01$; $nH = 4$; $K_{0.5} = 3.1$; $v_0 = 2$

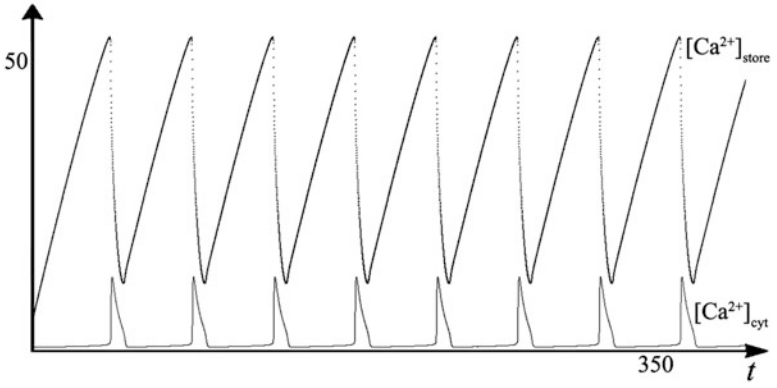


Fig. 2.5 Kinetics of oscillations of Ca^{2+} in cytosol and in store (Fig. 2.3) according to model [(2.3), (2.4)]. Parameter values: $k_2 = 1$; $k_4 = 2$; $k_5 = 1$; $k_6 = 0.01$; $nH = 4$; $K_{0.5} = 3.1$; $v_0 = 2$

equation with an argument delay. When the general evolution of a system in time is described deterministically but can demonstrate chaotic behavior, we talk about dynamic (deterministic) chaos.

At the turn of the twentieth century, French mathematician Henri Poincaré noticed such behavior in some mechanical systems. In his book *Science and Method* (1914) he wrote that in unstable systems completely insignificant reason, which we ignored for being small, leads to significant actions that we cannot foresee. Prediction becomes impossible, and we have a chance phenomenon.

However, the majority of physicists interpreted this result as a curious and amusing accident, and more than 70 years passed until mathematician and meteorologist Edward Lorenz (Lorenz 1963) discovered that a simple system of three nonlinear differential equations,

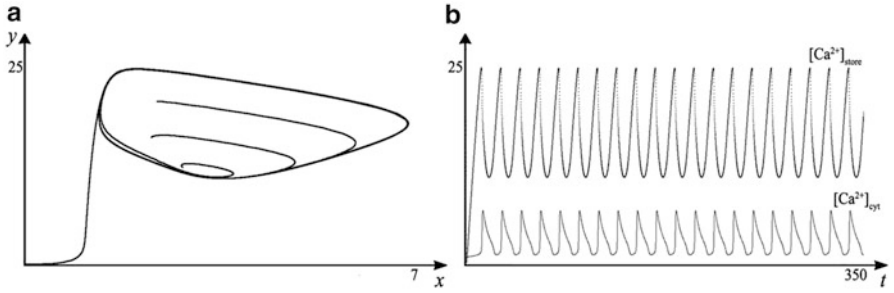


Fig. 2.6 Model of intracellular calcium concentration oscillations [(2.3), (2.4)] for values of parameters $k_2 = 1$, $k_4 = 2$, $k_5 = 1$, $k_6 = 0.01$, $nH = 4$, $K_{0.5} = 3.1$. The calcium influx parameter is $v_0 = 3.2$; other parameters are the same as in Fig. 2.5. (**a**) Kinetics of calcium concentrations in cytosol and in store. (**b**) Phase diagram

$$\begin{aligned} \dot{x} &= \sigma y - \sigma x, \\ \dot{y} &= rx - y - xz, \\ \dot{z} &= xy - bz, \end{aligned} \tag{2.5}$$

had chaotic trajectories (Fig. 2.7).

In subsequent decades the importance of Lorenz's discovery was recognized. He suggested one of the first examples of deterministic chaos in nonlinear systems. Chaotic behavior was later found in many different kinds of systems, including classical models of biological systems with oscillatory solutions and large numbers of dimensions: models of species interactions, models of glycolysis and cell cycles, models of enzyme catalysis, and others.

Chaotic behavior in such systems is not due to external sources of noise (there are no such sources in Lorenz's system), to an infinite number of degrees of freedom (only three in the Lorenz system), or to the uncertainty associated with quantum mechanics (the systems in purely classical and does not describe any quantum-mechanical phenomena).

The real cause of irregularity is that in a nonlinear system the distance between the initially close trajectories in a confined region of phase space increases exponentially. A confined region to which phase trajectories are attracted and where phase trajectories behave in a chaotic way is called a strange attractor (Fig. 2.7).

Sinai's billiard (Sinai, 1963, 1970) is an example of a mechanical system exhibiting deterministic chaos. In this system, billiard walls are curved inward. That is why for small initial deviations of the angle of incidence of a ball colliding with a wall, reflection leads to a large (exponential) divergence of trajectories. The same thing happens when particles are dispersed on spheres. In such systems, the path of an individual particle becomes unpredictable as time goes on.

Deterministic chaos can be demonstrated in various systems: liquids close to the threshold of turbulence, nonlinear optical devices (lasers), certain chemical reactions, meteorological processes, movement of piles of rocks during earthquakes, changes in population size, and processes of opening and closing of ion channels in cell membranes.

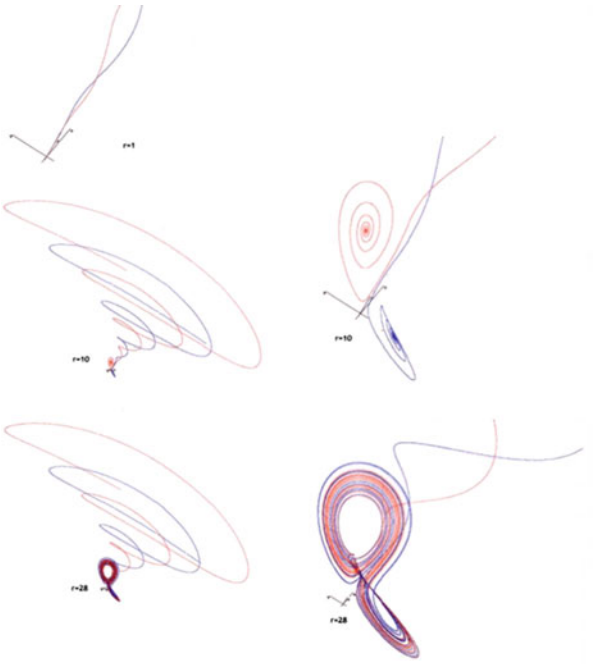


Fig. 2.7 Projections of phase trajectories of Lorenz system (2.5) for different values of r. $r = 1$—only the steady state; $r = 10$—two stationary states (stable spiral) in different planes; $r = 28$—region of strange attractor. *Right*: enlarged phase trajectories in vicinity of strange attractor

Chaos in Community of Three Species

One of the first examples of dynamic chaos in population dynamics was proposed by Bazykin. This model describes the dynamics of a three-species community consisting of a predator and two prey in the presence of internal competition. With certain values of the system parameters, bifurcation phenomena were observed leading to the emergence of quasistochastic regimes (Aponina et al. 1982; Bazykin 1985, 1998). In dimensionless variables the system is as follows:

$$\begin{aligned} \frac{du_1}{dt} &= u_1(\alpha_1 - u_1 - 6u_2 - 4v), \\ \frac{du_2}{dt} &= u_2(\alpha_2 - u_2 - u_1 - 10v), \\ \frac{dv}{dt} &= v(-1 + 0.25u_1 + 4u_2 - v). \end{aligned} \tag{2.6}$$

Here u_1 and u_2 are dimensionless numbers of the prey populations, v is the dimensionless number of the predator population, and α_1 and α_2 are parameters corresponding to the growth rates of prey.

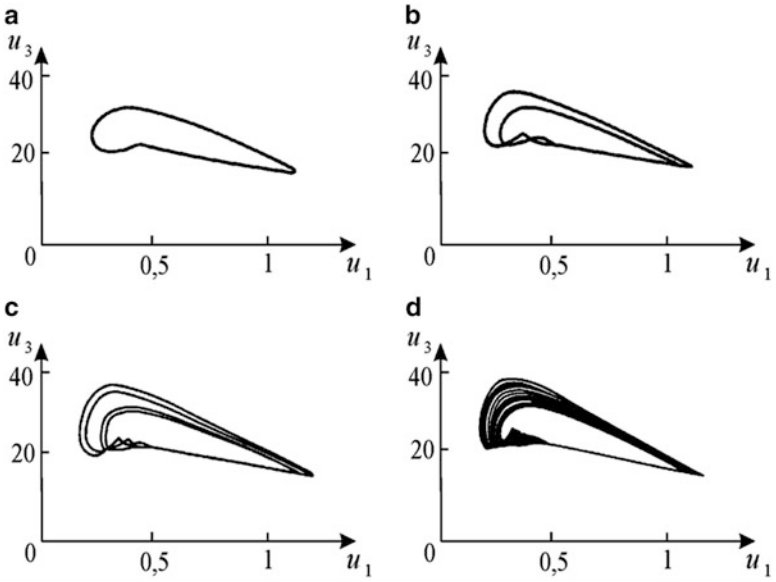


Fig. 2.8 Phase diagram of system describing interactions of three species: a predator and two prey (Aponina et al. 1982). A decrease in the growth rate parameter of the first victim leads to a complication of the trajectory: sequential doubling of limit cycle (**a-c**). Oscillating dynamics transform into quasistochastic (**d**), and a strange attractor appears (Bazykin 1998)

Along with a stable steady state, oscillatory changes in the numbers of all three species are possible. In a certain range of parameters the system has a limit cycle of complex shape. Decreasing α_2 leads to a series of successive doublings of the cycle (Fig. 2.8b). For a certain range of α_2 numerical simulation shows that the trajectory of the system completely fills a bounded domain of the phase volume. For these parameter values the system's behavior is indistinguishable from random, i.e., it becomes quasistochastic with a strange attractor. The modeling regime shown in Fig. 2.8d corresponds to observed quasistochastic behavior with an irregular change in the number of animals.

Periodic Supply of Substrate in System of Glycolysis

Stochastic regimes can be observed in a system of two variables when a periodic force acts upon the system (the system is nonautonomous). For example, the addition of a term corresponding to a periodic "supply" of the substrate ($A \sin w_0 t$) to the glycolysis (2.2) brings about a chaotic solution. The model can be written as

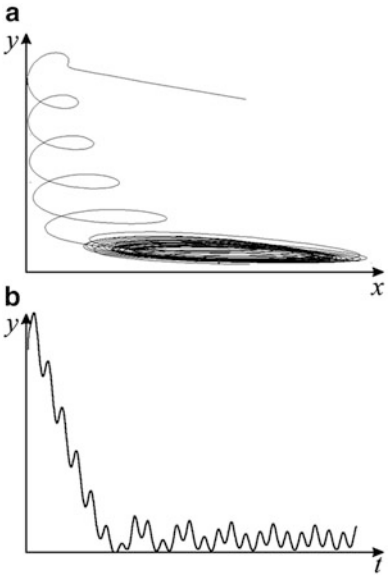


Fig. 2.9 Phase portrait and kinetics for glycolysis model with periodic influx of substrate

$$\frac{dx}{dt} = 1 + A \sin w_0 t - xy,$$

$$\frac{dy}{dt} = \alpha y \left(x - \frac{1+r}{1+ry} \right).$$

The corresponding phase diagram and chaotic kinetics are presented in Fig. 2.9.

It is remarkable that aperiodic stochastic changes in the concentration of NADH have been observed experimentally (Hess and Markus 1985). They were registered by recording the fluorescence of the compound in experiments on extracts of yeast cells with a continuous periodic addition of glucose. A study of systems with parameters distributed in space shows that random spatial and temporal behavior of variables can also occur in models consisting of two equations. Exchange processes between the compartments of a system play the role of additional variables and can lead to an increase or attenuation of chaos.

Recently a large number of experimental studies were conducted to estimate the degree of chaos (e.g., Lyapunov exponent, Kolmogorov entropy) in various biological processes. The question arises as to the biological, evolutionary reason for chaotic regimes. Why are they so widespread? The answer lies in the fact that in some sense quasistochastic systems are more stable, that is, they do not undergo drastic changes in their mode of operation in a wider range of external and internal parameters like oscillatory systems which have a limit cycle as the attractor (Loskutov and Shishmarev, 1994; Loskutov and Michailov, 2007).

Chapter 3
Spatiotemporal Self-Organization of Biological Systems

All biological objects—biomacromolecules, cells, tissues, and biocenoses—are active, distributed systems. Transformation of matter and energy in these systems occurs in bounded elementary media connected with each other via transfer of matter, whether diffusive or directed by external forces or by special adaptation mechanisms inherent in living organisms. Every elementary medium is an open system with respect to mass and energy exchange, usually far from thermodynamic equilibrium. Energy-carrying compounds or energy sources are distributed in space and connected with each other by fluxes of substances and energy. In such systems, so-called autowave processes are possible—propagation of pulses and excitation waves, formation of stationary, spatially inhomogeneous distribution of matter, and other self-organization phenomena (for details, see the next chapter).

Processes in excitable membranes in nerve fibers such as nerve pulses, waves in the brain's neural networks, and excitation waves in muscles, have been thoroughly examined. Waves of electric potentials propagate in the fibers of the cardiac muscle. Pathological states established here in the form of arrhythmia and fibrillation are related to the appearance of autonomous sources of waves. Other types of autowave processes manifest themselves in processes of morphogenesis during tissue differentiation. Transfer processes in living cells are performed by systems of active transmembrane transport. In some communities (collective amoebas) intercellular interactions are mediated via attractor substance secretions (e.g., cyclic AMP). Cells move to the signal source, and their aggregation has a wave character. Autowave processes also form the dynamic basis of the motions in the walls of blood vessels, peristalsis of the gastrointestinal tract, the mechanical movement of cells, and other processes.

A. Rubin and G. Riznichenko, *Mathematical Biophysics*, Biological and Medical Physics, Biomedical Engineering, DOI 10.1007/978-1-4614-8702-9_3,
© Springer Science+Business Media New York 2014

Waves of Life

The drive for growth and proliferation leads to propagation in space, occupation of new habitats, and the spread of living organisms. Life propagates as a flame over a steppe during a steppe fire. This metaphor reflects the fact that fire propagation (in the one-dimensional case, the propagation of a flame in a Bickford fuse) and the dynamics of species propagation are described by the same model. The famous combustion model was independently proposed by the great English biologist and statistician R. E. Fisher (1937) and by Russian mathematicians Kolmogorov, Petrovskii, and Piskunov (1937). Its biological formulation is a model of propagation in space of a dominating species. All three authors of this study are outstanding Russian mathematicians. Academician Ivan Petrovskii (1901–1973) is the author of some fundamental studies conducted in the areas of differential equations, algebra, geometry, and mathematical physics; he served as rector of Lomonosov Moscow State University (1951–1973). Andrey Kolmogorov—an internationally recognized scientist—headed the Russian mathematical school in the theory of probability and function theory. He was the author of fundamental works on mathematical logic, topology, the theory of differential equations, and the theory of information; he worked on improving high school and university mathematical education and wrote a number of studies related to biological problems.

Let us consider the problem of species propagation in an active, i.e., abundant, energy (food) medium. Let the propagation of species at any point of a straight line $r > 0$ be described by the function

$$f(C) = C(1 - C).$$

Initially, the whole domain to the left of zero is occupied by the species x whose numbers are close to unity. To the right of zero the territory is empty. At the moment $t = 0$ the species starts propagating (diffusing) to the right with constant diffusion coefficient D. This process is described by the equation

$$\frac{\partial C}{\partial t} = f(C) + D\frac{\partial^2 C}{\partial r^2}. \tag{3.1}$$

The initial condition is

$$C(0, r) = g(r) = \begin{cases} 1, & r > 0, \\ 0, & r > 0. \end{cases} \tag{3.2}$$

Kolmogoroff et al. (1937) considered the role of $f(C)$, which was equal to zero at $C = 0$ and $C = 1$, and positive in all intermediate points. Such a function is presented in Fig. 3.1a.

Assumptions concerning $f(C)$ mean that when C is small, the concentration rapidly grows due to the growth rate function $f(C)$. At values of C close to 1,

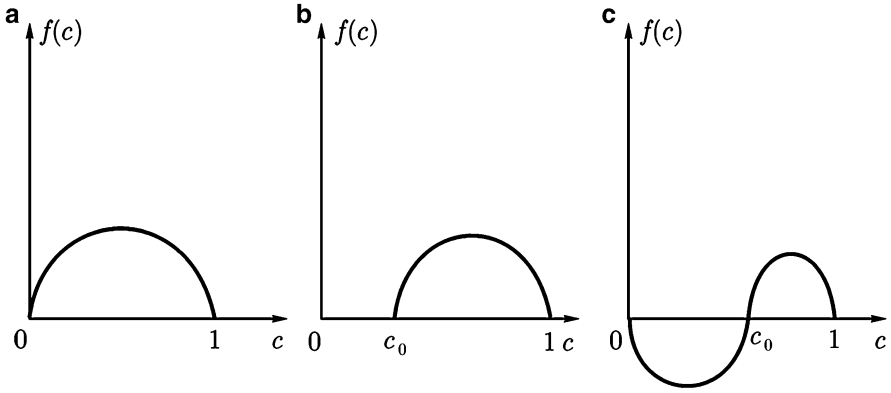


Fig. 3.1 Three possible shapes of function $f(C)$ for (3.2)

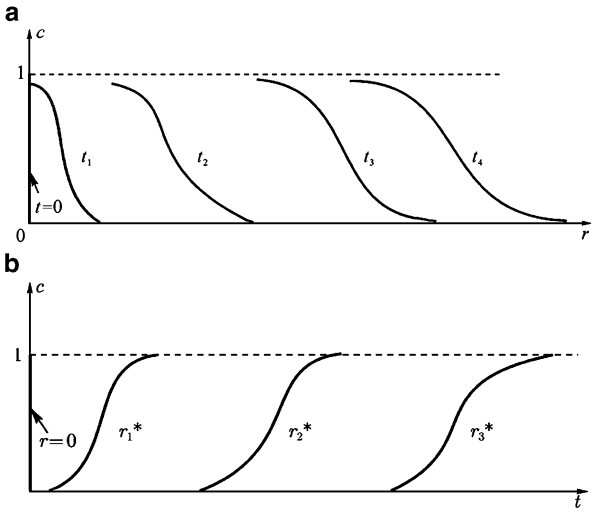


Fig. 3.2 (**a**) Profiles of density C depending on coordinate r in consecutive time moments: $t_4 > t_3 > t_2 > t_1 > t_0 = 0$. (**b**) Function $C(t)$ at fixed space points r^*, $r_1^* < r_2^* < r_3^*$

saturation is established. Profiles of the density C depending on the coordinate r at consecutive time moments are represented in Fig. 3.2a. At the initial time moment $t_0 = 0$, the curve looks like a step, and over time the wavefront moves to the right, and its shape becomes constant.

The duration of a lag period of the function $C(t)$ depends on the coordinate r^* (Fig. 3.2b). In a diffusion process, as soon as finite small concentrations have reached the point r^*, the rapid growth of C begins untill values approaching unity are established according to the function $f(C)$ (Fig. 3.1a). Patterns of $C(t)$ at the fixed points r^* are presented in Fig. 3.2b.

In the system [(3.1), (3.2)], if $t > 0$, then a concentration wave starts propagating into the domain $r > 0$, which is a result of two processes: the random motion of individuals (diffusion of particles) and the proliferation described by the function $f(x)$. With time the wavefront moves to the right and its form approaches a constant shape. The propagation velocity of the wave is determined by the diffusion coefficient and the shape of the function $f(x)$; since the function $f(x)$ is zero at $x = 0$ and at $x = 1$ and positive at intermediate points, the velocity is expressed by the simple formula

$$\lambda_0 = 2\sqrt{D \cdot f'(0)}.$$

Due to the factor $\sqrt{f'(0)}$, the wave propagation rate $\lambda_0 2\sqrt{Df'(0)}$ can be higher than the rate of distribution through diffusion. This growth rate is possible due to the multiplicator described by the function $f(C)$ (Fig. 3.1).

In some models there are other types of functions besides those depicted in Fig. 3.1a. For example, the function in Fig. 3.1b describes a case where propagation does not begin at arbitrarily small concentrations but starts only when a sufficiently high concentration C is reached. Functions of this type are found in some models of chemical kinetics and signal transmission in biological systems, where reactions begin only when the concentration reaches a threshold value. This function is used in the explosion theory, where the threshold variable has the meaning of the ignition temperature. In the case of nonlinearity shown in Fig. 3.1b, where the initial condition is a step, in a distributed system the concentration wave also propagates.

The shape of the function $f(C)$ in Fig. 3.1c appears in a number of problems in population genetics and ecology. The negativity of the function $f(C)$ at small C describes, for example, an effect associated with the fact that at low concentrations, the rate of reproduction is low, for instance, because of the low frequency of encounters between individuals of different sexes. This form of the growth function is used to describe populations with minimal critical numbers. In case presented in Fig. 3.1 (b) for the propagation of the concentration wave with constant amplitude it is also necessary for the value $\int_0^1 f(C)dC$ to be positive; otherwise, the region of small concentrations will extend (Freidlin and Sivak 1976).

In the important special case where $f(C) = C(1 - C)(C - \mu)$, the wave velocity, which is constant for high t values, can be calculated explicitly. This type of function is used in the Fitzhugh–Nagumo equation describing the propagation of nerve impulses (Part II). It turns out that in this case, the wave velocity is equal to

$$\sqrt{D}\left(\frac{1}{\sqrt{2}} - \mu\sqrt{2}\right).$$

It is assumed that $0 < \mu < \frac{1}{2}$; otherwise the range of small concentrations extends along the axis r (in space).

Modifications of the models of type (3.1), (3.2) made it possible to describe, for example, the propagation of waves in cardiac muscles and the formation of plankton patches in the ocean.

Analysis of the spatial distributions in the predator–prey model (1.10) shows that in such a system, in the case of unbounded space, waves of "escape and pursuit" appear (Chow and Tam 1976). In bounded space, depending on the system's parameters, stationary, spatially inhomogeneous structures (dissipative structures) or autowaves set in.

Autowaves and Dissipative Structures

Nonlinear interactions of system components coupled to transport processes lead to complex spatial and temporal behavior regimes. The first such model of interaction was examined by English mathematician and logician Alan Turing in his article "The chemical basis of morphogenesis." Turing (1912–1954) is famous for his studies on computer logic and cryptanalysis. In 1952, he published the first part of an investigation dedicated to the mathematical theory of structure formation in an initially homogeneous system where several chemical reactions occur simultaneously, including autocatalytic processes accompanied by energy consumption and passive processes of diffusive transport. Turing's work became a classic, and its ideas underlie the modern theory of nonlinear systems, the theory of self-organization, and synergetics. Consider a system of equations:

$$\begin{aligned} \frac{\partial x}{\partial t} &= P(x,y) + D_x \frac{\partial^2 x}{\partial r^2}, \\ \frac{\partial y}{\partial t} &= Q(x,y) + D_y \frac{\partial^2 y}{\partial r^2}. \end{aligned} \tag{3.3}$$

Equations of this type are called *reaction–diffusion* equations (see the next part). In linear systems, diffusion is a process that leads to the equalization of concentrations over a reaction volume. However, in the case of nonlinear interactions between variables x and y, a homogeneous stationary state can become unstable, and complex spatiotemporal regimes like autowaves or dissipative structures arise. The latter are represented by the distribution of concentration that is stationary in time and inhomogeneous in space, and require energy to maintain. The appearance of such structures in a system is connected with the difference in the diffusion coefficients of reagents, namely, by the presence of a short-range *activator* with a small diffusion coefficient and a long-range *inhibitor* with a large diffusion coefficient.

Basic Brusselator Model

Dissipative structures in a two-component system were examined in detail in the basic Brusselator model (Prigogine and Lefever 1968), named after the Brussels scientific school headed by I.R. Prigogine. Ilya Prigogine (b. 1917, Moscow, Russia; d. 2003, Brussels) worked in Belgium his entire life. In 1962, he became Director of the International Solvay Institute for Physical Chemistry and from 1967 served as Director of the Center for Statistical Mechanics and Thermodynamics at the University of Texas at Austin in the USA. In 1977 he was awarded the Nobel Prize in Chemistry for his works on nonlinear thermodynamics, in particular, on the theory of dissipative structures. Prigogine is the author or coauthor of several books: *Thermodynamic Theory of Structure*, *Stability*, *and Fluctuations* (Glansdorff and Prigogine 1971), *Order out of Chaos* (Prigogine and Stengers 1984), *The End of Certainty* (Prigogine 1997), and others. In these books he developed mathematical, physical, chemical, biological, and philosophical ideas on the theory of self-organization in nonlinear systems, examined the causes and regularities in the birth of order out of chaos under the action of random fluctuations in energy-rich systems open to matter and energy fluxes far from thermodynamic equilibrium.

In the Brusselator reaction, the so-called three-molecule reaction—the conversion of two X molecules and one Y molecule into X—is a key stage. Although third-order reactions in chemical kinetics are not as common as bimolecular ones, for some biochemical reactions the expression for the reaction rate can be presented as a cubic equation. As an example, let us consider the following sequence of enzyme reactions:

$$\begin{aligned} \mathrm{X} + \mathrm{E} &\longrightarrow \mathrm{EX}, \\ \mathrm{EX} + \mathrm{Y} &\longrightarrow \mathrm{EXY}, \\ \mathrm{EXY} + \mathrm{X} &\longrightarrow \mathrm{EX_2Y}. \end{aligned}$$

Here we assume that enzyme E has three catalytic sites that simultaneously bind two X molecules and one Y molecule. If the generated complexes dissociate rapidly and enzymes are present in small amounts, the whole chain of reactions can be presented in an expression for the rate of reaction as one stage: X^2Y.

The Brusselator describes the following chain of hypothetical chemical reactions:

$$\begin{aligned} A &\underset{k_{-1}}{\overset{k_1}{\rightleftarrows}} X \\ 2X + Y &\underset{k_{-2}}{\overset{k_2}{\rightleftarrows}} 3X \\ B + X &\underset{k_{-3}}{\overset{k_3}{\rightleftarrows}} Y + C \\ X &\underset{k_{-4}}{\overset{k_4}{\rightleftarrows}} R \end{aligned}$$

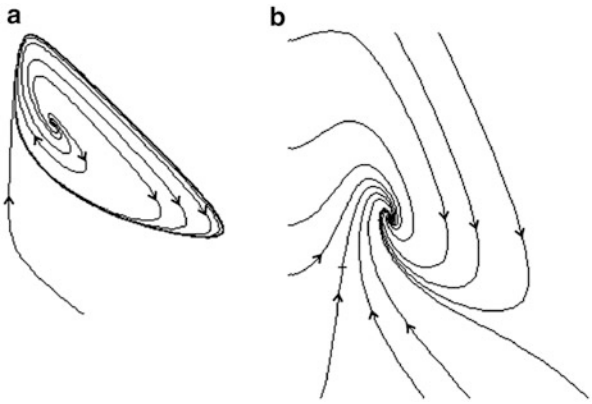


Fig. 3.3 Phase diagrams of Brusselator for $B > 1 + A^2$ (**a**) and $B < 1 + A^2$ (**b**)

Here A and B are initial substances, C and R are products, and X and Y are intermediates.

Let us assume that the final products C and R are immediately removed from the reaction space. This means that constants of the reverse reactions $k_{-3} = k_{-4} = 0$. If substrate A is in excess, then $k_{-1} = 0$. We also assume that $k_{-2} = 0$ and that other rate constants are equal to unity. Then the reaction scheme is described as follows:

$$\begin{aligned} \frac{dx}{dt} &= A + x^2 y - (B+1)x, \\ \frac{dy}{dt} &= Bx - x^2 y. \end{aligned} \tag{3.4}$$

System (3.4) is known as the classical Brusselator model. It has one steady state with coordinates:

$$\overline{x} = A, \qquad \overline{y} = \frac{B}{A}.$$

If $B < 1 + A^2$, then the steady state is stable; if $B > 1 + A^2$, then the steady state becomes unstable, and the system has a stable limit cycle. The bifurcation value is $B = 1 + A^2$; if B is close to the bifurcation threshold, then auto-oscillations are quasiharmonic. Phase diagrams of the Brusselator at different parameter values are presented in Fig. 3.3.

The Brusselator describes the reaction part of the *reaction–diffusion model*. The model can be considered a one-dimensional (1D) (reaction in a long narrow tube), a two-dimensional (2D) system (reaction on a surface), or a three-dimensional (3D) system (reaction volume).

Let the reaction proceed in a long, narrow tube (1D reactor) along which substances can diffuse. The diffusion coefficients D_x and D_y are assumed to be constant

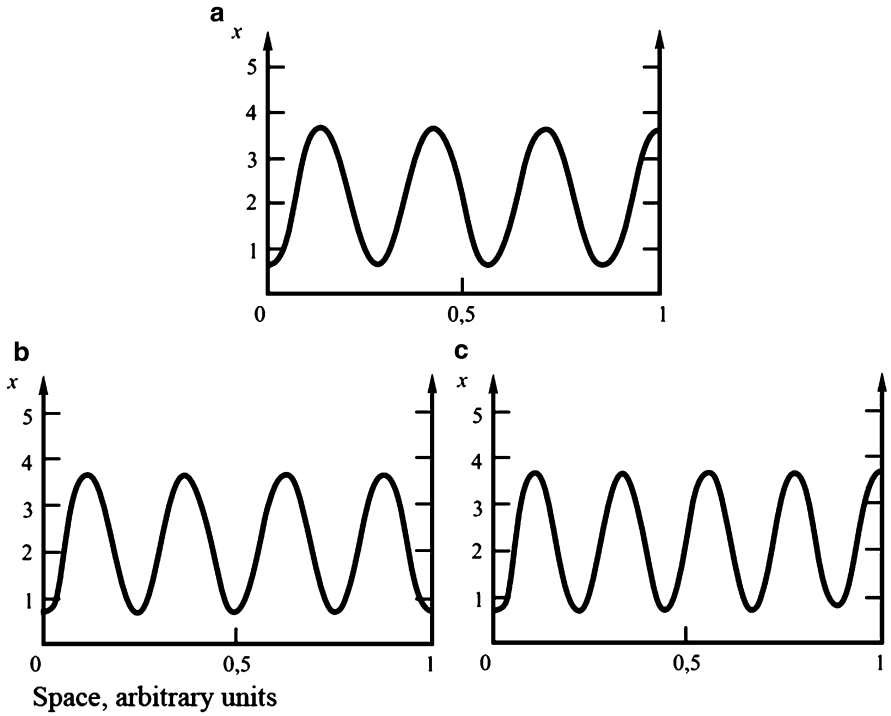


Fig. 3.4 Stationary dissipative structure obtained with equal values of parameters by imposition of a localized perturbation on a uniform steady state. The interval {0,1} is divided into 101 equal intervals, after which the perturbation of the same sign and the same amplitude is imposed at points in intervals with the numbers 9, 21, 48, 72 (**a**), 9, 17, 34, 43 (**b**), and 9, 55, 70 (**c**) (Nicolis and Prigogine 1977, Fig. 7.16)

parameters of the system. The ends of the tube, as well as its walls, are impermeable to the substances involved in the reaction. Equations describing the distributed Brusselator have the form

$$\begin{aligned} \frac{\partial X}{\partial t} &= A + X^2 Y - (B+1)X + D_x \frac{\partial^2 X}{\partial r^2}, \\ \frac{\partial Y}{\partial t} &= BX - X^2 Y + D_y \frac{\partial^2 Y}{\partial r^2}, \end{aligned} \tag{3.5}$$

where r is the space coordinate.

Computer experiments have shown that in the absence of flows at the tube boundaries several different dissipative structures may arise, depending on the localization of the perturbation of the homogeneous state. Stationary profiles of X for various perturbations are presented in Fig. 3.4.

Localized Dissipative Structures

The dissipative structures described previously are uniform throughout the entire system. This fact is a consequence of the assumption that the concentrations of precursors A and B remain constant at all points in space. This situation is ideal. In a real experiment, reagents A and B are introduced into the reaction volume through a boundary. This means that substances A and B will diffuse into the environment, and this will lead to the establishment of concentration profiles. An inhomogeneous spatial distribution of the precursors results in the localization of dissipative structures within certain boundaries.

In cases where substance B is uniformly distributed over the volume and the concentration of substance A is kept constant at the boundary, the system of equations (3.4) should be supplemented by an equation that describes the consumption and diffusion of substance A. This way we obtain a system of three equations:

$$\begin{aligned}
\frac{\partial X}{\partial t} &= A + X^2 Y - (B+1)X + D_x \frac{\partial^2 X}{\partial r^2}, \\
\frac{\partial Y}{\partial t} &= BX - X^2 Y + D_y \frac{\partial^2 Y}{\partial r^2}, \\
\frac{\partial A}{\partial t} &= -A + D_A \frac{\partial^2 A}{\partial r^2}, \quad (0 \le r \le l),
\end{aligned} \tag{3.6}$$

with boundary conditions

$$A(0) = A(l) = \overline{A}.$$

The concentration profiles for substance X, calculated according to (3.6) for different values of B, are presented in Fig. 3.5.

Belousov–Zhabotinsky Reaction

Spatiotemporal regimes predicted by the *reaction–diffusion* models can be observed using chemical models. The most famous among them is the reaction described in 1958 by Russian chemist Belousov (Belousov 1959): the oxidation of citric acid by potassium bromate catalyzed by the redox pair Ce^{4+}–Ce^{3+}. Examination of this reaction was continued by Zhabotinsky (1974), who showed that, instead of cerium, manganese and iron may serve as catalysts, and instead of citric acid, a number of organic compounds can be used as deoxidizers. These compounds contain a methylene group or form it as a result of oxidation. Malonic and brominemalonic acids are such compounds.

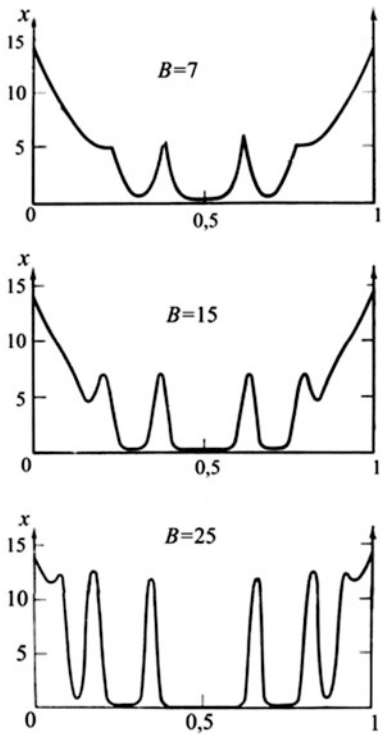


Fig. 3.5 Localized dissipative structures obtained by numerical solution of (3.4) for sequentially increasing values of B. At the boundaries the values of variables corresponding to a homogeneous steady state are constant. System parameters: $D_A = 0.026$, $D_x = 1.052 \times 10^{-3}$, $D_y = 5.26 \times 10^{-3}$, $l = 1$, *а* $- B = 7$, *б* $- B = 12$, *в* $- B = 25$ (Nicolis and Prigogine 1977, Fig. 7.25)

Usually, the reactions are carried on at 25 °C in a sulfate mixture of potassium bromate, malonic and brominemalonic acids, and cerium sulphate. In a closed vessel with vigorous stirring, after a short induction period fluctuations of Br^- and Ce^{4+} concentrations occur. Typical experimental curves are shown in Fig. 3.6. The initial oscillation is of a *hard excitation* character. Fluctuations in Ce^{4+} ion concentration recorded by a platinum electrode have a constant amplitude. A bromide electrode records any increases in the amplitude of [Br^-] oscillations, and its maximum value corresponds to the difference in Br^- ion concentrations by two orders. The shape of the oscillations varies somewhat over time; oscillations are maintained for 1.5 h with a period of approximately 2 min. After that, the amplitude decreases gradually, and the oscillations become irregular and slowly disappear.

The first model of the observed processes was proposed by Zhabotinsky. The preceding reaction cycle consists of two stages. The first stage (i) is oxidation of trivalent cerium by bromate:

$$Ce^{3+} \xrightarrow{BrO_3^-} Ce^{4+}. \qquad \text{(i)}$$

The second stage (ii) is reduction of tetravalent cerium by malonic acid:

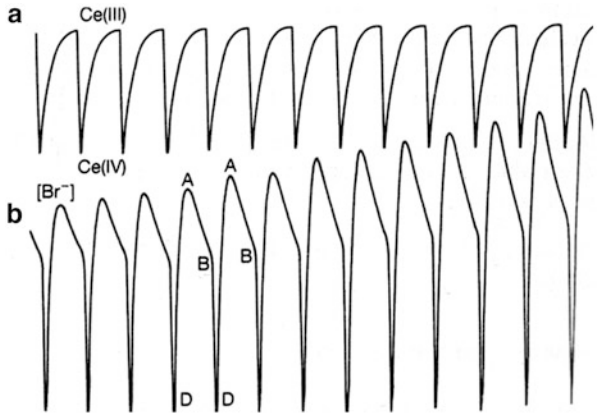


Fig. 3.6 (**a**) Experimentally observed readings taken by platinum electrode [Ce^{4+}]. (**b**) Electrode recording ion current of bromide [Br^-]. Initial concentrations of reagents: [BrO_3^-] = 6.25×10^2 M; [malonic acid] = 0.275 M; [Ce(IV)] = 2×10^{-3} M. The maximum amplitude of oscillations at the electrode is 100 mV, which corresponds to a 100-fold change in concentration; the period of oscillations is approximately1 min (Gray and Scott 1994)

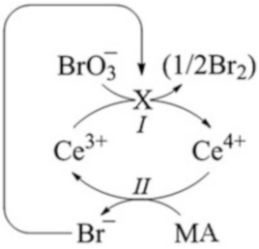


Fig. 3.7 Scheme of autocatalytic reaction of malonic acid (MA) oxidation

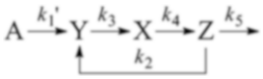
$$Ce^{4+} + CHBr(COOH)_2 \longrightarrow Ce^{3+} + Br^- + \textit{other products}. \qquad \text{(ii)}$$

At stage i, bromate reduction produces brominated MA. The resulting bromoderivatives of MA are broken with the release of Br^-. Bromide is a strong inhibitor of reactions. The scheme of self-oscillating reactions can be qualitatively described as follows.

Suppose a system contains Ce^{4+} ions. They catalyze the formation of Br^- (stage ii), which interacts with the particles *Y* of the reaction at stage i. If [Br^-] is high enough, then reaction i is completely inhibited. When [Ce^{4+}] in reaction ii is reduced to the threshold value, [Br^-] decreases, and thus inhibition of reaction i is removed. The rate of reaction i increases, and so does [Ce^{4+}]. When [Ce^{4+}] reaches the upper threshold value, [Br^-] also reaches high values, and this again results in the inhibition of reaction i, and so on. A scheme of the process is presented in Fig. 3.7.

To describe the processes, Zhabotinsky (1974) proposed a model consisting of three variables: ion concentration Ce^{4+} (x), concentration of intermediate in hypobromite to bromate recovery (y), and concentration of bromide, an inhibitor of phase I (z).

A scheme of the processes can be presented as



The notation x is the cerium ion concentration, y is the autocatalyst concentration, and z is the bromide concentration.

Taking into account the hierarchy of the reaction rate constants, one can replace the differential equation for z by an algebraic equation, and introducing dimensionless variables we obtain a system of two equations:

$$\begin{aligned} \frac{dx}{dt} &= y(1-x) - \delta x, \\ \varepsilon \frac{dy}{dt} &= y\left\{1 - x\left[1 + \alpha + (y-\alpha)^2\right]\right\} + \varepsilon. \end{aligned} \tag{3.7}$$

In (3.7), ε is a small parameter, which is why the oscillations have a relaxation character. A phase portrait of the system is shown in Fig. 3.8a. Figure 3.8b shows the fluctuations of the variable x corresponding to the dimensionless concentration of Ce^{4+} ions.

The flaw of the Zhabotinsky model is the presence of variable y—an "autocatalyst"; y does not relate to any real chemical compound. Several models of the mechanism of the BZ reaction have been proposed. The most popular of these is the reaction scheme proposed by Field et al. (1972) consisting of ten reactions with seven intermediates. Later, Field and Noyes (1974) proposed a simple scheme, called the Oregonator after Oregon State University (USA), where it was designed. The reaction scheme is as follows:

$$\mathrm{A} + \mathrm{Y} \xrightarrow{k_1} \mathrm{X},\ \mathrm{X} + \mathrm{Y} \xrightarrow{k_2} \mathrm{P},\ \mathrm{B} + \mathrm{X} \xrightarrow{k_3} 2\mathrm{X} + \mathrm{Z},\ 2\mathrm{X} \xrightarrow{k_4} \mathrm{Q},\ \mathrm{Z} \xrightarrow{k_5} \mathrm{fY}$$

Here A and B are initial reactants, P and Q are products, X, Y, and Z are intermediate compounds, $HBrO_2$ is bromic acid, Br^- is bromide ion, and Ce^{4+} is cerium ion. The concentrations of initial reagents are assumed to be constant in the model.

Let us denote by small letters the variables corresponding to concentrations of reagents and write an equation for their changes over time in accordance with the law of mass action:

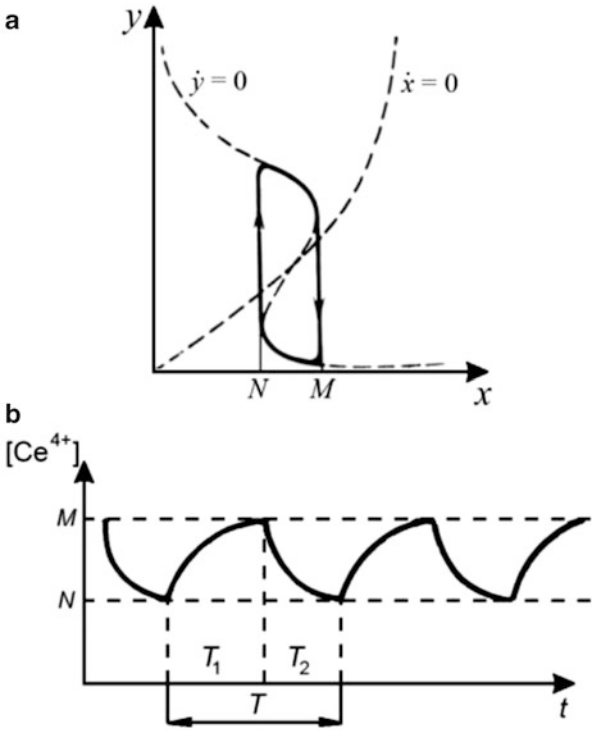


Fig. 3.8 (**a**) Phase portrait of system (3.5); *dashed lines*: nullclines; *thick line*: limit cycle; x is the dimensionless concentration of Ce^{4+} ions; y is the dimensionless concentration of the autocatalyst—the fast variable. (**b**) Kinetics of Ce^{4+} ions concentration—relaxation oscillations. N, M are the smallest and largest values of the variable, T_1 and T_2 are the times of rise and fall of the concentration of Ce^{4+} ions. T is the period of the oscillations (Zhabotinsky 1974)

$$\frac{dx}{dt} = k_1 ay - k_2 xy + 2k_3 bx - k_4 x^2,$$
$$\frac{dy}{dt} = -k_1 ay - k_2 xy + fk_5 z,$$
$$\frac{dz}{dt} = k_3 bx - k_5 z.$$

The numerical values of the rate constants of direct reactions were estimated by the authors from the experimental data. The values are as follows: [A] = [B] = 0.06 M; $k_1 = 1.34$ M/s, $k_2 = 1.6 \times 10^9$ M/s, $k_3 = 8 \times 10^3$ M/s, $k_4 = 4 \times 10^7$ M/s. The stoichiometric factor f, constant k_5, and parameters associated with the consumption of reagents are varied.

The dimensionless form of the Oregonator model is

$$\begin{aligned}\frac{dx}{dt} &= s\left(y - xy + x - qx^2\right),\\ \frac{dy}{dt} &= \frac{-y - xy + fz}{s},\\ \frac{dz}{dt} &= w(x - z).\end{aligned} \tag{3.8}$$

Here the dimensionless concentrations are $x - [BrO_2]$, $y - [Br^-]$, $z -$ metal ion concentration, the parameter f is considered to belong in the domain $0 < f < 2$ (Field and Noyes 1974).

System (3.8) has a zero steady state:

$$\overline{x} = 0, \quad \overline{y} = 0, \quad \overline{z} = 0,$$

which is always unstable, and one positive steady state:

$$\begin{aligned}\overline{x} &= \frac{1 - f - q + \sqrt{(1 - f - q)^2 + 4q(f + 1)}}{2q},\\ \overline{y} &= \frac{f\overline{x}}{1 + \overline{x}}, \quad \overline{z} = \overline{x}.\end{aligned} \tag{3.9}$$

Analysis of the stability of this steady state (Field and Noyes 1974) made it possible to find an area where the solution of (3.8) becomes unstable. A bifurcation diagram of a system in the plane of parameters (f, k_5) is presented in Fig. 3.9a; Fig. 3.9b shows the shape of oscillations of variable x. The parameter values are given in the figure caption.

The values of the parameters in the system are such that there is a hierarchy of characteristic times for variables, and x is a fast variable for which the differential equation can be replaced by an algebraic one.

The reduced model of the Oregonator with two equations is

$$\begin{aligned}\frac{dy}{dt} &= \frac{-y - yx(y) + fz}{s},\\ \frac{dz}{dt} &= w(x(y) - z).\end{aligned} \tag{3.10}$$

System (3.10) has a stable limit cycle with a large amplitude and an unstable limit cycle of small amplitude inside of it (Rinzel and Troy 1982).

It is in the form (3.10) (or something similar) that the system of Noyes–Field equations has been investigated by many authors as a local element of a distributed system of the reaction–diffusion type. Experimentally the BZ reaction demonstrates

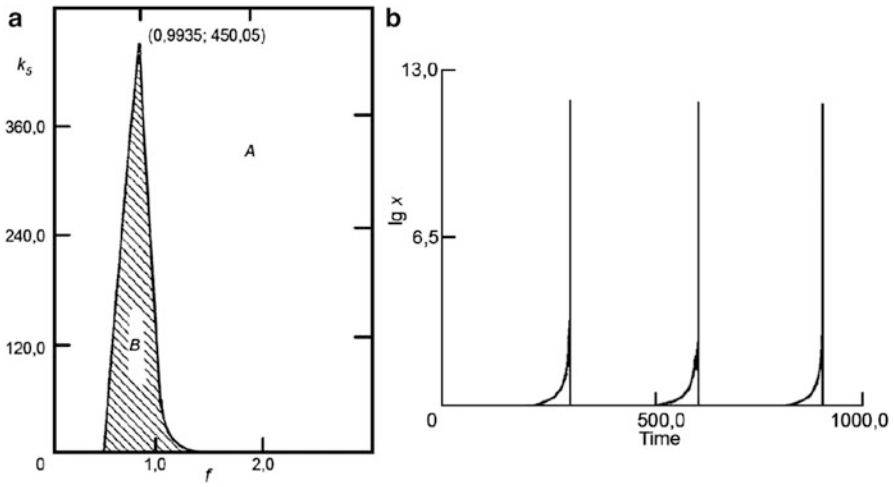


Fig. 3.9 (**a**) Domains of stability (A) and instability (B) of positive steady-state solution (3.9) of Oregonator model (3.8). (**b**) Oscillations of variable x with large amplitude. Parameter values: $s = 77.27$, $q = 8.375 \times 10^6$, $w = 0.161\ k_5$ (Field and Noyes 1974)

different types of autowave regimes (Fig. 3.10): leading centers (a), spiral waves (c), complex spatial and temporal distribution (b, d).

Model (3.8) was used to simulate different types of spacetime structures arising in 2D and 3D systems in the presence of different kinds of boundaries. The question arises as to whether it is possible for outside factors to affect the development of these complex structures in space and time. Such factors include a change in the flow rate of final and intermediate chemicals into the reaction, different modes of continuous and periodic illumination, and exposure to radiation with high-energy particles. Such studies are of great practical significance. They make it possible to find ways to control the activity of autowave regimes and to analyze the impact of spiral excitation waves in active cardiac tissue, which disintegrates atrial fibrillation. Indeed, even in the first axiomatic models of active media it was found that if there were a spiral wave in the system, exit of its tip to the border of the active region would lead to the attenuation of this wave (Ivanitskii et al. 1978). The BZ reaction is a good experimental model for studying the regulation of wave dynamics.

From an experimental point of view it is especially convenient to use different protocols of, for example, light exposure, constant illumination of the entire reaction system or its parts, or continuous illumination of varying intensity. Carrying out the control by light exposure is possible when a light-sensitive ion $[Ru(bpy)_3]^{2+}$ [tris(bipyridine)ruthenium (II) chloride] is used as a catalyst for the reaction. Usually the reaction is conducted in a Petri dish filled with a thin layer of silicone gel. In this system, there are divergent spiral waves, but the impact of a thin laser beam causes a gap in the front of the spreading wave and the emergence of two spiral waves (Fig. 3.11; Müller et al. 1986, 1988).

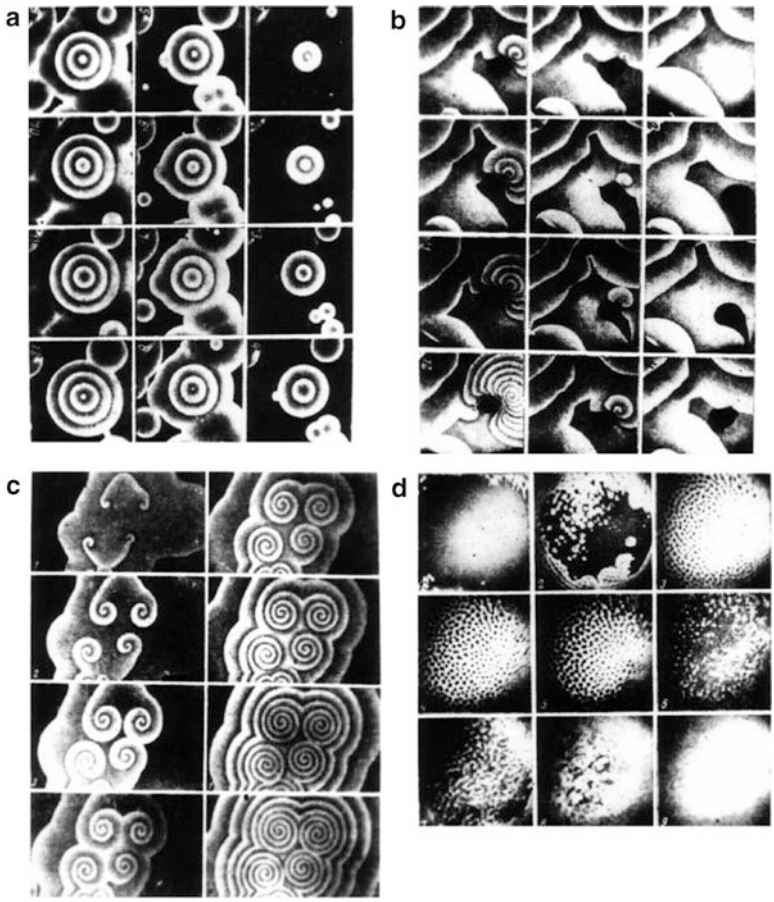


Fig. 3.10 Different spatial regimes in Belousov–Zhabotinsky reaction. In each series of images (**a**–**d**), the gradual development of processes over time is shown (Zhabotinsky 1974)

In the laboratory of Prof. Stefan Müller from the University of Magdeburg, Germany, a technique was developed that makes it possible to "lead" the tip of one of the waves to the boundary of the Petri dish, and subsequently observe the evolution of a single spiral wave. The tip of the wave performs complex spatial movements, and the trajectory depends on the mode of illumination (Grill et al. 1995).

Under constant illumination the tip describes a cycloid with four "petals" (Fig. 3.12, dashed line). The effects of light pulses on the trajectory of the tip of the spiral wave was studied by Grill et al. (1995).

The pulses were applied when the wavefront reached a certain point (marked by a cross in Fig. 3.13).

Two types of regimes were observed. In the case where the measuring point was close to the center of the unperturbed trajectory, the tip moved after some time along the asymptotic trajectory with the center of the measuring point, while the distance



Fig. 3.11 Spiral waves in thin layer of excitable reaction medium of Belousov–Zhabotinsky reaction (Müller et al. 1986)

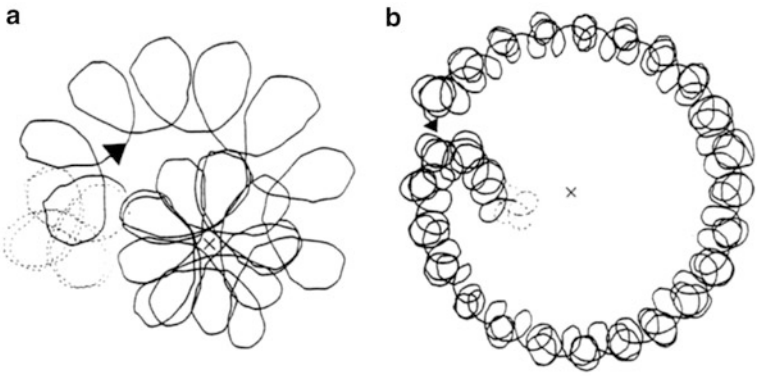


Fig. 3.12 Two types of spiral wave tip trajectories obtained in experiment for photosensitive BZ reaction. The distance from the center of the unperturbed trajectory (*dotted line*) to the point of measurement (X) in (**a**) is 0.49 mm and in (**b**) 0.57 mm (Grill et al. 1995)

between the position of the tip and the point of measurement did not exceed the size of the loops of the cycloid (Fig. 3.12a). The presence of the feedback led to synchronization—the period of the pulsed light device became equal to the time during which the tip of the spiral wave described one loop of the cycloid.

In the case where the measuring point was located relatively far from the center of the unperturbed trajectory, the tip of the spiral described a path shaped like a drift of a four-blade cycloid along a circle of large radius whose center, again, was the point of measurement. Both modes were stable with respect to small displacements of the measuring point, i.e., they were like attractors. A similar result is obtained if the light pulse is applied after some delay relative to the time of passage of the wave through the point of measurement. The radius of the large circle that moves the cycloid increases with the increasing time delay.

For a mathematical description the following model was used (Zykov et al. 1994):

$$\begin{aligned} \varepsilon \frac{du}{dt} &= u - u^2 - w(u - q), \\ \frac{dv}{dt} &= u - v, \\ \varepsilon' \frac{dw}{dt} &= fv - w(u + q) + \phi. \end{aligned} \tag{3.11}$$

Here the variables u, v, and w correspond to $HBrO_2$, catalyst, and bromide concentrations, respectively. A term ϕ in the third equation reflects the light-induced flux of Br^- ions, and f and q are dimensionless parameters. Evaluation of the rate constants of individual reactions shows the presence of a temporal hierarchy of processes in the system:

$$\varepsilon' << \varepsilon << 1.$$

If this inequality is valid, then we can consider the concentration of the bromide w to be a very fast variable; the right-hand side of the equation for this variable can be set equal to zero, and we find its expression in terms of the quasistationary values of concentrations of the slower variables:

$$w = \frac{fv + \phi}{u + q}.$$

Considering the diffusion of reactants, we obtain a modified model Oregonator, a system of the reaction–diffusion type:

$$\begin{aligned} \frac{\partial u}{\partial t} &= \nabla^2 u + \frac{1}{\varepsilon}\left[u - u^2 - (fv + \phi)\frac{u - q}{v - q}\right], \\ \frac{\partial v}{\partial t} &= u - v. \end{aligned} \tag{3.12}$$

Here the variables u and v correspond to $HBrO_2$ concentrations and catalyst, respectively. Using this model the system parameters were studied, and experimentally observed modes were reproduced (Fig. 3.13).

The model also makes it possible to explore the potential modes of behavior of the tip of the spiral waves with different amplitudes and frequencies of the periodic modulation of the light exposure. The overall picture of the trajectories is summarized in Fig. 3.14. A general theory of systems of this type was developed by

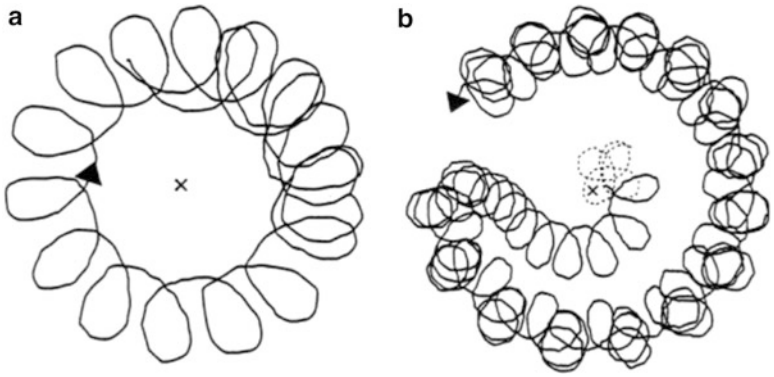


Fig. 3.13 Spiral wave tip trajectories for amplitude of impact $A = 0.01$ and different values of delay time τ of the light pulses calculated for model (3.12). *a* – $\tau = 0.8$; *б* – $\tau = 1.5$ (Grill et al. 1995)

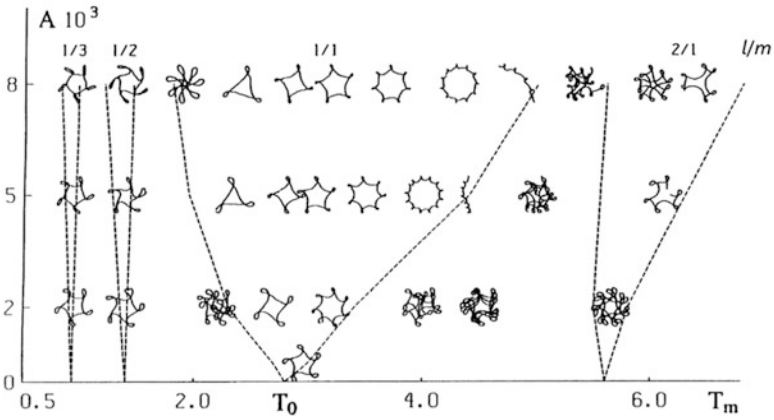


Fig. 3.14 Types of spiral wave tip trajectories obtained in the course of computational experiments on model (3.12) for different periods of the harmonic modulation parameter, which is sensitive to light exposure. The abscissa is the modulation period, the vertical axis the amplitude modulation. *Dotted lines*: boundaries of regions in which there is a resonant "capture" of the frequency of exposure with natural frequency. *l*/*m* is the ratio of the number of loops, which describes the tip of the spiral wave, to the number of modulation periods of light exposure. T_0 is the natural period of turnover of the spiral tip in the absence of external influence (Zykov et al. 1994)

Vladimir Arnold, and graphics areas in which there is a similar type of behavior are called Arnold tongues (boyland, 1986).

Model studies of autowave processes in the Belousov–Zhabotinsky reaction have made an important contribution to the study of the regulation power of autowave processes in vital organs such as brain and heart. A wide variety of

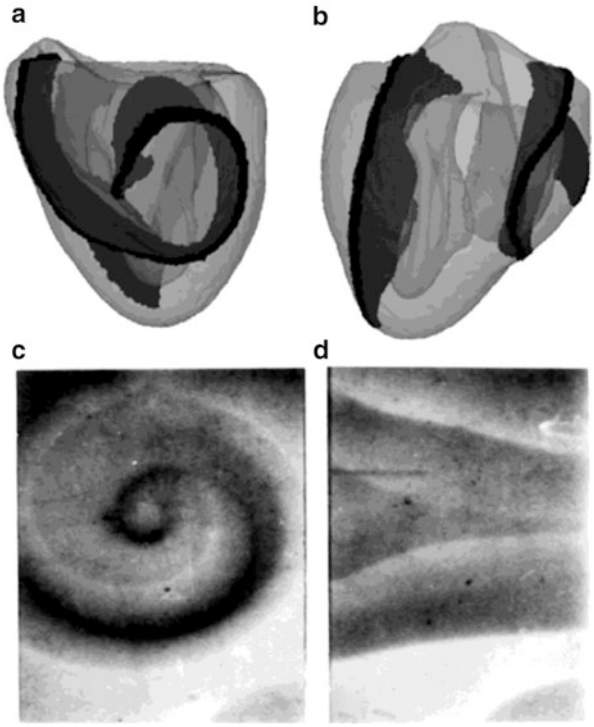


Fig. 3.15 Three-dimensional spinning vortex (reentry) in ventricles of dog (**a**, **b**), a model (Aliev and Panfilov 1996), and, in the Belousov–Zhabotinsky reaction, an experiment (**c**, **d**) (Aliev 2008). The complex shape of the vortex in a 3D model is due to the complex geometry of the ventricles and anisotropy of the medium

processes can be modeled by this reaction, including the formation of spiral waves—reentry, as it is called in cardiology—whose appearance in the myocardium is associated with atrial arrhythmias and various dangerous heart diseases (Fig. 3.15).

Chapter 4
Model of Impact of a Weak Electric Field on Nonlinear System of Transmembrane Ion Transport

In the process of evolution, a spatiotemporal organization of biological systems formed that makes systems extremely sensitive to external influence. As a rule, the response of systems to such effects is nonlinear. The term *nonlinear* usually refers to several factors:

- Disproportionate response of a system to external influences
- Threshold character of the response
- Resonance of system response

By *resonance* we mean special frequencies of the external force, where the response of the system becomes much higher compared to other frequencies.

Here, as an example, we consider a nonlinear system of transmembrane ion transfer and its response to the periodic action of an electric field, which in terms of the kinetic model can be expressed as a periodic variation of the system parameters. The analysis is based on the works of Riznichenko et al. (1994), Riznichenko and Plyusnina (1996), Plyusnina and Riznichenko (1996), and Plyusnina et al. (1994). The problem is important for understanding the mechanisms of weak, low-frequency, electromagnetic field effects on biological objects.

The problem of low-frequency electromagnetic radiation effects raises the question as to how the energy of incident photons, which is too small to cause structural and chemical changes in the target molecular system, can nevertheless cause biological effects. However, the problem can be analyzed, not from a "power" point of view but by considering the sensing target system as a nonlinear macro system that has different types of behavior depending on the internal parameters. Under the influence of the weak periodic electromagnetic field the behavior of such systems can be significantly transformed, especially when the parameters are near their bifurcation values. The frequency of the external action may not correspond to the difference between the energy levels of the elementary molecular structures, but it may be in "resonance" with large-scale subcellular systems at much lower frequencies.

A. Rubin and G. Riznichenko, *Mathematical Biophysics*, Biological and Medical Physics, Biomedical Engineering, DOI 10.1007/978-1-4614-8702-9_4,

© Springer Science+Business Media New York 2014

Transmembrane Ion Transport Model

Consider the system of transport of K^+ ions and H^+ ions across the cell membrane by the carrier T^-. A corresponding example is the system of K^+-H^+ antiport by nigericin molecules, which have binding sites for both proton and potassium (Fig. 4.1).

When constructing the model we used the following assumptions:

- The inflow and outflow of ions in the system occurs in near-membrane layers, V_H and V_K are ion flow rates in the reaction zone.
- The negatively charged carrier T can transfer a proton or ion through the membrane in the form of neutral complexes TH and TK or in the form of the charged complex THK^+.
- The binding constant of the THK^+ complex is much greater than that of the TK complex. K^+ ions are not able to replace H^+ ions in the TH complex, so their transport through the membrane occurs in the form of THK^+.

$$V_H \longrightarrow H_1^+ + T^- \underset{k_{-1}}{\overset{k_{+1}}{\rightleftharpoons}} TH \xrightarrow{k_{+2}} T^- + H_2^+ \longrightarrow V'_H,$$
$$V'_K \longleftarrow K_1^+ + TH \xleftarrow{k_{+4}} THK^+ \underset{k_{-3}}{\overset{k_{+3}}{\rightleftharpoons}} TH + K_2^+ \longleftarrow V_K.$$

The considered processes are depicted in the preceding scheme. Here V_H is the flow rate of protons in the membrane region 1 (Fig. 4.1), $[H_1^+]$ and $[K_1^+]$ are the ion concentrations in this area, V'_K is the outflow rate of K^+ ions from the region 1, V_K is the inflow rate of K^+ ions in membrane region 2, $[H_2^+]$ and $[K_2^+]$ are the ion concentrations in this area, V'_H is the outflow rate of protons in region 2 (Fig. 4.1), $k_{\pm 1,3}$ are constants of association and dissociation of complexes, and k_{+2} and k_{+4} are effective constants of complex transmembrane transport and dissociation.

We write the system of equations describing the change in concentration of proton, potassium ions, $[T^-]$ and T-complexes in regions 1 and 2 as follows:

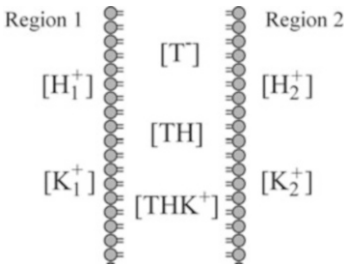


Fig. 4.1 System of transfer of K^+ ions and H^+ ions across plasma membrane

$$\frac{d\left[\mathrm{H}_1^+\right]}{dt} = V_H - k_{+1}[\mathrm{H}^+][\mathrm{T}^-] + k_{-1}[\mathrm{TH}],$$
$$\frac{d\left[\mathrm{H}_2^+\right]}{dt} = k_H[\mathrm{TH}],$$
$$\frac{d\left[\mathrm{K}_1^+\right]}{dt} = k_K[\mathrm{THK}^+],$$
$$\frac{d\left[\mathrm{K}_2^+\right]}{dt} = V_K - k_{+3}\left[\mathrm{K}_2^+\right][\mathrm{TH}] + k_{-3}[\mathrm{THK}^+],$$
$$\frac{d[\mathrm{T}^-]}{dt} = -k_{+1}\left[\mathrm{H}_1^+\right][\mathrm{T}^-] + \left(k_{-1} + k_{+2}\right)[\mathrm{TH}],$$
$$\frac{d[\mathrm{THK}^+]}{dt} = k_{+3}[\mathrm{TH}]\left[\mathrm{K}_2^+\right] - \left(k_{-3} + k_{+4}\right)[\mathrm{THK}^+],$$
$$[\mathrm{T}] + [\mathrm{TK}] + [\mathrm{THK}^+] = T_0.$$

Here $[T_0]$ is the total concentration of the carrier in the free form and the form of complexes.

The second and third equations for the concentration of $[\mathrm{H}_2^+]$ and $[\mathrm{K}_1^+]$ can be separated, and we consider the following system:

$$\begin{aligned}
&\frac{d\left[\mathrm{H}_1^+\right]}{dt} = V_H - k_{+1}[\mathrm{H}^+][\mathrm{T}^-] + k_{-1}[\mathrm{TH}],\\
&\frac{d\left[\mathrm{K}_2^+\right]}{dt} = V_K - k_{+3}\left[\mathrm{K}_2^+\right][\mathrm{TH}] + k_{-3}[\mathrm{THK}^+],\\
&\frac{d[\mathrm{T}^-]}{dt} = -k_{+1}\left[\mathrm{H}_1^+\right][\mathrm{T}^-] + \left(k_{-1} + k_{+2}\right)[\mathrm{TH}],\\
&\frac{d[\mathrm{THK}^+]}{dt} = k_{+3}[\mathrm{TH}]\left[\mathrm{K}_2^+\right] - \left(k_{-3} + k_{+4}\right)[\mathrm{THK}^+],\\
&[\mathrm{T}] + [\mathrm{TK}] + [\mathrm{THK}^+] = T_0.
\end{aligned} \tag{4.1}$$

We introduce the following dimensionless parameters:

$$\varepsilon = \frac{T_0}{\overline{K}_m}, \quad V'_H = \frac{V_H \overline{K}_m}{k_{+4} T_0 K_m}, \quad V'_K = \frac{V_K}{k_{+4} T_0}, \quad a = \frac{\overline{K}_m k_{2+}}{K_m k_{+4}}. \tag{4.2}$$

Let the carrier concentration be significantly less than the ion concentration in the reaction. In this case, the inequality $T_0 \ll K_m$ is true, which allows us to draw a conclusion concerning the hierarchy of characteristic times to perform a reduction of the system. That is, when $\varepsilon \to 0$, the third and fourth equations of system 1 can be replaced by algebraic ones.

To analyze system (3.10) we move to dimensionless variables:

$$x = \frac{[H_1^+]}{K_m}, \quad y = \frac{[K_2^+]}{\overline{K}_m}, \quad t' = \frac{tT_0k_{+4}}{\overline{K}_m},$$
$$K_m = \frac{k_{-1} + k_{+2}}{k_{+1}}, \quad \overline{K}_m = \frac{k_{-3} + k_{+4}}{k_{+3}}. \tag{4.3}$$

Now the system includes dimensionless concentrations: x is protons in area 1 and y is potassium ions in area 2 (primes on the time t, V_H and V_K are omitted):

$$\frac{dx}{dt} = V_H - \frac{ax}{1 + x + xy},$$
$$\frac{dy}{dt} = V_K - \frac{yx}{1 + x + xy}. \tag{4.4}$$

The system has a single, stable steady state—a node or focus. The stationary values of the variables are

$$\overline{x} = \frac{V_H}{a(1 - V_K) - V_H},$$
$$\overline{y} = \frac{aV_K}{V_H}. \tag{4.5}$$

Linearizing the system in the vicinity of the steady state and solving the characteristic equation, we obtain the condition where a singular point is a focus:

$$V_H(1 - V_R) + [a(1 - V_K) - V_H]^2 < 2V_H^{1/2}[a(1 - V_K) - V_H].$$

Under this condition damped oscillations occur in the system. The phase portrait of the system is shown in Fig. 4.2a and kinetics variables in Fig. 4.2b, c, curve 1.

The application of the periodic low-frequency field changes in the reaction rates in the system. Assuming a constant gradient value of the electric potential across the membrane layer, this effect can be taken into account in the equations in the form of periodic changes in the rate constants of the ion flows since these coefficients in the membrane region are determined by electrodiffusion processes. The applied field causes negligible effects on the transport processes in the membrane itself because the field strength in the membrane greatly exceeds that of the external field.

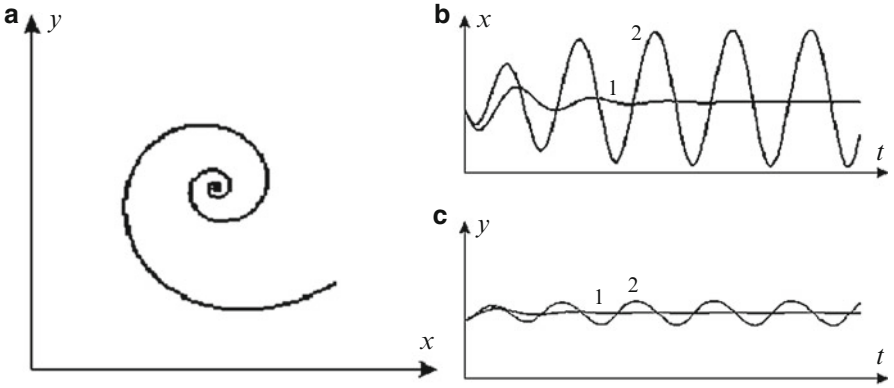


Fig. 4.2 (**a**) Phase diagram of system (4.4), Parameter values: $V_H = 1$, $V_K = 0.96$, $a = 30$. (**b**, **c**) Dimensionless concentrations (**b**)—protons (x-axis) and (**c**)—K^+ ions (y-axis) changes over time. Curve 1 is in accordance with system of equations (4), curve 2 is in accordance with system (4.6), with periodic exposure. $V_H = 1$, $V_K = 0.96$, $a = 30$, $A = 0.0005$, $\omega = 0.064$

Equations with periodically changing coefficients can be written in the following form:

$$\begin{aligned} \frac{dx}{dt} &= V_H(1 + A\sin\omega t) - \frac{ax}{1 + x + xy}, \\ \frac{dy}{dt} &= V_K(1 + A\sin\omega t) - \frac{yx}{1 + x + xy}. \end{aligned} \tag{4.6}$$

Here ω is the dimensionless frequency of the external field, and A is the dimensionless amplitude showing the ratio of external electric field to internal electric field intensities in the membrane region.

The periodic impact leads to sustained oscillations of the system variables, their amplitude being dependent on the frequency of the external field. Figure 4.2b, c presents the kinetic curves of changes in these variables over time for a system without an external influence, damped oscillations (curve 1), and under an external effect on the resonance frequency (curve 2), continuous waves of sufficiently high amplitudes.

Figure 4.3 presents a frequency response of the system that has a resonance character. Thus, the system can operate as an amplifier. Under the influence of a weak low-frequency field, the ion concentrations begin to change periodically. Estimates show that at the resonance frequency the amplitude of these oscillations can reach tenths (to unity) of pH units. As estimated, the resonance frequency in this case varies from a few tenths to a few tens of Hertz (Fig. 4.3).

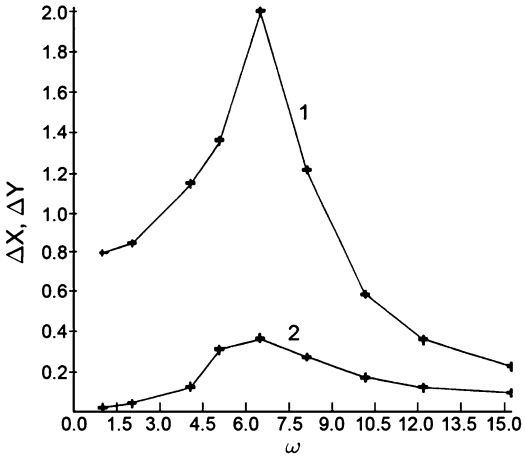


Fig. 4.3 Dependence of ΔX and ΔY, the concentration amplitudes of protons (curve 1) and ions K^+ (curve 2), respectively, on the frequency ω of the external electric field (frequency response function)

Bistable Model

A more detailed analysis of the process of the K^+-H^+ antiport in the membrane gives a bistable model. Weak periodic exposure can have a significant effect on a system, the frequency of exposure being a control parameter.

Let us take into account the formation of an inactive complex with two hydrogen ions: TH + H + $\leftrightarrow$ $(TH^2)^+$. The scheme of chemical transformations is as follows:

$$
\begin{array}{ccccccccc}
V_H & \underset{k_H}{\rightleftharpoons} & H_1^+ + T^- & \underset{k_{-1}}{\overset{k_{+1}}{\rightleftharpoons}} & TH & \xrightarrow{k_{+2}} & T^- + H_2^+ & \longrightarrow & V'_H \\
 & & H_1^+ + TH & \underset{k_{-5}}{\overset{k_{+5}}{\rightleftharpoons}} & \left(TH^2\right)^+ & & & & \\
V'_K & \longleftarrow & K_1^+ + TH & \xleftarrow{k_{+4}} & THK^+ & \underset{k_{-3}}{\overset{k_{+3}}{\rightleftharpoons}} & TH + K_2^+ & \longleftarrow & V_K
\end{array}
$$

Writing a system of kinetic equations and performing a reduction of the system, taking into account a hierarchy of characteristic times, we obtain a system of equations for the dimensionless concentrations of protons and K^+ ions:

$$
\begin{aligned}
\frac{dx}{dt} &= V_H - k_H x - \frac{ax}{1 + x + xy + bx}, \\
\frac{dy}{dt} &= V_K - \frac{xy}{1 + x + xy + bx}.
\end{aligned}
\tag{4.7}
$$

The dimensionless variables are introduced by formulas (4.2) and the dimensionless parameters by formulas (4.3). System (4.7) has two more dimensionless parameters:

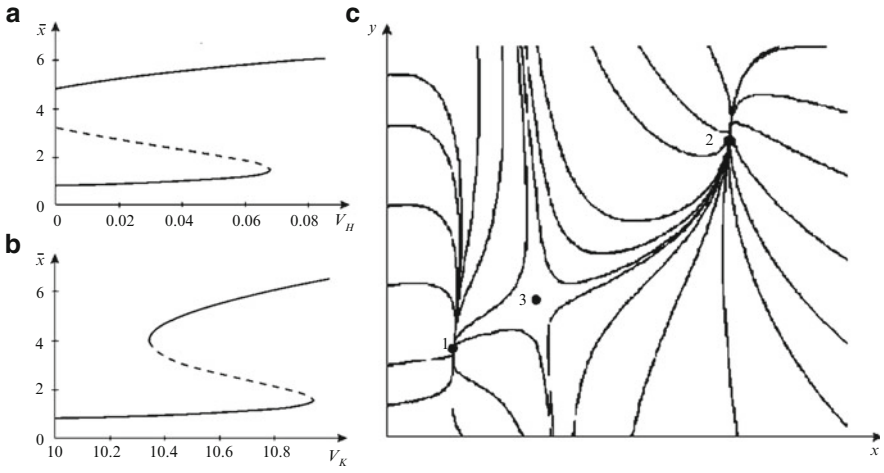


Fig. 4.4 **a**, **b** Dependence of stationary proton concentration on proton flow rate V_H (**a**) and potassium ion flow rate V_K (**b**) to the reaction sphere. *Solid line*: stable branches; *dashed line*: unstable branch of solutions. (**c**) Phase portrait of system (4.3). The system has three stationary solutions: two stable nodes (1 and 2) and a saddle (3). $V_H = 10.637$, $V_K = 0.0325$, $k_H = 1$, $a = 26.44$, $b = 0.696$

$$b = \frac{K_m k_{+5}}{k_{-5}}, \quad k'_H = \frac{k_H \overline{K}_m}{T_0 k_{+4}}. \tag{4.8}$$

In what follows, the prime on the k_H is omitted. The steady-state solution can be obtained from the equations

$$\begin{gathered} V_H - k_H \overline{x} - \frac{a\overline{x}}{1 + \overline{x} + b\overline{x} + \dfrac{V_K a x}{V_H - k_H \overline{x}}} = 0, \\ \overline{y} = \frac{V_K a}{V_H - k_H \overline{x}}. \end{gathered} \tag{4.9}$$

The steady-state concentration of protons is the solution of the cubic equation

$$-bk_H(\overline{x})^3 + (\overline{x})^2(bV_H - k_H) - \overline{x}(k_H - V_K a + a - V_H) + V_H = 0. \tag{4.10}$$

Equation (4.10) may have one, two, or three positive roots. In the latter case, two steady points are stable singular points of system (4.7), with the third point—located between them—the saddle (Fig. 4.4c).

Figure 4.4a shows the dependence of the steady-state concentration of protons on the parameter V_H. There is a range of values of V_H that corresponds to three stationary solutions. The dotted line denotes the unstable branch of solutions, and the dependence of the steady-state proton concentration on V_K (Fig. 4.4b) has the

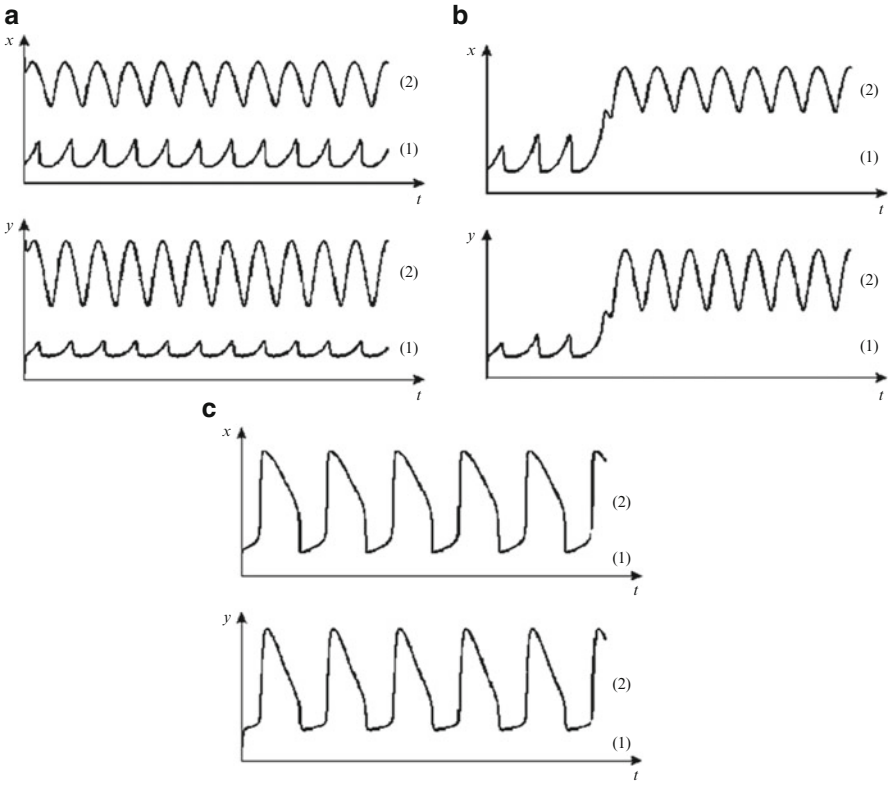


Fig. 4.5 Kinetics of variables of bistable system (4.4) in presence of external periodic excitation at different values of frequency of applied oscillations. The initial values of the variables are in the vicinity of the stable stationary states. Curve 1 is in the vicinity of a stable node (1), curve 2 is in the vicinity of a stable node (2). (**a**) $\omega < \omega_1$; (**b**) $\omega_1 < \omega < \omega_2$; (**c**) $\omega > \omega_2$. System parameters: $V_H = 10.637$, $V_K = 0.0325$, $k_H = 1$, $a = 26.44$, $b = 0.696$, $A = 0.03$

same character. A phase portrait of system (4.7) is shown in Fig. 4.4c; stationary states 1 and 2 are stable nodes, and state 3 is a saddle point.

When periodic changes in the values of V_H and V_K defined in formula (4.7) occur, the computer experiment gives the following result. Let the initial variable values be close to one of the two steady-state points. At the high frequency of the exposure, the system oscillates in the vicinity of the corresponding steady-state point (Fig. 4.5a, x: protons, y: potassium ions). For curve 1 the initial variable values correspond to steady state 1 in Fig. 4.4c; for curve 2 they correspond to steady state 2 in Fig. 4.4c.

We will gradually reduce the frequency ω of the external field. There exists a certain critical value ω_1 at which the system performs several oscillations near state 1 and then proceeds to the neighborhood of the second steady state, where subsequent oscillations occur (Fig. 4.5b). For the parameters specified in the legend to Fig. 4.5, the value of the critical frequency is $\omega_1 = 0.047$.

After reaching the next critical ω_2 value (for the parameters given previously $\omega_2 = 0.023$) the system demonstrates oscillations between stationary states 1 and 2 corresponding to the frequency of the external influence. The kinetics of the variables are presented in Fig. 4.5c.

Thus, the frequency of the external periodic exposure can serve as a control parameter that can "switch" the system from one stationary state to another. In some range of frequencies, that switch becomes irreversible.

Auto-oscillating System

A more detailed consideration of chemical reactions that occur in the K^+-H^+ antiport leads to a system in which the self-oscillations of the variables are possible. The kinetic scheme includes the formation of an inactive complex with a proton transporter as follows:

$$
\begin{array}{lllllll}
V_H \underset{k_H}{\rightleftharpoons} & \mathrm{H}_1^+ + \mathrm{T}^- & \underset{k_{-1}}{\overset{k_{+1}}{\rightleftharpoons}} & \mathrm{TH} & & & \\
 & \mathrm{H}_1^+ + \mathrm{TH} & \underset{k_{-5}}{\overset{k_{+5}}{\rightleftharpoons}} & \left(\mathrm{TH}^2\right)^+ & & & \\
 & \mathrm{H}_1^+ + \mathrm{TK} & \underset{k_{-7}}{\overset{k_{+7}}{\rightleftharpoons}} & \mathrm{THK}^+ & \xrightarrow{k_{+6}} & \mathrm{TK} + \mathrm{H}_2^+ & \longrightarrow V'_H \\
V'_K \longleftarrow & \mathrm{K}_1^+ + \mathrm{TH} & \xleftarrow{k_{+4}} & \mathrm{THK}^+ & \underset{k_{-3}}{\overset{k_{+3}}{\rightleftharpoons}} & \mathrm{TH} + \mathrm{K}_2^+ & \longleftarrow V_K.
\end{array}
$$

The system of equations in dimensionless variables taking into account the external periodic effect is

$$
\begin{aligned}
\frac{dx}{dt} &= V_H(1 + A\sin\omega t) - k_H x - \frac{bxy}{1 + b(x + xy + y) + cx^2}, \\
\frac{dy}{dt} &= V_K(1 + A\sin\omega t) - \frac{bxy}{1 + b(x + xy + y) + cx^2}.
\end{aligned}
\tag{4.11}
$$

In addition to the parameters used in formulas (3.11) and (4.5), (4.8) also includes a parameter

$$
c = \frac{K_m^2 k_{+1} k_{+5}}{k_{-1} k_{-5}}.
$$

Analysis shows that in the absence of external exposure ($A = 0$), system (4.11) at certain parameter values satisfies the Hopf conditions. Thus the system possesses a supercritical bifurcation. In an analytical study and computer modeling, values of the control parameter V_H were obtained when bifurcation changes arose in the

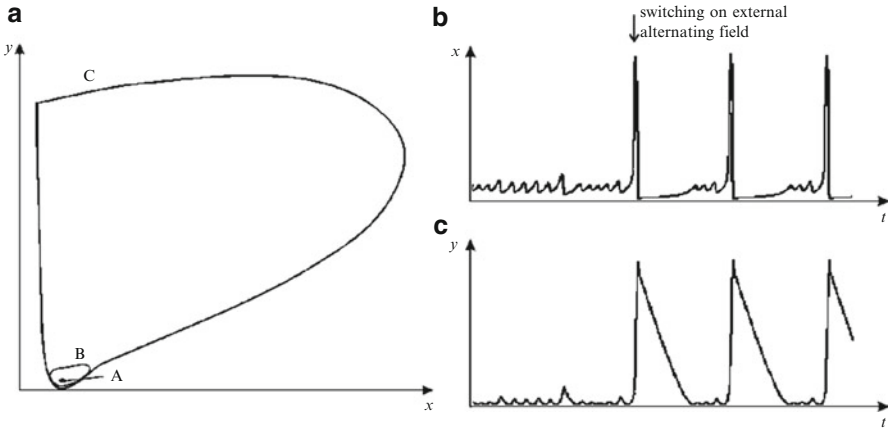


Fig. 4.6 (**a**) Phase portrait of system (4.8) in absence of external field ($A = 0$) for different values of parameter V_H close to values corresponding to Andronov–Hopf bifurcation. x and y are the dimensionless concentrations of potassium ions and protons; $V_K = 0.5$, $k_H = 0.01$, $b = 1$, $c = 1$. When $V_H = 0.5241$, a stable focus is realized (A), at $V_H = 0.5242$ there is a limit cycle (B); at $V_H = 0.5245$ the cycle amplitude increases sharply (curve C). (**b**) Kinetics of dimensionless proton concentration (x) and potassium ions (y) in (4.8). In response to a weak external periodic disturbance in the system, transitions occur from oscillations of small amplitude to oscillations of large amplitude. Parameter values: $V_K = 0.5$, $k_H = 0.01$, $b = 1$, $c = 1$, $V_H = 0.5243$, $A = 0.0003$, $\omega = 0.004$

system (Plyusnina et al. 2005). The area of a bifurcation is very narrow: a change in the ten-thousandths of a parameter leads to a transition from a regime of damped oscillations to limit cycles of varying amplitudes. Two attractors arise, one of which is a stable focus and the other is a stable limit cycle of large amplitude. Changes in the structure of the phase portrait, depending on the parameter V_H near the Andronov–Hopf bifurcation, are shown in Fig. 4.6.

We studied the impact of the external periodic field on the parameter V_H, in cases where it depended on the potential gradient in the vicinity of the bifurcation point and in cases where the parameter values were far from the bifurcation. At a distance from the bifurcation points the system remains stable in a wide range of amplitudes and frequencies; the characteristics of the self-oscillations do not change.

Near the critical values of V_H a small perturbation of the external field causes a change in the regime operation. At the lower critical value of the parameter $V_H = 0.5241$, corresponding to a stable focus, weak external action takes the system from a damped oscillation to the self-oscillation mode. If the exposure occurs when the system is in the self-oscillation domain (at V_H, close to the bifurcation), a transition from low-amplitude vibrations to large-amplitude vibrations takes place. Figure 4.6a shows the transition from the B cycle to the limit cycle C. The corresponding kinetics of the variables is shown in Fig. 4.6b.

The phase portrait of this system in an unperturbed state for large values of the parameter V_H is shown in Fig. 4.7a.

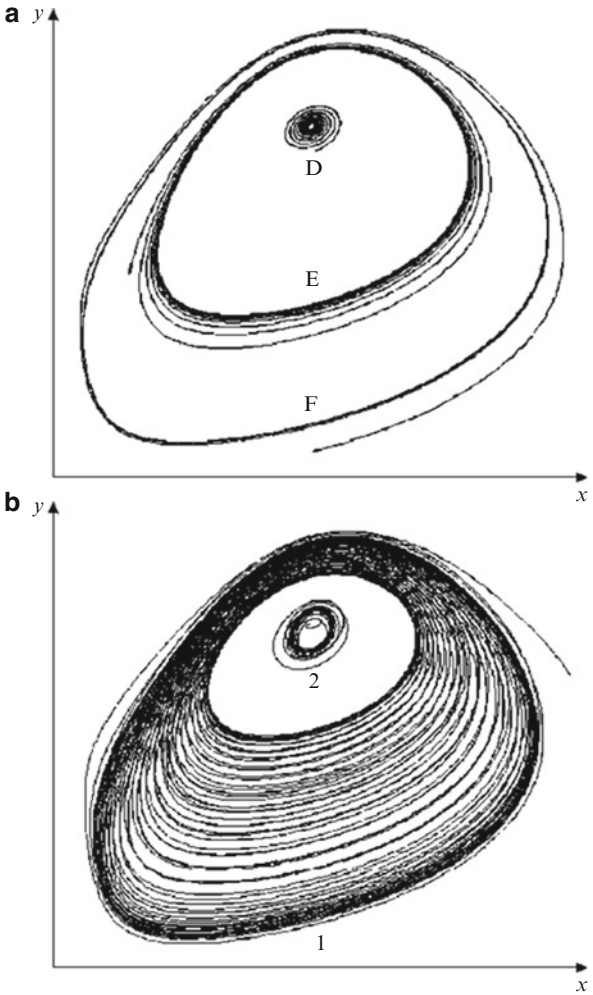


Fig. 4.7 (**a**) Phase diagram of unperturbed system (4.8) near critical value of parameter V_H. In the range of values of $V_H = 0.701$–0.706 in the system at the same time there is a steady focus D, an unstable limit cycle E, and a stable limit cycle F. $V_K = 0.5$, $k_H = 0.01$, $b = 1$, $c = 1$. (**b**) Quasistochastic regime in system (4.8) in presence of low-intensity periodic effect. $V_K = 0.5$, $k_H = 0.01$, $b = 1$, $c = 1$; $V_H = 0.7065$, $A = 0.003$, $\omega = 0.0025$

Near the upper critical value $V_H = 0.706$, the response of the system to a weak external periodic impact may be different depending on the frequency. At relatively high frequencies of an impact the system either oscillates in the vicinity of a stable focus (D in Fig. 4.7a) or tends to a limit cycle (F in Fig. 4.7a) depending on the initial conditions. With a decrease in the frequency of the exposure, there is a certain critical frequency at which the system, located near the stable focus, can

be "thrown" in the neighborhood of the limit cycle. We have seen a similar phenomenon of "flipping" (turnover) from one attractor to another in a bistable system.

With a decrease in the frequency of the external action in the vicinity of the limit cycle a limit set of the strange attractor type occurs. Phase trajectories for the parameter value $\omega = 0.0025$ are shown in Fig. 4.7b.

The preceding model is one possible basic model to describe the processes that occur in excitable membranes and other processes characterized by a set of complex patterns of behavior.

Part II
Models of Complex Systems

Real biological systems are complex heterogeneous structures containing hundreds of thousands of components and a multilevel system of regulation where processes simultaneously occur that differ in their physical and chemical mechanisms.

In the first part we considered the various basic models that describe the main types of biophysical interactions. Thus, the processes of random movement (Brownian motion) in energy-rich media can be described by equations of reaction–diffusion, and nerve impulse distributions can be described by cable equations used in the theory of electricity. In cases where one finds a compelling analogy between biological and physical processes, it is possible to construct mathematical and computer models that quite satisfactorily reproduce natural processes. Models constructed on this principle, for example, those of cardiac activity or of blood flow in blood vessels, have become a serious tool in the development of effective medical technologies that address the biophysical properties of systems subject to regulation.

In Part II we will look at examples of real biological systems and their mathematical models, which describe various mechanisms of simultaneous processes.

In the first chapter a model is considered describing processes of self-organization of striped structures of acid and alkaline zones along the cell wall of a giant cell (up to 10 cm in length), *Chara corallina*, under the action of light. The basis of this phenomenon lies in the combination of the propagation of electric potential along a cell membrane and the functioning of molecular machines (proton ATPases) embedded in the membrane, which together lead to the emergence of spatially inhomogeneous structures. The process is maintained by the energy stored during photosynthesis under illumination. Thus, the cell of *Chara* is a unique model object for the study of real and varied processes in biological systems.

The second chapter is devoted to the modeling of morphogenesis. For simulation of this biological process the approaches of mathematical physics, i.e., reaction–-diffusion equations, have proved effective. The foundation of this approach was laid in the mid-twentieth century by Turing, Kolmogorov, Prigogine, and others. The most impressive models in this case are those that reproduce different patterns

of coloring of animal skins, the shapes of shells and leaves of plants, or fancy patterns of colonies of microorganisms.

The third chapter is devoted to the basics of modeling of nerve pulse propagation and heart activity. The models in this area of investigation are based on the results of Hodgkin and Huxley, who conducted experimental studies on the giant squid axon and proposed the first model of propagation of nerve impulses. The basis of this research field was also laid down with axiomatic models of active media by Wiener, Rosenbluth, and Gelfand. They demonstrated the existence of different autowave regimes, including spiral waves.

Subsequent models of cardiac activity in two and three dimensions used continuous (reaction–diffusion models) and discrete (cellular automata) approaches. In contemporary models, the heart is considered a heterogeneous system of interacting cardiomyocytes with complex geometry. Regular wave activity in these models simulates the normal functioning of the heart. Randomization (chaotization) of the spiral waves in the model can be interpreted as atrial fibrillation. This area of research is in high demand by modern medicine, which has been facing a sharp increase in cardiovascular events due to the global increase in human longevity.

Finally, the fourth chapter of this part is devoted to a physical model of the unwinding of DNA—a physical process that forms the basis of self-reproduction of biological macromolecules. The phenomenon of DNA splitting is described on the basis of mechanical analogies. Considering interacting nucleotides as physical pendulums, biophysical models make it possible to describe the spread of the conformational wave and long-range interactions in DNA. The selection of complex biological systems, models of which are included in this chapter, is quite arbitrary, although it conveys an idea about the features of biophysical models of living systems.

Chapter 5
Oscillations and Periodic Space Structures of pH and Electric Potential Along the Cell Membrane of Algae *Chara corallina*

Few biological systems allow us to observe and reproduce in direct experiments nonlinear phenomena at the level of an individual cell. Gigantic algae *Chara corallina* and *Nitellopsys abtusa* demonstrate the phenomena of pH nonlinear dynamics in time and space—oscillations and pattern formation along cellular membranes that arise under illumination. The essence of the current chapter is based on the results of the modeling of processes occurring in a cell membrane and the simulation of these dynamics obtained in the Department of Biophysics, Biological faculty, Moscow State University (Bulychev et al. 2001; Plyusnina et al. 2005, 2008; Lavrova et al. 2005).

The existence of pattern formation and oscillations of cell pH and transmembrane potential is a well-known phenomenon for many living organisms. It has been shown that for some plant roots and root fuzz, potential patterns play an important role in tissue differentiation and growth (Fisahn and Lucas 1992, 1995; Feijo et al. 1999; Miller and Gow 1989). It has been found that the spatial distribution of ionic electric currents along the cell membrane of a zygote of the algae *Pelvetia* and *Fucus* determines the development of the cell structure (Gibbon and Kropf 1991). In most cases, various regimes of nonlinear cell membrane dynamics occur as a response to the application of external stimuli such as illumination, changes in the media pH or temperature, or application of an electric impulse.

Gigantic algae cells are convenient objects for studying nonlinear electrophysiological phenomena because of their large size (diameter of 0.6–1 mm and length of 40–80 mm) and simpler structure in comparison with cells of higher plants. Illumination of the algae cell causes the appearance of potential and pH patterns near the cell membrane. It has been shown that pH patterns originate when the intensity of the applied light exceeds a critical value. The pH of alkaline pattern bands is approximately 9.5–10 and that of acidic bands approximately 7–6.5. Thus the difference in pH values in acid and alkaline zones can reach up to 2.5–3 units (Fisahn et al. 1989).

A. Rubin and G. Riznichenko, *Mathematical Biophysics*, Biological and Medical Physics, Biomedical Engineering, DOI 10.1007/978-1-4614-8702-9_5,

© Springer Science+Business Media New York 2014

Local pH and potential changes near the cell membrane can demonstrate oscillations that could be connected to pattern formation or arise independently. Damped and undamped oscillations were registered at fixed points between acidic and alkaline bands. Under low-intensity light illumination, undamped oscillations of pH and potential with a period of 60 min have been observed (Fisahn et al. 1986). Damped oscillations have been observed after the application of a short pulse of light (Fisahn et al. 1989; Boels and Hansen 1982; Hansen 1978). It was previously thought that pH banding was produced by a heterogeneity membrane structure. Later it was proposed (Toko et al. 1985, 1988; Leonetti and Pelce 1994) that the heterogeneity of ionic currents is caused by activity of intrinsic transport systems: ATPase and ion channels. From this point of view pH bands are an example of actual dissipative structures generated in a living system.

The pH pattern emergence can be simulated by means of Turing-type reaction–diffusion models, where ions of hydrogen and HCO_3^- serve as reactants (Leonetti and Pelce 1994; Toko et al. 1988). Polezhaev, in Bulychev et al. (2001) and Polezhaev (2010), also considered proton and bicarbonate ion fluxes and their diffusion. Their research suggests that it is the difference in diffusion coefficients that leads to pH banding.

The main feature of previous models is the description of pattern formation, but our objective is to understand the definite biological processes and mechanisms that might offer an explanation of the observed phenomena. In papers by Plyusnina et al. (2005, 2008) and Lavrova et al. (2005) we describe the interactions between transmembrane ion fluxes, lateral diffusion of H^+ ions along the membrane, and electric potential distribution. The local element of this spacetime model is a submodel of the H^+-ATPase catalytic cycle and ion channel operation. In the model, the kinetics of proton transport are described in detail, and fluxes of other ions are taken into account as a common additional term. To describe the potential distribution along the membrane, the cable equation is used.

Our model uses the detailed kinetics of proton transfer via ATPase and passive leakage through proton channels (Plyusnina et al. 2005). There are abundant experimental data on ATPase function (Gradmann 2001; Shartzer et al. 1992; Sanders et al. 1981; Takeuchi et al. 1985) that show that ATPase actively pumps out protons to the external media, and then protons passively return through the channels into the cell. It was supposed that ATPase and proton channels were tightly coupled and together could be taken as a single structural component (Takeuchi et al. 1985).

Kinetic Model of Proton ATPase (Pump)

Proton ATPase pumps out protons from the inner volume (cytosole) out of the cell into the environment. Through passive channels, H^+ ions return to the cell; together ATPase and proton channels form a common transport system. To determine

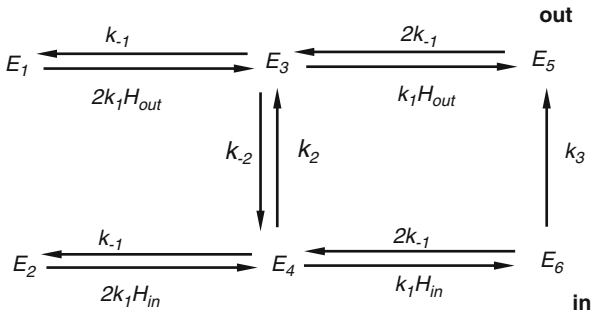


Fig. 5.1 Detailed kinetic scheme of ATPase transport system activity; *out* denotes the environment of the cell; *in* denotes cytosol. H_{in} is the proton concentration in the cytosole; H_{out} is the proton concentration near the external side of the plasmalemma. E_1 and E_2 are conformational states of the transport system without protons. E_3 and E_4 are the conformational states of the transport system with one bound proton. E_5 and E_6 are conformational states of the transport system with two bound protons. k_i, k_{-i} $(i = 1, 2)$ are rate constants of the corresponding reactions; the transition $E_6 \rightarrow E_5$ is assumed to be irreversible

a specific expression for the proton flux through the H^+-ATPase let us consider a kinetic scheme of the enzyme operation (Fig. 5.1).

In the model we assume that there are two enzyme sites for substrate (proton) binding. The processes of proton association at these two sites are independent. Rate constants k_1 (mol s^{-1} m^{-3}) and k_{-1} (s^{-1}) determine proton association and dissociation. Factor 2 (in the expressions 2 k_{-1} and 2 k_1 H_{in}) defines an equal probability of proton association or dissociation at each site. Rate constants k_2 (s^{-1}) and k_3 (s^{-1}) determine proton transfer to the vicinity of the cell, whereas k_{-2} (s^{-1}) determines proton transfer into the cell. We assume that the probability of proton transfer across the membrane depends on the transmembrane electric potential φ. The transfer probabilities correspond to the kinetic rate constants of the electrogenic transfer k_{-2}, k_2, and k_3. In the model, the following dependence of the rate constants of the proton transfer from one side of the membrane to the other on the potential φ is considered:

$$k_{-2} = k_{-2}^0 \exp\left(-\frac{F\varphi}{2RT}\right), \quad k_2 = k_2^0 \exp\left(\frac{F\varphi}{2RT}\right), \text{and} \quad k_3 = k_3^0 \exp\left(\frac{F\varphi}{2RT}\right).$$

We assume that the probability of the simultaneous transfer of two protons from the outer side to the inner side is very small, which is why we did not consider the transfer from state E_5 to state E_6, which corresponds to the transfer of the second proton.

On the basis of the kinetic scheme in Fig. 5.1, we can write the following set of kinetic equations:

$$\begin{aligned}
\frac{d[H_0]}{dt} &= k_{-1}[E_3] - 2k_1[H_0][E_1] - k_1[H_0][E_3] + 2k_{-1}[E_5],\\
\frac{d[E_1]}{dt} &= k_{-1}[E_3] - 2k_1[H_0][E_1],\\
\frac{d[E_2]}{dt} &= k_{-1}[E_4] - 2k_1[H_i][E_2],\\
\frac{d[E_3]}{dt} &= 2k_1[H_0][E_1] - k_{-1}[E_3] + 2k_{-1}[E_5] - k_1[H_0][E_3] - k_{-2}[E_3] + k_2[E_4],\\
\frac{d[E_4]}{dt} &= 2k_1[H_i][E_2] - k_{-1}[E_4] + 2k_{-1}[E_6] - k_1[H_i][E_4] - k_{-2}[E_3] + k_2[E_4],\\
\frac{d[E_5]}{dt} &= k_3[E_6] + k_1[H_0][E_3] - 2k_{-1}[E_5],\\
[E_1] + [E_2] &+ [E_3] + [E_4] + [E_5] + [E_6] = E_0.
\end{aligned} \tag{5.1}$$

Here $[H_0]$ is the proton concentration in the vicinity of the membrane (mol m^{-3}), $[H_i]$ is the proton concentration in the cytosole (mol m^{-3}), $[E_1]$–$[E_6]$ are enzyme concentrations in different conformation states (mol m^{-3}), $[E_1]$ is the enzyme concentration in active form and $[E_2]$ is that in inactive form, $[E_3]$ and $[E_4]$ are enzyme concentrations in the state in which one site is occupied by the substrate (proton), $[E_5]$ and $[E_6]$ are enzyme concentrations in the state in which both sites are occupied by protons, and E_0 is the total enzyme concentration. In this model $[H_i]$ serves as a parameter.

The first equation of the ODE system (5.1) describes changes in the proton concentration $[H_0]$ in the vicinity of the cell caused by the operation of the ATPase. The last equation reflects the assumption that the total concentration of the enzyme in all considered states of H^+-ATPase is constant. The remaining five equations describe the kinetics of different states of the enzyme.

Equation Describing Dynamics of Proton Concentration in Vicinity of Cell

The main assumption of the model is that changes in concentration of each ATPase state occur more rapidly than changes in proton concentration in the cell vicinity. This gives us reason to consider the enzyme state concentrations E_i to be in their quasi-steady state, so we can introduce algebraic equations for these variables. Further, we assume that the processes of proton transport from one side of the membrane to the other ($E_4 \leftrightarrow E_3$; $E_6 \rightarrow E_5$; Fig. 5.1) occur at much slower rates

than the processes of proton association and dissociation ($E_1 \leftrightarrow E_3$; $E_3 \leftrightarrow E_5$; $E_2 \leftrightarrow E_4$; $E_4 \leftrightarrow E_6$; Fig. 5.1). This time hierarchy allows for the reduction of the first equation of ODE system (5.1), which describes changes in the proton concentration outside the cell. Finally, this equation can be written in the following form:

$$\frac{dH_0}{dt} = E_0 k_{-2} \frac{\frac{H_0}{K_1} e^{\psi}(1-n)}{2q\frac{H_0}{K_1} + e^{2\psi}\left(1+\frac{H_0}{K_1}\right)^2 (n+1)}. \tag{5.2}$$

Here $\psi = \frac{\varphi F}{2RT}, n = \frac{1}{K_3 h_i + 1}, q = \frac{(1+h_i)^2 K_2 n}{h_i}, h_i = \frac{[H_i]}{K_1}, K_1 = \frac{k_{-1}}{k_1}, K_3 = \frac{k_3^0}{2k_2^0}$, $K_2 = \frac{k_{-2}^0}{k_2^0}$.

The total changes in the proton concentration outside the cell depend on the flux through the ATPase and on the passive transmembrane diffusional flux across the membrane. Furthermore, proton diffusion along the cell membrane occurs. Since the length of the *Chara corallina* algal cell (4–6 sm) is many times greater than its diameter (~1 mm), we shall consider proton diffusion along the single space coordinate r (1D diffusion).

The equation for the total changes in proton concentration outside the cell in dimensionless variables is

$$\frac{\partial h_0}{\partial \tau} = \frac{h_0 e^{\psi}(1-n)}{2qh_0 + e^{2\psi}(1+h_0)^2(n+1)} - \gamma h_0 + D_1 \frac{\partial^2 h_0}{\partial r^2}. \tag{5.3}$$

Here $h_0 = \frac{[H_0]}{K_1}, \tau = \frac{t}{t_0}, t_0 = \frac{K_1}{k_{-2}[E_0]}, r = \frac{x}{L}$, and L is the length of the cell (m).

The first term describes the proton flux through the ATPase, the second γh_0 the proton exchange between the cell and the environment due to the proton flux from the cell surface to the environment and the passive flux through the proton channels, independent of the ATPase, inside the cell. $D_1 = \frac{Dt_0}{L^2}$, where D ($m^2\ s^{-1}$) is a diffusion coefficient of protons along the cell membrane outside the cell.

Equation for Potential Dynamics

The equation for the transmembrane potential distribution is based on the cable properties of the membrane (Fig. 5.2).

Taking into account ion fluxes across the membrane, similar to the models of nerve pulse distribution (see below), the equation for the potential is

$$\frac{p}{2R_i}\frac{\partial^2 \varphi}{\partial x^2} = -(I_{ATP} + I_l) + C\frac{\partial \varphi}{\partial t}. \tag{5.4}$$

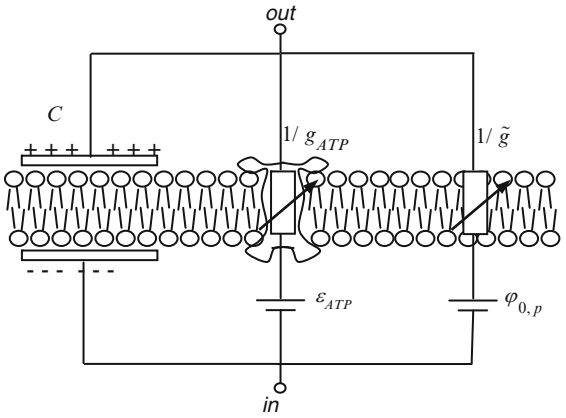


Fig. 5.2 Equivalent electrical circuit model of membrane structure and its electrical characteristics. Here capacitor C is a lipid bilayer, $\varepsilon_{\mathrm{ATP}}$ is an analog of the battery corresponding to ATPase, g_{ATP} is the membrane conductance produced by ATPase, $\varphi_{0,p}$ is the resting potential with the ATPase switched off, $\tilde{g}$ is the conductance of passive ion channels

The total flux across the membrane $\left(\frac{p}{2R_i}\frac{\partial^2\varphi}{\partial x^2}\right)$ equals the sum of the capacity $\left(C\frac{\partial\varphi}{\partial t}\right)$ and ion (I) currents. In our case the ion current (I) consists of the proton flux through the ATPase (I_{ATP}) and the leakage current (I_{l}), including fluxes of other ions. Here φ is the transmembrane potential, R_i the cytoplasm reluctance (Ohm m); C the membrane capacity (μF m^{-2}), and I_{ATP} the current through the H^+-ATPase (A m^{-2}):

$$I_{\mathrm{ATP}} = E_0 k_{-2}\frac{\frac{H_0}{K_1}e^{\psi}(1-n)}{2q\frac{H_0}{K_1}+e^{2\psi}\left(1+\frac{H_0}{K_1}\right)^2(n+1)}Fp, \tag{5.5}$$

where I_l is the leakage current, including other ion fluxes (A m^{-2}), F is the Faraday constant (C mol^{-1}), and p is the cell diameter (m). The leakage current can be written as $I_{\mathrm{l}} = \tilde{g}(\varphi - \varphi_{0,p})$, where $\tilde{g}$ is the conductivity of the passive fluxes (Ohm^{-1} m^{-2}) and $\varphi_{0,p}$ the resting potential of the membrane.

The final reduced mathematical model consists of two partial differential equations and describes variations in the proton concentration outflow near the external side of the cell membrane (h_0) and the transmembrane electric potential (ψ):

$$\begin{aligned}\frac{\partial h_0}{\partial\tau} &= \frac{h_0 e^{\psi}(1-n)}{2qh_0+e^{2\psi}(1+h_0)^2(n+1)} - \gamma h_0 + D_1\frac{\partial^2 h_0}{\partial r^2},\\ \frac{\partial\psi}{\partial\tau} &= \frac{-h_0 e^{\psi}(1-n)}{2qh_0+e^{2\psi}(1+h_0)^2(n+1)}z - g(\psi-\psi_0) + D_2\frac{\partial^2\psi}{\partial r^2},\end{aligned} \tag{5.6}$$

where $n = \dfrac{1}{K_3 h_i + 1}$, $q = \dfrac{(1+h_i)^2 K_2 n}{h_i}$, $K_3 = \dfrac{k_3^0}{2k_2^0}$, $K_2 = \dfrac{k_{-2}^0}{k_2^0}$, $g = \dfrac{\widetilde{g} K_1}{C k_{-2}[E_0]}$, $K_1 = \dfrac{k_{-1}}{k_1}$, $z = \dfrac{pF^2 K_1}{2CRT}$, $\psi_0 = \dfrac{\varphi_{0,p} F}{2RT}$, $D_2 = \dfrac{pK_1}{2L^2 R_i C k_{-2}[E_0]}$.

The initial conditions are the stationary values of proton concentrations near the outer side of the membrane and the membrane potential. The boundary conditions are zero fluxes:

$$\frac{\partial h_0}{\partial r}(0,\tau) = \frac{\partial h_0}{\partial r}(1,\tau) = 0, \quad \frac{\partial \psi}{\partial r}(0,\tau) = \frac{\partial \psi}{\partial r}(1,\tau) = 0.$$

In the papers by Plyusnina et al. (2005, 2008) and Lavrova et al. (2005), an analysis of the dynamic properties of the local system without diffusion and the system with diffusion terms (5.6) was performed in detail. The parameter identification according to the experimental data allows for a comparison of the simulation results with the experimentally observed nonlinear phenomena. Below we consider the most interesting results.

Oscillations in Local System

In experiments on the membrane of *Nitella* cells, local damped and continuous oscillations of the membrane potential and pH were observed. It was of special interest that both types of oscillations could be registered at the same light intensity (20 W m^{-2}). Damped oscillations with a period of 2 min occurred after switching on the light after darkness. Nondamped oscillations with a period of about 15 min appeared spontaneously under continuous illumination. Figure 5.3 shows a phase diagram of the local system, where at different initial conditions two steady regimes can be realized—a stable spiral and a stable limit cycle—and the attraction basins of these two regimes are separated by an unstable limit cycle.

Depending on the initial values of h_0 and ψ, both damped and undamped oscillations of the potential and proton concentrations can exist. The phase diagram of the system reflects the existence of a subcritical Hopf bifurcation in the system and corresponds to the regime classified by Winfree as a black hole (Winfree 2001).

pH Patterns Along Cellular Membrane

A linear analysis of system (5.6) with diffusion gives values of parameters at which the Turing instability appears. The found parameters were used for calculations, and small variations from the steady states were taken as the initial values of the variables. It was shown that at specific values of the parameter h_i in the system,

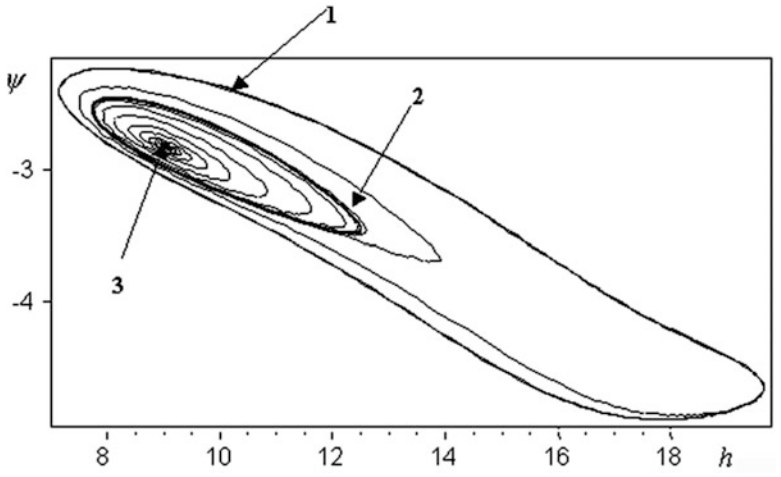


Fig. 5.3 Phase diagram of local system (5.6) demonstrating existence of two steady regimes. (1) stable limit cycle (undamped oscillations), (2) unstable limit cycle, (3) stable spiral (damped oscillations). System parameters: $z = 0.6$, $n = 0.9$, $q = 0.001$, $\gamma = 0.085$, $g = 0.03$, $\psi_0 = -1.28$, $h_i = 0.3$ (Plyusnina et al., 2005)

dissipative structures appeared that correspond to zones with different pH values in real systems (Fig. 5.4a, b). When the parameter h_i decreases (which corresponds to an increase in the illumination intensity), the structure amplitude increases; a similar phenomenon was observed in the experiments of Bulychev et al. (2001).

Dependence of Processes on Light Intensity: Hysteresis

In the majority of experiments the pattern formation process depends on the light intensity. In the experiments of Bulychev et al. (2002, 2003) the dependence of the pH structure amplitude on the light intensity was analyzed. In an intensity range of 1–100 W m^{-2}, the changes in illumination affect mainly the number of alkaline and acidic zones, but barely affect the pH difference between the zones. When the illumination intensity drops to less than 1 W m^{-2}, the character of the pattern formation changes. At the same value of light intensity, a homogenous pH distribution as well as pH zones can appear, depending on whether the light intensity decreases or increases. Observation of two steady pH profiles in one cell was confirmed by data obtained on different cells (Fig. 5.5).

The experimental results shown in Fig. 5.5 demonstrate the existence of two states of pH distribution at the same light intensity. A transition from the homogeneous state (no structures) to a state with a high amplitude of pH peaks occurs when the light intensity increases for each successive experiment. In an intensity range of

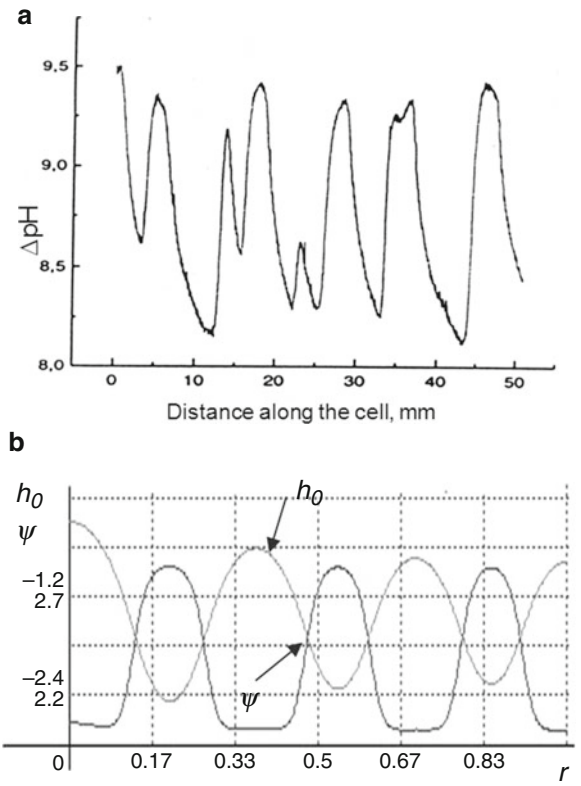


Fig. 5.4 (**a**) pH profile along algae *Chara corallina* cell, experimental data (Bulychev et al. 2001). (**b**) pH profile and electric potential along cell obtained in model. System parameters: $z = 0.65$, $n = 0.9$, $q = 0.001$, $\gamma = 0.01$, $g = 0.035$, $\psi_0 = -1.301$, $h_i = 0.67$, $D_1 = 1.44 \times 10^{-3}$, $D_2 = 3.6 \times 10^{-4}$

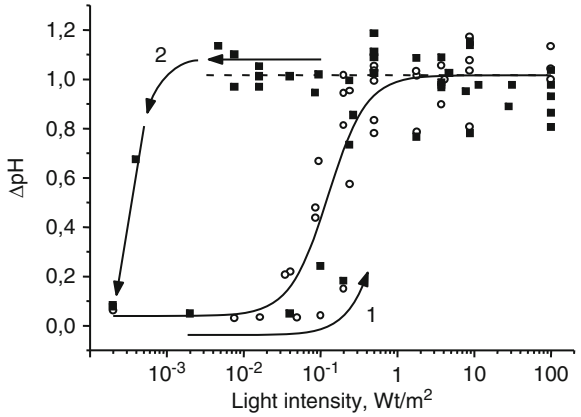


Fig. 5.5 Hysteresis in pH distribution near cell membrane of *Chara corallina*. Values of ΔpH on the cytoplasm membrane are presented that were obtained by light illumination with intensity increasing for each successive experiment (*light circles*) and decreasing for each successive experiment (*black squares*) (Bulychev et al. 2003)

10^{-2}– 1 Wt m^{-2} amplitude, the pH structure gradually increases. Further increase in the intensity does not lead to ΔpH growth.

When registration begins with high light intensities, which promote appearence of the structures, and the light intensity gradually decreases for each successive

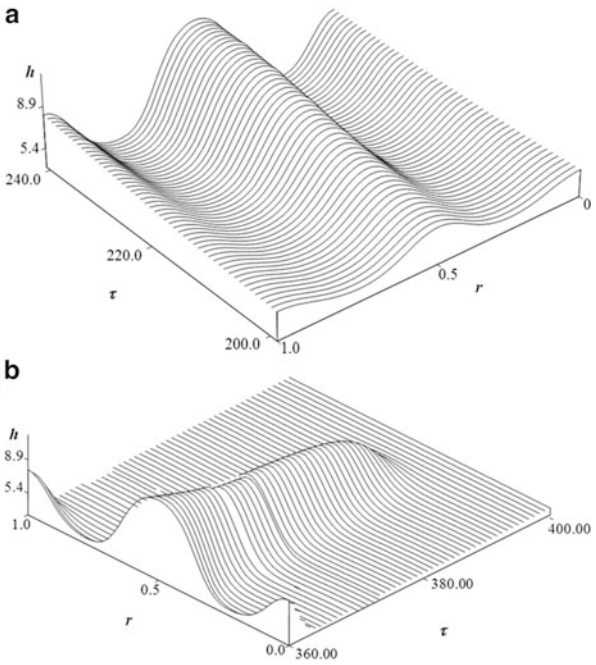


Fig. 5.6 Results of simulation. (**a**) Structure growth at light intensity close to but higher than the threshold value. (**b**) Decrease in structure amplitude in time at light intensity below threshold value (Lavrova et al. 2005)

experiment, the amplitude of ΔpH does not change until the value of the light intensity reaches 5×10^{-3} Wt m^{-2}. Thus the transition to the homogeneous state (no structures) in this case occurs at lower light intensities. The phenomenon of hysteresis takes place.

The experimental results were simulated on model (5.6), and the model parameters were identified according to experimental data (Plyusnina et al. 2005; Lavrova et al. 2005). The time evolution of the space structures of the variable h, corresponding to the proton concentration near the cell membrane, is presented in Fig. 5.6.

Figure 5.7 presents the results of a computer experiment that simulated the real experiment presented in Fig. 5.5.

The mechanism of the observed hysteresis could be connected to the inertia properties of the system. It takes some time for the formation of steady pH zones to complete. The structures begin to grow when the control parameter (light intensity) reaches its threshold value. The closer a parameter value is to the critical value, the more time is needed for pattern formation. Close to the bifurcation point the time of the structural growth can be several orders of magnitude longer than the growth time at the control parameter value far from the bifurcation point. The time intervals between the switching of the light intensity (30 min in a laboratory experiment, which corresponds to 40,000 steps in calculations) are limited. This might be why the structures arising under increasing light intensity do not have enough time to grow, whereas under decreasing light intensity they do not have enough time

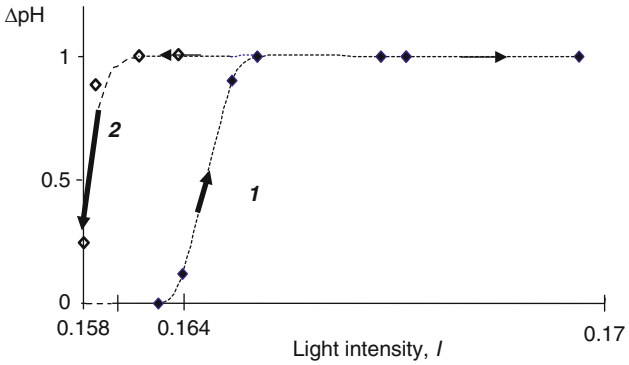


Fig. 5.7 Changes in maximum ΔpH between acid and alkaline zones at increase (*arrow 1*) and decrease (*arrow 2*) of light intensity; simulation results (Lavrova et al. 2005)

to disappear. That is why with increasing light intensity after equal periods of time we observe a gradual increase in the amplitude of the structures up to the maximal value. When the light intensity decreases, the amplitudes begin to decrease at light intensity values that are much lower than the critical one (Fig. 5.7). Thus, hysteresis appears in the system that is caused by the inertial properties of the system. The balance between the fluxes changes in response to the on-and-off switching of the light with a delay because of the gradual adjustment of the transport system parameters to the environmental changes.

Scheme of Interactions of Photosynthesis and Ion Fluxes Leading to Nonlinear Dynamics

The developed model allows us to make some assumptions concerning the mechanisms of interactions between proton transfer through the ATPase and the channels and the membrane potential, and to evaluate their role in heterogeneous pattern formation and oscillations of the transmembrane potential and pH near the algal cell (Fig. 5.8). Let us consider the sequence of the processes.

Under illumination as a result of photosynthesis, proton flux inside thylakoids leads to alkalization of the chloroplast stroma (stage 1). Proton flux goes from the cytosole through the chloroplast membrane inside the chloroplast (stage 2). As a result, alkalization of the cytoplasm takes place (stage 3), which in turn leads to an increase in the inward proton fluxes through the channels (stage 4). Growth of the passive flux inside the cell induces membrane depolarization and growth of proton concentration inside the cell.

This in turn leads to an increase in the proton flux through the ATPase (stage 6), which is accompanied by a decrease in the membrane potential (hyperpolarization). The flux through the ATPase leads to an increase in the proton concentration in

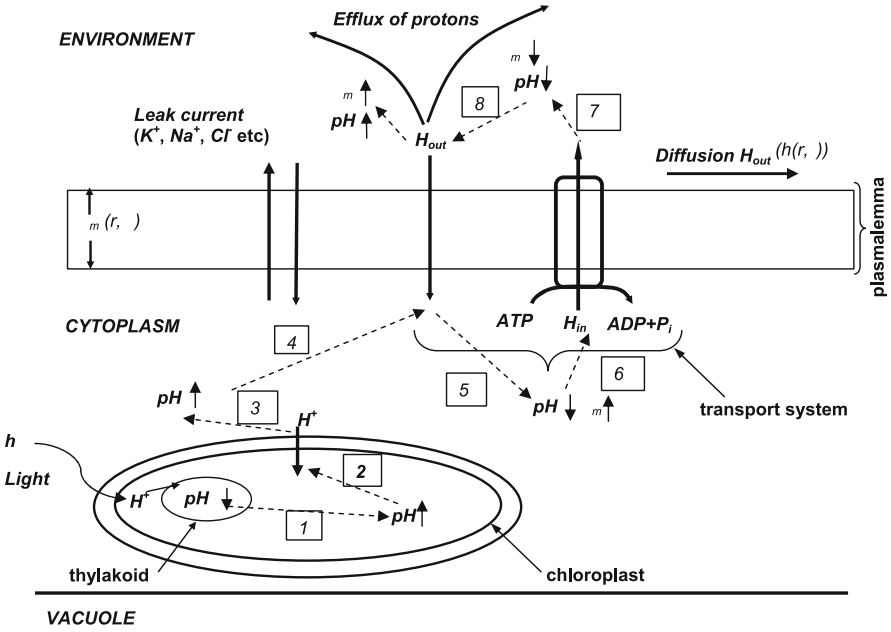


Fig. 5.8 Scheme of processes in algal cell (not scale). Here φ_m is the membrane potential. *Dashed arrows*: regulation: light-induced photosynthetic processes acidify the thylakoid (1), alkalization of the chloroplast stroma (2) induces proton import from the cytoplasm, which (3) raises the cytoplasmic pH and (4) activates the plasma membrane inward channels. Enhanced proton influx from the outside causes cytoplasmic acidification and membrane depolarization (5), which (6) activates the ATPase proton pump. The efflux of protons (7) lowers the external pH and causes membrane hyperpolarization, with ensuing (8) activation of proton channels. The cycle repeats itself from step 5. The numbers in *squares* and the *dotted arrows* denote the processes described here; *bold arrows*: transport through plasma membrane and chloroplast membrane; *small arrows* at pH and φ_m: increase and decrease in these variables (Plyusnina et al. 2008)

the environment near the cell membrane (stage 7), which stimulates a decrease in the proton flux from the cell through the ATPase and an increase in the flux through the proton channels into the cell (stage 8). Then the cycle is repeated.

Thus, the model helps to make clear the mechanisms that cause the observed nonlinear spacetime regimes. Cytosole alkalization may take place, which leads to the channel's opening and to an increase in the passive proton flux into the cell, initiating membrane depolarization and proton concentration growth inside the cell. The following increase in the proton flux through the ATPase is accompanied by membrane potential decay (hyperpolarization). The resulting growth of the proton concentration outside the cell induces ATPase inhibition and activation of the proton channels, which provides the passive proton influx into the cell. The cycle repeats. Thus the light signal stimulates proton channel activation and further ATPase activation. Then the processes of active and passive proton transfer mutually amplify each other, positive feedback is established, and the oscillations of potential and proton concentration occur. Due to the opposite directions of the

fluxes through the channels and ATPase, local acidic and alkaline domains appear that differ by the value of the membrane potential near the membrane outside the cell, which can be registered experimentally. Stable pH zones are generated due to the difference in the values of the diffusion coefficients of protons (D_1) and the potential (D_2) between these domains.

Potential-dependent ATPases and channels can be found in the membranes of different types of cells, which is why it can be assumed that potential-dependent pH regulation is one of the main control mechanisms of the nonlinear spacetime dynamics near the membrane.

Chapter 6
Models of Morphogenesis

In the process of organism growth and development, cell diversity increases in both metabolic (cell differentiation) and structural (morphogenesis) respects. This is related to a cell's ability to switch between different dynamic modes of operation. The evolutions of an organism's shape and cell metabolism are tightly interconnected. For instance, as early as the gastrula state the evolution of the shape of the cell ensemble (inner cavity appearance) and the cell functional variations (mesoderm and endoderm appearance) originate simultaneously and thus comprise the first step of differentiation.

It is known that all information necessary to build a complex multicellular organism is contained in the genome of each cell of an organism. The influence on specific genes responsible for certain traits (directed mutations) may lead to changes in, for example, eye color, color scheme of insect wings, and even the number of fingers. But modern genetics and molecular biology show that the genome itself does not contain direct information about the shape and structure of an organism. This information is generated according to specific laws during the organism's development. The biophysical approach and mathematical modeling play a special role in shedding light on these laws, and they make it possible to test hypotheses on the elementary interactions that lie at the base of self-organization.

Turing Instability

The spontaneous transfer from the homogeneous steady state to the spatially heterogeneous steady state signifies birth of autoregulated structures in the system. Thus, the study of the conditions responsible for the appearance and regulation of these generated dissipative structures can reveal the relationship between pattern formation and genome information.

The basic work of Alan Turing, who was the first scientist to obtain the conditions necessary for the existence of stable heterogeneous structures in a simple mathematical reaction–diffusion model, was published in 1952. Its title was "The chemical

A. Rubin and G. Riznichenko, *Mathematical Biophysics*, Biological and Medical Physics, Biomedical Engineering, DOI 10.1007/978-1-4614-8702-9_6,

© Springer Science+Business Media New York 2014

basis of morphogenesis." This work gave impetus to the use of a mathematical approach to analyzing the problem of morphogenesis.

Turing studied a general set of two equations describing the interactions and diffusion of two chemical substances.

Let us consider a system of two kinetic variables describing substances that undergo chemical transformations and diffuse in the reaction volume. For the 1D chemical reactor the system can be written as

$$\begin{aligned} \frac{\partial x}{\partial t} &= P(x, y, r) + D_x \frac{\partial^2 x}{\partial r^2}, \\ \frac{\partial y}{\partial t} &= Q(x, y, r) + D_y \frac{\partial^2 y}{\partial r^2}, \end{aligned} \tag{6.1}$$

where r is the space variable, and D_x and D_y are diffusion coefficients. The boundary conditions are taken as the conditions of impenetrability of the walls of the 1D reactor:

$$\left.\frac{\partial x}{\partial r}\right|_{r=0} = \left.\frac{\partial x}{\partial r}\right|_{r=l} = \left.\frac{\partial y}{\partial r}\right|_{r=0} = \left.\frac{\partial y}{\partial r}\right|_{r=l} = 0. \tag{6.2}$$

The behavior pattern of such a system can vary over time. In the simplest case, at $t \to \infty$, in all points of the reactor the equal concentrations $\overline{x}$ and $\overline{y}$ are established, so the system reaches its stable steady state, which is homogeneous in space. If the homogeneous state is unstable at $t \to \infty$, then other regimes can be realized. These regimes can present other homogeneous steady states or heterogeneous steady structures. It is possible also that in each point in space the variables do not acquire definite constant values, but oscillations or quasistochastic regimes form in the system.

Thus, as in the case of a local model, the first step in the analysis of a distributed system model is the analysis of the stability of its homogeneous steady state.

Let us consider spatially homogeneous solutions to system (6.1):

$$x = \overline{x}_k = Const; \quad y = \overline{y}_k = Const, \tag{6.3}$$

where $\overline{x}_k$ and $\overline{y}_k$ are the roots of the following set of algebraic equations:

$$\begin{aligned} P(x, y) &= 0, \\ Q(x, y) &= 0. \end{aligned} \tag{6.4}$$

The homogeneous steady state is stable if small perturbations of the forces (including those distributed in space) that affect the system bring about small perturbations of its solutions. We assume that these perturbations remain small at $t \to \infty$.

We will perform an analysis of the stability on the basis of the analysis of a linearized system. Let $\xi_k(t, r)$ and $\eta_k(t, r)$ be the small deviations from the spatially

homogeneous solutions $\overline{x}_k$ and $\overline{y}_k$. Then for ξ_k and η_k the distributed linearized system (the bottom index k is omitted for brevity) is

$$\begin{aligned}\frac{\partial \xi}{\partial t} &= a\xi + b\eta + D_\xi \frac{\partial^2 \xi}{\partial r^2},\\ \frac{\partial \eta}{\partial t} &= c\xi + d\eta + D_\eta \frac{\partial^2 \eta}{\partial r^2},\end{aligned} \tag{6.5}$$

where

$$\begin{aligned}a &= \frac{\partial P(\overline{x},\overline{y})}{\partial x}, \quad b = \frac{\partial P(\overline{x},\overline{y})}{\partial y},\\ c &= \frac{\partial Q(\overline{x},\overline{y})}{\partial x}, \quad d = \frac{\partial P(\overline{x},\overline{y})}{\partial y}.\end{aligned}$$

The diffusion coefficients are

$$D_x = D_\xi, D_y = D_\eta \tag{6.6}$$

We will look for a solution in the form

$$\xi(t,r) = Ae^{pt}e^{ikr}, \quad \eta(t,r) = Be^{pt}e^{ikr}. \tag{6.7}$$

Here the factor e^{ikr} defines the variable deviations from the homogeneous steady state at the point with coordinate r for the eigenfunction corresponding to wavenumber k. For a tube of length l, the wavenumber acquires the discontinuous (discrete) values $k = k_n = \frac{\pi n}{l}$. The factor e^{pt} defines the time behavior of the deviation from the steady state. Substitution of expression (6.7) into (6.5) and division by $e^{pt}e^{ikr}$ gives

$$\begin{aligned}Ap &= aA + bB - D_\xi k^2 A,\\ Bp &= cA + dB - D_\eta k^2 B,\end{aligned} \tag{6.8}$$

or

$$\begin{aligned}A\left(p - a + D_\xi k^2\right) - bB &= 0,\\ cA - \left(p - d + D_\eta k^2\right)B &= 0.\end{aligned} \tag{6.9}$$

The values of A and B are not both equal to zero only if the determinant of system (6.9) is equal to zero:

$$\left(p - a + k^2 D_\xi\right)\left(p - d + k^2 D_\eta\right) - bc = 0. \tag{6.10}$$

Equation (6.10) is called a dispersion equation. Its solutions are

$$p_{1,2} = \frac{a + d - \left(D_\xi + D_\eta\right)k^2 \pm \sqrt{\left[a - d - k^2\left(D_\xi - D_\eta\right)\right]^2 + 4bc}}{2}. \qquad (6.11)$$

Thus, we obtained the expression for the values $p_{1,2}$, which determine the system's behavior over time depending on the system parameters and wavenumber k. As in the case of local systems, the sign of the real part of $p_{1,2}$ shows whether the homogeneous steady state is stable or unstable. In the domain of parameter values where both Re $p_{1,2} < 0$, solution (6.3) is stable. The variables can approach their stable steady state in an oscillating or nonoscillating manner depending on the sign under the radical in formula (6.11). If the radicand is negative, then the roots $p_{1,2}$ are complex, and at each point of space damped oscillations around the stationary values occur. If the radicand is positive, then one root is negative and the other is positive, and the variables approach values (6.3) in a nonoscillating manner. In the case where the real parts $p_{1,2}$ are positive or have different signs, the homogeneous steady state is unstable. Here, different types of instability are also possible. If $p_{1,2}$ are real and positive, then there will be a node-type instability; if $p_{1,2}$ are complex and Re $p_{1,2} > 0$, then it will be a spiral-type instability; and if p_1 and p_2 have different signs, then it will be a saddle-type instability (Fig. 6.1).

In Fig. 6.1 we see the possible types (a−c) of dependencies of the real part $p_{1,2}$ on the wavenumber k. In cases (d) and (f) there is a domain $k_1^2 < k^2 < k_2^2$ where one of the characteristic numbers is negative and the other is positive. This is a domain of a saddle or Turing instability. The boundaries of this domain are determined by the values k_1^2, k_2^2, at which one of the real parts Re $p_{1,2}$ changes to zero:

$$k_{1,2} = \left[\left(aD_\eta + dD_\xi\right) \pm \sqrt{\left(aD_\eta + dD_\xi\right)^2 - 4D_\xi D_\eta(ad - bc)}\right] \frac{1}{2D_\xi D_\eta}. \qquad (6.12)$$

Perturbations in domain I (Fig. 6.1) of the nonlinear distributed system can lead to the rise of waves with finite amplitude, stable waves, and leading centers. In a 2D system such regimes can appear only if the local system ($D_\xi = 0, D_\eta = 0$) is auto-oscillating. Fluctuations in domain II can lead to disturbances in system homogeneity and to the formation of heterogeneous patterns.

Analysis of the stability of the homogeneous steady state in systems of higher order shows that

$$\frac{\partial x_i}{\partial t} = F_i(x_1, x_2, \ldots, x_n) + D\frac{\partial^2 x_i}{\partial r^2}, \quad i = 1, 2, \ldots n \qquad (6.13)$$

so the number of roots of the dispersion equation with a positive real part determines the type of instability. If there is an even number of roots p_{mk} with $\delta > 0$, then the instability is called *oscillating*. An odd number of such roots corresponds to

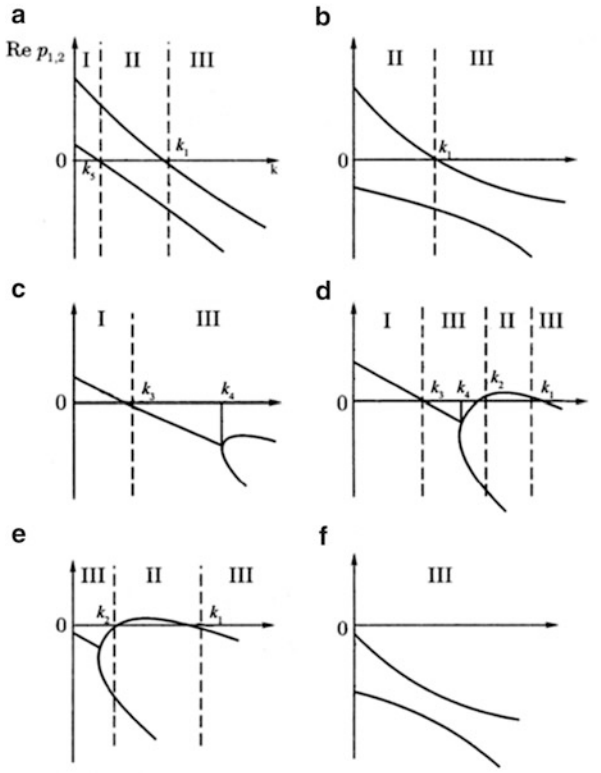


Fig. 6.1 Different types of dependencies of real part of roots of dispersion equation (6.10) on wavenumber k. k_1 is the wavenumber at which the system becomes stable to this type of perturbation; k_2 denotes the wavenumber of perturbation to which the system loses stability; k_3 corresponds to the transfer from domain of oscillating nonstability to domain of damping oscillations; k_4 corresponds to the transfer from the oscillating system to the nonoscillating system; k_5 corresponds to the transfer from the unstable node domain to the saddle instability domain (adopted from Romanovsky et al. 2004). In all cases (**a**–**f**) three domains can be pointed out: I: both roots have a positive real part: Re $p_{1,2} > 0$; II: one root has a positive real part and the other a negative real part: Re $p_1 > 0$, Re $p_2 < 0$; III: both roots have a negative real part: Re $p_{1,2} < 0$

the Turing instability, which determines the formation of stationary heterogeneous patterns, so-called *dissipative structures* (DSs). This term emphasizes the thermodynamic aspect of the problem—DSs arise and exist in thermodynamically open systems due to the dissipative processes of energy transformation.

In his mathematical analysis, Turing tried to explain the dynamic mechanism of the origin of biological morphogenesis. Of course, a pure mathematical description of the elementary interactions responsible for the nonlinear properties of local functions does not reveal the mechanisms of the processes in each particular case. Nevertheless, mathematical analysis proves that the possibility of pattern formation in a nonlinear system in the presence of transfer processes does in fact exist, and this is the main implication of Turing's work.

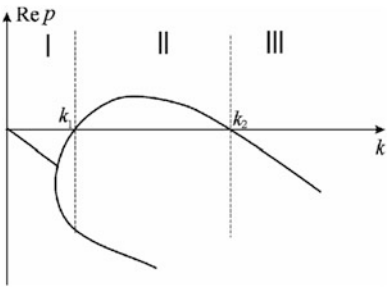


Fig. 6.2 Dependence of real part of dispersion equation roots Re p on wavenumber k in the case of Turing instability

Imagine a system containing some volume filled with cells excreting in the medium certain chemical substances. The transfer of such a system into a heterogeneous state can create conditions necessary for different types of cell function—cell differentiation. A chemical "prestructure" will manifest itself biologically in different types of cells. Thus, cell differentiation and morphogenesis will occur. It is assumed, of course, that local kinetics in the models under consideration are physically possible, which means that the local system has no infinitely growing solutions.

Turing asserted two conditions for the existence of dissipative structures (Turing 1952):

1. The steady state of a local system is a stable spiral (for a model with two variables)
2. A wavenumber domain ($k_{\min}$, $k_{\max}$) exists where the dispersion equation has two real roots of different signs

   A diagram Re p_{mk} (k) for these conditions is presented in Fig. 6.2.

Analysis of the dispersing equation (6.12) shows that the homogeneous system state, which is stable in the absence of diffusion, can become unstable under the following conditions:

$$\begin{aligned} &ad - bc > 0, \\ &a + d < 0, \\ &D_2 a + D_1 d > 2\sqrt{D_1 D_2 (ad - bc)}. \end{aligned}$$

The fulfillment of the first two inequalities provides the negative real parts of the eigenvalues λ at $k = 0$ (k is the wavenumber) and the stability of the system in the absence of diffusion. The third inequality means that in some wavenumber domain one of the eigenvalues becomes positive, i.e., the homogeneous state loses its stability based on the corresponding wavelengths. It is crucial that the inequalities be realized simultaneously—only if one of the variables (e.g., x) is autocatalytic (it is often called an activator) and the diffusion coefficient of the second variable y ("inhibitor") is much greater than the diffusion coefficient of the activator: $D_y > D_x$.

Vasiljev and Romanovsky (1976) obtained more general conditions: if the constant term of the dispersion equation is negative at some value of the wave-number k: $q_0(k) < 0$, then the distributed system has at least one steady state of the DS type. This condition means that the dispersion equation has an odd number of roots with positive real parts and the homogeneous state has an instability of the Turing type.

In the 2D case, these conditions follow from the solution of the dispersing equation [(6.10), (6.11)] and correspond to an instability of the saddle type:

$$\left(aD_x + dD_y\right)^2 - 4D_xD_y(ad - bc) \geq 0,$$
$$a + d < 0, \quad bc < 0, \quad D_x \neq D_y \neq 1, \quad D_x \neq \infty, \quad D_y \neq \infty.$$

The aforementioned conditions for the existence of DSs are similar to those for the existence of a trigger in local systems, described by ODEs. The reaction volume can be considered a distributed trigger with many steady states, or DS patterns, which depend on the system parameters and on the manner in which these parameters change. Patterns of one shape can transform into other shapes.

In some cases, for instance, for the "Brusselator" (Chap. 3), where the local system has an oscillating instability, the steady heterogeneous solutions, DSs, are periodic in space and can be presented as a harmonic series:

$$x(r) = A + \sum_{k=1}^{\infty} p_k \cos\left(\frac{\pi k r}{L}\right), \qquad y(r) = \frac{B}{A} + \sum_{k=1}^{\infty} p_k \cos\left(\frac{\pi k r}{L}\right).$$

The period depends on the system parameters, namely, on the reactor length L. The transfer from a DS with one period to a DS with another one has a hysteresis character.

A hopping transfer from one DS to another, provided the system length increases, is the principal model of cell division. In fact, growth of some living cells is manifested primarily as in increase in length (for instance, for *E. coli*). When a certain cell length is attained, the conditions for the division of the cell in two is achieved, i.e., a new DS pattern is born. If the process of trigger switching occurs, transfer back becomes practically impossible. It is interesting that, according to the model, the switching takes place at smaller L if the rate of growth in the length $\frac{\partial L}{\partial t}$ is fast. From a thermodynamic point of view, DS switching and system division into two parts lead to a decrease in enthropy and energy production in the system.

In 2D systems, the oscillating instability of waves of finite length appears only if the corresponding local system is oscillating, as opposed to the Turing instability, which can occur even if the steady state of the local system is stable (it is impossible for a 1D system). If the local system is auto-oscillating, then the domain of the diffusion coefficient values always exists where the Turing instability is realized.

In systems with three or more variables, there are cases where even with an auto-oscillating local system the Turing instability is impossible at any values of the coefficients. But the oscillating instability of a distributed system can be realized even if the local system is not oscillating.

In the case of mutual diffusion, the diversity of spatiotemporal behavior patterns increases. In particular, local systems can be stable at any parameter values, but autowave patterns arise nonetheless. Thus analysis of the regimes even in comparatively simple systems shows the enormous diversity of spatiotemporal behavior patterns, and in 2D and 3D systems this diversity increases manyfold.

Morphogenetic Field

Spatial cell differentiation arises in initially homogeneous cell ensembles. As was suggested by the Russian scientist Gurvich in 1914 (Gurvich 1944) during the ensemble evolution, cells generate a so-called informational "morphogenetic field."

Gurvich imagined morphogenesis as a cascade of morphogenetic acts in which the initial morphogenetic field of the embryo divides into many morphogenetic fields, each of them corresponding to a certain type of differentiated cell. Each of these morphogenetic acts includes the "spatial marking" of the area, i.e., generation of spatial information, which afterward is fixed through a corresponding act of cell differentiation.

The results of Driesch's experiments on embryo regulations (Driesch 1914) support these ideas. Driesch showed that after experimentally disturbing the embryo structure through microsurgical removal or addition or displacement of material, the organism nevertheless reconstitutes its structure. This occurs despite the fact that the development of the corresponding embryo elements changes as compared to the fate of the same elements under normal conditions.

The Turing hypothesis was that the morphogenetic field is induced due to active chemical media (for example, an activator and an inhibitor).

Later it became clear that not only chemical interactions play an important role in spatial self-organization during morphogenesis but also certain mechanical contacts between cells and changes in the geometric properties of the cell volume contribute to the processes.

Morphogenesis and differentiation are often examined separately in theoretical considerations. Although cell differentiation is the result of cell interactions, the main characteristic of cell morphogennesis—the triggering mechanism—can be simulated in a one-cell model. Morphogenesis is the process of space pattern formation where the biochemical and mechanical mutual effects of cells are equally important.

The first rather simple models of morphogenesis described interactions between cells capable of differentiation. Other models based on similar principles simulated the pigmentation pattern formation and coat marking of animals, the complex

shapes of sea stars and shells, and other pattern formation processes (Murray 1993, 2002; Meinhardt 1995, 2000).

In Chap. 3 we mentioned that trigger (multistable) systems possess the ability to switch between states. We considered a model of a genetic trigger of protein synthesis based on the scheme of Jacob and Monod. Depending on the parameter values, this model can have one or three steady states (the third one is unstable). Thus according to this model we can follow the transfer from a unistationary to a multistationary regime. The Brusselator model (Chap. 3) can be used to describe the formation of patterns that are stable in time and heterogeneous in space, thus morphogenesis. But the local model of this system has only one steady state, so it is unfit to describe cell differentiation.

Model of a Distributed Trigger

Let us consider a distributed model of a genetic trigger developed by Chernavskii and his colleagues (Romanovsky et al. 2004). This model is based on the Jacob and Monod trigger model described in Chap. 2. The variables correspond to the dimensionless concentrations of the reaction products. Let us examine the behavior of a distributed system with local functions similar to those in (1.8) and diffusion of products. The system has the following form:

$$\begin{aligned} \frac{dx_1}{dt} &= \frac{L_1}{1+x_2^m} - x_1 + D_1 \frac{\partial^2 x_1}{\partial r^2}, \\ \frac{dx_2}{dt} &= \frac{L_2}{1+x_1^m} - x_2 + D_2 \frac{\partial^2 x_2}{\partial r^2}, \end{aligned} \tag{6.14}$$

where x_1 and x_2 are dimensionless concentrations of the first and second synthesis systems, and L_1 and L_2 are effective parameters.

Since at $m = 1$ the phase diagram of the local system has one stable steady state, such a model cannot describe the trigger processes in the system. At $m = 2$ and a certain value of the ratio $L_1/L_2 > \gamma$, the system acquires the trigger property. The phase diagram of such a system has two stable steady states and an unstable saddle between them (Fig. 1.6). Three spatially homogeneous solutions of distributed system (6.14) are

$$(1)\ \overline{x}_1 = \frac{L}{2} + \sqrt{\left(\frac{L}{2}\right)^2 - 1}; \quad \overline{x}_1 = \frac{L}{2} - \sqrt{\left(\frac{L}{2}\right)^2 - 1} \tag{6.15}$$

$$(2)\ \overline{x}_1 = \frac{L}{2} - \sqrt{\left(\frac{L}{2}\right)^2 - 1}; \quad \overline{x}_1 = \frac{L}{2} + \sqrt{\left(\frac{L}{2}\right)^2 - 1} \tag{6.16}$$

$$(3)\ \overline{x}_1 = \overline{x}_2 = \overline{x}_0 \tag{6.17}$$

The value $\overline{x}_0$ in formula (6.17) is the positive root of an equation:

$$\overline{x}_0{}^3 + \overline{x}_0 - L = 0. \tag{6.18}$$

To analyze the stability of the homogeneous solutions of system (6.14) at $m = 2$, the following methods can be used. Let us introduce new variables—deviations of the x and y variables from their steady states:

$$\xi(r,t) = x_1 - \overline{x}_1; \quad \eta(r,t) = x_2 - \overline{x}_2.$$

A linearized system with the new variables can be written as follows:

$$\begin{aligned} \frac{\partial \xi}{\partial t} &= -\xi - \alpha\eta + D_1 \frac{\partial^2 \xi}{\partial r^2}, \\ \frac{\partial \eta}{\partial t} &= -\beta\xi - \eta + D_2 \frac{\partial^2 \eta}{\partial r^2}. \end{aligned} \tag{6.19}$$

Here

$$\alpha = \frac{2L_1\overline{x}_1}{1+\overline{x}_2{}^2}, \quad \beta = \frac{2L_2\overline{x}_2}{1+\overline{x}_1{}^2}. \tag{6.20}$$

As shown, we seek a solution in the form $\xi(t,r) = Ae^{pt}e^{ikr}$, $\eta(t,r) = Be^{pt}e^{ikr}$, where p is the exponent index of the time factor, k is the wavenumber, $k = 2\pi r/\lambda_n$, where n is the harmonic number of the expansion into Fourier series $n = 1, 2, \ldots$.

The dispersion equation for system (6.19) is

$$\left(p + 1 - k^2 D_1\right)\left(p + 1 + k^2 D_2\right) - \alpha\beta = 0. \tag{6.21}$$

Its solution is

$$p_{1,2} = -1 - (D_1 + D_2)\frac{k^2}{2} \pm \sqrt{(D_1 - D_2)^2 \frac{k^4}{4} + \alpha\beta}. \tag{6.22}$$

Constituting expressions (6.15)–(6.17) and (6.20) into (6.22) we obtain a stable solution for the small fluctuations of any wavelength for the case of nonsymmetric roots (1), (2) [formulas (6.15) and (6.16)]. The dependence Re $p_{1,2}$ (k) is presented in Fig. 6.1d.

The analysis of the stability of symmetrical solution (3) shows that it is unstable relative to perturbations of wavelengths larger than a certain critical value. The dependence Re $p_{1,2}(k)$ has the shape shown in Fig. 6.1b. The expression for the critical wavelength is

$$\Lambda_K = \frac{2\pi^2\left[-D_1 - D_2 + \sqrt{(D_1 - D_2)^2 + 4D_1D_2\alpha\beta}\right]}{1 - \alpha\beta}. \tag{6.23}$$

If D_1 and D_2 converge to zero, then $\Lambda_{\kappa p}$ also converges to zero, and the symmetrical system becomes unstable relative to any disturbances. For example, we have an ensemble of identical cells whose symmetric states are unstable. In the presence of diffusion, metabolite exchange complicates the switching of individual cells at small fluctuations so that only the triggering of large areas becomes possible, when each cell switches the next one into its own regime. Analysis shows that in a system where only metabolite exchange between cells is taken into account, such stable, periodic, DSs, such as those observed in the distributed Brusselator system, do not arise.

A model that considers the exchange of products as well as the substrates demonstrates a more complex behavior (Soljanik and Chernavskii 1980). In this model it is assumed that parameter L of each product is proportional to the concentration of the corresponding substrate; dimensionless variables are designated as y_1, y_2. The regime of each cell depends on the competition between the diffusion of the products x_1 and x_2 and the diffusion of the substrates. In Chap. 2 we considered two types of switching: the specific trigger switching performed by changing the variable values and nonspecific trigger switching by changing the parameter values, which determines changes in the phase portrait. In the model under consideration, substrate concentrations serve as parameters for the equations describing the trigger properties of product transformations. The corresponding equations are written for these parameters as substrate concentrations. It is clear that the notions of *variable* and *parameter* are relative. The values that were taken as parameters (constants) in one model can become variables in a more detailed model.

For the substrate concentrations the following equations are written:

$$\begin{aligned}\frac{\partial y_1}{\partial t} &= B_1 - \frac{A_1 y_1}{1 + {x_2}^2} - y_1 + D_{y1}\frac{\partial^2 y_1}{\partial r^2},\\ \frac{\partial y_2}{\partial t} &= B_2 - \frac{A_2 y_2}{1 + {x_1}^2} - y_2 + D_{y2}\frac{\partial^2 y_2}{\partial r^2}.\end{aligned} \tag{6.24}$$

They take into account:

1. Constant inflow of the substrates in the system (B_1, B_2)
2. Substrate consumption in enzyme reactions that are proportional to the concentrations and the rate of product concentration increase

3. Substrate outflow that is proportional to concentration ($-y_1$, $-y_2$)
4. Diffusion

The equations for the product concentrations take into account the fact that the rate of each product increase is proportional to the corresponding substrate concentration. Thus, instead of (6.14), the equations for the product concentrations x_1 and x_2 are

$$\begin{aligned}\frac{\partial x_1}{\partial t} &= \frac{1}{\tau_0}\left(\frac{A_1 y_1}{1+{x_2}^2} - x_1\right) + D_{x1}\frac{\partial^2 x_1}{\partial r^2},\\ \frac{\partial x_2}{\partial t} &= \frac{1}{\tau_0}\left(\frac{A_2 y_2}{1+{x_1}^2} - x_2\right) + D_{x2}\frac{\partial^2 x_2}{\partial r^2}.\end{aligned} \tag{6.25}$$

For simplicity let us consider $A_1 = A_2 = A$, $B_1 = B_2 = B$. Equation (6.25) can be reduced to (6.14) if $L_1 = Ay_1, L_2 = Ay_2$. In addition, it can be suggested that the characteristic times of the processes connected with the product metabolism are considerably less than the characteristic times of the influx and outflux processes. According to the time hierarchy of the local system, differential equations for the products can be replaced by algebraic ones. Due to the dependence on parameters A and B, system [(6.24), (6.25)] can have one or three homogeneous steady states. At high rates of substrate influx there are three steady states in the system; one is symmetric, the other two are asymmetric. In some parameter domain, the symmetric state loses its stability and the system acquires trigger properties. This corresponds to a cell's ability to differentiate.

In cells that can differentiate, the appearance of morphological DSs is possible. The width of the parameter domain depends on the ratio of the diffusion coefficients of the main metabolites to the corresponding substrates and is greater the lower this ratio is. Systems with higher metabolic levels (greater values of parameter A) possess greater possibilities (in the parametric sense) for spatial heterogeneous pattern formation.

System transition via saddle bifurcation from a one-state regime to a three-state regime is accompanied by the emergence of instability. This corresponds to the points of the process of development when the system "chooses" one of the possible states. The crucial role here is played by parametric regulation under the effect of genetic programming as well as environmental conditions.

In morphogenesis, the final structure pattern is determined by the system parameters: the metabolism intensity and the ratio of the diffusion coefficients of the main metabolites. But the structure can be realized only in the presence of small (but finite) heterogeneities in the metabolite distribution, whereas morphogenetic heterogeneities appear only in the presence of deep differentiation.

Animal Coat Markings

Models based on reaction–diffusion mechanisms were used to describe animal coat markings (Bard 1981; Murray 1981; Young 1984). One of the best specialists in this field is James Murray, whose works are presented in original papers as well as in books published by Springer-Verlag (Murray 1993, 2002, 2003).

Observed animal skin coloring is determined by the distribution of chemical substances set up during the first weeks of embryogenesis. Examples of zebra and leopard are presented in Fig. 6.3.

Genetically determined cells—melanoblasts—migrate to the embryo surface and transform into special pigment cells called melanocytes, which are situated in the basal layers of the epidermis. Hair coloration is determined by melanocytes, which bring melanin to the hair follicle, which later passes to the hair and determines its color. Independently of the biochemical and cell details of the process, it is very important for modeling that the characteristic size of color heterogeneities be much greater than the size of an individual cell. For instance, it is known that an embryo pattern corresponding to future spots on a leopard is approximately 0.5 mm in diameter, which corresponds to the size of about 100 cells.

The models by Murray (1981, 1993, 2000), Meinhardt (1995, 2000), and others are Turing-type models describing the chemical interactions of two substances (morphogenesis) capable of diffusing, and their diffusion coefficients differ greatly from each other. Starting from the classic works (Gierer and Meinhardt 1972; Gierer 1981; Meinhardt 1982), it is assumed that the morphogene distribution supplies the positional information that is necessary for morphogenesis processes. In particular, the morphogene concentration will determine the color of animal skin in the fixed site. The general form of the model is



Fig. 6.3 Wild animal coat markings. (**a**) Leopard (*Panthera pardus*) with cubs. (**b**) Zebras (*Equus grevyi*)



Fig. 6.4 Hydra

$$\begin{aligned}\frac{\partial A}{\partial t} &= F(A,B) + D_A \nabla^2 A,\\ \frac{\partial B}{\partial t} &= G(A,B) + D_B \nabla^2 B,\end{aligned} \tag{6.26}$$

where $F(A, B)$ and $G(A, B)$ are nonlinear functions describing the local interactions of system components A and B, the Laplace operator ∇^2 describes the diffusion, and D_A and D_B are diffusion coefficients, where $D_A < D_B$.

In one of the first works on morphogenesis modeling (Gierer and Meinhardt 1972) a similar system to simulate the process of cell differentiation of a *hydra* was used.

A hydra is a simple, well-studied, almost 1D organism with a cylinder body; at one end of this cylinder is situated a foot, and at the other end is a head with a palpus (feeler) (Fig. 6.4). Self-organization processes were observed in experiments on the regeneration of this organism. Morphologically identical pieces were cut and put into a nutrient medium. In 2 days, the full-grown animals regenerated from fragments, and the initial orientation from the head to the foot was reproduced. This confirmed the idea of positional differentiation of *hydra*. More complicated experiments were performed (Webster and Wolpert 1966) that indicate the existence of two agents—an activator of the "head" formation and an inhibitor acting in the opposite way in the process of pattern formation. The inhibitor is produced in the same spatial area as the activator but diffuses at much greater distances.

The functions $F(A, B)$ and $G(A, B)$ in system (6.26) in the Gierer–Meinhardt model are

$$\begin{aligned} F(A,B) &= k_1 - k_2 A + \frac{k_3 A^2}{B}, \\ G(A,B) &= k_4 A^2 - k_5 B. \end{aligned} \tag{6.27}$$

The function $F(A, B)$, describing the local dynamics of the activator concentration, is of the autocatalytic type with respect to A and decreases when B increases. The results of calculation show that the model demonstrates a good qualitative correspondence to the experimental data in cases where the diffusion coefficient of the inhibitor is larger than the diffusion coefficient of the activator: $D_B \gg D_A$. Afterward, real biochemical substances were found that activate and depress hydra head formation. But it was shown that these substances did not interact in the manner assumed in the model, and the values of their diffusion coefficients were close to each other. Although the Gierer–Meinhardt model was not confirmed in direct experimental corroboration, it played a great role in mathematical modeling and stimulated detailed studies of hydra morphogenesis processes.

In simulating animal skin coloring, Murray (1981) used a system where morphogene interactions were described as an enzyme system with substrate inhibition. Such a type of the F and G functions was proposed by Thomas (1975) to describe reactions in a system where oxygen interacts with the enzyme uricase. The expressions for the functions describing the interaction of substrate A and enzyme B in the Thomas model are

$$F(A,B) = k_1 - k_2 A - H\big(A,B\big),$$

$$G(A,B) = k_3 - k_4 B - H\big(A,B\big),$$

$$H(A,B) = \frac{k_5 AB}{k_6 + k_7 A + k_8 A^2}.$$

The functions $F(A, B)$ and $G(A, B)$ include terms corresponding to the constant influx and outflux of the reaction medium, with rates proportional to the corresponding reactant concentrations. The third summand describes the rate of enzyme–substrate complex formation in the form of the H function, reflecting the substrate inhibition.

Later such types of function were used by different authors to describe pattern formation of a different nature. Naturally, the parameter values for each case will be different—the form of nonlinearity in the rate dependence on the reactant concentrations is important. Many examples of such models are presented in books by Murray (1993, 2002).

Murray in his models used the following dimensionless system:

$$\begin{aligned}
\frac{\partial u}{\partial t} &= \gamma f(u,v) + \nabla^2 u, \\
\frac{\partial v}{\partial t} &= \gamma g(u,v) + d\nabla^2 v, \\
f(u,v) &= a - u - h(u,v), \\
g(u,v) &= \alpha(b - v) - h(u,v), \\
h(u,v) &= \frac{\rho u v}{1 + u + K u^2},
\end{aligned} \tag{6.28}$$

where u and v are dimensionless morphogene concentrations, and a, b, α, ρ, and K are positive parameters. The meaning of the coefficients can be interpreted as follows (Murray 1993):

1. In the 1D case, $\gamma^{1/2}$ is proportional to the linear dimension of the region where the reaction occurs. In the 2D case, the coefficient γ is proportional to the area of such a region
2. γ reflects the relative contribution of the biochemical reaction to the processes of evolution of concentrations (relative to diffusion)
3. An increase in the γ value is equivalent to a decrease in the diffusion coefficient ratio d

Numerous computer experiments were performed on model (6.28) that made it possible to describe flecked (spotted) and striped animal skin coloring. It was assumed that the mammalian skin was a closed area with periodic boundary conditions. The initial conditions were set as perturbations based on values corresponding to a homogeneous steady state. On the 2D systems a series of computer experiments was performed for various surface shapes and parameter values. Coloring patterns similar to those observed in nature were obtained (Figs. 6.5 and 6.6).

In experiments with the 2D model, it was shown that the geometry of the area under consideration restricted the types of possible spatial structures. When the area is narrow, only simple stripes can exist; in essence it is a 1D structure. For spots to appear, the area needs to be sufficiently wide and long (Fig. 6.5). The model makes it possible to simulate structures in an area of more complicated geometry (on the border between the leg and the body) and to clarify general coloring regularities. In books by Murray (1993, 2003) the theoretical bases and numerous examples of simulation of the skin coloring of different animals and butterfly wings are presented, and the book by Meinhardt (1995) presents examples of the 3D simulations of shell shapes.

In subsequent years, models were developed taking into account mechanical deformation (stretching) of the epithelium cell layer (Belintsev et al. 1985) and pattern formation in ensembles of mesenchymal cells—e.g., bird feather bud formation and limb formation (Oster et al. 1983; Murray 1993, 2002).

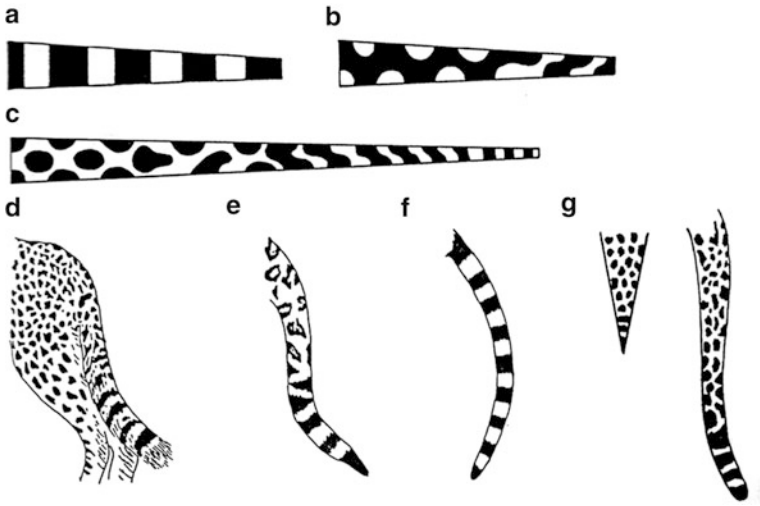


Fig. 6.5 Examples of leopard tail coloring simulation. (**a, b**) *Dark color* corresponds to exceedance of morphogene concentration u over stationary value. Parameter values: $a = 92$, $b = 64$, $\alpha = 1.5; \rho = 18.5, K = 0.1$. Steady state: $\overline{u} = 10$, $\overline{v} = 9$. For the same geometry as the system in (**a**) $\gamma = 9$ represents stripes, and in (**b**) $\gamma = 15$ represents spots. (**c**) $\gamma = 25$, a longer domain is considered, and spots turn into stripes. (**d**) Adult cheetah (*Acinonyx jubatus*) tail coloring. (**e**) Jaguar (*Pantera onca*) tail. (**f**) pre-natal tail markings in a male genet. (**g**) Adult leopard tail; on tail tip the spots turn into stripes (Murray 1993)

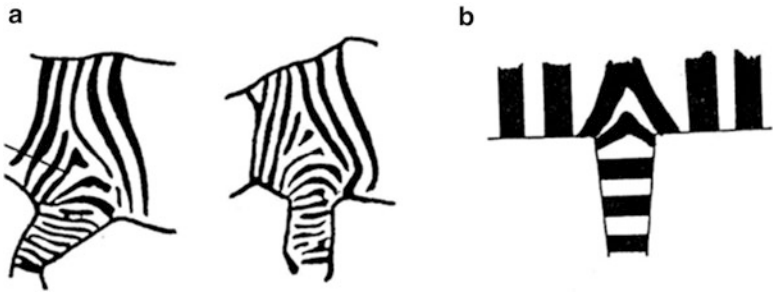


Fig. 6.6 (**a**) Stripe formation on foreleg of zebra. (**b**) Results of simulation (Murray 1993)

Models of Amoeba Aggregation. The Role of Chemotaxis

Complex space structures can appear in organism communities, for instance, algae. The phenomenon of phytoplankton spot formation in the ocean is well known. Rather complex regular patterns can be observed in the colonies of bacteria and amoebae. It was shown that an important condition for pattern formation is the presence of chemotaxis—a cell's ability to choose the direction of its movement

depending on the chemical substance gradients. The principal mechanism of such structure formation is that the homogeneous distribution of the active (dividing and mobile) cells loses its stability when the cell density reaches a certain threshold due to chemotaxis in the direction of the attractant, extracted in the medium by the cells themselves. The front of the growing colony begins to move. In the rear of the front the cells turn to the passive state because of the large local density and small substrate concentration.

A widely studied chemotactic phenomenon is exhibited by slime mold (*Dictyostelium discoideum*). In starvation conditions, the population aggregates due to the cyclic AMP (cAMP) waves produced by the amoebae themselves. At the moment when the wavefront passes the cell, the cell moves according to the cAMP concentration gradient, that is, in the direction opposite to the wave motion. As a result, the amoebae form a compact aggregate in the center, which produces the attractant waves. Several models of this process are described in the book by Segel (1984), and more detailed models were proposed in papers by Martiel and Goldbeter (1987), Monk and Othmer (1989), and Polezhaev et al. (1998, 2005).

Let us consider the model of Polezhaev et al. (1998, 2005). This model contains three variables: chemoattractant cAMP concentration v, receptor concentration g, and cell concentration u:

$$\begin{aligned}
\frac{\partial v}{\partial t} &= \gamma u \left(g \frac{v^2 + A^2}{v^2 + 1} \delta v \right) + D_v \Delta v, \\
\frac{\partial g}{\partial t} &= B - (1 + Hv) g, \\
\frac{\partial u}{\partial t} &= D_u \Delta u - \nabla \left(\chi (g - g_0)^4 u \nabla v \right).
\end{aligned} \tag{6.29}$$

The first equation describes the local evolution of the cAMP concentration, which is proportional to the cell number and to a nonlinear function consisting of the two summands. The first summand (increase) depends nonlinearly on the v variable and is proportional to the number of cAMP receptors g, and the second summand (outflux) is proportional to v. The last term of this equation describes the cAMP diffusion. The second equation describes the evolution over time of the portion of active receptors g on a cell surface depending on the cAMP concentration. The last equation describes the spatial amoebae redistribution and contains two terms corresponding to the cell stochastic wandering and the cells' movement in the direction of the cAMP gradient. The formulation of the model is presented in more detail in a paper by Polezhaev et al. (1998).The results of the simulation are presented in Fig. 6.7.

The equations of model (6.29) can be divided into two subsystems. The first two equations describe the active chemical medium where the autowave structures appear. They are spiral or round depending on the value and spatial distribution of the cell density. As a matter of fact, cell density serves as a control parameter for

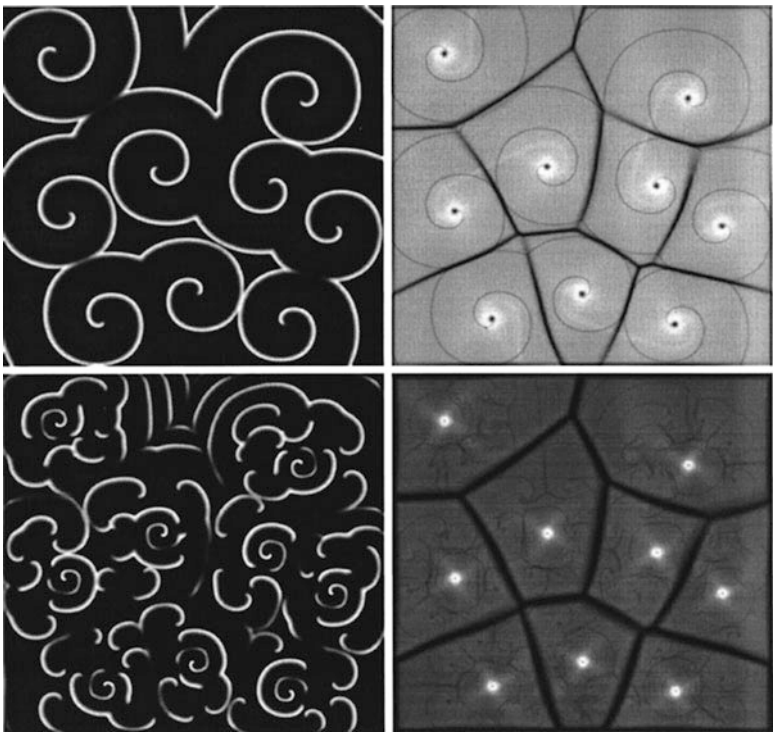


Fig. 6.7 Simulation results for model (6.29). *Top row*: initial stage of aggregation; *bottom row*: terminal stage of aggregation. *Left*: cAMP concentration; *right*: amoebae density (Polezhaev 2010)

the chemical subsystem. cAMP waves in turn lead to amoebae spatial redistribution. Thus, there is feedback between the active medium properties, determined by cell density, and the formation of structures in this medium. The aggregation mechanism of the amoeba *D. discoideum* differs from the classic Turing mechanism of pattern formation on which the previous models were based. In both cases, an active chemical medium is formed that is described by reaction–diffusion equations. But in the Turing models, in this medium dissipative structures are formed, and in the second case, spiral and circle waves are formed. In the Turing models, chemical marking leads to cell differentiation without cells' spatial movement, and in the case of the amoeba *D. discoideum*, it leads to directed movement due to chemotaxis.

Chapter 7
Autowave Processes, Nerve Pulse Propagation, and Heart Activity

The main property of nerve cells is their ability to conduct nerve pulses—electrical waves spreading along the nerve fiber. The conduction property is based on the fact that the elementary volume of a membrane is a local active element possessing the ability to amplify an incoming electrical signal. Nerve pulse propagation is one of the most striking examples of autowave processes in living systems. In the middle of the nineteenth century it was found that nerve pulses in frogs spread without visible damping over rather large distances, up to 10 cm (Helmholtz 1850). German scientist Hermann Ludwig Ferdinand von Helmholtz (1821–1894) was the first scientist to measure the speed of excitation spread in a nerve—in experiments on frogs in 1850, and in 1867–1870 together with Russian scientist Nikolai Bakst—in a human being and determined the conditions of the threshold electrical stimulation of nerve fibers. Helmholtz also made the first experimental attempt to determine the rhythm of pulses sent by the brain to muscles and determined the period of muscle response to sensory irritation.

The excited part of a fiber becomes the generator of electrical current. This current leaks into adjacent areas of the nerve fiber and makes them generate a current, which translates into new excitation sites. Thus, nerve and muscle fibers in their electrical nature are like a cable, that is, the comprise a relatively highly conductive core (cytoplasm) surrounded by a membrane of a fiber with high resistance and high capacity.

The main role in the formation and propagation of a pulse is played by the membrane: if the protoplasm of the nerve fiber is removed and replaced with sea water, such a nerve fiber may transfer excitation for a long time. The fiber is excited when the potential difference on both sides of the membrane reaches a certain threshold. In other words, the potential difference across the membrane serves as a parameter determining current generation.

Only 100 years after the work of Helmholtz, mechanisms of the generation of nerve impulses were clarified. Here, the main contribution was made by Hodgkin and Huxley (1952).

A. Rubin and G. Riznichenko, *Mathematical Biophysics*, Biological and Medical Physics, Biomedical Engineering, DOI 10.1007/978-1-4614-8702-9_7,

© Springer Science+Business Media New York 2014

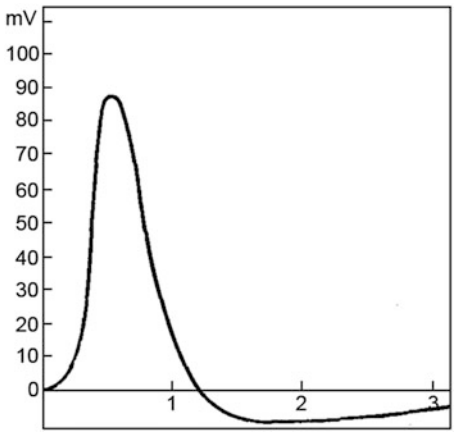


Fig. 7.1 Form of nerve pulse in time. The potential is measured from the level of the resting potential. Abscissa: time in milliseconds, ordinate: potential in millivolts

Their work was performed on the giant squid axon, which is a long cylindrical tube extending from a neuron. Electrical signal travels along the outer membrane of the tube. This nerve fiber reaches a thickness of 0.5–1 mm, which is hundreds of times greater than the thickness of the nerve fibers of mammals and is a very convenient object for such studies.

The pulse is generated in the following way. There is a potential difference of approximately 60–90 mV in the resting state between the outer surface of the nerve fibers and the cytoplasm inside, so that the cell surface is positively charged relative to the cytoplasm. This potential difference is called the *resting potential*. It is due to the fact that the ionic composition of the protoplasm of nerve and muscle cells is very different from the ionic composition of the surrounding extracellular fluid. In the protoplasm, potassium ion concentration is approximately 30–50 times greater, and sodium approximately 10 times smaller than on the outside. The positively charged potassium ions coming out through the cell membrane create a resting potential. Sodium ions (also charged positively) passing in the opposite direction create the opposite effect, but because at rest the membrane is much more permeable to potassium ions than sodium ions, the first process dominates, and as a result a potential difference appears.

In the excited state (e.g., under external influence or the excitation of neighboring sites of the membrane), the membrane selectively changes its permeability to various ions. First, there is a sharp increase in the sodium permeability of the membrane, and the flow of positively charged sodium ions rushes into the cell. In this case, the potential difference on both sides of the membrane is first reduced to zero and then changes its sign: the axoplasm (cytoplasm of the axon) becomes positively charged relative to the extracellular environment, and the potential difference reaches a maximum of approximately 30 mV.

Thus, the total change in membrane potential compared to the initial value is approximately 100–120 mV. Then again the flow of potassium ions outward begins to dominate, and the system gradually returns to its original state of rest. Potential change upon excitation is shown in Fig. 7.1.

Experiments and Model of Hodgkin and Huxley

In addition to the experimental study, Hodgkin and Huxley proposed a model describing processes of ion transport through a membrane and the passage of the pulse potential along the membrane. The work of the British scientists was awarded the Nobel Prize in Physiology or Medicine in 1963 (along with Sir John Eccles of Australia).

Experiments using pharmacological agents allowed them to divide the current flow across a membrane into separate components corresponding to Na^+ and K^+ currents (I_{Na} and I_K). In the formation of the total potential, other ion currents are involved, in particular Ca^{2+} ions. In the model, Hodgkin and Huxley described the contribution of other ions as an effective current I_L. The total current $I(t)$ can be represented as a sum of the currents of individual ions through the membrane and a *capacitive current* caused by variations in the transmembrane potential V. Thus:

$$I(t) = C\frac{dV}{dt} + I, \tag{7.1}$$

where C is the membrane capacity, and $I = I_{Na} + I_K + I_L$.

On the basis of experimental data on the conductivity of the membrane for different ions, Hodgkin and Huxley described the values of ion currents by means of functions that depend on concentrations of some hypothetical particles moving in the membrane in an electric field. Their model is the following system of nonlinear differential equations (Hodgkin and Huxley 1952):

$$\frac{a}{2R}\frac{\partial^2 V}{\partial x^2} = C\frac{\partial V}{\partial t} + (V - E_K)\overline{g}_K n^4 + (V - E_{Na})\overline{g}_{Na} m^3 h + (V - E_0)\overline{g}_0, \tag{7.2}$$

$$\frac{dn}{dt} = \alpha_n(1 - n) - \beta_n n, \tag{7.3}$$

$$\frac{dm}{dt} = \alpha_m(1 - m) - \beta_m m, \tag{7.4}$$

$$\frac{dh}{dt} = \alpha_h(1 - h) - \beta_h h, \tag{7.5}$$

where n, m, and h are functions of capacity and time that determine the behavior of sodium and potassium currents; a is the radius of the fiber; R is the specific resistance of the protoplasm; C is the specific capacitance of the membrane; E_K, $E_{Na}, E_0, \overline{g}_K, \overline{g}_{Na}$, and $\overline{g}_0$ are constant parameters; and, finally; α_n, α_m, α_h, β_n, β_m, and β_h are potential functions of the following form:

$$\alpha_n = \frac{0.01(V+10)}{\exp\dfrac{V+10}{10}-1}, \quad \alpha_m = \frac{0.1(V+25)}{\exp\dfrac{V+25}{10}-1},$$

$$\alpha_h = 0.07\ \exp(V/20), \quad \beta_n = 0.125\ \exp\big(V/80\big), \tag{7.6}$$

$$\beta_m = 4\ \exp(V/18), \quad \beta_h = \frac{1}{\exp\dfrac{V+30}{10}+1}.$$

The coefficients in the formulas are chosen empirically. Model (7.2), (7.3), and (7.4) allows us to describe the basic properties of conducting nerve fibers. Let us consider some of them.

Pulse Generation Assume that a nerve fiber is initially at rest and then stimulated for a short time by an external current source. An analysis of the equations shows that at first the value of $m(V, t)$ starts to increase, which leads to an increase in the sodium current $(V - E_{\mathrm{Na}})\overline{g}_{\mathrm{Na}} m^3 h$. As a consequence, the potential difference between the protoplasm and the external environment (i.e., depolarization of the fiber) grows. With increasing depolarization the value of m increases, and the value of h decreases. These changes in m and h are connected in such a way that the value of $m^3 h$ in the expression for the sodium current first increases and then begins to decrease.

Threshold of Stimulation It is known that changes in the membrane potential lead to the excitation of nerve fibers and the appearance of a pulse only if the initial change in the potential exceeds a certain value, called the threshold. Small subthreshold changes in the potential decay without generating a pulse. The presence of such a threshold is similar to the existence of a certain ignition temperature. Heated to that temperature, a given substance can catch on fire.

Refractory Period The presence of nerve and muscle fiber refractoriness, that is, a period of nonexcitability, coming after a pulse also follows naturally from this model. As we have seen, during some time period after the occurrence of a pulse in a fiber, parameter h becomes small and parameter n increases. In these circumstances, at any increase in the membrane potential the corresponding potassium current is greater than the sodium current, that is, any stimulation is subthreshold. This phenomenon is the refractory period.

Accommodation From experiments it is known that if the nerve fiber is acted on by a gradually increasing current, then a pulse in the fiber forms only if the current growth rate exceeds a certain definite value. With a very slow increase in the current the fiber cannot be excited (this phenomena is called the accommodation or adaptation of the fiber). In the Hodgkin–Huxley model, the presence of accommodation is due to the fact that upon slow increases in the current, sodium inactivation has enough time to take place, whereby the sodium current cannot

exceed the potassium and no pulse arises. The minimum rate of current rise that still allows the emergence of a pulse can be determined by numerical solution of the Hodgkin–Huxley equation.

Reduced FitzHugh–Nagumo Model

System (7.2), (7.3), (7.4), (7.5), and (7.6) is too complicated for analytical analysis. Some simplified models have been suggested that are capable of describing the same properties of nerve fibers. The most popular model was independently developed by FitzHugh (1961) and Nagumo et al. (1962).

Excited Element of Local System

In this model the local system is described by a 2D ODE system, which in dimensionless form is

$$\begin{aligned} &\frac{du}{dt} = f(u) - v + I_a, \quad \frac{dv}{dt} = bu - \gamma v, \\ &f(u) = u(a-u)(u-1). \end{aligned} \tag{7.7}$$

Variable u here plays the role of the membrane potential V, and v performs the role of all three particle variables m, n, h in (7.3), (7.4), and (7.5).

In the case where $I_a = 0$, the nullcline arrangement in the phase diagram (u, v) is presented in Fig. 7.2a, b. The plots in Fig. 7.2a, b differ with respect to the b/γ ratio value. In Fig. 7.2a, the system has one stable solution, corresponding to the zero value of the potential, whereas in Fig. 7.2b the system has three stationary solutions, two of them stable (0 and S_2) and the third, S_1, unstable.

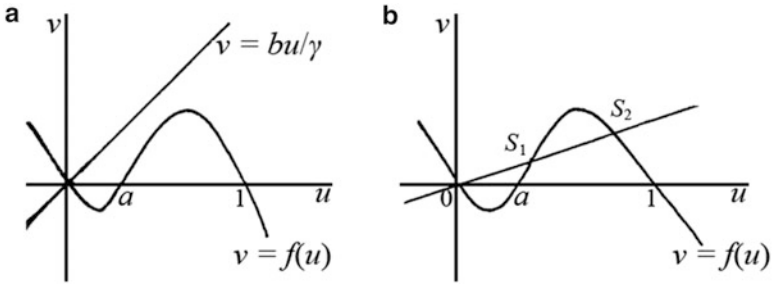


Fig. 7.2 Main nullclines of system (7.7) on phase diagram (u, v) at $I_a = 0$ for different values of ratio b/γ. (**a**) One stable steady state (0, 0). (**b**) Two stable steady states, (0, 0) and S_2, and one unstable steady state, a saddle, S_1

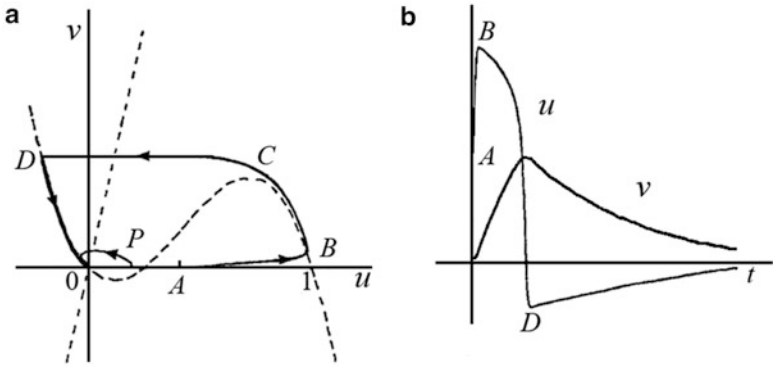


Fig. 7.3 (**a**) Phase diagram of system (7.7) at $I_a = 0$, $a = 0.25$. (**b**) $\gamma = 0.002$ for small (point P) and large (point A) initial potential fluctuations from zero steady state. *Dashed line*: isocline of horizontal tangents (*straight line*) and the isocline of the vertical tangents, which is N-shaped. B is the time course of variables u and v in the case where the phase trajectory starts at point A, the case of overthreshold excitation (Rinzel 1981)

The shape of the function is well known. In the problem of wave propagation (Chap. 3), this shape of the local source function indicated that the process of multiplication starts only when the variable value exceeds some threshold value a. Equation (7.7) reflect the fact that the rapid upsurge of the potential starts after the potential value becomes larger than the threshold potential [a in dimensionless Eq. (7.7)]. Otherwise the potential damps. Let us consider how the pulse is generated in such a system (Fig. 7.3).

In Fig. 7.3a the null isoclines are designated by the dashed curves. Let us give some initial deviation of the potential u. If this deviation is small, less than the value a in the second equation of system (7.7) (point P), then the system will return to the initial state along a short trajectory. This type of behavior is called *subthreshold excitation*. If the deviation of the variable u is large, more than a (point A), then the phase trajectory is different. The representing point moves according to the trajectory $ABCD0$ and reaches the vertical tangent isocline (AB), then moves along this cline (BC), then rapidly passes to the negative area (CD), crossing the horizontal tangent isocline, and then along the vertical tangent isocline returns to the steady state ($D0$). In Fig. 7.3b the time course of the variables u and v at the overthreshold excitation is presented. The local element with such behavior is called an *excitable element*.

If the equilibrium potential across the membrane is not zero, the isocline of vertical tangents will intersect the v axis not in the zero point, as shown in Fig. 7.3a, but in the point $v = I_a$. The possible cases of a main isocline arrangement at $I_a \neq 0$ in system (7.7) are presented in Fig. 7.4a–d. In cases a and c, the system has only one stable steady state, but the variable kinetics in case a can have the pulse shape, as we saw previously. In case b, the unique steady state is unstable, and the

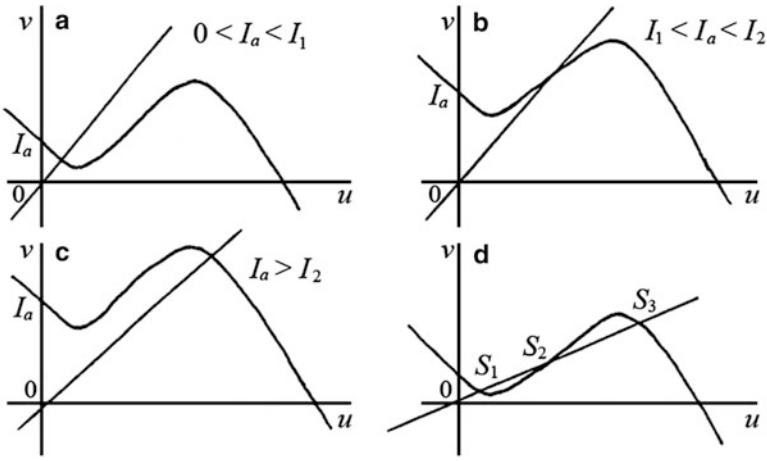


Fig. 7.4 Main nullclines in FitzHugh–Nagumo model (7.7) for different values of initially applied voltage. In (**a**) and (**c**), the steady state is locally stable but excited in the sense that for sufficiently large voltage deviations, the representative point moves along the trajectory corresponding to a single pulse (Fig. 7.3). In (**b**), the stationary state is unstable, and limit cycle oscillations can occur. In (**d**), the state S_2 is unstable, and S_1, S_3 are stable and switching between them is possible (Murray 1993)

oscillating instability and the limit cycle can be realized in the system. In case d, the two steady states S_1 and S_3 are stable, whereas the state S_2 is unstable. The system has a trigger character.

The previously discussed local behavior for the distributed system causes autowave events: pulse propagation in cases (a) and (c), standing and running waves and stable heterogeneous concentration distributions in case (b) (oscillating instability) and saddle instability in case (d).

Running Pulses

In the spatially distributed FitzHugh–Nagumo model, the propagation of the potential along the nerve fiber (cable) is taken into account:

$$\begin{aligned} \frac{du}{dt} &= f(u) - v + I_a + D\frac{\partial^2 u}{\partial x^2}, \\ \frac{dv}{dt} &= bu - \gamma v, \\ f(u) &= v(a-u)(u-1). \end{aligned} \tag{7.8}$$

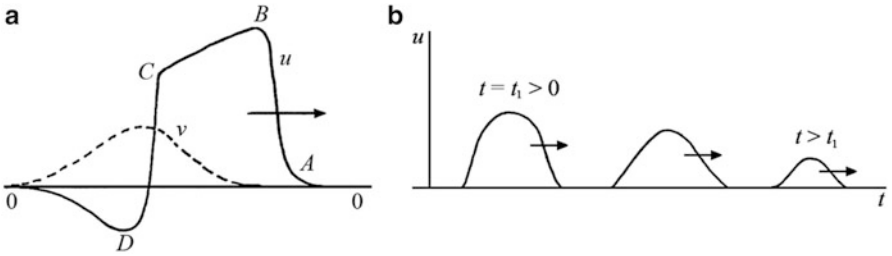


Fig. 7.5 Pulse propagation in case of overthreshold (*a*) and subthreshold (*b*) impact. (**a**) At the initial potential above the threshold value $u = a$, a running pulse appears in the system that propagates along the nerve without changing its shape (solitary wave). Points *A*, *B*, *C*, and *D* correspond to points on the phase portrait Fig.7.3a. (**b**) If the initial potential at the point of excitation is less than the threshold value $u = a$ (point *P* in Fig. 7.3a), then the running pulse decays rapidly

Let us see how the running pulse appears in such a system (Fig. 7.5).
For simplification we assume that b and γ are small values:

$$b = \varepsilon L, \quad \gamma = \varepsilon M, \quad 0 < \varepsilon < 1. \tag{7.9}$$

At $I_a = 0$ system (7.8) can be written as

$$\begin{aligned} \frac{\partial u}{\partial t} &= D\frac{\partial^2 u}{\partial x^2} + f(u) - v, \\ \frac{\partial v}{\partial t} &= \varepsilon(Lu - Mv). \end{aligned} \tag{7.10}$$

Let us consider the leading edge of the pulse, presented in Fig. 7.5. At $\varepsilon \to 0$ from (7.10) it follows that $v = \text{const}$. We arrive at an equation for the potential u,

$$\frac{\partial u}{\partial t} = D\frac{\partial^2 u}{\partial\ x^2} + f(u),$$

which is the Kolmogorov–Petrovsky–Piskunov–Fisher Eq. (3.1) with the function $f(u) = u(a - u)(u - 1)$.

In Chap. 3, we showed that in such a system the wave distribution velocity is constant and equal to $\sqrt{\frac{D}{2}}(1 - 2a)$. Taking into account slow changes of the variable v on the BC interval of the phase trajectory (Fig. 7.3a, b) Murray arrives at the following expression for the spreading rate of the single pulse (Murray 1993):

$$= \sqrt{\frac{D}{2}}(u_C - 2u_P + u_D).$$

Adding to model (7.10) the equation, describing transmembrane Ca^{+2} ion transfer, Plant (1978, 1981) simulated the periodic appearance of a pulse train running along a nerve fiber.

The FitzHugh–Nagumo model is, in some sense, a simplified model of the Hodgkin–Huxley system. It allows us to visualize by means of phase portraits those properties of the Hodgkin–Huxley system that determine its qualitative behavior, in particular, the existence of an excitation threshold.

Recently, X-ray data on the molecular structure of channels, providing ion gates and currents carrying ion transport Na^+, K^+, and Ca^{2+} in excitable membranes of nerve cells, have become available. Taking into account these data, the Hodgkin–Huxley model, which proved to be a very good empirical model, requires a new biological interpretation.

Detailed Models of Cardiomyocytes

Denis Noble (1962) suggested how to use the Hodgkin–Huxley-type model to describe action potentials of the working myocardium and pacemaker Purkinje fibers. Since then, his model has been constantly improved and has become much more complicated as experimental results on the details of the system were obtained. Many of the results were obtained in Noble's laboratory or in the course of the project led by Noble.

To simulate the activity of heart cells—cardiomyocytes—similar principles of model building were used. Contemporary models of cardiomyocytes include a significantly larger number of membrane currents. In the first Noble model (Noble 1962), as in the Hodgkin–Huxley model, the total current of the membrane had three components: Na^+, K^+, and a leakage current, which is at least partly attributed to the chloride ions. Subsequent versions of the model took into account the role of Ca^{2+}—an important depolarizing current (McAllister et al. 1975).

A scheme of the membrane and intercellular currents in the cells of the rabbit sinus node of the heart (Aliev and Chailakhyan 2005) is shown in Fig. 7.6. It includes a detailed transcript of the major membrane currents, functional differences between true and latent pacemakers, changes in intracellular concentrations of sodium, potassium, and calcium, and a function of the sarcoplasmic reticulum. The model allows one to study the mechanisms of regulation of a wide range of experimental actions and explains many observed phenomena.

Axiomatic Models of Excited Medium: Autowave Processes and Cardiac Arrhythmia

To study processes in the heart muscle, 2D and 3D models must be considered. The first success in the analysis of autowave processes in biological objects was obtained in the study of much simpler models than those described by systems of partial differential equations. Two pioneers in this field were Wiener and

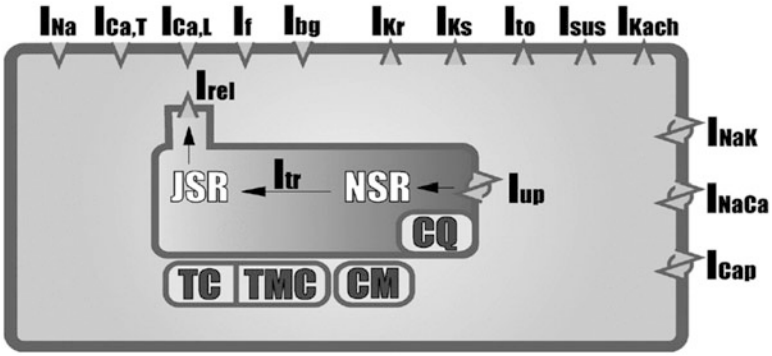


Fig. 7.6 Scheme of membrane and intercellular currents in cells of rabbit sinus node of heart. I_{Na}, sodium current; $I_{Ca,T}$, $I_{Ca,L}$, calcium currents of T and L types; I_f, current activated at hyperpolarization; I_{bh}, background current; I_{Kr}, I_{Ks}, fast and slow potassium currents of delayed rectifier; I_{t0}, I_{sus}, components of the current sensitive to 4-amidopirine; I_{Kach}, potassium current activated with acetylcholine; $I_{ca,T}$, I_{NaK}, Na–K pump; I_{NaCa}, Na–Ca exchanger; I_{Cap}, Ca pump; I_{rel}, ryanodine calcium current; I_{up}, Ca pump of sarcoplasmic reticulum (CP); I_{tr}, calcium current inside SR (sarcoplasmatic reticulum); NSR and JSR, network SR and terminal tanks; TC, TMC, CM, CQ, troponine, troponine-Mg sites, calmodulin, calsecwestrin (Aliev and Chailakhyan 2005)

Rosenblueth (1946), who proposed an approach to the analysis of waves in excitable tissues based on the study of a formal excitable medium.

In a more general form, similar ideas were developed by Gelfand and Tsetlin (Gelfand et al. 1963, 1966) and later by other authors in models of cellular automata. In constructing the models they took into account that the process of emergence and spread of excitation in biological systems, particularly in nerve tissue, has a number of distinct properties that may serve as a basis for the model.

Wave propagation in excitable tissues is different from the normal distribution of electromagnetic and mechanical waves. First, the excitation wave can propagate without attenuation due to energy stored in the cells. Second, after a period of excitement comes the *refractory* period, during which the cell does not respond to incoming signals. This property makes the interference and reflection of waves impossible. After a period of refractoriness the properties of the cells are fully restored, and the nerve tissue can once again propagate excitation.

A simple axiomatic description of excitable tissues can be formulated as follows. We assume that the excited tissue is composed of many elements with some definite properties:

1. Each element x of set X can be in one of three states: rest, excitation, and refractoriness.
2. The state of excitation has some duration τ, which is generally different for different x. Following excitation, element x keeps changing in the refractory state before returning to the resting state.
3. From each of the excited elements the excitation spreads at a certain velocity v to the other surrounding elements of set X that had been in the resting state.

4. If x is not excited by the neighboring elements within a certain time $T(x)$, then after that time it spontaneously goes into an excited state. Time $T(x)$ is called the period of spontaneous activity of x. An extreme case is where $T(x,\infty) = \infty$, in which there is no spontaneous activity.

Obviously, the use of an axiomatic theory does not require detailed knowledge of the kinetics of the real processes. Formal models of excitable media allow us to describe the mechanisms of birth and interaction of wave sources in homogeneous and heterogeneous environments.

By means of axiomatic models wave sources of two important types were first predicted: rotating spherical waves, which are called reverberators (Wiener and Rosenblueth 1946; Balakhovskii 1965) and leading centers mutually igniting activity in the neighboring elements (Krinskii et al. 1967; Ivanitskii et al. 1978).

Thus, by means of axiomatic models, the simulation of various pathologies of the heart muscle, above all heart arrhythmias that occur at abnormal modes of propagation of excitation waves, was initiated. One of the most dangerous heart arrhythmias is ventricular fibrillation of the heart, where the rates of individual muscle cells get desynchronized and the heart ceases to pump blood, resulting in a lethal outcome. Let us consider the treatment of some important phenomena in excitable tissues by means of axiomatic models.

Synchronization Consider a medium in which periods of spontaneous activity of the different elements are different. In this medium, synchronization occurs, and the rhythm of excitation of the whole is determined by the rhythm of the fastest element. Suppose there are two interrelated elements, A1 and A2, with periods of spontaneous activity T1 and T2, with $T1 < T2$. When one of the elements is excited, it also excites the second one (we assume that the time of excitation transfer to the next element is negligible). After time T1 the element A1 spontaneously excites and transfers the excitation to the A2 element. This makes the element A1 a *pacemake*r. In the medium, which consists of many elements, the process of establishing the smallest period of excitation takes a long time, which depends on the time of excitation transfer, the refractory period, and the number of elements. If we take into account these factors, the analysis gets more complicated, but the fact of synchronization of the elements with different periods remains true under general assumptions.

The synchronization mechanism is very important for normal heart functioning. Sinus node cells, which serve as the pacemaker of the heart rate, exhibit spontaneous activity. The periods of spontaneous activity of different cells are close to each other. The fastest cells set the rhythm of the heart. If any of the cells cease to function, the role of the leading elements is transferred to the fastest surviving one.

These mechanisms of regulation provide greater reliability and stability of the heart. A study of the activity of individual elements on more detailed models showed that the leading element can only be a group of cells with high natural frequency, the number of cells in a group being defined by the system parameters (Mazurov 2008).

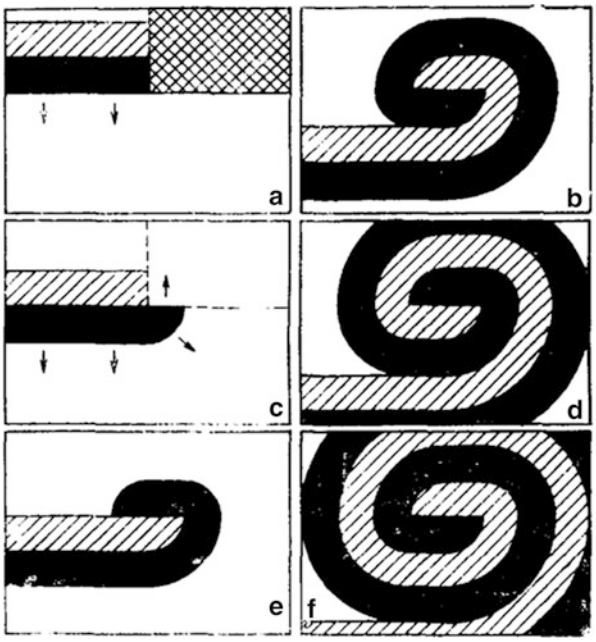


Fig. 7.7 Scheme of reverberator formation. A wave of excitement comes from the top down; *black*: excited medium; *shading*: refractory medium; grid (in **a**): nonexcitable medium domain that becomes excitable (in **b**) at the moment when a wave of excitement passes through it. (**b–f**) Further course of waves during reverberator formation

Atrial fibrillation is one of the worst malfunctions of the heart. In atrial fibrillation, instead of rhythmic, coordinated contractions local excitations, devoid of periodicity, occur in the heart. Cardiac arrhythmias usually occur on the basis of a heart disease (e.g., heart attacks, coronary circulation failure) and disturb the homogeneity of cardiac tissue. Formal analysis of excitable media shows how a local inhomogeneity can lead to an anomalous regime.

Reverberator Consider a 2D excitable medium where an excitation wave periodically propagates. Suppose that in a certain time period when the next wave is propagating, some of the medium's domains are temporarily inhibited and become unresponsive to stimulation.

In Fig. 7.7, the excited medium is in black, the refractory medium is shaded, and the grid is a nonexcitable domain of the medium. Suppose that at the moment when the wave goes around the region where an excitation is inhibited, the latter comes out of its stagnation state. Then the wave begins to spread into a previously inhibited area (Fig. 7.7b).

If the dimensions of this region are large enough, a wave of excitation passes over it, goes around the refractory area, and starts to run periodically around this domain (successive stages of the process are shown in Fig. 7.7d, e). Such a spiral is called a *reverberator*. As a result of this phenomenon of rate transformation in time, reverberators can disappear or generate new reverberators. If more reverberators are formed rather than disappear, an avalanche process of irregular activity develops, similar to the real atrial fibrillation of the heart muscle.

Numerical calculations of 2D distributed dynamic models showed that in active kinetic media at certain values of parameters, spiral waves of reverberators can appear. In general, the question of the relevance of axiomatic and dynamic models has been resolved using a number of mathematical theorems that, *inter alia*, state that any discrete automaton can be dynamically presented, while the converse is generally false.

Despite the abstractness and simplicity of axiomatic models of excitable media (and, in many ways, due to this simplicity), they allowed the development of a fundamental understanding of the mechanisms of propagation of excitation and the mechanisms of cardiac arrhythmias. Images of spiral waves—reverberators—made it possible to explain many important phenomena in cardiac tissue vulnerability, single or multiple extrasystoles, atrial fibrillation, the phenomena of "critical mass" of atrial fibrillation, and the spontaneous termination of atrial fibrillation.

The description of a complex 2D or 3D excitable medium like heart tissue using nonlinear differential equations is a rather complicated problem. This area is now being intensively developed. Some results on the theoretical basis of the capacity to control spatial chaos through the periodic pinpoint action of weak force are presented in Kovaleva and Loskutov (2004) and Loskutov and Mikchailov (2007). Computer and experimental studies aim at the selection of actions that might be applied to actual heart tissue in a fibrillation regime.

Chapter 8
Nonlinear Models of DNA Dynamics

To understand the mechanisms that mediate the activity of biological systems at the molecular and subcellular levels, it is necessary to study the physical processes involving biological macromolecules. Following this approach, application of the ideas and methods of modern nonlinear physics turns out to be especially productive. Up-to-date nonlinear DNA physics is a special field of scientific research that makes it possible to considerably promote our understanding of the laws underlying the function of this molecule of life.

In recent decades, a number of linear and nonlinear mathematical models of DNA mobility and double-helix unwinding mechanisms of different degree of complexity have been suggested. There is a whole spectrum of models—qualitative models, which describe the principles of DNA unwinding, and very detailed models, which include descriptions of each atom's motion, as well as advanced DNA molecular dynamics and quantum-mechanical models of charge distribution along the DNA chain (Guéron et al. 1987; Lebrun and Lavery 1998; Cuenda and Sánchez 2004; Varnai and Lavery 2006; Prévost et al. 2009).

We shall consider dynamic processes in relation to the main biological function of DNA—storage and transmission of biological information. The ability of the DNA double helix to unwind is determined by certain complex dynamic properties of this molecule, which consists of a great number of atoms and possesses a quasi-1D structure with unusual symmetry, several degrees of freedom, many types of motion, and a specific distribution of inner interactions. Two threads of DNA consisting of four bases are presented in Fig. 8.1.

The specific features of the system are as follows:

1. The threads are parallel but have the opposite polarities.
2. The bases are situated inside and connected to each other by weak hydrogen bonds.
3. Two bases connected by hydrogen bonds form a base pair. According to the Chargaff rule, only two types of complementary base pairs are possible in DNA: A–T pairs and G–C pairs (Fig. 8.2).

A. Rubin and G. Riznichenko, *Mathematical Biophysics*, Biological and Medical Physics, Biomedical Engineering, DOI 10.1007/978-1-4614-8702-9_8,

© Springer Science+Business Media New York 2014

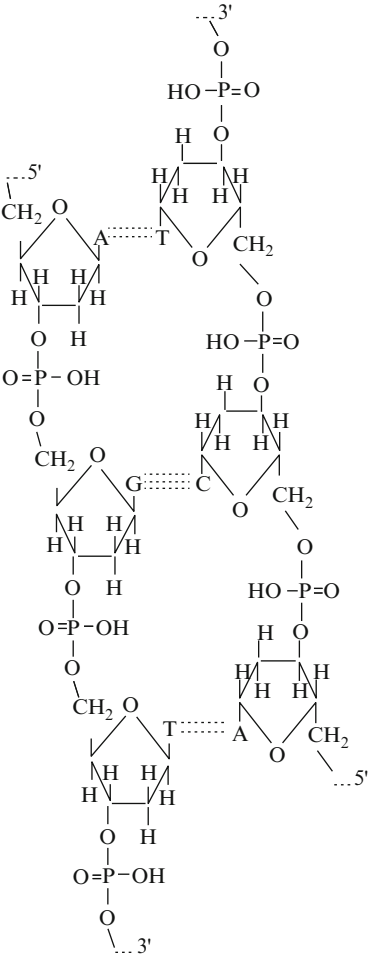


Fig. 8.1 Two DNA threads. *Dotted lines*: hydrogen bonds between bases A, T, G, C

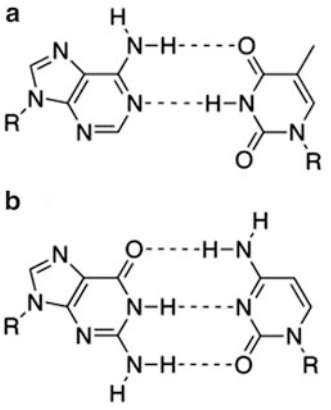


Fig. 8.2 Base pairs: (**a**) A–T; (**b**) G–C

The fact that a DNA molecule has a quasiregular chemical structure is very important when proposing mechanical analogs for the subsequent mathematical simulation. A regular part (a sugar-phosphate skeleton) is formed by differently modified sugars and phosphate groups, combined in regular alternate 3′, 5′-phosphate-ether units, whereas a nonregular part is formed by the bases, connected by sugars and thereby forming a DNA sequence.

In constructing DNA models one takes into account only the most important structural properties. First, DNA consists of long chains of atoms. Second, these chains have an almost regular structure, that is, a DNA molecule has a "skeleton" (a sugar-phosphate chain) with a precisely repeating pattern of atoms along the chain. Thanks to these two facts, the DNA structure is similar, to a certain extent, to 1D periodic structures, which are known in physics as quasi-1D structures, which is why DNA is called a life chain crystal (Bann 1964).

In other respects, a DNA molecule is more like a polymer than a crystal because a DNA molecule is not a rigid but an elastic system. Thus, to construct a more realistic DNA model, we need to take into account, for example, its elastic nature, its ability to intertwine, convolve, and form superstructures.

Besides the skeleton with its regular repetition of atoms and atom groups, DNA has some elements of a nonregular structure. It is necessary to take into account the nonregularity of the base sequence. In the first approximation, we can consider it a small perturbation of the skeleton's regular pattern and therefore use perturbation theory for the theoretical calculations.

The principal properties of a DNA double helix were established by Crick and Watson (1954), Franklin and Ghosting (1953), and Wilkins et al. (1953). More details are given in Saeger (1984). A scheme for the construction of mechanical models is presented in Fig. 8.3. The diameter of a double helix is 20 Å, the distance between the neighboring bases turned at a 36º angle relative to each other is 3.4 Å. One turn of the helix contains ten nucleotides, which corresponds to a distance of 34 Å.

The majority of DNA properties can be described by mechanical models. DNA function is mediated via physical mechanisms of interactions between the main structural elements of the molecule. The most important interactions involve forces responsible for the stabilization of the secondary structure: horizontal hydrogen interactions between the bases inside the pairs, vertical or stacking interactions between the neighboring bases along the DNA axis, and long-range interactions inside and outside of the sugar-phosphate skeleton.

Successful models should describe the mobility of the DNA molecule, which underlies its biological function. The simplest of such models are mechanical ones.

The complex structure of DNA allows a whole set of different types of mobility to proceed simultaneously. In a first approximation, mobility can be characterized by several parameters: time scale and values of energies and frequencies related to inner motions. The dynamic motions occur within a wide time domain from femtoseconds to seconds. The general picture of the inner mobility is quite complex. It covers various motions of separate atoms, small atomic groups, and whole fragments of the double helix.

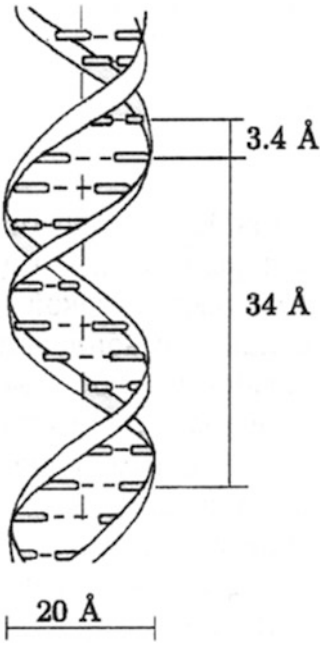


Fig. 8.3 Image of double helix. A sugar-phosphate skeleton is present as two bands. The bases are presented as short transverse bars

These motions include fast and slow motions, simple motions such as oscillations of separate atoms, or atomic groups near the steady state with amplitudes of less than 0.1 Å and also complex motions: local unwinding of the double helix and transitions of some local DNA segments into other conformation states. Frequencies related to the inner motions fall in the range of 1–100 s^{-1}. It means that these values are much smaller than the inner oscillations of a small isolated molecule. Limited motions and oscillations of sugars, bases, and phosphates, as well as the rotation and bending motions of the double helix have activation energy of about several kilocalories per mole. Their characteristic frequency is approximately several per second. To describe small amplitude motions, linear models are applicable.

But if the motion has a rather large amplitude, the generation of collective motions becomes possible. These motions are accompanied by the generation of open states or double-helix unwinding, with a characteristic time value of milliseconds. To describe them, it is necessary to develop nonlinear models. The term *open state* designates a DNA domain, where hydrogen bonds between the bases are broken. Such domains can be of different dimensions—from one base pair (b.p.) up to several. The establishment of open states in a DNA molecule is considered a necessary element of its activity—DNA breathing (Gueron et al. 1987; Krueger et al. 2006).

Hierarchy of Structural and Dynamic Models

In the construction of mathematical models of DNA dynamics, usage of mechanical analogs has proved especially fruitful—including mechanical model systems with similar numbers of constituting structural elements, types of motion, and interactions. Hundreds of such different models exist that describe DNA motion within a nanosecond time domain. Their classification is presented in Yakushevich (2004, 2007), including continuous and discrete models, spiral models and those ignoring the spiral structure, models simulating the motion of each or nearly each atom of a fragment or simulating only the motion of the main subunits, homogeneous models, and models taking into account the existence of the DNA base sequence.

In the monograph of Yakushevich (2004, 2007) the DNA motion models are classified according to their level of complexity. A scheme of the model hierarchy levels is presented in Fig. 8.4.

The simplest models (level 1 in Fig. 8.4) are those of the elastic bar with a circular cross chapter (in microphotographs, DNA looks like an elastic thread). The discrete analog is a chain of connected disks (or beads), each of which corresponds to one nucleotide pair. The dynamics of an elastic bar is well known in physics and is characterized by three types of motion: transitional displacements, rotations (or torsion motions), and transversal motions.

Models of the second type take into account the fact that the DNA molecule consists of two polynucleotide chains interacting via hydrogen bonds and intertwining in such a way that a double helix is formed. The model presents two elastic bars interacting weakly with each other. In a spiral version, it is supposed that the bars are twisted in a double helix. In a straight (nonspiral) version, the mutual winding is ignored. Both versions of the model have six types of inner motion: transition, transversal displacement, and rotation of each bar. The intrinsic structure of the chains is not taken into account. In the discrete analog of such a model there are two chains of disks connected by means of longitudinal and transversal springs. The rigidity of the longitudinal springs is much stronger than that of the transversal ones.

Models of the third level of hierarchy take into account the fact that each chain consists of three types of subunit: sugars, phosphates, and bases. These models simulate motions of these atom groups as motions of rigid bodies weakly connected to each other. It is assumed that the bonds between separate groups are weak and soft, and the bonds between atoms inside the subunits are strong and rigid.

Let us count the number of equations in such a model. If we suppose that each subunit has six degrees of freedom, then we must multiply this number by the number of nucleotide subunits, equal to three, and multiply again by the number of DNA chains, equal to two. In this way, we obtain 36 equations. If we accept the possibility of two conformational states C'-endo and C'-exo, then the total number of equations increases to 38 (3 for the first level of modeling and 6 for the second level). The problem can be considerably simplified if we restrict our simulation to the most important functional motions.

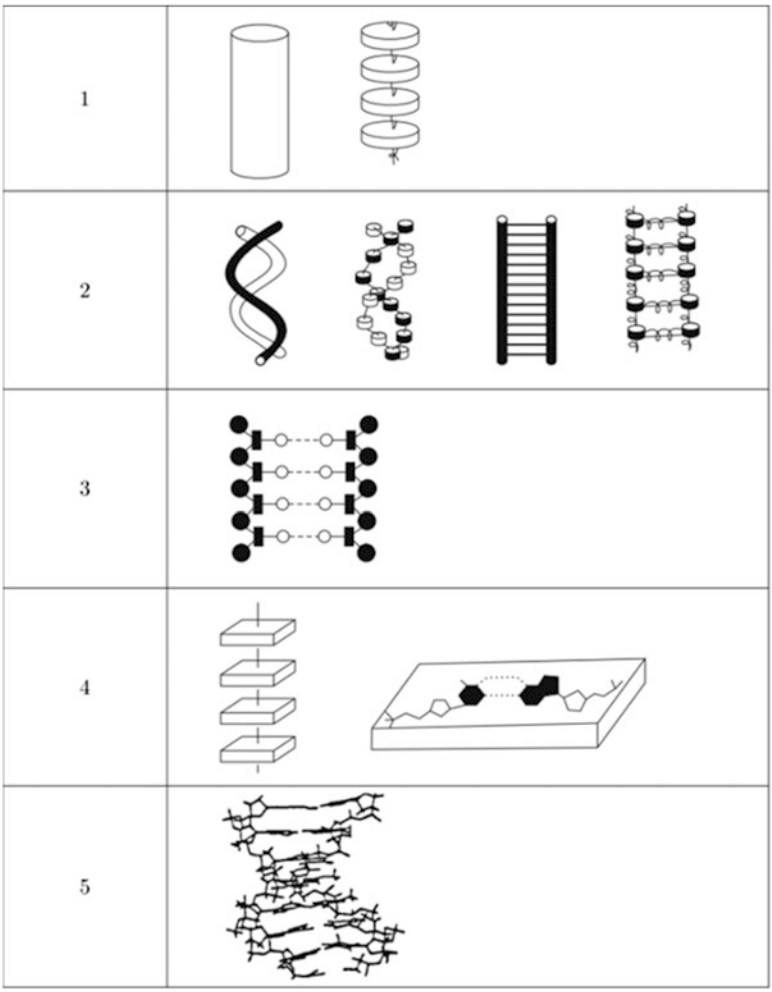


Fig. 8.4 Hierarchy of dynamic DNA models; continuous and discrete forms (Yakushevich 2004)

The fourth hierarchy level describes the inner motions in the lattice with an individual cell formed by atom groups (pairs of nucleotides, for example), which are periodically repeated along the DNA molecule. In this approximation all displacements of nucleotide atoms are taken into account, but these models include only homogeneous (homopolymer) chains.

Models of the fifth level reside at the top of the hierarchy of models. These are the molecular dynamics models. They simulate the DNA structure and motions in detail. Their complexity is much higher, and such modeling demands vast computer resources (Schlick 2002).

Linear DNA Theory

In linear models, in the first approximation using a general theoretical description of DNA mobility, the problem of statistics of DNA excitation and light and neutron dispersion is considered. The DNA molecule is presented as an ensemble of linear waves (phonons). The number of equations in such a model depends on the particular method of selection of the dominant motions, which in turn is determined by the biological problem under consideration.

Simple Linear Model of an Elastic Bar

A homogeneous elastic bar with a circular cross section represents the simplest DNA model. The model takes into account three types of motion connected with stretching (tension), twisting, and bending, respectively. For such a system, the Hamiltonian can be written as

$$H = H_{\mathrm{s}} + H_{\mathrm{t}} + H_{\mathrm{b}} + H_{\mathrm{s-t}} + H_{\mathrm{s-b}} + H_{\mathrm{t-b}}, \tag{8.1}$$

where the terms H_{s}, H_{t}, H_{b} correspond to the longitudinal displacements (stretching), torsion displacements (twisting), and bending displacements (bending), respectively. The terms $H_{\mathrm{s-t}}$, $H_{\mathrm{s-b}}$, $H_{\mathrm{t-b}}$ correspond to interactions between these three types of motion. As evidenced in the book by McCommon and Harvey (1987), the amplitude and frequency values of bending movements are significantly different from those of stretching and twisting oscillations, and therefore terms the $H_{\mathrm{s-b}}$, $H_{\mathrm{t-b}}$ can be neglected. The remaining Hamiltonian can be divided into two independent terms:

$$H = H^{(1)} + H^{(2)}, \tag{8.2}$$

where $H^{(1)} = H_2 + H_{\mathrm{t}} + H_{\mathrm{s-t}}$ and $H^{(2)} = H_{\mathrm{b}}$.

First let us consider a discrete analog of the elastic bar. In the discrete form the model consists of a number of disks (or beads) connected by springs and located at a distance of 3.4 Å from each other (Fig. 8.5).

The Hamiltonian of the system is constructed taking into account three types of inner motion related to tension, twisting (torsion), and winding. In the first approximation, these three types of oscillations can be considered independent.



Fig. 8.5 Chain of connected disks (Yakushevich 2004)

The terms H_s and H_t can be written as

$$\begin{aligned} H_s &= \sum_n \left(\frac{M}{2} \left(\frac{du_n}{dt} \right)^2 + \frac{K}{2} (u_{n+1} - u_n)^2 \right), \\ H_t &= \sum_n \left(\frac{I}{2} \left(\frac{d\varphi_n}{dt} \right)^2 + \frac{k}{2} (\varphi_{n+1} - \varphi_n)^2 \right), \end{aligned} \tag{8.3}$$

where u_n and φ_n are stretching and torsional displacements of the nth disk, M and I are the mass and inertia moments of the disk, and K and k are coefficients of the stretching and torsion rigidity, respectively.

In the linear approximation, stretching and torsion motions can be considered independent, and the dynamic equations adopt the following simple form:

$$\begin{aligned} M \frac{d^2 u_n}{dt^2} &= K_0 (u_{n+1} - 2u_n + u_{n-1}), \\ I \frac{d^2 \varphi_n}{dt^2} &= k_0 (\varphi_{n+1} - \varphi u_n + \varphi_{n-1}). \end{aligned} \tag{8.4}$$

Let us assume the following boundary conditions:

$$u_n = u_{n+N}, \varphi_n = \varphi_{n+N}. \tag{8.5}$$

Then the solutions of (8.4) have the form of flat waves:

$$u_n = u_{n0}\exp(i(qna - wt)),$$
$$\varphi_n = \varphi_{n0}\exp(i(qna - wt)). \tag{8.6}$$

By substituting (8.6) into (8.4) we shall find the frequencies of these waves:

$$w_l = \left(\frac{2K_0[1 - \cos(qa)]}{M}\right),$$
$$w_t = \left(\frac{2k_0[1 - \cos(qa)]}{I}\right).$$

In the lattice model (fourth level in Fig. 8.4), the DNA atomic motions are considered as a superposition of normal oscillations. In linear approximation (for small displacements), all normal oscillation modes are independent. In normal mode analysis, one can assume that in the harmonic approximation, the potential energy surface where the DNA atoms move has a quadratic form. Limiting the analysis to homopolymer chains, the dynamics of a long DNA molecule can be reduced to the atomic motion of a single base pair. Each base pair contains 41 atoms, and each atom has three degrees of freedom. Thus the corresponding matrix of the dynamic force constants has a rank of 123. Matrix diagonalization gives 123 eigenvalues, each of them a second power of the oscillation frequency of a specific mode, whereas eigenvectors correspond to the amplitude displacements of the individual atoms involved in these oscillations. The resulting spectrum of the phonon dispersion has, in this case, 123 branches. In the general case, the solution can be presented as an ensemble of flat waves (phonons), where the roots of the corresponding dispersion equations determine the normal mode frequencies.

Linear models of DNA motion proved to be very productive and made it possible to analyze a large amount of experimental data, including data on the rates of longitudinal sound propagation and elastic neutron dispersion.

Results of the calculations, performed in linear approximation, reproduce Raman peaks and shifts observed during conformational transitions and explain the low frequency spectrum of DNA microwave and infrared absorption. However, there was not much success in analyzing the processes of DNA unwinding, which are related to the most important function of this biomacromolecule.

Nonlinear Models of DNA Mobility: Mechanical Analog

The pioneering work in the study of inner DNA dynamics was the work by Englander and coworkers (Englander et al. 1980). The work consists of two parts: experimental and theoretical. Using the method of hydrogen-tritium exchange, the existence of open DNA states was proved. The latter were determined as mobile domains, their lengths varying from one to several base pairs. Inside the open domains, hydrogen bonds were broken. The appearance of such open states is connected with the considerable angular deviations of the bases from steady-state values (Fig. 8.6).

Mathematically this process was described by means of the Hamilton formalism (Yakushevich 2004, 2007), which is widely applied in theoretical and mathematical physics. In contrast to the linear models described previously, the authors do not limit their simulations by small deviations from the steady state but consider motions with large amplitude (anharmonic or nonlinear approximation). It was found that the nonlinear wave solutions of the sine-Gordon equation

$$\varphi_{tt} - \varphi_{zz} + \sin\varphi = 0 \tag{8.7}$$

provide mathematical modes that can simulate open DNA states. Here the function φ (z, t) describes deviations of angles from the steady-state value.

Let us consider the Englander model and its modifications in more detail (Yakushevich 2004, 2007), taking into account the peculiarities of DNA underlying the mechanisms of the biological functions of DNA.

Nonlinear models describe the rotatory motions of the bases around the sugar-phosphate chains, which have large amplitudes. These motions induce hydrogen bond splitting and the appearance of open states. In descriptions of dynamic properties, an analogy between a DNA molecule and a chain of connected pendulums is used. The bases in a DNA molecule, bound to sugars, play the role of rotating pendulums, and the sugar-phosphate chain plays the role of the horizontal chain (Fig. 8.7). The field, induced by the second DNA thread, which weakly interacts with the first DNA thread via hydrogen bonds between the bases, plays the role of the outer gravitational field.

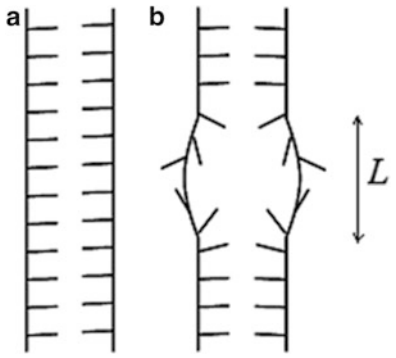


Fig. 8.6 Open (**a**) and closed (**b**) states of double-helix DNA (Yakushevich 2004)

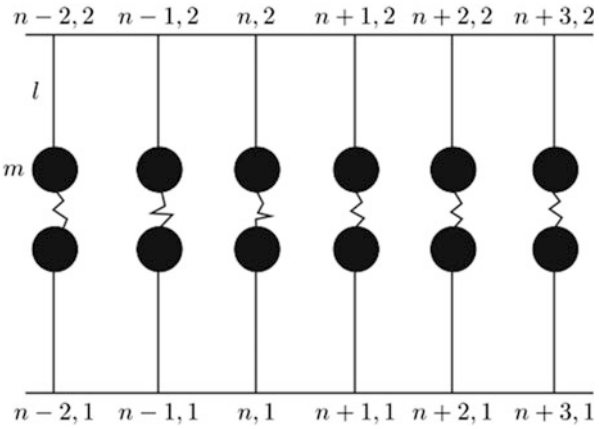


Fig. 8.7 Mechanical DNA analog used in Englender model. Two pendulum chains are connected by springs (Yakushevich 2007)

Pendulum chain dynamics is well studied in mechanics. It is described by a set of n nonlinear equations. For the nth pendulum the equation can be written as

$$I\frac{d^2\varphi_n}{dt^2} = K\left(\varphi_{n+1} - 2\varphi_n + \varphi_{n-1}\right) - mgh\sin\varphi_n, \tag{8.8}$$

where φ_n is the angular deviation of the nth pendulum from the steady state, I is the moment of inertia of the pendulum, K is the rigidity coefficient of the horizontal chain, m and h are the pendulum mass and length, respectively, and g is the gravitational constant.

Let us shift to the continuous approximation:

$$z_n \to z; \varphi_n(t) \to \varphi(z,t).$$

Following the analogy of a chain of pendulums, the equation for the rotatory oscillations of DNA bases can be written as

$$I_0\varphi_{tt} - K_0\varphi_{zz} + V_0\sin\varphi = 0. \tag{8.9}$$

Here I_0 is the moment of inertia of the base, K_0 is the rigidity coefficient of the sugar-phosphate chain, and $V_0\ \sin\varphi$ is the force acting between bases inside the pairs. This equation of the sine-Gordon type has an autowave solution of a kink type. The solution can be written as a function of the value of the angular deviation from the direction perpendicular to the sugar-phosphate chain, with space coordinate z and time t:

$$\varphi(z,t) = 4arctg\{\exp(\gamma\xi/d)\}. \tag{8.10}$$

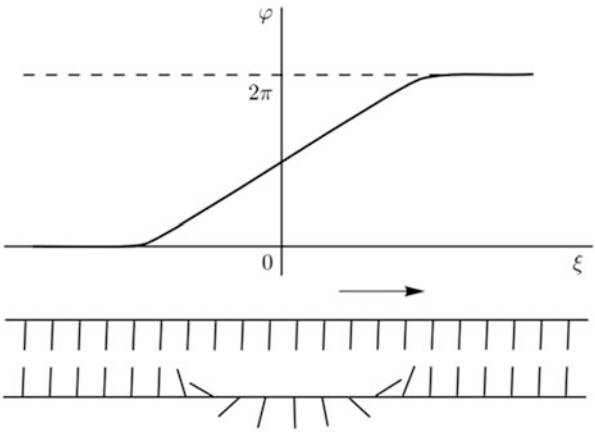


Fig. 8.8 Solution (8.11) of sine-Gordon Eq. (8.7) and qualitative picture corresponding to this solution (Yakushevich 2004)

Here $\gamma = [1 - Iv^2/K_0a^2]^{-1/2}$, $\xi = z - vt$, v is the rate of distribution of the nonlinear wave (kink); $d = (K_0a^2/V_0)^{1/2}$, and a is the distance between the neighboring base pairs in the chain.

The qualitative picture corresponding to this solution is presented in Fig. 8.8. Two sugar-phosphate chains are represented here as two long lines and the bases as short lines. A local domain with broken base pairs corresponds to the kink.

The described model has one essential drawback—it takes into account the base mobility of only one of the two DNA chains. The second chain plays a passive role providing some averaged field. In reality, both chains are similar. A mechanical analog is a model that includes two weakly connected elastic bars. A discrete analog of such a system is a double chain of disks connected by longitudinal and transversal springs.

The Hamiltonian of such a system consists of three terms:

$$H = T + V^{(1)} + V^{(2)}.$$

Here T is the kinetic energy of the rotatory oscillations, and $V^{(1)}$ and $V^{(2)}$ are potential energies of the longitudinal and transversal strings. These values are determined by the angle displacement, moment of inertia, and disk radius, as well as by the length and the rigidity of the strings.

For the DNA structure an assumption that the disk radius is much larger than the distance between disks is valid. It allows us to write the following simplified equations:

$$\begin{aligned} I\varphi_{1tt} &= Ka^2\varphi_{1zz} - kR^2[2\sin\varphi_1 - \sin(\varphi_1 + \varphi_2)], \\ I\varphi_{2tt} &= Ka^2\varphi_{2zz} - kR^2[2\sin\varphi_2 - \sin(\varphi_1 + \varphi_2)], \end{aligned} \tag{8.11}$$

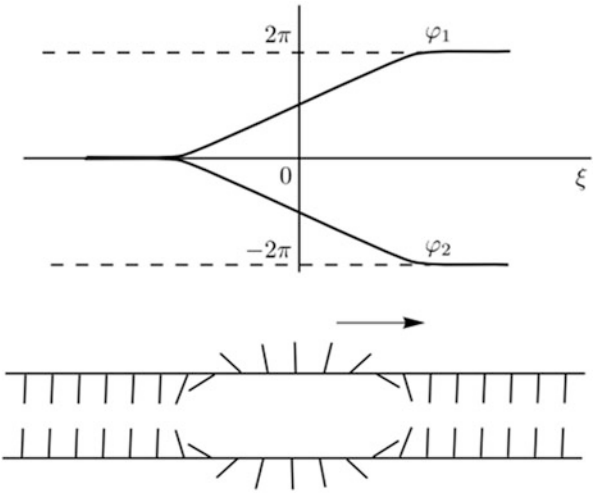


Fig. 8.9 Solution to equation system (8.11) and corresponding picture (Yakushevich 2004)

where $\varphi_{1,2}$ is the angle displacements of the disks, a is the distance between the neighboring disks, and K and k are the rigidity of the longitudinal and transversal strings, respectively. As was shown by Yakushevich, Eq. (8.11) can be solved using a preliminary decomposition of the sinuses in infinite sets, switching to another coordinate system, and introducing an autowave variable:

$$\xi = z - vt.$$

The solution is

$$\varphi_1 = -\varphi_2 = 4arctg\{\exp q(\xi - \xi_0)\} \tag{8.12}$$

For real and positive values of q

$$q = \left[\frac{2}{1 - v^2}\right]^{\frac{1}{2}}, \quad v^2 < 1.$$

A graphical solution of this equation and the corresponding drawing are presented in Fig. 8.9. It describes the local deformation (the base pair opening) moving along the DNA molecule at a rate v.

The model can be more specific taking into account the spiral character of the DNA structure. In this case, instead of the straightened chain of pendulums oscillating in the "gravitational" field of the second chain, the pendulum chain is considered ringed in such a way as to form a spiral. In the spiral model the fixed pendulum points are situated on the spiral, and the pendulum threads are directed normal to the axis. Thus, in the steady state neighboring pendulums are at an angle of 36°, and the direction of the "gravitational field," induced by the second chain, also changes following pendulums along the chain (Fig. 8.10).

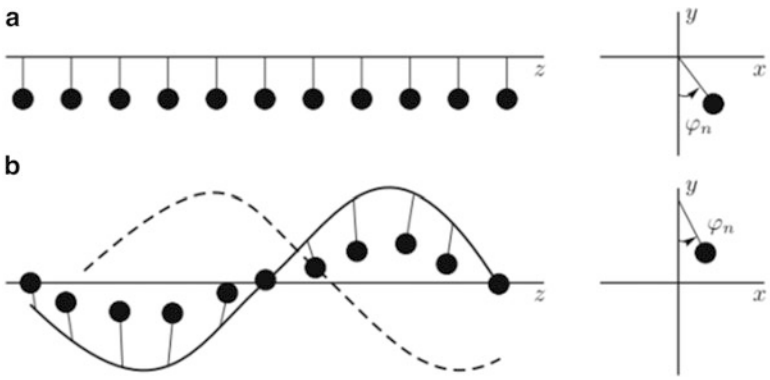


Fig. 8.10 Mechanical DNA models: (**a**) linear model; (**b**) spiral model (Yakushevich 2004)

Mathematical Model Simulating Single DNA Base's Nonlinear Oscillations

Accounting for the important role of different DNA fragment oscillations let us consider in more detail the simplest mechanical oscillations—rotational oscillations of individual DNA bases, adenine (A), thymine (T), guanine (G), and cytosine (C), around a sugar-phosphate chain (Fig. 8.11). Phase diagrams and the analogy of rotational oscillation of a DNA base as rotational oscillation of a single mechanical pendulum (Awrejcewich 1996) were used. In this approximation, the influence of the other bases is simulated as an external periodic force (Yakushevich et al. 2009).

According to the Englander equation, the rotational oscillations of a single DNA base can be described by the following equation:

$$I\varphi_{tt} + V\sin\varphi = -\beta\varphi_t + F. \tag{8.13}$$

Here $\varphi(t)$ is the angular displacement of the base, I is its moment of inertia, V is the parameter that determines the hydrogen interactions between the bases in a pair, β is the dissipation coefficient, and F is the generalized external force.

In dimensionless form (8.13) has the form

$$\varphi_{\tau\tau} + \omega_0^2\sin\varphi = -b_0\varphi_\tau + k_0, \tag{8.14}$$

where $t = \lambda\tau$, $\omega_0^2 = V\lambda^2/I$, $b_0 = \beta\lambda/I$, $k_0 = F_0\lambda^2/I$.

To present the dynamic properties of the system in a phase diagram, it is more convenient to use an equivalent system of two differential equations:

$$\begin{aligned} \psi &= \varphi_\tau, \\ \varphi_\tau &= -\omega_0^2\sin\varphi - b_0\psi + k_0. \end{aligned} \tag{8.15}$$

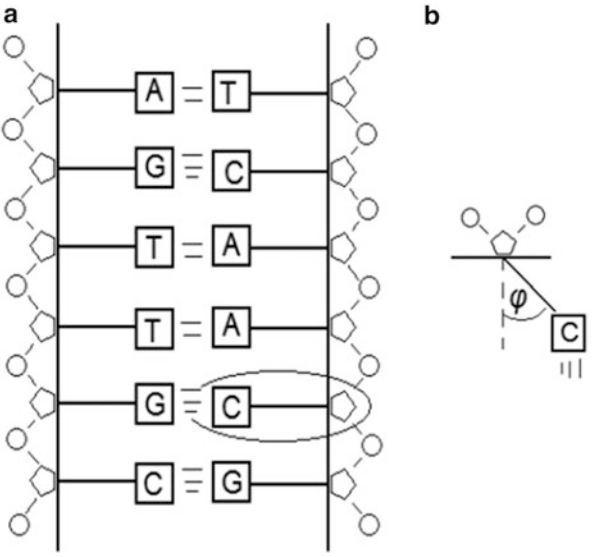


Fig. 8.11 Schematic diagram of fragment of double helix DNA chain including A, T, G, and C bases (**a**) and a single base oscillator (**b**) (Yakushevich 2007)

Phase trajectories in the case $\varphi << 0$ (small oscillations) for each of the four DNA base oscillations (A, T, G, C) are stable spirals, with rather slow damping (Fig. 8.12); the system parameters are estimated according to the data presented in detail elsewhere (Yakushevich et al. 2005).

In the presence of a periodic force (which simulates the influence of other bases), Eq. (8.15) can be written as follows:

$$I\varphi_{tt} + V\sin\varphi = -\beta\varphi_t + F_0\cos\Omega t \tag{8.16}$$

or, in dimensionless form,

$$\varphi_{\tau\tau} + \omega_0^2\sin\varphi = -b_0\varphi_\tau + k_0\cos\gamma\tau. \tag{8.17}$$

Here $\gamma = \Omega/\lambda$.

The phase trajectories of such a system can be presented in three dimensions with the following variables as the axes:

$$\begin{aligned} \psi &= \varphi_\tau, \\ \varphi_\tau &= -\omega_0^2\sin\varphi - b_0\psi + k_0\cos\theta, \\ \theta_\tau &= \gamma. \end{aligned} \tag{8.18}$$

ODE system (8.18) is equivalent to (8.17). 3D phase trajectories for the bases (A, T, G, C) are presented in Fig. (8.13). The pattern of oscillations becomes complicated (Fig. 8.14).

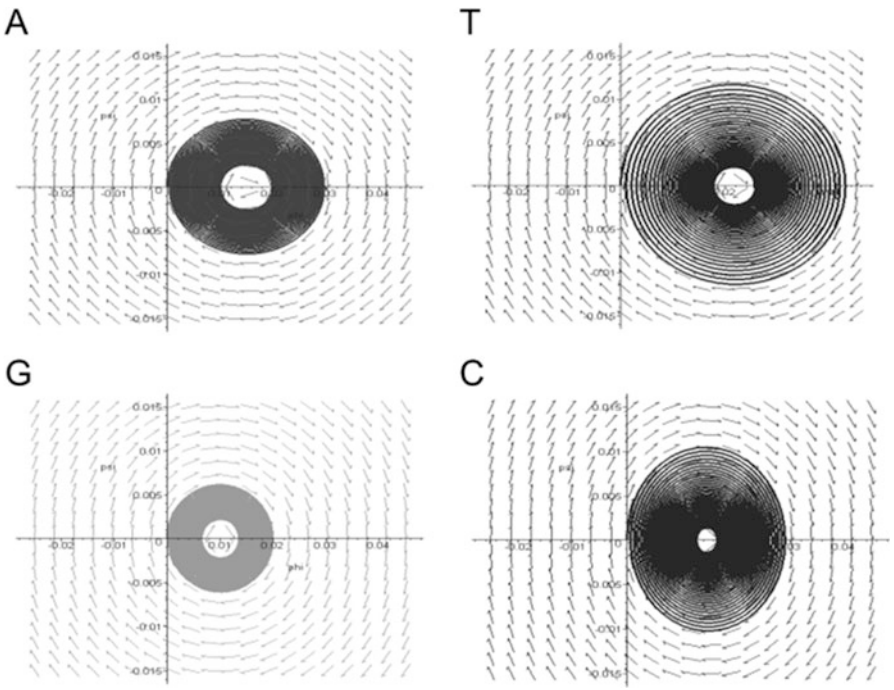


Fig. 8.12 Phase trajectories of small rotational oscillations of adenine (A), thymine (T), guanine (G), and cytosine (C). Effects of dissipation and action of constant generalized force are taken into account (Yakushevich et al. 2009)

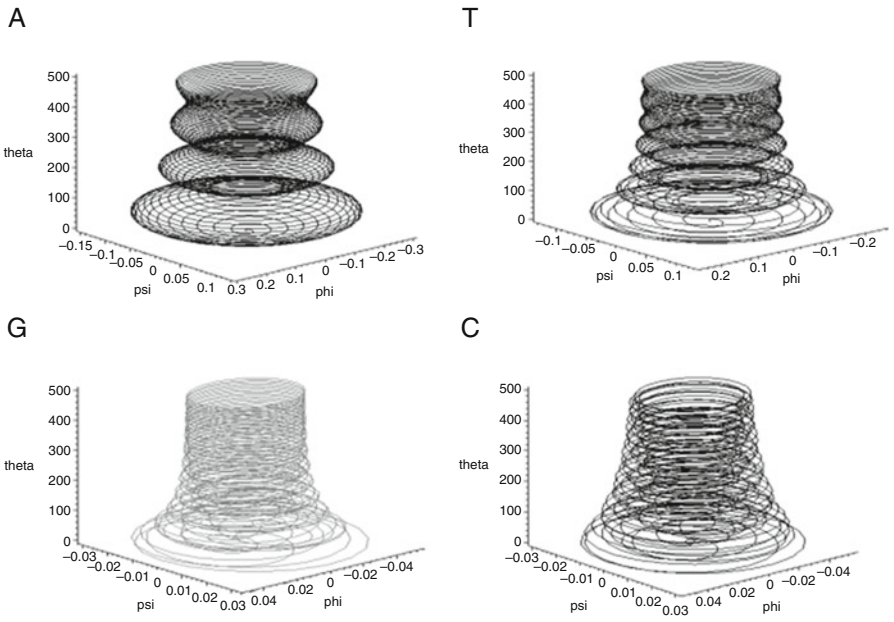


Fig. 8.13 Phase trajectories of small amplitude oscillations of adenine (A), thymine (T), guanine (G), and cytosine (C) in 3D space (φ, ψ, θ) in the presence of an external periodic generalized force

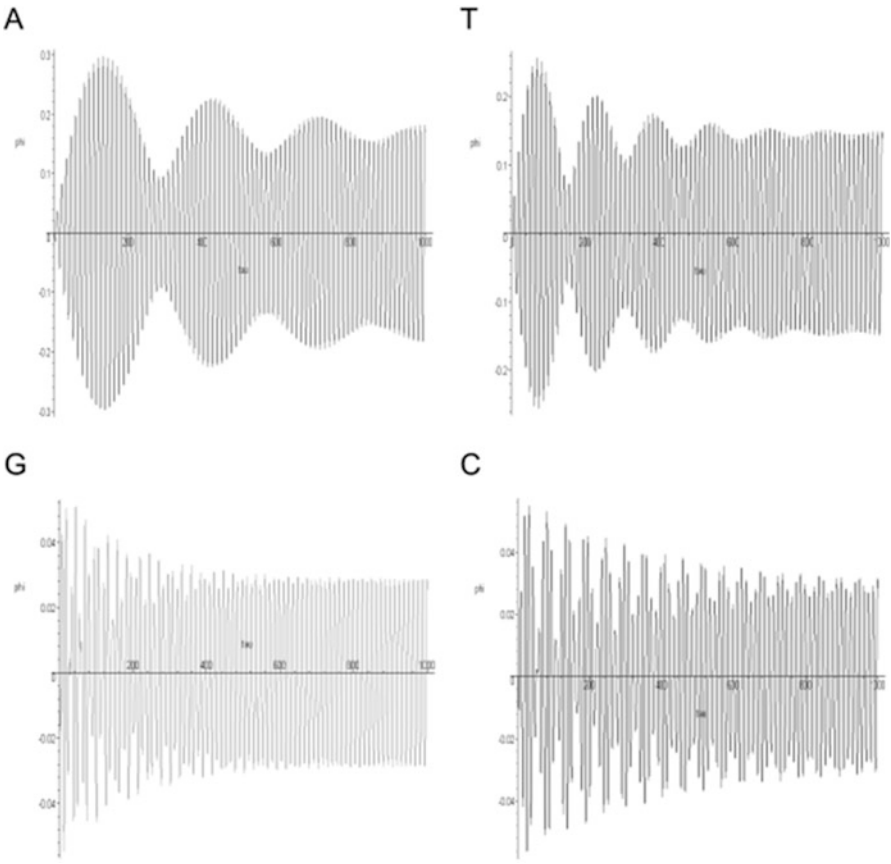


Fig. 8.14 Small amplitude oscillations $\varphi(t)$ of adenine (A), thymine (T), guanine (G), and cytosine (C) in the presence of an external periodic generalized force

A detailed analysis of a more complicated system of two bound bases forming a central pair in a short DNA fragment of three pairs was performed in Yakushevich (2011). Taking into account hydrogen interactions between the bases inside the pairs, stacking interactions between the pairs, and DNA helicity the difference in the oscillation patterns of the bases A, T, G, C and the trajectories of the central pairs AT and GC were shown (Fig. 8.15).

A mechanical analogy approach helps to find a relationship between the dynamic activity and functional properties of a DNA molecule.

Physical Analogs of Real DNA Sequences

Papers published in the last few years by Cadoni et al. (2008, 2010), De Leo and Demelio (2008), and Derks and Gaeta (2011) present simulations of DNA torsion dynamics for values of parameters within a physical range. The simulations were

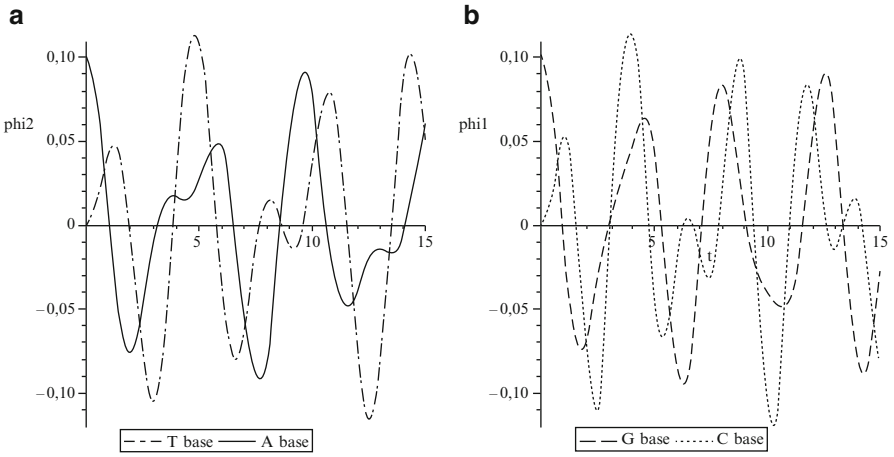


Fig. 8.15 Different oscillation patterns of bases (**a**) adenine (A), thymine (T), (**b**) guanine (G), and cyanine (C) (Yakushevich 2011)

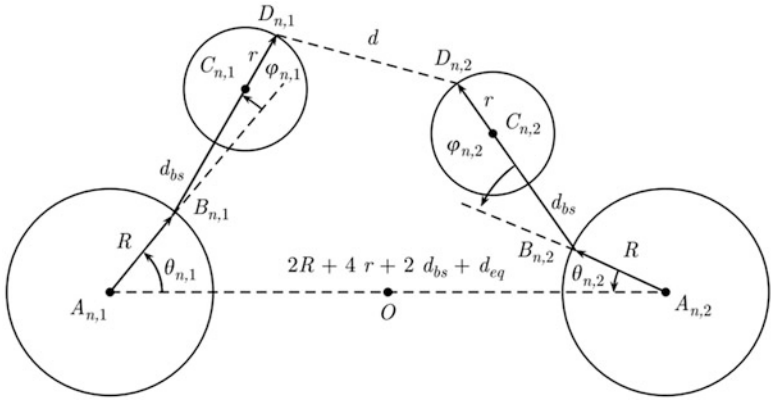


Fig. 8.16 Geometry of nucleotide pair in model (Cadoni et al. 2010)

performed for a completely homogeneous chain, a chain with a random base sequence, and for a real DNA chain of human adenovirus 2 (Cadoni et al. 2010). The model is a natural generalization of the previously considered model by Yakushevich, taking into account more details of the DNA geometry. The state of each nucleotide at site n on chain $i = \pm 1$ is described by two angles: rotation angle $\theta_n^{(i)}$ of the sugar-phosphate group around the backbone chain and rotation of the nitrogen base around the sugar atom (angle $\varphi_n^{(i)}$) (Fig. 8.16). The Yakushevich model can be derived from the Cadoni et al. model by freezing the angles $\varphi_n^{(i)}$.

Thus the mechanical analog of a nucleotide is a double-pendulum chain (Fig. 8.17, left), and the DNA molecule model can be presented as a double-

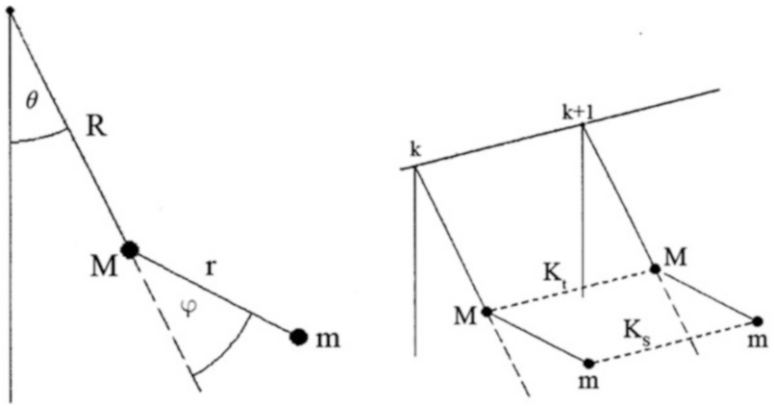


Fig. 8.17 The model of Cadoni et al. (2010) can be presented as a chain of interacting double pendulums. $M = I/R^2$, I is the moment of inertia of the sugar-phosphate group, and m is the mass of the nitrogen base (Cadoni et al. 2010)

pendulum chain (Fig. 8.17, right). Thus in this model the inhomogeneity of real DNA is entirely contained in bases, while the sugar-phosphate backbone is homogeneous.

The simulations show that twist solitons of size of approximately 60 base pairs propagate at considerable distances (up to ten times the soliton size) before stopping due to phonon emission. This result demonstrates that twist solitons may indeed be present in real DNA and play a considerable role in its transcription, as first suggested by Englander et al. (1980).

The considered models are very important for understanding DNA activity and for the theory of nonlinear dynamics. They show that soliton propagation is possible in a fully inhomogeneous medium with a suitable structure. Indeed, this possibility is determined by the existence of a homogeneous part of DNA molecules that supports a topological soliton (sugar-phosphate groups) and an inhomogeneous part (the bases) that plays the role of a dissipative medium. Model simulations confirm that solitons are also present in a randomly heterogeneous medium, which means that their existence does not depend on the actual sequence of inhomogeneities.

Long-Range Effects

The model considered here allows us to explain qualitatively the so called long-range effects in the DNA molecule. The main characteristic of these effects is illustrated in Fig. 8.18, where a rather long DNA fragment with two specific sites (S_1 and S_2) and two protein molecules (P_1 and P_2) is presented.



Fig. 8.18 Schematic image of DNA with two special sites, S_1 and S_2, and two bound proteins, P_1 and P_2

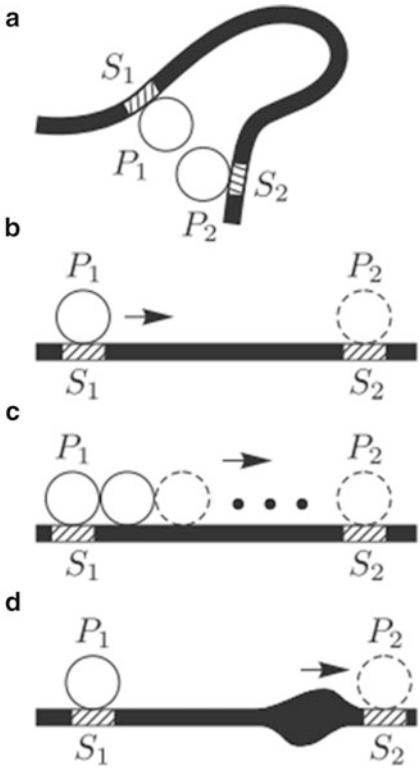


Fig. 8.19 Models of long-range interactions in DNA: (**a**) loop development model; (**b**) slip model; (**c**) model of consecutive binding; (**d**) model based on suggestion of conformational wave spreading in DNA (Yakushevich 2007)

Numerous experiments demonstrate that the interaction of the P_1 molecule with the site S_1 may influence and drastically change the character of the interactions of the P_2 molecule with the site S_2, the distance between the sites S_1 and S_2 being rather large—from hundreds up to thousands of base pairs. This is why these effects are called *long-range effects*. Different models, which can explain the long-range effects, are presented in Fig. 8.19.

Within the frameworks of the considered *mechanical* model, the mechanism of the long-range effects may be as follows. P_1 binding with the site S_1 induces local conformational changes in the vicinity of this site, so that a conformation wave starts to spread along the DNA. When it reaches the site S_2, it induces a conformation change of this site, and this in turn leads to changes in the binding constant of the site S_2 for the P_2 molecule (panel d in Fig. 8.19).

Nonlinear Mechanisms of Transcription Regulation

The process of transcription (RNA synthesis) includes three main stages: initiation, elongation, and termination. At the first stage a special enzyme (RNA polymerase) binds to a promoter domain of the DNA molecule. After RNA polymerase assumes the right position and forms several phosphodiester bonds, the second stage of the process starts. A small fragment (subunit σ) separates from the RNA polymerase, and its remaining part moves along the DNA and elongates the RNA molecule step by step.

When the third stage of the process completes, RNA polymerase separates from the DNA molecule. There exists a special domain on the DNA molecule (terminator) that gives a stop signal to the transcription process.

Let us consider an essentially heterogeneous DNA model of a fragment of the DNA molecule that contains the following important functional blocks necessary for RNA synthesis and its regulation: promoter domain P, coding domain C, several regulation domains R_1, R_2, R_3, and terminator domain T (Fig. 8.20).

At the first stage, RNA polymerase is bound to the promoter P; this act is accompanied by considerable changes in the bound domain conformation, which can spread along the double DNA helix. It corresponds to the excitation and spreading of a nonlinear conformation wave in the DNA. When passing the coding domain C, such an excitation changes its conformation, which leads to changes in the DNA matrix properties and in the synthesis rate of the elongation stage. In terms of nonlinear dynamics, such excitation can be considered a soliton, and the excitation motion the spreading of the soliton in the kink form.

After passing the C domain, the conformation wave reaches the terminator domain T, which divides two genes, the *i*th and the (*i*+1)-th. Experimental data show that this domain has a varied heterogeneous structure.

In Fig. 8.20 the T domain is presented as a cross. When passing such a domain the wave can be completely absorbed or it can overcome this barrier, but in the latter case it changes its profile and rate. The first result can be interpreted as termination, the second as a signal to start transcription of the second gene.

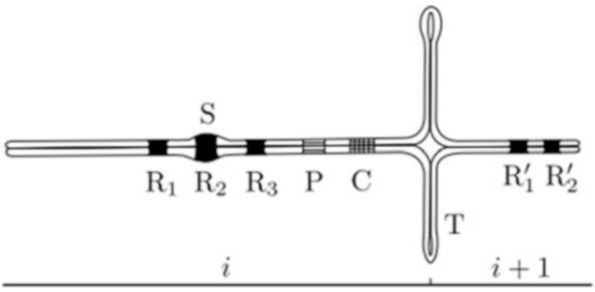


Fig. 8.20 Schematic representation of DNA fragment. P, C, T are the promoter, coding, and terminator domains of the *i*th gene, respectively; R_1, R_2, R_3 are the regulation domains of the (*i*+1)-th gene; S is the conformational excitation moving along the DNA (Yakushevich 2007)

Propagation of conformational waves along the regulatory domains R_i is accompanied by changes in these domain conformations and, consequently, by changes in the binding constants of regulatory proteins for these domains, which is especially important for the regulation of DNA activity. Nonlinear conformational waves spreading along the DNA can also play a special role in the coordination of the activities of several genes.

From numerous biological experiments it is widely known that the direction of the transcription process is different not only for the DNA molecules of different living organisms but even for promoter domains in the same DNA molecule. By means of the nonlinear models (Salerno 1992, Salerno and Kivsher 1994) it has been shown that the motion direction of an initially fixed soliton depends on the base sequence near the starting point. By means of the model of the $T7A_1$ promoter of the plasmide pB R322 DNA molecule, it has been shown that when a soliton at the initial time moment comes out of a promoter, it remains motionless.

On the other hand, if the soliton was initially inside the promoter domain and the soliton wave began to move, then the motion direction depends on the base sequence near the starting point. These results show that the dynamically active promoter domains correspond to the domains of functional activity.

Part III
Kinetic Models of Photosynthetic Processes

Chapter 9
Models of Photosynthetic Electron Transport: Electron Transfer in a Multienzyme Complex

This chapter is devoted to the modeling of electron transport processes, which are the basis of the primary photosynthetic light stage where the transformation of solar energy into the energy of chemical bonds takes place. We shall discuss the structure and main functional mechanisms operating in a system as well as the problem of adequate mathematical apparatus for the description of the primary photosynthetic processes and the formulation and analysis of related kinetic models.

The system of primary photosynthetic processes is a subcellular system. It is a unique object in terms of mathematical modeling. In recent decades, the system has been intensively investigated in a number of laboratories in different countries. The practical goal of these studies is to use mechanisms of light energy transformation in photosynthesis in biotechnical areas and make it available in industry. Although the goal has not been fully realized, considerable progress in our fundamental knowledge has been achieved. In particular, this is evidenced by the six Nobel Prizes awarded for achievements in photosynthetics.

In many studies the rate constant values of individual reactions in native photosynthetic systems were determined directly, though generally for the majority of biological processes it is very difficult to solve this problem. The rate constants of individual reactions can serve as parameters in the kinetic models of biochemical reactions. The evaluation of the rate constants of photosynthetic reactions became possible due to the special properties of photosynthetic systems. Electron transport processes may be triggered simultaneously by either a delta-function-shaped short light flash or a rectangular continuous light pulse. Therefore, the photosynthetic system itself can be considered as a technical device triggered by a light signal. Spectral methods (differential spectroscopy, fluorescence, electron paramagnetic resonance method) allow us to record in direct experiments kinetic curves describing the evolution of different redox states of individual components in real time and to use this information in mathematical models.

Another important, distinctive feature of a primary photosynthetic system is that its constituents—photosynthetic reaction centers of Photosystem I (PSI) and Photosystem II (PSII)—can be isolated from the whole photosynthetic membrane

A. Rubin and G. Riznichenko, *Mathematical Biophysics*, Biological and Medical Physics, Biomedical Engineering, DOI 10.1007/978-1-4614-8702-9_9,

© Springer Science+Business Media New York 2014

in an intact form with their ability to absorb light and to transform light quanta of energy into the energy of separated and stabilized charges preserved. Hence it has become possible to estimate the values of parameters of elementary steps of electron transfer by studying isolated membrane fragments and then to use these obtained parameters in the models of whole systems of photosynthetic electron transport reactions.

Organization of Processes in Photosynthetic Membrane

In the primary photosynthetic processes in subcellular systems the absorbed light energy is transformed into the free energy of chemical bonds. These events proceed in chloroplast thylakoids of green plants and algae and in chromatophores of photosynthetic bacteria. A schematic view of green plant chloroplasts is presented in Fig. 9.1.

The structure and function of a photosynthetic energy-transforming membrane was thoroughly investigated in many experiments, and the results of these studies are summarized in a number of books and reviews (e.g., Nelson and Yocum 2006; Series: Advances in Photosynthesis and Respiration. V 1–34, Springer). A scheme of the structures and processes in the photosynthetic membrane performing the solar energy transformation are given in Fig. 9.2. Elements of the structure and processes are listed in the figure legend.

In the last few years structural data on the protein complexes PSI, PSII, and cytochrome complex were obtained. The X-ray structures with 2–3 Å resolution are now available. Figure 9.3 presents a scheme of a photosynthetic membrane according to these structural data.

The main participants of photosynthetic electron transport—multienzyme complexes—are embedded in the bilayer lipid membrane and provide the path for directed electron transport across the membrane. Rapid (10^{-12} s) charge separation in primary photochemical pairs of PSII and PSI, electron transport from the inner (luminal) to the outer (stromal) membrane surfaces, and the following

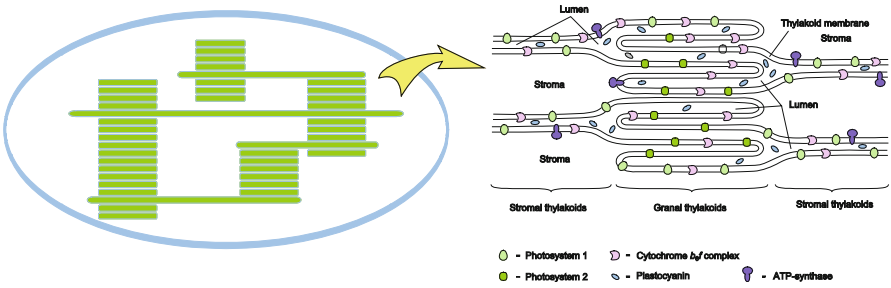


Fig. 9.1 Schematic view of green plant chloroplasts. *Right*: arrangement of main molecular complexes in photosynthetic membrane. In Fig. 9.2 these complexes are presented in more detail

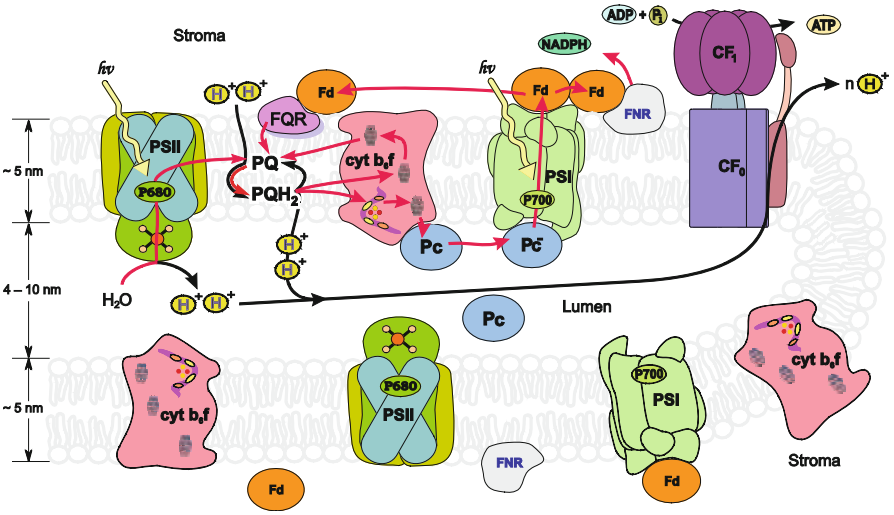


Fig. 9.2 General scheme of primary photosynthetic processes. PSI, PSII, Photosystems I and II; Pc, plastocyanin; Cyt b_6f, cytochrome b_6f complex; PQ, plastoquinone; FQR, ferredoxin:plastoquinone-reductase; Fd, ferredoxin; FNR, ferredoxin:$NADP^+$-reductase. *Red lines*: paths of electron transfer along electron transport chain; *black lines*: H^+-ion fluxes after illumination is switched on

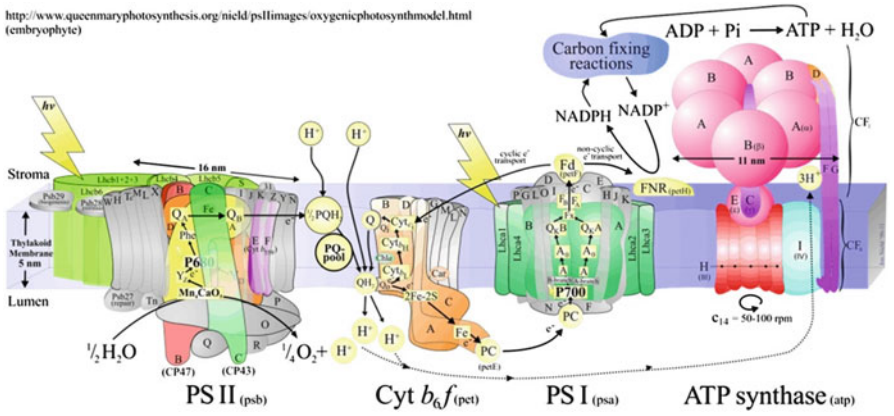


Fig. 9.3 Multienzyme complexes in photosynthetic membrane. *Arrows*: paths of electron transfer. Designations are the same as in Fig. 9.2 (Jon Nield, http://photosynthesis.sbcs.qmul.ac.uk/nield/downloads.html)

quasistabilization of the separated charges at opposite membrane sides correspond to capacitor membrane properties.

Electron transport is coupled to proton transport from the outer (stromal) to the inner (luminal) thylakoid space. The first location of proton transport (one proton

per electron) into a lumen is related to the water oxidizing complex (WOC) at the donor site of PSII. The other location of proton transport is at the lumen site of the cytochrome b_6f complex (Fig. 9.3). Here the protons are carried by mobile plastoquinone molecules (two-electron carriers) that take up two electrons from the acceptor site of PSII at the outer space of a thylakoid membrane and, in the form of PQH_2, diffuse inside the membrane. Interacting with the luminal site of the cytochrome complex they let two protons enter the lumen space, giving one electron to the linear electron in the transport chain and the second electron to the inner cytochrome complex electron transport chain (the so-called Mitchell cycle). There is another possibility: so-called cyclic electron transport around PSI, during which electrons, instead of proceeding to ferredoxin:$NADP^+$-reductase (FNR) and further to the carbon-fixation (Calvin) cycle, are carried once again by PQ molecules via the cytochrome complex to PSI. Thus for each light-released electron transported along the linear chain, two or three protons are transferred into a lumen. One of them comes from the WOC, the other from the PQH_2 transmembrane transport system. If the cyclic transport around PSI is active, it provides the lumen with the third proton per electron.

The driving force behind electron transport can be represented as a redox potential difference between the electron donor, H_2O ($E_{H_2O/O_2} = +0.82$ V), and the final acceptor $NADP^+$ ($E_{NADPH/NADP} = -0.32$ V). The path of an electron from the water splitting system to the terminal acceptor $NADP^+$ is

$$H_2O \rightarrow PSII \rightarrow PQ \rightarrow Cyt\, b_6f \rightarrow Pc \rightarrow PSI \rightarrow Fd \rightarrow NADP^+ \rightarrow$$

This scheme is known as the Z-scheme because of the shape of the electron transport pathway where the electron carriers are arranged according to their middle-point potentials. Hill and Bendall (1960) were the first to propose this scheme.

Figure 9.4 shows the Z-scheme as presented by an outstanding photosynthetic scientist, Govindjee. On the left side is a scale of middle-point potentials of the electron carriers (V). The chain of the electron transfer from water to NADPH, the high-energy compound, and the basic cofactor of the CO_2 fixation cycle (Calvin cycle) and other biochemical networks is called the linear electron transport path.

The transmembrane electric potential and, as was established later, electrochemical potential (in the form of a proton gradient) constitute an intermediate form of energy supply. By means of the molecular machine ATP–synthase the energy of a proton gradient is consumed in the synthesis of high-energy compounds—ATP molecules that in the majority of metabolic reactions play the role of the so-called energy currency of the cell. A similar mechanism of ATP formation takes place also in mitochondria—respiration factories of plant and animal cells.

Experimental data about the functional organization of the primary photosynthetic reactions allow us to construct mathematical models in which mathematical apparatus used to describe the individual steps of the processes is based on data on the interactions between individual components. The parameters in these models have a definite physical meaning.

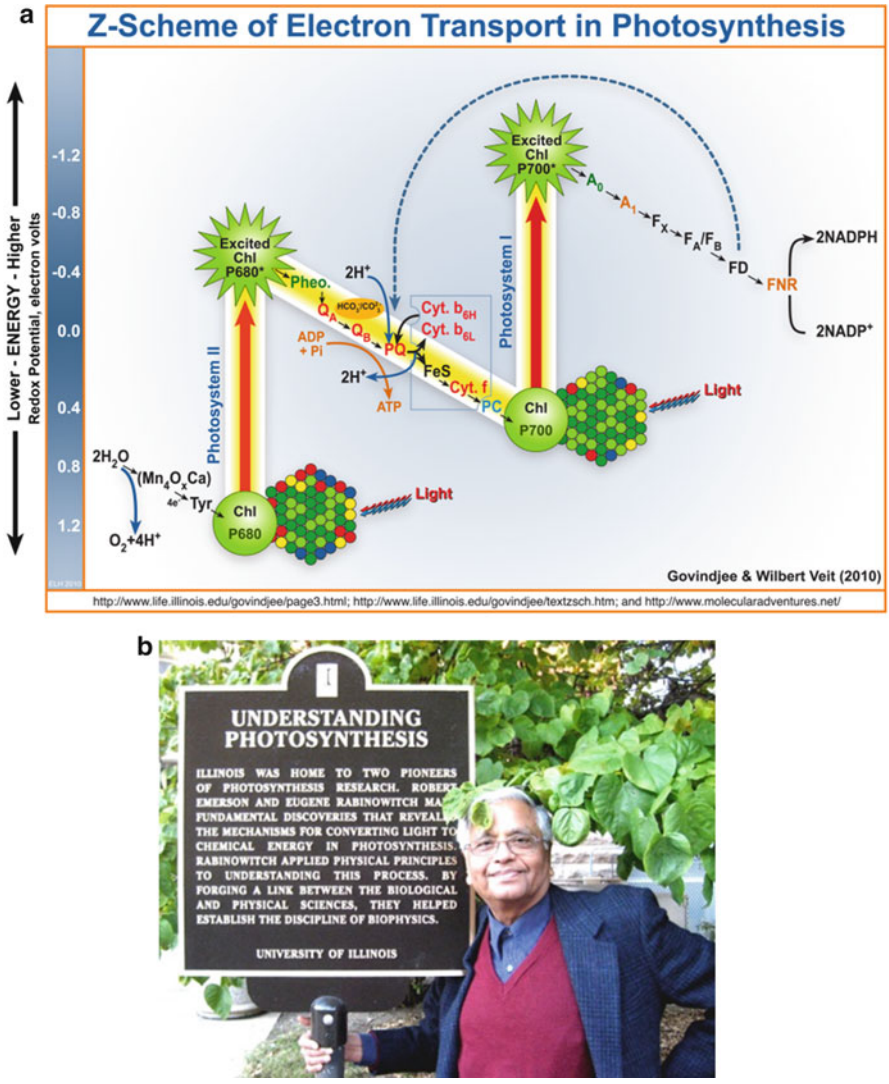


Fig. 9.4 (**a**) Z-scheme of photosynthesis after Govindjee (Orr L., Govindjee Photosynthesis online // Photosynthesis Research, Vol. 105, Issue 2, 2010. DOI: 10.1007/s11120-010-9570-8 http://www.life.illinois.edu/govindjee/). (**b**) Govindjee—American scientist—one of the most distinguished researchers in photosynthesis, author of hundreds of papers and several classic texts, editor of series *Advances in Photosynthesis and Respiration* (Springer). To date 34 volumes have been published

Coefficients in the kinetic equations of the models can be rate constant values of electron transfer at different steps of the electron transport chain, ratios of reagents' concentrations, and other characteristics of photosynthetic apparatus. Although their values cannot be measured directly in experiments, they can nevertheless be

evaluated by a fitting procedure with the best accordance between the modeling results and experimental data. Thus the model can serve as an efficient method to obtain the actual characteristics of the simulated system.

From 1970 to the 1980s the majority of photosynthetic studies were conducted using fractioned fragments of pigment–protein complexes of green plants and bacterial photosynthetic reaction centers. Isolated fragments are rather simple compared to the native photosynthetic chloroplast membrane, let alone the whole cell.

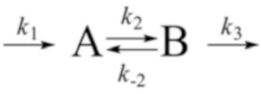
To simulate electron transfer processes in such isolated complexes, comparatively simple models can be constructed, and these models make it much easier to carry out the procedure of parameter identification. Due to studies on photosynthetic reaction center fragments, the rate constants of elementary redox reactions involved in the photosynthetic electron transport chain have been established.

Obviously, the question remains as to whether the values of the reaction rates thus evaluated in studies of isolated photosystem fragments in solution correspond to those in native objects. We shall discuss this problem later in more detail.

Kinetic Description of Redox Reactions in Solution

For the kinetic description of redox reactions proceeding in solution, equations based on the mass action law are traditionally used. Let there be molecules of substances A and B in solution. Let us suggest they can be found in one of the two states, reduced and oxidized, and between these two types of molecules electron exchange is possible. The corresponding reduction–oxidation reaction can be presented as Scheme 9.1.

Scheme 9.1



Here k_1 is the rate constant of the electron influx into A from the outer source, k_2 and k_{-2} are rate constants of the direct and reverse reactions of the electron transfer from the A molecule to the B molecule, and k_3 is the rate constant of the electron outflux from the molecules of the B type to the outer acceptor.

The reduced form of the molecule, i.e., the form with an electron, is designated by the superscript "–", and the oxidized form in the absence of an electron is designated by the superscript "+". The total concentration of each of substances A and B in oxidized and reduced forms during the reaction is considered to remain constant:

$$[A^+] + [A^-] = [A]_0, \quad [B^+] + [B^-] + [B]_0, \tag{9.1}$$

The equations describing the reaction of the electron transfer from the A molecules to the B molecules according to Scheme 9.1 are

$$\begin{aligned}\frac{d[A^-]}{dt} &= k_1[A^+] - k_2[A^-][B^+] + k_{-2}[B^-][A^+],\\ \frac{d[B^-]}{dt} &= k_2[A^-][B^+] - k_{-2}[B^-][A^+] - k_3[B].\end{aligned} \tag{9.2}$$

The validity of the mass action law implies that each of the reduced molecules A^- of donor A can interact with each of the oxidized B^+ molecules of acceptor B. This approach is based on the postulates of statistical physics and is valid if the reduced donor and oxidized acceptor molecules interact via random collisions in solution.

For the reaction (an electron transfer from the donor to the acceptor) to occur, the formation of a complex, in which an electron tunneling from the reaction center of the donor to the reaction center of the acceptor, is necessary. The rate constant of the formation of a complex between two molecules interacting according to the mass action law is easy to calculate for the irreversible reaction of two substances whose initial concentrations are equal: $[A]_0 = [B]_0 = N_0$.

Let us consider the simple bimolecular reaction between A and B, during which the complex C is formed. Each of the substances at each time moment can either be free (concentrations $[A(t)]$, $[B(t)]$) or bound in the complex (concentration $[C(t)]$):

$$\mathrm{A} + \mathrm{B} \xrightarrow{k} \mathrm{C}.$$

Thus, a number of free molecules of each type equals the difference between the total number of molecules of this type and the number of molecules bound in the complex: $[A] = [B] = N_0 - [C]$.

The corresponding kinetic equation describing the rate of complex formation is

$$\frac{dC}{dt} = k \cdot (N_0 - C)^2.$$

Here C is a number of generated complexes, N_0 the initial number of A and B molecules, and k the rate constant of the reaction. Integrating this equation, we obtain the hyperbolic function of time:

$$C(t) = N_0 - \frac{N_0}{N_0 kt + 1}.$$

However, in general, photosynthetic redox reactions are rather peculiar. Most of them proceed in multienzyme photosynthetic reaction complexes embedded in the photosynthetic membrane (see Figs. 9.1, 9.2, and 9.3). In these complexes the components of the photosynthetic electron transport chain are arranged in strict order, and the electron transfer between individual carriers occurs along the

electron path. An electron can be transferred from the reduced donor to the oxidized acceptor only if both of them are included in one multienzyme complex of PSI, PSII, or a cytochrome complex. In this case we cannot assume that free and random collisions of the molecules occur as happens in solution.

For an adequate description of the processes in a complex the following mathematical approach is used. The reaction involves transitions between possible states of a multienzyme complex that differ from each other with respect to the presence or absence of the charge on the individual carrier included in the complex. Malkin (1971) and Sorokin (1973) were the first to use this approach independently to describe the electron transfer in PSII. One monograph (Rubin and Shinkarev 1984) describes the mathematical background and methods of the analysis of electron transfer in biological multienzyme complexes. The book by Riznichenko (1991) is devoted to the application of this method to describing electron transport processes in isolated complexes of PSI, PSII, and bacterial reaction centers.

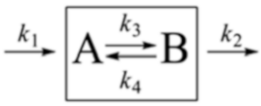
Modeling Electron Transfer in a Multienzyme Complex

Systems of ODEs, where variables are probabilities of the states of the complex (master equations), are used to describe electron transfer in multienzyme complexes. Equations of this type can be used to describe different processes, for instance, transitions between different conformational states of an enzyme. As an example, let us consider a complex consisting of two electron carriers, each of which can exist in two states—oxidized (without an electron) and reduced (with an electron).

Electron Transfer in a Two-Component Complex

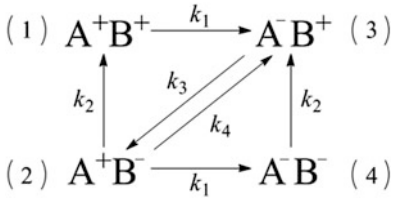
Let us consider two components, A and B, composing a complex. These components, depending on their redox state, can exchange electrons (the rate constants of the direct and reverse reactions are k_3 and k_4). Also, an influx of electrons into the complex from the outside (rate constant k_1) is possible, as is an outflux of electrons from the complex (k_2). Scheme (9.2) of the processes is as follows:

Scheme 9.2



If each component of the complex can be presented in two states—oxidized A^+ and B^+ or reduced A^- and B^-, then to describe the redox states of the complex [AB], we need to consider four possible states of the pair of carriers (Scheme 9.3):

Scheme 9.3



The arrows in the scheme designate the possible transitions between the states. The electron transfer from donor A to acceptor B occurs only if carrier A is in the reduced form and B is in the oxidized form [state (3)–state (2) transition]. The rate of the electron transfer from A to B is proportional to the probability p_3 of the state $[A^-B^+]$.

Let us introduce the state probabilities $p_i(t)$, $i = \overline{1,4}$. The constants of the direct and reverse transition between the states correspond to first-order reactions. Differential equations of the evolution of the state probabilities $p_i(t)$ are linear with respect to the complex state probabilities and can be written as follows:

$$\begin{aligned}
\frac{dp_1}{dt} &= -k_1 p_1 + k_2 p_2, \\
\frac{dp_2}{dt} &= -(k_4 + k_1 + k_2) p_2 + k_3 p_3, \\
\frac{dp_3}{dt} &= -k_3 p_3 + k_1 p_1 + k_4 p_2 + k_2 p_4, \\
\frac{dp_4}{dt} &= -k_2 p_4 + k_2 p_2.
\end{aligned} \tag{9.3}$$

If events (1)–(4) are incompatible (mutually exclusive) and form the total of possible states of the [AB] complex, then the following equality is true:

$$\sum_{i=1}^{4} p_i(t) = 1.$$

The initial values of the variables are determined by experimental conditions. To pass from $p_i(t)$ as the solutions of system (9.3) to the experimentally observed concentration values of carriers A and B in reduced or oxidized forms, we must add the probabilities of the complex states in which a particular carrier exists in a particular state. For example, the probability that carrier A will be oxidized is equal to the sum of probabilities of the first and second states of the complex:

$$P(A^+) = p_1 + p_2.$$

Such a description of the electron transfer in the complex allows us to take into account the rate constant dependencies on the states of carriers and on the rates of

the electron transitions that do not take part directly in the redox reaction. For example, for Scheme 9.3 we can consider the dependence of the electron influx to component A (rate constant k_1) on the degree of the reduction of component B. This may be very important because at the molecular level electrostatic interactions play a considerable role and influence the rate of direct electron transfer.

Electron Transfer in an *n*-Carrier Complex

Let us consider a complex consisting of several components $C_i (i = 1, \ldots, n)$. Such complexes are embedded into the photosynthetic membrane as PSI, PSII, and cytochrome complexes (Figs. 9.2 and 9.3).

Similar complexes operate in mitochondria membranes, where they also play the key role in the electron transfer reactions.

According to the master equation approach the state of a complex consisting of n components $C_1, C_2, \ldots, C_n$ (depicted in square brackets)

$$\rightarrow [C_1, C_2, \ldots, C_n] \rightarrow \tag{9.4}$$

is considered as a consecutive order of different states of electron carriers C_i, included in the complex. Transitions between the states are described by ODEs, which are linear with respect to probabilities of the corresponding states:

$$\frac{dp_i}{dt} = \sum_{j=1}^{l} \left(p_j k_{ji} - p_i k_{ij} \right). \tag{9.5}$$

Here p_i is the probability to find the complex in the i-th state; k_{ij}—the rate constant of the transition from the i-th to the j-th state. Under the sum there is a difference between the probabilities of transitions to the i-th state from all other states (positive term) and the probability of the transitions from i-th state to all other states (negative term). The initial probabilities are

$$p_i(0) = b, \quad i = 1, \ldots, l.$$

In vector form the equations (9.5) can be written as:

$$\frac{dP}{dt} = K^{\mathrm{T}} P, \quad P(0) = B. \tag{9.6}$$

Here P is a vector of probabilities of all states of the complex under consideration, B—a vector of the initial states, K^{T}—transposed matrix of the rate constants of transitions between the states.

The probability to find the carrier q in the certain state G is presented as:

$$P_q(G) = \sum_{S_q \in G} p(S_q, t). \tag{9.7}$$

Here we sum over all states S_q, where the q-th component is present in the state G.

Thus p_i corresponds to the fraction of the complexes in the i-th state. To obtain the total concentration of complexes in the i-th state it is necessary to multiply p_i by the total concentration of all complexes $[C_1, C_2, \ldots, C_n]$. To find the probability of the carrier to be in a certain state (oxidized, reduced, etc.) it is necessary to sum all probabilities to find the complex in all states, in which the carrier exists in this certain state. The resulting sum will be equal to the fraction of that carrier found in this particular state. To find the concentration of a specific carrier in a specific state we multiply the value of the final integrated probability by the total concentration of the complexes.

The rate constants k_{ij} of the transitions between the states may not be constant values, but may depend on the state of the whole complex (for example, location in the stromal or in the granal part of a thylakoid) as well as on other variables or parameters of the system: temperature, transmembrane potential, external electric field, etc. Thus the system of differential equations, describing the transitions between the states in a real photosynthetic complex, is usually nonlinear.

The ODE system has the number of dimensions:

$$l = \prod_{j=1}^{n} m_j, \tag{9.8}$$

where m_j is the number of possible states of the j-th carrier, and n is the number of components of the complex. If each component can exist in two states—oxidized and reduced—the total number of the states is 2^n. Taking into account that photosynthetic reaction centers can contain five or more electron carriers (see Figs. 9.2 and 9.3) and some of them can be presented in three states (for instance, photoactive chlorophyll can be neutral, excited, and reduced), the total number of the states becomes rather large. The number of the states can be reduced under special experimental conditions, for example if the complex is closed and contains fixed number of electrons. This can be true if the experiment is performed on the isolated complexes at low temperatures when the electron exchange with the environment is impossible. In case of a single short laser flash we can consider only the relaxation processes proceeding after the flash. We can obtain some simplifications of the graph of the states if we take into account the time hierarchy of the fast steps of the processes in the system according to the A.N. Tikhonov's theorem (Tikhonov 1952) and substitute corresponding ODE by algebraic equations. Sometimes it is advisable to substitute several one-electron carriers with a single multielectron carrier. All these methods are used to simulate different photosynthetic processes.

Electron Transport via Mobile Carriers

In a real photosynthetic chain there are multienzyme complexes as well as electron paths, where electron transport occurs via mobile carriers (plastocyanin Pc in lumina, plasoquinone PQ inside the membrane, ferredoxin Fd in the stromal space). The evolution of the redox states of these mobile carriers in the majority of the models so far has been described by means of the mass action law.

Below we shall show that it is not always valid, because the movement of the mobile molecules in the photosynthetic membrane is restricted so that the assumption of free diffusion, which is the basis of the mass action law does not hold true. But the mass action law is quite adequate if we describe the interactions of isolated reaction center complexes with mobile donors and acceptors in solution. If the rate of the reaction is determined by the probability of collision of the complex with donor and acceptor molecules, added to the solution, such reaction is "diffusion controlled."

The diffusion controlled step of the electron transfer between the complex $[C_1,C_2, \ldots,C_n]$ and the mobile carrier D can be presented in a simple scheme:

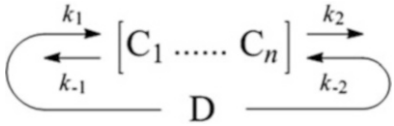
$$\Rightarrow [\mathrm{C_1C_2 \ldots C}_n] \underset{k_{-out}}{\overset{k_{out}}{\rightleftarrows}} \mathrm{D} \xrightarrow{K}$$

Changes of the concentration of the mobile carrier D in the reduced form can be described by the mass action law equation:

$$\frac{d[D^-]}{dt} = k_{\text{out}}[C_n{}^-][D^+] - k_{-\text{out}}[C_n{}^+][D^-] - K[D^-] \tag{9.9}$$

Here $[D^+]$, $[D^-]$ are concentrations of the mobile carrier in the oxidized and reduced forms. $[D^+] + [D^-] = [D_0]$, where $[D_0]$ is the total concentration of the mobile carrier; $[C_n{}^+]$ and $[C_n{}^-]$ are concentrations of the components of the complex which interact with the mobile carrier in the oxidized and reduced forms, calculated according to (4); k_{out} and $k_{\text{-out}}$ are the bimolecular rate constants of the redox reaction between the complex $[C_1,C_2, \ldots,C_n]$ and the mobile carrier D; K is the rate constant of the electron outflow from the mobile carrier D.

Let the mobile carrier generate cyclic transport around the complex $[C_1, C_2, \ldots, C_n]$, by taking electrons at the acceptor side (C_n) and donating electrons to the donor side (C_1) of the complex. In experiments on the PSI fragments to generate cyclic transport an intermediate ascorbate is often used. Interactions of the complex $[C_1, C_2, \ldots, C_n]$ with the mobile carrier D can be presented in Scheme 9.4:



Scheme 9.4

The equation for the evolution of the mobile carrier D concentration in the reduced form is:

$$\frac{d[D^-]}{dt} = k_2\left[C_n^-\right][D^+] - k_{-2}[D^-]\left[C_n^+\right] - k_1[D^-]\left[C_1^+\right] + k_{-1}\left[C_1^-\right][D^+]. \quad (9.10)$$

Here k_i—bimolecular rate constants of the reactions, concentration values $[C_i]$ can be obtained according to formula (3.1.5.) as the solutions of the ODE system for the state probabilities of the complex $k_{\text{in}} \leftrightarrow [C_1, C_2, \ldots, C_n] \leftrightarrow k_{\text{out}}$.

The values of the parameters k_{in}, $k_{-\text{in}}$, k_{out}, and $k_{-\text{out}}$, which characterize the electron influx into and outflux out of the complex, are determined by the portion of the oxidized molecules of the mobile carrier D:

$$k_{\text{in}} = k_1[D^-], \quad k_{-\text{in}} = k_{-1}[D^+],$$

$$k_{\text{out}} = k_2[D^+], \quad k_{-\text{out}} = k_{-2}[D^-].$$

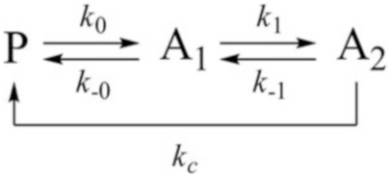
The full system, including electron transport inside the complex as well as the interactions with environmental donors and acceptors, is described by a nonlinear ODE system of large dimensions.

The problem of identification is to find the system parameters k_i that provide the best fit between results of the simulation and experimental data. The initial conditions of the model are determined by the redox state of the surrounding media and light intensity and shall be determined additionally as parameters of the model.

Let us consider models of two simple systems as a base for complex models of electron transport processes in photosynthetic objects.

Electron Transport in an Isolated Photosynthetic Reaction Center

Let us consider an isolated electron transport chain of the photosynthetic reaction center consisting of the photoactive pigment P and two acceptors, A_1 and A_2, existing in the neutral form in the dark: P^0, $A_1{}^0$, $A_2{}^0$. Under illumination P becomes oxidized P^+, while the acceptors become reduced $A_1{}^-$, $A_2{}^-$. Scheme 9.5 of the electron fluxes is as follows:

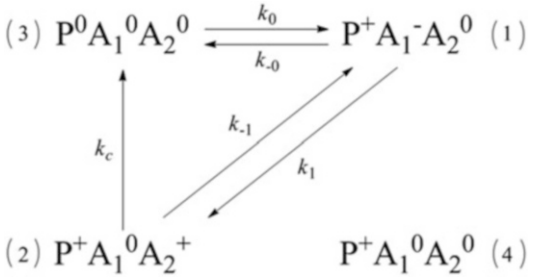


Scheme 9.5

Here k_0 and k_{-0} are rate constants of the forward and backward reactions of the charge separation initiated by illumination, k_1 and k_{-1} are rate constants of the forward and backward reactions of the electron transfer between the first and second acceptors, and k_c is a rate constant of the cyclic electron flow. If there is no electron exchange between the system and the environment, the system will contain only one electron. The insularity of the system decreases the number of its possible states.

The graph of the system states is as follows (Scheme 9.6):

Scheme 9.6



The ODE system for Scheme 9.6 is as follows:

$$\begin{aligned}
\frac{dp_1}{dt} &= k_0 p_3 - (k_{-0} + k_1)p_1 + k_{-1}p_2,\\
\frac{dp_2}{dt} &= k_1 p_1 - (k_c + k_{-1})p_2,\\
\frac{dp_3}{dt} &= -k_0 p_3 + k_c p_2 + k_{-0} p_1,\\
p_1 + p_2 + p_3 &= 1.
\end{aligned} \tag{9.11}$$

The last algebraic equation corresponds to the isolation of the system. Taking into account this condition, we can reduce the system to two ODEs:

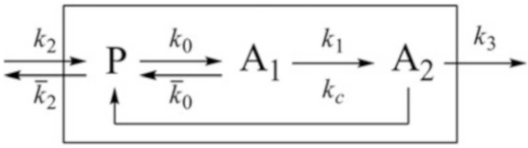
$$\begin{aligned}
\frac{dp_1}{dt} &= k_0 - (k_0 + k_{-0} + k_1)p_1 + \big(k_{-0} - k_0\big)p_2,\\
\frac{dp_2}{dt} &= k_1 p_2 - (k_c + k_{-1})p_2.
\end{aligned} \tag{9.12}$$

System (9.12) can be solved analytically if the initial conditions are known.

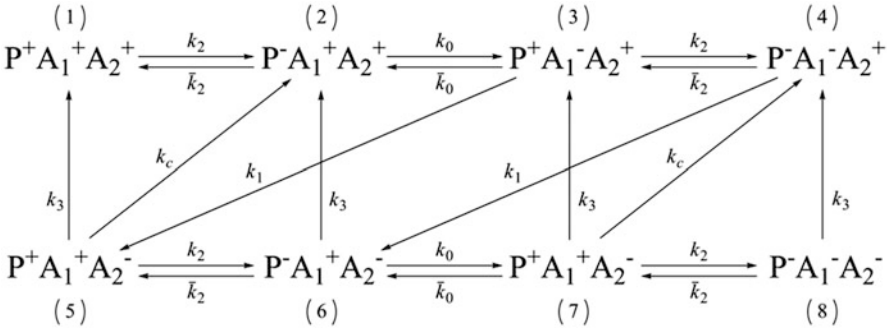
In experiments, the insularity of the system can be provided by particular redox conditions or by means of inhibitors. When illumination is provided by a short laser flash, electron transport reactions in the photosynthetic reaction center occur much more rapidly than the reactions of electron exchange with the outer donors and acceptors, and the system can also be considered a closed one.

If the electron exchange between the system and the environment is possible (Scheme 9.7), then the complex can contain as many as three electrons:

Scheme 9.7



The graph of the states of the complex contains eight states (Scheme 9.8):



Scheme 9.8

The corresponding model consists of eight ODEs. In other cases, one of the equations can be substituted by an algebraic equation that corresponds to the condition when the total sum of all probabilities equals one. In what follows we will consider more realistic mathematical models used to identify the rate constants of individual reactions and to characterize states of the photosynthetic apparatus.

Chapter 10
Kinetic Model of Interaction of Two Photosystems

There are two different types of photosynthetic electron transport reaction. The first type refers to the electron transfer inside multienzyme PSI, PSII, and Cyt b_6f complexes that are embedded in the photosynthetic membrane. Here an electron tunnels from one electron carrier to the other along the electron path. The second type of reaction includes an influx and outflux of electrons via complexes that are mediated by mobile electron carriers.

Types of Regulation of Photosynthetic Processes

Identification of the model parameters on the basis of experimental data shows that regulatory mechanisms operating inside and outside of photosynthetic multienzyme complexes are rather different (Riznichenko 1991; Riznichenko et al. 1999; Rubin and Riznichenko 2009).

Multienzyme complexes are very stable in their functional and structural organization and retain their kinetic characteristics in a wide range of environmental conditions. The main regulatory factor in PSII and PSI complexes is light intensity. Light quantum absorption leads to charge redistribution in the primary photosynthetic pair followed by conformational changes in the protein components, which prevent backward electron transport and energy losses. In all types of the investigated isolated systems—fragments of photosystems I and II, chromatophores and various species of bacterial reaction centers—illumination brings about changes in the parameters of electron transport within one order of magnitude. This results in an increase in efficiency of the electron flow from the reaction center to the primary acceptor. Obviously, the mechanism of light regulation plays a role analogous to allosteric regulation in enzyme catalysis, which is performed through conformational transformations of a protein globule.

It must be pointed out that the rate constants at the electron transfer inside the photosynthetic reaction center are influenced by the electric field, as evidenced in

A. Rubin and G. Riznichenko, *Mathematical Biophysics*, Biological and Medical Physics, Biomedical Engineering, DOI 10.1007/978-1-4614-8702-9_10,
© Springer Science+Business Media New York 2014

Parson et al. (1990), Zheng et al. (1990), and Dau and Sauer (1992). This means that the rate parameters' values depend on the transmembrane electric field ($\Delta\varphi$). However, when modeling the processes in isolated reaction centers it is not necessary to take this into account because during the process of isolation the thylakoid membrane is destroyed. But the dependence of the rate parameters on the transmembrane electric field becomes very important if the models of photosynthetic reaction centers are introduced as elements of the generalized model of the full system of primary photosynthetic reactions in the thylakoid (Lebedeva et al. 2000; Belyaeva et al. 2003, 2008).

The second type of regulation operates on the level of input and output fluxes through the complexes, through interactions of the molecular complexes with mobile carriers. One example is provided by the interaction of the PSII complex with the cytochrome b_6f complex via plastoquinone and interaction of the cytochrome complex with the PSI complex via plastocyanin (Fig. 9.2). At these electron chain steps diffusion parameters play the main role and often determine the total efficiency of the electron transport. Identification of the corresponding parameters shows that the range of their changes under different conditions (pH, redox conditions, viscosity) is of several orders of magnitude. We shall also discuss in Part IV their dependence on the geometry of the reaction volume. Electron fluxes here are controlled by, for example, intercellular regulating factors, endogenous inhibitors, and metabolites.

From the kinetic modeling viewpoint the input and output rates determine the steady-state values of internal variables and influence their kinetics. Thus, signals registered by spectral methods reflect the kinetic characteristics of the reaction center components and at the same time provide information about the processes, proceeding in photosynthetic surroundings far from the reaction centers. An adequate quantitative analysis of this information is impossible without mathematical formalization of the data on the organization of photosynthetic processes. Simulation of different processes in the integrated system requires different mathematical and computer approaches.

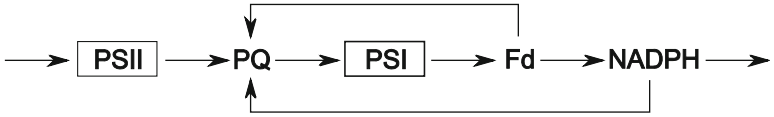
Selection of the details of the simulated processes to be included in the model depends on the aim of the research. To study the mechanisms of electron transport, energy dissipation, and conformation changes inside photosynthetic reaction centers, detailed models are necessary. On the other hand, to simulate the main features of the primary photosynthetic processes, organic synthesis, and metabolism of a living cell, a simplified dynamic model can be used. In this chapter we shall construct a simplified model describing the interactions between the two photosystems.

Model of PSI and PSII Interaction

In Fig. 9.2 protein complexes and mobile carriers that form the electron transport chain are shown. In the previous chapter we discussed their role in detail. The main energy-transducing components are PSI and PSII, which are complex multienzyme structures. Their interaction is mediated by a plastoquinone (PQ) pool, a cytochrome b_6f complex (Cyt b_6f), and mobile plastocyanine (Pc) molecules.

As a result of linear electron transport from water the reduced nicotinamide adenine dinucleotide phosphate (NADH) is generated which is one of the main cofactors in the carbon fixation cycle (Calvin cycle)—takes place. Cyclic electron transport from the acceptor side from PSI backward to the PQ pool is also possible. The cyclic path, as well as the linear path, is coupled to the proton transfer across the thylakoid membrane. The generated electrochemical proton gradient is consumed by ATP–synthase for ATP production.

Let us consider a simplified scheme that includes two photosystems, PSI and PSII, a quinone pool located between them, and mobile carriers interacting with the acceptor side of PSI—Fd and NADPH—which also serve as intermediates of the cyclic electron transport around PSI. Let us take into account the fact that the cyclic electron transport to PQ can be performed in two ways: directly from Fd or with the participation of NADPH (Scheme 10.1). The frames around PSII and PSI indicate that both of them are multicomponent complexes:



Scheme 10.1

Now we shall construct a model corresponding to Scheme 10.1. A corresponding simplified model allows us to study the effects of electron transport steps on the characteristics of kinetic curves observed in experiments. In the constructed simplified model, we simulate some real chains of consecutive reactions where the total rate is determined by the slowest step in the full chain.

The model can be presented as a sum of subsystems: complexes of PSII and PSI, including electron transfer inside them. The latter will be simulated by ODEs for the probabilities of the states of these complexes and a subsystem of mobile carriers whose interactions with complexes are described by means of the mass action law formalism.

To evaluate the adequacy of the model, we compare the results of simulation with the experimental data. Most often in the experiments, fluorescence induction curves and kinetic curves corresponding to the oxidation of photoactive PSI pigment P_{700}^{+} are observed. Excited chlorophyll molecules of PSII comprise the source of fluorescence. These data are obtained using spectral methods: absorption spectroscopy (at 820–840 nm) and electron paramagnetic resonance (EPR). Below we shall compare the results of the simulation with these two sets of experimental data.

Subsystem PSII

PSII can be presented as the sum of donor (P_{680}) and acceptor (Q) parts. Light-excited chlorophyll P_{680} passes electrons to the acceptor part and thus P680 becomes oxidized. The reduction of the oxidized P_{680} occurs due to the water oxidizing complex (WOC) (see Fig. 10.1).

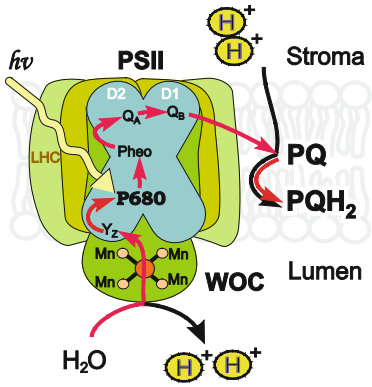


Fig. 10.1 Scheme of electron transport inside PSII

The acceptor part of PSII includes many electron carriers: pheophytin (Pheo), primary quinone acceptor (Q_A), and secondary quinone acceptor (Q_B), which is a PQ molecule anchored at the stromal side of PSII. In the next chapter, Chap. 11, we shall consider the details of the electron transport chain of PSII. Here, in constructing the simplified model, we consider the PSII complex as a donor–acceptor pair, a complex consisting of two components—a donor P_{680} containing all donor components and an acceptor Q containing all acceptor components.

The donor component P_{680} can exist in the two redox states: a neutral state, P^0_{680}, in which the transfer of an electron to the acceptor side is possible, and an oxidized state, P^+_{680}. In the latter, the electron flux into the complex occurs. The reduction of P^+_{680} by donor components corresponds to the transfer of P_{680} to the neutral state P^0_{680}.

The acceptor component Q in the neutral state (Q^0) takes an electron from P^0_{680} (process of charge separation), and after that Q^- (in reduced form) gives electrons to the PQ pool.

Scheme of PSII States

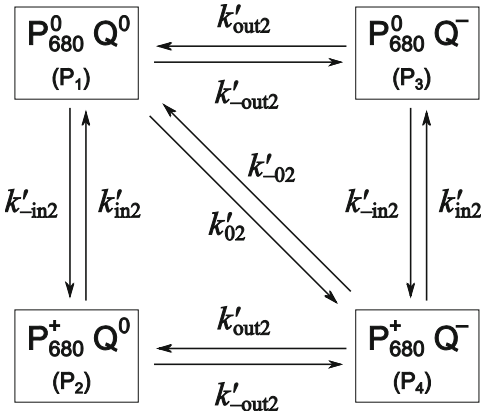
At any given moment each of the PSII complexes can be only in one of four states: 1 *II* $[P^0_{680}\ Q^0]$, 2 *II* $[P^+_{680}\ Q^0]$, 3 *II* $[P^0_{680}\ Q^-]$, 4 *II* $[P^+_{680}\ Q^-]$.

The probability P_k ($k = 1 \div 4$) that the population of PSII complexes will be in one of the states 1 *II*, 2 *II*, 3 *II*, or 4 *II* is equal to the ratio of complex concentration in the corresponding state to the total concentration of the complexes:

$$P_{1II} = \frac{[P^0_{680}\ Q^0]}{[P_{680}\ Q]_0}, \quad P_{2II} = \frac{[P^+_{680}\ Q^0]}{[P_{680}\ Q]_0},$$
$$P_{3II} = \frac{[P^0_{680}\ Q^-]}{[P_{680}\ Q]_0}, \quad P_{4II} = \frac{[P^0_{680}\ Q^-]}{[P_{680}\ Q]_0}. \tag{10.1}$$

The sum of state probabilities is $\sum_k 1^k = 4 P_{kII} = 1$.

Electron transfer in a PSII complex is described as a transition between states. The initial values of the state population are determined by experimental conditions. The scheme of the transition between the states of PSII corresponding to electron transfer is presented in Scheme 10.2.



Scheme 10.2

Monomolecular rate constants are designated by apostrophes.

Charge Separation

In biological systems, charge separation is a result of a sequence of the following processes: light absorption by antenna pigment molecules, energy migration inside the antennae of the light-harvesting complex, energy trapping by the photoactive P_{680} pigment, electron transfer from P_{680} to pheophytin and further to the primary and secondary quinone acceptors. In the model, all processes are combined into one step of transition from state P_{1II} to state P_{4II} with the effective rate constant k'_{02}.

The value of the effective rate constant is determined by the slowest step: an act of charge separation whose frequency is determined by the frequency of light quanta hitting the light-harvesting antennae and by the effective absorption cross-chapter area of the antenna complex. The antenna dimensions can be changed by illumination due to the processes of spillover (transition of Chl antenna molecules from PSII to PSI), which are accompanied by changes in the composition of carotenoids included in the antenna. The value of k'_{02} changes correspondingly, but these modifications occur at a much slower rate (minutes) compared to electron transfer along the photosynthetic chain.

The reverse transfer from state P_{4II} to state P_{1II} is described by the rate constant k'_{-02}. This transfer corresponds to irradiative and nonirradiative charge recombination.

Electron transfer to PSII complex In a real system, Mn-containing clusters of WOC and tyrosine (Tyr or Z) take part in the reduction of the oxidized P^{+}_{680}. The processes involve the S-cycle of water oxidation and the subsequent electron transfer to Tyr. In our simplified model, all these steps are included in one transition step from state P_{1II} to state P_{2II} and from the state P_{4II} to the state P_{3II} with rate constant k'_{in2}. The S-cycle activity is the slowest step of P^{+}_{680} reduction; characteristic times of individual steps of the S-cycle are 0.01–0.3 s. The corresponding rate constant k_{in2} equals 3–100 s^{-1}. The reverse electron flux from P_{680} is characterized by the rate constant $k'_{-\text{in2}}$.

Electron transfer from PSII to PQ pool In real systems, PSII gives two electrons in succession to the PQ molecule, which is anchored at the stromal site (the so-called Q_B site) of PSII. Supposedly a two-electron process takes place. The reception of each of the electrons by PQ is coupled to the capture of one proton from the stromal space. In the PQH_2 form, reduced PQ can leave the stromal site of PSII and diffuse freely inside the membrane. Anchored at the luminal site of the cytochrome b_6f complex, PQH_2 transports two electrons to the complex and releases two protons into the luminal space of the thylakoid.

In our model, we suggest that PQ molecules can exist in two forms: neutral (PQ) and reduced (PQ^{-}). All the processes described previously are combined into one step of transition from the reduced acceptor Q (states P_{3II} and P_{4II}) of PSII to the mobile component PQ with the rate constant k_{out2}. We simulate PSII interaction with the mobile carriers according to the mass action law. The parameter k_{out2} corresponds to the outflow of electrons from PSII, and $k_{-\text{out2}}$ corresponds to the reverse process (return of electrons to PSII).

The electron outflow from the complex is determined by the first-order rate constant k'_{out2}. The bimolecular rate constant k_{out2} (interaction of Q^{-} with PQ) is related to the monomolecular constant k'_{out2} in the following way: $k'_{\text{out2}} = k_{\text{out2}}[PQ^0]$. The relationship between the rate constants of the reverse reaction $k_{-\text{out2}}$ and k'_{out2} is $k'_{\text{out2}} = k_{-\text{out2}}[PQ^{-}]$.

We consider the total number of molecules in the pool to be constant: $[PQ] + [PQ^{-}] = [PQ]_0$. The number of PQ molecules in the pool is α times greater than the number of P_{680} molecules: $[PQ]_0 = \alpha[P_{680}]_0$.

The ODEs for the PSII state probabilities are as follows:

$$
\begin{aligned}
\frac{dP_{1II}}{dt} &= -\left(k'_{-\text{out2}} + k_{-\text{in2}} + k'_{02}\right)P_{1II} + k'_{\text{in2}}P_{1II} + k'_{\text{out2}}P_{3II} + k'_{-02}P_{4II},\\
\frac{dP_{2II}}{dt} &= k'_{-\text{in2}} \cdot P_{1II} - \left(k'_{\text{in2}} + k'_{-\text{out2}}\right)P_{2II} + k'_{\text{out2}}P_{4II},\\
\frac{dP_{3II}}{dt} &= k'_{-\text{out2}}P_{1II} - \left(k'_{\text{out2}} + k'_{-\text{in2}}\right)P_{3II} + k'_{\text{in2}}P_{4II},\\
\frac{dP_{4II}}{dt} &= k'_{02}P_{1II} + k'_{-\text{out2}}P_{2II} + k'_{-\text{in2}} \cdot P_{3II} - \left(k'_{\text{in2}} + k'_{-02} + k'_{\text{out2}}\right)P_{4II}.
\end{aligned}
\tag{10.2}
$$

The concentration of the carrier P_{680} in neutral and oxidized states and the concentration of the carrier Q in neutral and reduced states can be expressed as the sums of probabilities of the complex states, in which a particular carrier is presented in the corresponding redox state. The total concentration $[P_{680}]_0$ is the same for the donor and acceptor components:

$$\begin{aligned} \left[P^0_{680}\right] &= [P_{680}]_0(P_{1II} + P_{3II}), \quad \left[P^0_{680}\right] = [P_{680}]_0\left(P_{2II} + P_{4II}\right), \\ \left[Q^0\right] &= [P_{680}]_0(P_{1II} + P_{2II}), \quad [Q^-] = [P_{680}]_0\left(P_{3II} + P_{4II}\right). \end{aligned} \tag{10.3}$$

Submodel of PSI

The donor side of PSI is represented by the binding site for Pc, which serves as an electron donor for PSI. The acceptor side of PSI is constituted by a sequence of carriers transporting an electron from the chlorophyll of PSI P_{700} to Fd: special chlorophyll a (A_0), phylloquinone (A_1), and iron-sulfur centers $F_x - F_a - F_b$.

As in the case of PSII, we shall not consider the details of electron transport inside PSI. The donor side of PSI is represented by a photoactive pigment P_{700}, which can be in the neutral (P^0_{700}) or oxidized (P^+_{700}) state. The acceptor side of PSI is represented by an acceptor A, which can be in the neutral (A^0) or reduced (A^-) state. In the neutral state (A^0), the acceptor takes an electron from P_{700}, and in the reduced state (A^-), it transfers an electron to Fd.

At each moment, any of the PSI complexes can be present in one of the four different states with the following probabilities:

$$\begin{aligned} P_{1I} &= \frac{\left[P^0_{700}\ A^0\right]}{[PA]_0}, \quad P_{2I} = \frac{\left[P^+_{700}\ A^0\right]}{[PA]_0}, \\ P_{3I} &= \frac{\left[P^0_{700}\ A^-\right]}{[PA]_0}, \quad P_{4I} = \frac{\left[P^+_{700}\ A^-\right]}{[PA]_0}, \end{aligned} \tag{10.4}$$

where $[PA]_0$ is the total concentration of PSI complexes. The sum of the state probabilities is $\sum_{i=1}^{n=1} P_{nI} = 1$. Similar to PSII, the evolution of the PSI complex state is described by an ODE system for the transitions between states (Scheme 10.3).

Electron transfer to PSI In reality, electron transfer from PSII to PSI includes transfer steps from PQH_2 (coupled to the release of protons into the lumen) to the cytochrome b_6f complex and subsequent transfer of an electron from the cytochrome b_6f complex to PSI by Pc. Pc picks up an electron from the Cyt f subunit of the cytochrome b_6f complex and diffuses in the luminal space of the thylakoid. When it anchors itself at the luminal site of PSI, transfer of the electron to the oxidized photoactive PSI pigment P_{700} takes place. The detailed kinetic model of

cytochrome complex operation will be described in Chap. 12. The details of Pc interaction with PSI complexes will be considered in Chap. 14.

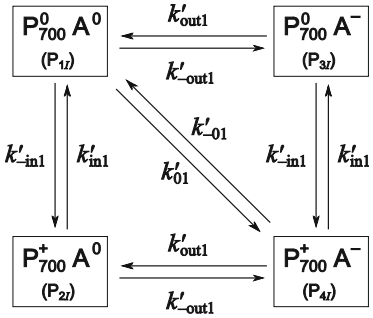
In the simplified model we are constructing now, all processes discussed earlier are combined in one step: the PQ molecule gives an electron directly to PSI. The reduction of P_{700} follows the mass action law, whereas an electron influx is proportional to the production of PQ molecules in the reduced form $[PQ^-]$ and the concentration of P_{700} in the oxidized form $[P^+_{700}]$. The reverse electron flux from PSI to PSII is neglected.

We describe electron transport from PSI to the mobile acceptors Fd and NADPH according to the mass action law. A cyclic electron flux around PSI can proceed directly from Fd to PQ or with the participation of NADPH.

The parameter $k'_{\text{out1}} = k_{\text{out1}} \cdot [\text{Fd}]$ characterizes the outflow from PSI, and the rate constant of the reverse reaction is $k'_{\text{out1}} = k_{-\text{ out1}} \cdot [\text{Fd}^-]$. Fd can be presented in neutral and reduced forms:

$$\left[\text{Fd}^0\right] + [\text{Fd}^-] = [\text{Fd}]_0.$$

The number of Fd molecules is β times greater than the number of PSI complexes: $[\text{Fd}]_0 = \beta[\text{P}_{700}]_0$. The scheme of state transitions of PSI and electron transfer ways in PSI are presented in Scheme 10.3 and Fig. 10.2.



Scheme 10.3

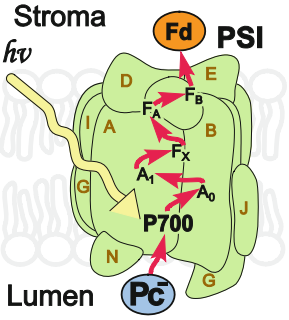


Fig. 10.2 Scheme of electron transport inside PSI

The ODE system for the state probabilities' evolution for PSI is as follows:

$$\begin{aligned}
\frac{dP_{1I}}{dt} &= -P_{1I}\left(k'_{-\text{out1}} + k'_{01} + k'_{-\text{in1}}\right) + k'_{\text{in1}}P_{2I} + k'_{\text{out1}}P_{3I} + k'_{-01}\cdot P_{4I},\\
\frac{dP_{2I}}{dt} &= k'_{-\text{in1}}P_{1I} - \left(k'_{\text{in1}} + k'_{-\text{out1}}\right) + k'_{\text{out1}}P_{4I},\\
\frac{dP_{3I}}{dt} &= k'_{-\text{out1}}P_{1I} - \left(k'_{\text{out1}} + k'_{-\text{in1}}\right)P_{3I} + k'_{\text{in1}}P_{4I},\\
\frac{dP_{4I}}{dt} &= k_{01}P_{1I} + k'_{-\text{out1}}P_{2I} + k'_{-\text{in1}}P_{3I} - \left(k'_{\text{out1}} + k'_{\text{in1}} + k'_{-01}\right)P_{4I}.
\end{aligned} \tag{10.5}$$

The concentration of the photoactive pigment P_{700} in the reduced form, which determines the intensity of the EPR signal, is given by

$$\left[P^{+}_{700}\right] = [P_{700}]_0(P_{2I} + P_{4I}). \tag{10.6}$$

The concentration of P_{700} in the neutral form is given by

$$\left[P^{0}_{700}\right] = [P_{700}]_0(P_{1I} + P_{3I}). \tag{10.7}$$

Obviously, the concentrations of the donor and acceptor components of PSI are equal: $[P_{700}]_0$. The concentration of the acceptor component A in the neutral state is expressed by

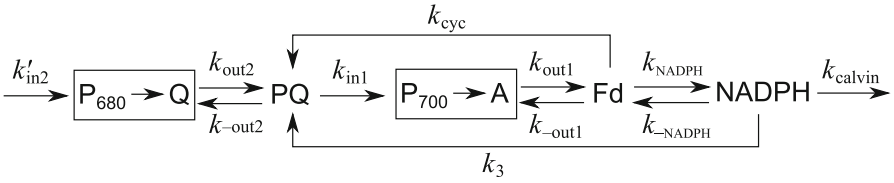
$$[A] = [P_{700}]_0(P_{1I} + P_{2I}). \tag{10.8}$$

The concentration of A in the reduced state is given by

$$[A^{-}] = [P_{700}]_0(P_{2I} + P_{4I}). \tag{10.9}$$

Description of Mobile Carrier Redox Evolution

In the model, we assume that the interactions between mobile carriers (Fd ↔ NADPH Fd ↔ PQ, NADPH ↔ PQ) and between mobile carriers and the active sides of the multienzyme complexes PSII↔ PQ, PQ↔ PSI, PSI↔ Fd occur according to the mass action law. For the mobile carriers PQ, Fd, NADPH we assume the conservation of the total number of molecules in neutral (without an electron) and reduced (with an electron) forms: $[C^0] + [C^-] = [C]_0$. Here $[C^0]$ is the carrier in the neutral state, $[C^-]$ is the carrier in the reduced state, and $[C]_0$ is the total concentration of mobile carriers of a given type. The processes included in the subsystem of mobile carriers are presented in Scheme 10.4:



Scheme 10.4

The system of ODEs for the mobile carriers in the reduced state is as follows:

$$\begin{aligned}
\frac{d[PQ^-]}{dt} &= k_{out2} \cdot \left([Q^-] + k_3 \cdot [NADPH] + k_{cyc} \cdot [Fd^-]\right)[PQ] \\
&\quad - \left(k_{in1} \cdot \left[P_{700}^+\right] + k_{-out2} \cdot [Q]\right)[PQ^-], \\
\frac{d[Fd^-]}{dt} &= \left(k_{out1}[A^-] + k_{-NADPH}[NADPH]\right) \cdot [Fd] \\
&\quad - \left(k_{NADPH}[NADP] + k_{cyc}[PQ] + k_{-out1}\left[A^0\right]\right)[Fd^-], \\
\frac{d[NADPH]}{dt} &= \left(k_{NADPH}[Fd^-] + k_{-3}[PQ^-]\right)[NADP] \\
&\quad - \left(k_{-NADPH}[Fd] + k_3[PQ] - k_{calvin}\right)[NADPH].
\end{aligned} \tag{10.10}$$

The conservation equations are

$$\begin{aligned}
\left[PQ^0\right] + [PQ^-] &= [PQ]_{0,} \\
\left[Fd^0\right] + [Fd^-] &= [Fd]_{0,} \\
[NADP] + [NADPH] &= [NADPH]_0.
\end{aligned} \tag{10.11}$$

Relationships Between Total Concentrations of Electron Carriers

Usually, the ratio between the concentrations of photoactive pigments of PSI to those of PSII in green plants are 2:3. For cyanobacteria (blue-green microalgae) this ratio can be 10:20. We designate this ratio as

$$\alpha = \frac{[P_{700}]_0}{[P_{680}]_{0.}} \tag{10.12}$$

The ratios of mobile carrier concentrations to PSII concentrations are as follows:

$$\beta = \frac{[PQ]_0}{[P_{680}]_0}, \quad \gamma = \frac{[Fd]_0}{[P_{680}]_0}, \quad \delta = \frac{[NADPH]_0}{[P_{680}]_0}. \tag{10.13}$$

Equations (10.1)–(10.13), together with the initial conditions, represent a kinetic model of linear and cyclic electron transfer in green plants, which includes two photosystems. The simulation kinetic curves obtained by means of this simplified model can be compared with the experimental data, that is, with, for example, the kinetics of fluorescence induction and the kinetics of $[P_{700}^{+}]$ evolution.

To describe a particular biological situation, it is necessary to know the characteristics of the model. This means that it is necessary to know how the kinetics of the model variables depend on the values of different parameters. Moreover, model parameter values (rate constants of individual reactions, concentration ratios of electron carriers) must be consistent with the parameters of the real system. We choose the rate constant values of each reaction in the model according to the literature data, and since some data for different rate constants are often obtained in different types of experiments, we can use them as starting values, which should be determined more precisely in the process of simulation and model analysis.

Modeling of Electron Transport Chain of Wild-Type and Mutant *Arabidopsis thaliana*

The model formulated previously was used to simulate the photosynthetic activity of the wild-type and mutant forms (*pgr5* and *crr* genes) of the higher plant *Arabidopsis thaliana* (MS Thesis "Modeling of regulatory mechanisms of primary photosynthetic processes" by Maxim Patrin, Biological Faculty MSU, 2008).

The characteristics of mutant photoactivity that is registered experimentally differ greatly for the wild type and mutants (Munekage et al. 2004). The question actively discussed in the literature is whether in these mutants the cyclic Fd- and NADPH-dependent electron flows around PSI are merely suppressed or absent entirely.

The experimentally observed dependencies of the stationary oxidation state of P_{700}^{+} on the light intensity for the wild type and for the crr mutant compared to the pgr5 mutant are of an opposite character (Fig. 9.10a). For the wild type and crr mutants the stationary P_{700}^{+} level increases with the increasing light intensity, whereas for pgr5 mutants the stationary P_{700}^{+} level decreases with increasing light intensity, and for crr pgr5 double mutants P_{700} is not oxidized at high intensities at all.

An analysis of the model showed that the dependence of P_{700}^{+} on the light rate constant (k_{0I}, k_{0II}), which is proportional to the light intensity, can have an increasing pattern only in the case of active electron transport at the acceptor side of PSI (at great enough rate constant values $k_{\text{out1}} = 150$, $k_{\text{NADPH}} = 180$). In the cases where the electron transfer from PSI to the acceptors is suppressed (rate constants k_{out1}, k_{NADPH} are small), the dependence of P_{700}^{+} on the light intensity decreases.

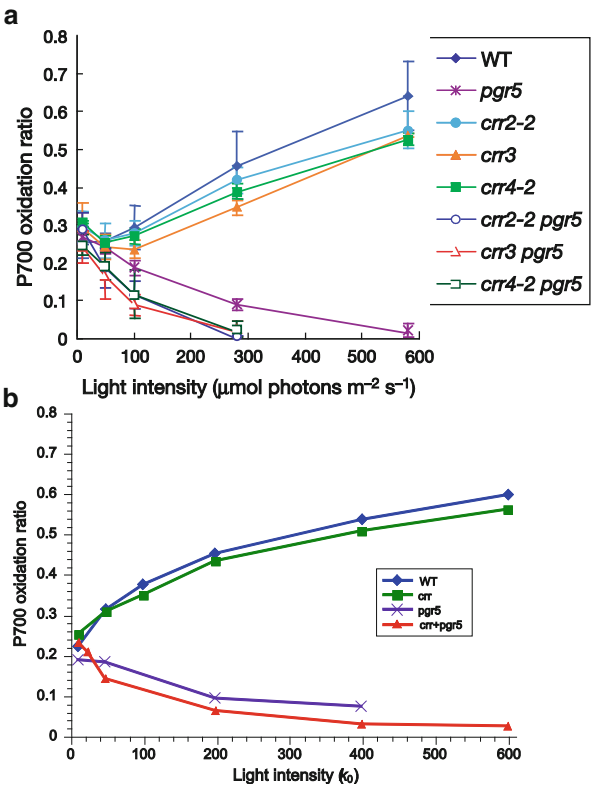


Fig. 10.3 Dependence of stationary level of P_{700}^{+} on intensity of light illumination. (**a**) Experimental data (Munekage et al. 2004). (**b**) Simulation results for different values of light constants k_{01}, k_{02} for wild type, crr mutants, pgr5 mutants, and crr pgr5 double mutants. $k_{in2} = 50$; $k_{in2} = 0.5$; $k_{out2} = 100$; $k_{out2} = 1$; $k_{02} = 1$; $k_{01} = 200$; $k_{01} = 0.05$; $k_3 = 5$; $k_{in1} = 100$; $k_{in1} = 2$; $k_{out1} = 180$; $k_{out1} = 1$; $k_{NADPH} = 150$; $k_{NADPH} = 0$; $k_{cyc} = 5$

The results of qualitative simulations of experimental dependencies of the P_{700}^{+} level on light intensity as well as the corresponding experimental results for the wild type and mutants are presented in Fig. 10.3. On the basis of simulation, we can conclude that crr mutants have a suppressed NADH-dependent cyclic electron transport, and pgr5 mutants also have suppressed Fd-dependent cyclic transport and suppressed electron flow on the acceptor side.

The initial values of the states of a complex are determined as follows: for PSII $P_{1II} = 1, P_{2II} = 0, P_{3II} = 0, P_{4II} = 0$; for PSI $P_{1I} = 1, P_{2I} = 0, P_{3I} = 0, P_{4I} = 0$.

These values correspond to the neutral states of the donor and acceptor parts of the complexes. The initial degree of the reduction of the mobile carriers was 0.5 for PQ and 0.1 for Fd and NADPH. The ratio of the total concentration of the carriers relative to the PSI concentration is as follows:

$$\frac{[PQ]_0}{[P_{700}]_0} = 6, \quad \frac{[P_{680}]_0}{[P_{700}]_0} = 0.5, \quad \frac{[NADP^+]_0}{[P_{700}]_0} = 10, \quad \frac{[Fd]_0}{[P_{700}]_0} = 10.$$

Simulation results for the fluorescence kinetics after switching off the illumination also qualitatively correspond to the experimental data for the wild type and

mutants. For pgr5 mutants the stationary P_{700} oxidation level decreases with increases in the illumination intensity, and for wild type and other mutants the stationary P_{700} oxidation level increases with increases in the illumination intensity.

The model demonstrates kinetic reasons for these differences for the wild type and mutants. The wild type has an intensive linear electron flow and less intensive Fd-dependent and NADPH-dependent cyclic fluxes. The increase in light intensity leads to an increase in the light constant (which is the limiting step) and to an increase in $(P^+_{700})_{st}$. the crr mutant has a suppressed Fd-dependent cyclic flow, which does not considerably affect the pattern of $(P^+_{700})_{st}(I)$ (Fig. 10.3).

The Pgr5 mutant has suppressed cyclic NADPH-dependent transfer (as was assumed in the literature), but also suppressed electron flow from the acceptor PSI side to the Calvin cycle, which is performed through FNR (ferredoxin:$NADP^+$-reductase). Blockage of linear transport leads to an increase in the cyclic Fd-dependent transport and provides a high level of P_{700} reduction (and correspondingly a low level of P^+_{700}) at high intensities of illumination. For crr pgr5 double mutants P_{700} oxidation is very low because the outer acceptors taking up electrons from the acceptor components A of PSI are suppressed (k_{out} is small), so that full oxidation of P_{700} is impossible. This is the reason for the qualitatively different dependencies of $(P^+_{700})_{st}(I)$ on the intensity of light illumination for the wild type and various mutants.

To conduct more detailed quantitative analysis of experimental data on the regulation of photosynthetic processes, we are currently working on specification of the model. In more detailed models, we must take into account all processes proceeding in the photosynthetic membrane: for example, details of the electron transfer inside PSII, PSI, and cytochrome b_6f complexes as coupled processes of the proton transmembrane transfer, transfer of other ions, generation of electric and electrochemical potentials and their effects on electron flows, ATP–synthase activity, and the role of buffer groups in the luminal and stromal thylakoid space.

Chapter 11
Detailed Model of Electron Transfer in PSII

Fluorescence as an Indicator of the State of the Photosystem

Fluorescence (Fl) measurements provide the most popular method of estimating photosynthetic activity. [The title of Volume 19 (2004) of the Springer Series *Photosynthesis and Respiration* is *Chlorophyll a Fluorescence: A Signature of Photosynthesis*]. The main sources of fluorescence are excited Chl molecules of PSII, but fluorescence intensity is determined by a network of all the processes occurring in the photosynthetic membrane. Analyzing the time kinetics of fluorescence induction under various conditions, we can obtain information about processes occurring at different stages of energy transduction in the photosynthetic membrane (Krause and Weiss 1991; Papageorgiou et al. 2007).

The fluorescence induction curve observed after switching on the illumination has two main phases. The fast phase is an increase in fluorescence intensity from the initial level F_0 up to the maximal level P for a period of approximately 1–2 s (depending on the applied light intensity) with two intermediate steps at 2 ms and approximately 30 ms. These processes contribute to the so-called OJIP shape (Strasser et al. 1995, 2004). The slow phase is the subsequent fluorescence intensity relaxation to the steady-state level within a period of approximately several tens of seconds. The complicated shape of the fluorescence transients, including several maxima and quasi-steady states (J and I), is usually attributed to different components of the photosynthetic apparatus; thus the measured shape of the fluorescence induction curve reveals information about these components (Edwards and Baker 1993; Schreiber and Bulger 1993; Govindjee 1995; Bernhardt and Trissl 1999; Lazar 1999, 2006; Bukchov et al. 2004; Strasser et al. 2004).

A great variety of models exist for the simulation of Fl(t) curves measured under different excitation conditions (Fig. 11.1). There are basically three approaches can be distinguished with respect to the excitation by actinic light (1) continuous wave (CW) illumination, (2) multiturnover flashes (mostly in the form of pulse amplitude modulation techniques), and (3) single-turnover flashes.

A. Rubin and G. Riznichenko, *Mathematical Biophysics*, Biological and Medical Physics, Biomedical Engineering, DOI 10.1007/978-1-4614-8702-9_11,

© Springer Science+Business Media New York 2014

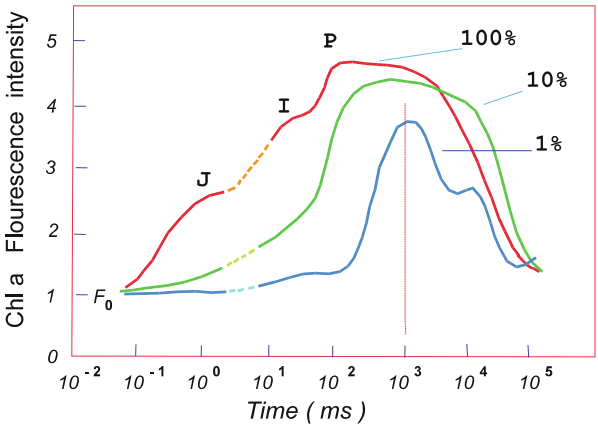


Fig. 11.1 Chlorophyll fluorescence yield induction curves at different light intensities: 600 (100 %), 60 (10 %), and 6 (1 %) W m^{-2} (Strasser et al. 1995). Experimental data are obtained on *Pisum sativum* leaves

Typical Fl(t) curves of type (1) are characterized by an OJIP rise followed by decay via intermediary S-M states to stationary level T. Several models have been proposed for a qualitative description of OJIP transients (Renger and Schulze 1985; Bukhov et al. 1988; Laisk and Walker 1989; Baake and Schroder 1992; Karavaev and Kukushkin 1993; Stirbet et al. 1998; Lazar 2003; Strasser et al. 2004; Vredenberg 2005; Zhu et al. 2005). These models are based mainly on calculations of the normalized population of photochemical fluorescence quencher Q_A and typically cover a time range of approximately 1 s. However, at time periods longer than 500 ms, the formation and decay of an electric potential ($\Delta\Psi$) and ΔpH difference across the thylakoid membrane must be taken into account for an accurate description of Fl(t) curves (Van Kooten et al. 1986; Bulychev et al. 1987; Bulychev and Vredenberg 1999, 2001; Leibl et al. 1989; Dau and Sauer 1992; Gibasiewicz et al. 2001; Lebedeva et al. 2002; Belyaeva et al. 2003; Vredenberg and Bulychev 2003; Belyaeva 2004).

Several models have been proposed to simulate the fast initial phases of photosynthesis. Some of these (Renger and Schulze 1985; Baake and Strasser 1990; Baake and Shloeder 1992; Hsu 1992; Hsu 1993) are limited to processes occurring in PSII at low light intensities. Others (Stirbet and Strasser 1995, 1996; Stirbet et al. 1998; Lazar 2003, 2006; Strasser et al. 2004; Zhu et al. 2005; Belyaeva et al. 2008, 2011) successfully simulated the characteristic features of the initial fast phase of fluorescence induction curves at high illumination intensities—specifically the intermediate maximum and points of inflection (typical OJIP-shape).

In this chapter we will describe a model of electron transfer in PSII constructed by us as a submodel of the generalized model of the processes in a photosynthetic membrane to be considered in Chap. 12 (see also Riznichenko et al. 2009; Rubin and Riznichenko 2009). To specify the parameters of the PSII submodel, we simulated, using the isolated PSII model, the processes that occur in PSII after a very short (nanosecond) laser flash, when the influence of other processes in a photosynthetic membrane can be neglected (Belyaeva et al. 2008, 2011). Fitting the experimental fluorescence data obtained in the experimental group of

Renger with the simulation curve allowed us to evaluate the rate constants of the processes in PSII that cannot be measured experimentally, namely, the processes of nonradiative energy dissipation, which is especially important when the intensity of illumination is high.

Scheme of PSII States

Figure 11.2 shows a scheme of the states and their transitions that are used in the model of the PSII reaction pattern (Riznichenko et al. 1999; Lebedeva et al. 2000, 2002; Belyaeva 2004).

Each box in Fig. 11.2 represents a redox state of the corresponding component: antenna and PSII reaction center chlorophyll—$\left\langle \begin{matrix} \text{Chl} \\ \text{P680} \end{matrix} \right\rangle$, pheophytin—Phe, primary quinone acceptor—Q_A, secondary quinone acceptor—Q_B. The model describes the processes of light-induced charge separation (reaction numbers 2, 9, 16, 29), charge stabilization by Q_A^- formation (3, 4, 10, 11, 17, 18, 30, 31), electron transfer from Q_A^- to Q_B (7) and from $Q_A^- Q_B^-$ to $Q_B H^-$ (14), protonation of $Q_B H^-$ under PQH_2 release (21–27), and refilling of the empty Q_B site with oxidized plastoquinones (PQ) (34–40). Two sequential protonation steps are described by reactions 14 and 21–27.

Note that the general involvement of $\left\langle \begin{matrix} \text{Chl} \\ \text{P680} \end{matrix} \right\rangle$ (three different states), Phe (two redox states), Q_A (two redox states), and Q_B (four redox states) would result in $3 \times 2 \times 2 \times 4 = 48$ possible states in the main scheme. Our model represents a reduction of 48 possible states to 28 states based on the simplifications that are outlined in Lebedeva et al. (2000) and Belyaeva (2004).

To achieve a reduced description we shall introduce the term *form* to designate PSII states that are characterized by the same redox state of carriers P680, Phe, and Q_A but differ with respect to the possible states of the Q_B site (empty, neutral occupied, single reduced and double reduced, and protonated Q_B). In Fig. 11.2, each form is represented by a corresponding column.

We assume that for each electron transferred from the water oxidizing complex (WOC) to the oxidized chlorophyll $P680^+$ reaction center (reactions 4, 11, 18, 31), one proton is released into a lumen, although the actual stoichiometry depends on the redox state S_i of the WOC (Renger 2001).

The electronically excited singlet states are assumed to be delocalized among the chlorophylls via rapid equilibration (Schatz et al. 1988; Laible et al. 1994; Renger and Holzwarth 2005) over the antenna pigments of PSII including the P680 reaction center pigment in the picosecond time domain. Excitation of $\left\langle \begin{matrix} \text{Chl} \\ \text{P680} \end{matrix} \right\rangle$ and its transfer into state $\left\langle \begin{matrix} \text{Chl} \\ \text{P680} \end{matrix} \right\rangle^*$ is described by the light rate constant k_L, which is

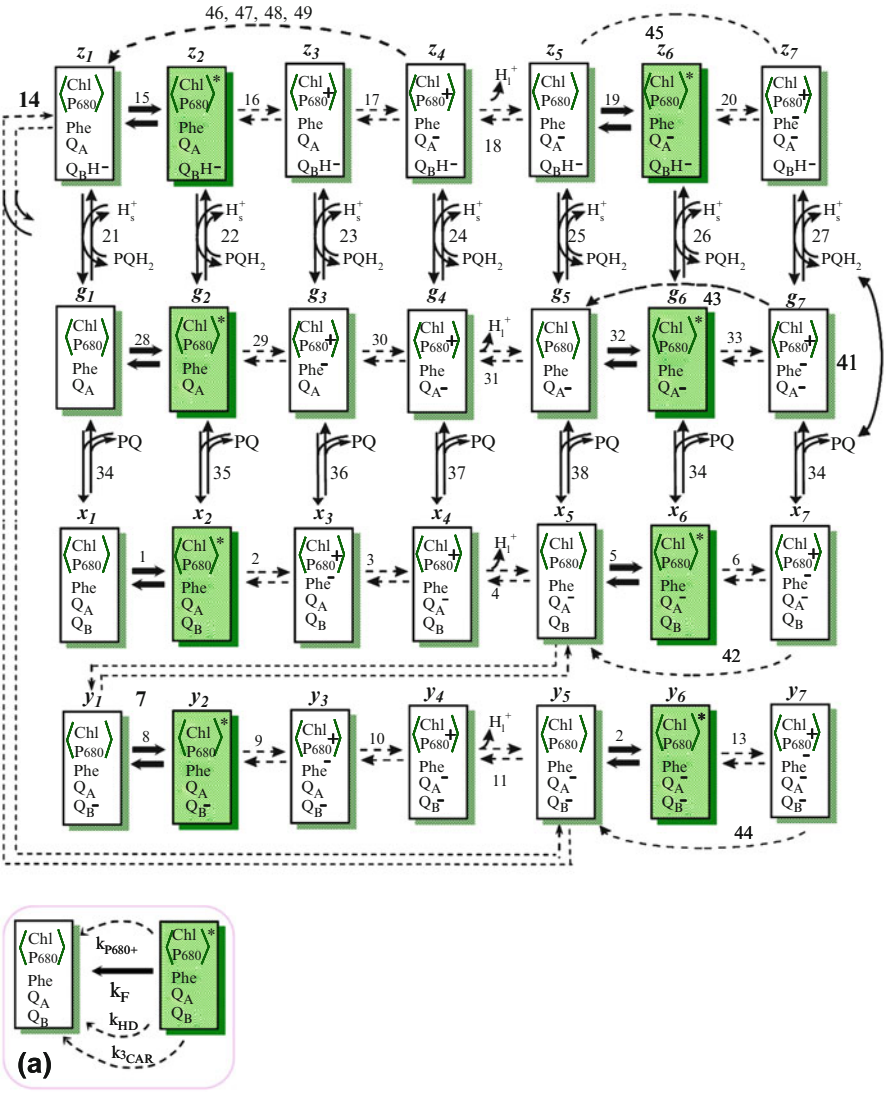


Fig. 11.2 Scheme of catalytic cycle of photosystem II. Each *box* refers to one of the states of the photosystem II complex, which is determined by the redox states of the involved electron carriers. $\left\langle \begin{matrix} \text{Chl} \\ \text{P680} \end{matrix} \right\rangle$ denotes the total PSII chlorophyll including the antenna and P680 pigments, and $\left\langle \begin{matrix} \text{Chl} \\ \text{P680} \end{matrix} \right\rangle^*$ is used to determine singlet excited states of ^{1}Chl* with an electron delocalized over all pigments in antenna and reaction centers. P680: photochemically active pigment; Phe: primary electron acceptor pheophytin; Q_A and Q_B: primary and secondary quinone acceptors; PQ: plastoquinone; PQH_2: plastoquinol; H_L^+: protons released into lumen; H_S^+: proton absorbed from stroma. *Letters above rectangles* (x_i, y_i, z_i, g_i, $i = 1, \ldots, 7$) correspond to model variables. *Shaded areas*: excited states capable of emitting fluorescence quanta; *dotted arrows*: fast steps

assumed to be independent of the redox state of Q_A and the state of population of the Q_B site, i.e., $k_L = k_n$, $n = 1, 5, 8, 12, 15, 19, 28, 32$ (n is the number of the reaction in the PSII scheme).

The $\left\langle \begin{matrix} \text{Chl} \\ \text{P680} \end{matrix} \right\rangle^*$ decay leads to fluorescence emission with the radiative rate constant k_F ($k_F = k_{-n}$, $n = 1, 5, 8, 12, 15, 19, 28, 32$), charge separation in open and closed reaction centers with the rate constants k_n, $n = 16, 29, 2, 9$ and k_n, $n = 19, 32, 5, 12$, respectively, and dissipative reactions with the rate constants k_{P680+}, k_{3Car}, and k_{HD} (Fig. 11.2). The simulations are also simplified by the assumption that $P680^{+\bullet}$ reduction can be satisfactorily described by a single efficient rate constant of 50 ns. This approximation is reasonable because the contribution of this component is high when dark adapted systems are illuminated by a single short flash (Kühn et al. 2004). Within the framework of the model of Fig. 11.2, the time dependence of the summed states ($x_2 + y_2 + z_2 + g_2 + x_6 + y_6 + z_6 + g_6$) determines the shape of the fluorescence induction curve. Thus, to calculate the time dependence of fluorescence intensity normalized to the initial fluorescence level F_0, the sum of these states was multiplied by a normalization factor A (with the normalization of F_0 to 1):

$$F(t) = A \cdot (x_2(t) + y_2(t) + z_2(t) + g_2(t) + x_6(t) + y_6(t) + z_6(t) + g_6(t)). \quad (11.1)$$

Equations Describing Processes in PSII

Kinetic changes in the different PSII state populations, including the different forms of the plastoquinone pool (PQH_2, PQ), can be described by a set of linked ODEs. The differential equation for the evolution of each component has the general form

$$\frac{dX_i}{dt} = v_{\text{production}}(X_i(t)) - v_{\text{consumption}}(X_i(t)), \quad (11.2)$$

where $X_i(t)$ is the time-dependent concentration of the ith component, measured in millimoles. Furthermore, $v_{\text{consumption}}(X_i(t))$ and $v_{\text{production}}(X_i(t))$ are the overall rates (in millimoles per second) of production and consumption of the state $X_i(t)$. These rates are the functions both of the variables $X_j(t)$ involved at the given step ($i, j = 1 \div 30$) and of the model parameters $\widetilde{k}_n, \widetilde{k}_{-n}$ ($n = 1 \div 49$), which are the rate constants of the reactions $n = 1, \ldots, 49$ included in the model.

Fig. 11.2 (continued) (characteristic time values less than 1 ms); *bold arrows*: light-induced steps; *numbers near arrows* step numbers; *dotted arcs*: two types of irreversible reactions of processes of nonradiative recombination: Phe^- with $P680^+$ (42–45), Q_A^- with $P680^+$ (46–49). **a** Decay to ground state occurs via (1) radiative fluorescence emission (k_F), (2) nonradiative dissipation of excited chlorophyll singlets by quenching by triplet carotenoid states (k_{3Car}), and (3) nonradiating dissipation of excitation into heat (k_{HD})

The rate constant for the forward $\widetilde{k}_n$ and reverse $\widetilde{k}_{-n}$ reactions are interrelated via the corresponding equilibrium constant:

$$\widetilde{k}_n = \widetilde{k}_{-n} \cdot \widetilde{K}_{n_{\mathrm{eq}}}.$$

To describe the electron transfer steps between the carriers grouped within the PSII states shown in Fig. 11.2, (11.2) were recorded for each possible state. The transitions between the PSII states are presented by the matrix of population probabilities (Chap. 9), while the interactions of the PSII complexes with mobile carriers are described according to the mass action law. The variables $X_i(t)$ for the different PSII state concentrations are the products of the population probability of state i and the overall PSII complex concentration. In the model, the values of proton concentrations in lumina and stromata ($[H_S^+]$ and $[H_L^+]$) are considered fitting parameters. The second oxidation act of the mobile carrier PQH_2 is described by a single reaction (41) (Fig. 11.2). This process is related to reactions proceeding at the luminal site of the cytochrome b_6f complex and is thus dependent on the luminal pH, i.e., the PQH_2 oxidation (reaction 41) depends on the parameter $[H_L^+]$:

$$PQH_2 \leftrightarrow PQ + 2H_L^+ + 2e^-$$

The total PSII complex concentration values of the system were taken from the data of Govindjee (1982) and Hope et al. (1992), with the concentrations of all PSII states summing up to 1.6 mM. The stoichiometric ratio of total PQ molecules to PSII complexes was taken in the range 6–10 (Govindjee 1982; Hope et al. 1992). Thus the concentrations $X_i(t)$ for different PSII states are related to the population probabilities in the following way:

$$\sum_{i=1}^{28} X_i(t) = 1.6\,\mathrm{mM} \cdot \sum_{i=1}^{7} \big(x_i(t) + g_i(t) + y_i(t) + z_i(t)\big),$$

where $x_i(t)$, $g_i(t)$, $y_i(t)$, $z_i(t)$ are the population probabilities of the PSII states with

$$\sum_{i=1}^{7} \big(x_i(t) + g_i(t) + y_i(t) + z_i(t)\big) = 1. \tag{11.3}$$

The total population probability of all PSII core complexes with a particular redox component attaining a specific redox state is obtained using the sum of the corresponding state population probabilities that contain the electron carriers in this specific redox state, e.g., the summarized population probability of all PSII states containing Q_A^- is given by the formula

$$\sum_{i=4}^{7} \big(x_i(t) + g_i(t) + y_i(t) + z_i(t)\big). \tag{11.4}$$

Likewise, the term *form 4* ($x_4 + g_4 + y_4 + z_4$) will correspond to the population of all redox states where P680 is oxidized to the $P680^+$ carrier and Q_A is reduced to Q_A^-:

$$\begin{aligned} x_4(t) + g_4(t) + y_4(t) + z_4(t) = {} & P680^+PheQ_A^-Q_B(t) + P680^+PheQ_A^-\Pi(t) \\ & + P680^+PheQ_A^-Q_B^-(t) \\ & + P680^+PheQ_A^-Q_B^{-2}(t). \end{aligned} \tag{11.5}$$

The empty Q_B site (g_i, $i = 1, \ldots, 7$) is symbolized by "Π."

Dependence of Rate Constants on Thylakoid Transmembrane Electric Potential

A photosynthetic membrane can be considered a special capacitor. Transmembrane electron and ion transport is accompanied by the formation of a transmembrane electric potential $\Delta\Psi$, which in turn affects electron and ion fluxes. Numerous experiments on the influence of external electric fields have suggested that the rates of electron transfer inside the PSI, PSII, and Cyt b_6f complexes depend on the thylakoid transmembrane potential (Dau and Sauer 1992; Zheng et al. 1990).

In our model, we assume that the rates of electron transport at the transfer steps directed normally to the membrane surface depend on $\Delta\Psi$. According to the Reynolds formalism (Reynolds et al. 1985) our model takes into account the dependence of the rate constants on the transmembrane electric potential $\Delta\Psi$ as follows:

$$\widetilde{k}_+(\Delta\Psi) = \exp(-\delta \cdot \alpha \cdot \Delta\Psi \cdot (F/RT)) \cdot k_+$$

$$\widetilde{k}_-(\Delta\Psi) = \exp(-\delta \cdot \alpha \cdot \Delta\Psi \cdot (F/RT)) \cdot k_-.$$

Here is the portion of that is generated at a given step by charge transfer across the membrane; is the portion of the membrane potential that affects the rate constant of the direct reaction; k_+ and k_- are the corresponding direct and reverse rate constants, respectively, at $\Delta\Psi = 0$; α is the fraction of $\Delta\Psi$ that affects the rate of the reaction; F is Faraday's constant; R is the gas constant; and T is temperature.

In the model of the isolated PSII a simple exponential law

$$\Delta\psi = \Delta\psi_0 \cdot \exp\left(-t/\tau_\psi\right)$$

is assumed to describe the transmembrane electric potential $\Delta\Psi$ changes (Bulychev and Vredenberg 1999). Here $\Delta\Psi_0$ and τ_Ψ are the initial amplitude and the characteristic decay time of $\Delta\Psi$, respectively.

Energy Loss Processes

Electron transport in PSII is accompanied by energy loss processes. The most interesting for us is fluorescence (emission) by excited Chl* molecules. Three other types of dissipation process of Chl* are included, as shown in Fig. 11.2a. Nonradiative dissipation processes of the excited singlet state occur via ^{1}Chl* quenching by the cation radical P_{680}^+ (k_{P680^+}) or heat dissipation in light-harvesting antennae (k_{HD}) (see also: Lazar 2003; Zhu et al. 2005; Steffen et al. 2005a, b). The third dissipative process is dissipative ^{1}Chl* relaxation by intersystem crossing of Chl into ^{3}Chl (triplet), with subsequent quenching by carotenoids occurring with the rate constant k_{3Car} by the time-dependent population of triplet carotenoid states ^{3}Car. This time dependence is taken in accordance with Steffen et al. (2005) to be

$$\left[{}^3\mathrm{Car}(t)\right] = a_{\mathrm{Car}} \cdot \exp(-t/\tau_{3\mathrm{Car}}).$$

Here a_{car} describes the population of the ^{3}Car states generated by the actinic flash normalized to the total population of PSII complexes and τ_{3Car} is the lifetime of the nonradiative decay for this ^{3}Car state population.

Two more types of irreversible nonradiative recombination processes are designated in the scheme by dotted arcs. The first type indicates the recombination of the reduced Phe^- with the oxidized $P680^+$ in closed reaction centers. These reactions (42–45) are included in the model as transitions from the seventh form to the fifth form. The second type is the recombination of the reduced primary plastoquinone Q_A^- with the oxidized electron donors $P680^+$ and tyrosine (Y_z^{ox}) and the redox states S_2 and S_3 of the WOC. This type of nonradiative recombination is indicated in the model as transitions from the fourth form to the first form (reactions 46–49).

To perform calculations by the previously formulated model, we used DBSolve software, versions 7.01 and Optimum, which was designed for simulations of biochemical kinetics (Gizzatkulov et al. 2010).

Experiment

Identification of the parameters of the isolated PSII model was performed on the basis of experimental data on the single-flash-induced transient fluorescence yield (SFITFY) monitored on *Chlorella pyrenoidosa* cells in the 100 ns to 10 s time range (Belyaeva et al. 2008). The scheme of the experiment is presented in Fig. 11.3.

Laser-flash-induced transient changes in the fluorescence yield were measured in the Max-Volmer-Laboratory and Institute of Optics and Atomic Physics, Technical University Berlin, Germany, with the experimental setup described in Steffen

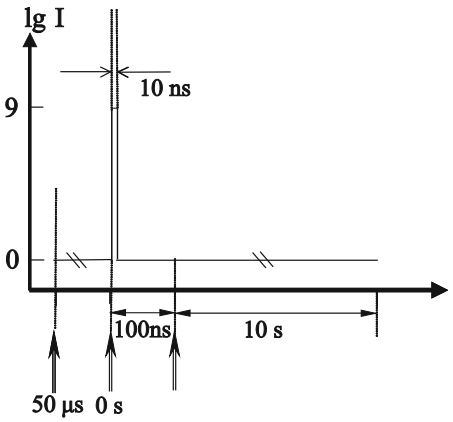


Fig. 11.3 Time scheme of experiment specifying illumination modes used for fluorescence measurements. *Arrows along horizontal axis*: moments when illumination modes were switched on; *vertical axis*: logarithm of relationship between light intensities of flash and measuring light (Belyaeva et al. 2008)

et al. (2001, 2005a). A sample in a cuvette was excited by a single actinic flash ($\lambda = 532$ nm for 10 ns) from a frequency-doubled Nd-YAG laser (Spectrum, **Grosshansdorf, Germany**). The pulse energy used for approximately 100 % saturation of F_m was around 0.4 mJ cm^{-2}. In 10 ns this corresponds to a photosynthetic photon flux density (PPFD) of approximately 1,800 mol photons m^{-2} s^{-1}. The time course of flash-induced changes in the relative fluorescence quantum yield was obtained by monitoring the fluorescence emission caused by the weak measuring light flashes supplied by an array containing a set of light-emitting diodes (LEDs) (Toshiba TLRA 190P, $\lambda_{max} = 660$ nm). The temporal distance of the weak measurement light flashes varied from 2 µs (first measurement flash at 100 ns, second measurement flash at 2 µs after actinic flash) up to 0.5 s (in the time domain $>$ 1 s after the actinic flash) in the experiment.

The fluorescence was detected by a multichannel plate photomultiplier tube (MCP-PMT) from Hamamatsu Photonics. It contained a red-sensitive photocathode and can be gated with $\tau \cong 1$ ns and has a high switching ratio of 1.7×10^8 (at $\lambda = 500$ nm). The F_0 level was determined by means of 3 weak measuring light flashes 50 µs prior to sample excitation with an actinic laser flash. The LED array providing the weak measuring light was switched on and off synchronously with the gate function of MCD-PMT via delay/pulse generator DS-345 (Stanford Research System). The data collected before and after each laser flash were transferred via a GPIB bus (PC IIA, National Instruments, Austin, TX) to a computer. The sample cuvette was flushed and refilled after each series of eight laser flashes with a computer-controlled home-built flow system. To improve the signal-to-noise ratio, 80 measurements of series of eight laser flashes were averaged.

The experimental data obtained on a dark adapted suspension of whole cells of thermophilic *Chlorella pyrenoidosa Chick* are presented in Fig. 11.4 (diamonds). These data are shown at a logarithmic time scale in a range of −50 µs before switching on to 100 ns to 10 s after switching off the strong actinic laser pulse that lasted 10 ns ($t = 0.10$ ns).

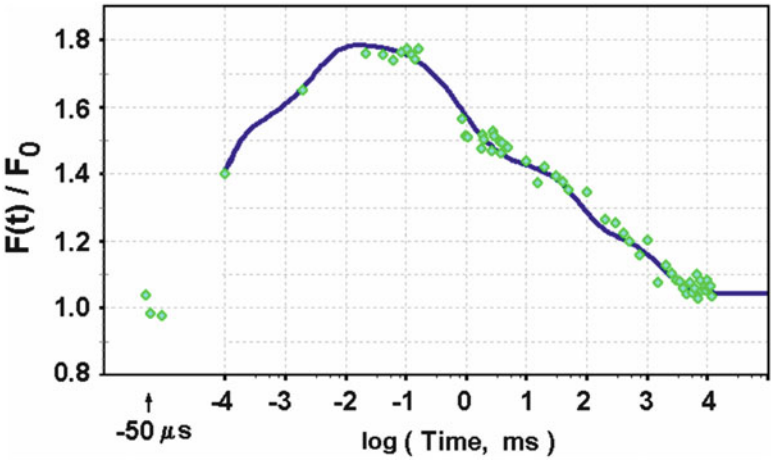


Fig. 11.4 Experimental data on fluorescence yield transients obtained on thermophilic *Chlorella pyrenoidosa* cells (*diamonds*). The samples were excited by actinic laser flash (duration = 10 ns). Measuring light of low intensity was applied to register F_0 value before saturating flash (−50 µs) and to monitor time course of flash-induced changes in relative fluorescence quantum yield in 100 ns to 10 s time domain. The curve was simulated using the PSII model

Description of Events in PSII Electron Transport System After a Short Light Flash

The actinic laser pulse transfers PSII from the initial (dark) form [(x_1 + g_1 + y_1 + z_1) in the first column in the scheme (Fig. 11.2)] to form 4 [(x_4 + g_4 + y_4 + z_4) in the fourth column] with oxidized $P680^+$ of the reaction center. This process comprises a reaction sequence from the states of form 1 (with neutral carriers P680 $PheQ_A$) via form 2 (with excited $^1P680^*$) and form 3 (with separate charges $P680^{+\bullet}Phe^{-\bullet}Q_A$) to form 4 (with stabilized charge separation $P680^{+\bullet}PheQ_A^{-\bullet}$) and is accomplished within 1 ns (Renger and Holzwarth 2005).

Our model simulations describe the effect of the measuring light after reaching an initial population at t = 10 ns immediately after the actinic laser flash. The photosynthetic photon flux density of the measuring light was estimated to be 0.8 µmol photons m^{-2} s^{-1} (Goh et al. 1999), which corresponds to a light constant $k_L = 0.2\ s^{-1}$.

Initially the sample is in the dark adapted state, i.e., in the model, the light constant k_L equals zero. Therefore, only the states x_1 ($P680PheQ_AQ_B$) and g_1 ($P680PheQ_A$) are occupied (Fig. 11.2). The population probabilities x_1 and g_1 are determined by interactions of the PSII acceptor site with the pool of mobile plastoquinone (PQ) molecules. The excitation by laser flash corresponds to $k_L = 6 \times 10^8\ s^{-1}$ from 0 to 10 ns. Therefore, high population probabilities for states with separate charges exist at t = 100 ns. These values were the initial ones to simulate the single-turnover laser-flash-induced transients of fluorescence yield.

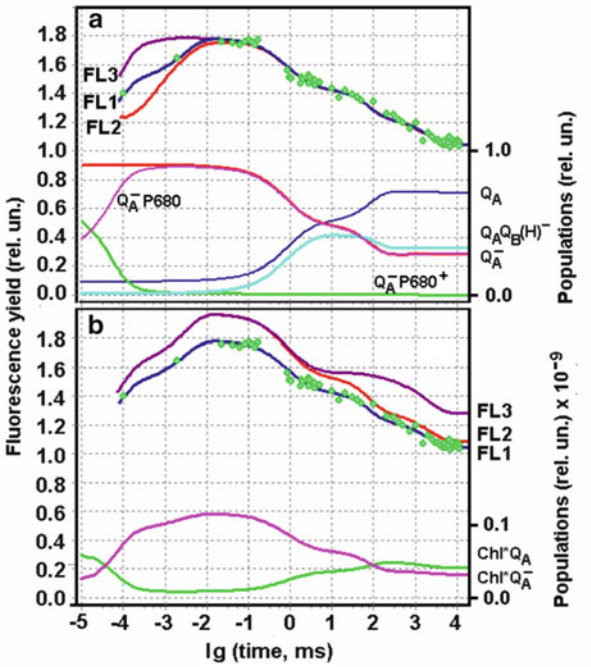


Fig. 11.5 Theoretical curves calculated to simulate processes in sample that was initially dark-adapted ($k_L = 0$ in model) then excited by actinic laser flash (corresponding $k_L = 2 \times 10^8\ s^{-1}$) and illuminated by measuring light ($k_L = 0.2\ s^{-1}$) in time domain from 100 ns to 10 s. *Diamonds*: Chl *a* fluorescence yield transients obtained in experiment. (**a**) Simulated Chl *a* fluorescence yield transients calculated with different values of $P680^+$ reduction ($k_{WOC} = k_n$, $n = 4, 11, 18, 31$) rate constant: FL1, FL3: $k_{WOC} = 2 \times 10^7\ s^{-1}$; FL2: $k_{WOC} = 4 \times 10^6\ s^{-1}$. For quenching by ^{3}Car states the following values were used: FL1, FL2: $k_{3Car}, = 2.8 \times 10^8\ s^{-1}$; FL3: $k_{3Car} = 0$. Time course of PSII redox state populations calculated for $k_{WOC} = 2 \times 10^7\ s^{-1}$ and $k_{3Car}, = 2.8 \times 10^8\ s^{-1}$: $P680^+Q_A^-$: states including oxidized Chl *a* reaction center ($x_4 + g_4 + y_4 + z_4$); Q_A^-: sum of closed reaction center states ($x_4 + g_4 + y_4 + z_4 + x_5 + g_5 + y_5 + z_5$); $P680Q_A^-$: sum of closed reaction center states for fifth form ($x_5 + g_5 + y_5 + z_5$); Q_A: open reaction center state population ($x_1 + g_1 + y_1 + z_1$); $Q_AQ_B(H)^-$: open reaction center states with one or two electrons on secondary quinone ($y_1 + z_1$). (**b**) Chl *a* fluorescence yield transients simulated depending on values of nonradiative charge recombination rate constants for backward electron transfer to $P680^+$ from Phe^- ($k_{42 \div 45}$, in closed reaction centers of PSII) and from Q_A^- ($k_{46 \div 49}$) leading to ground state of P680. *Curves* are denoted according to input pairs of values ($k_{42 \div 45}, k_{46 \div 49}$): FL1: ($5.5 \times 10^8, 6 \times 10^3\ s^{-1}$), FL2: ($2 \times 10^8, 6 \times 10^3\ s^{-1}$); FL3: ($2 \times 10^8, 2.5 \times 10^3\ s^{-1}$). For $k_{42 \div 45} = 5.5 \times 10^8\ s^{-1}, k_{46 \div 49} = 6 \times 10^3\ s^{-1}$ time courses of PSII redox state concentrations with excited ^{1}Chl* were calculated and denoted as Chl*Q_A for open ($x_2 + g_2 + y_2 + z_2$) and Chl*Q_A^- for closed ($x_6 + g_6 + y_6 + z_6$) reaction centers

The strong actinic illumination with a saturating laser flash of 10 ns duration is assumed to transfer nearly all reaction centers to a metastable state with separate charges $P680^+PheQ_A^-$ (Christen et al 1999, 2000; Steffen et al. 2001, 2005a), i.e., we simulate the illumination by the measuring light of the LEDs by $k_L = 0.2\ s^{-1}$ in a time domain of 100 ns to 10 s (Figs. 11.4 and 11.5).

The shapes of different simulated curves with different parameter values were compared with the experimental data to achieve the best fit. A large number of parameter values were taken from the literature data (Crofts and Wraight 1983; Brettel et al. 1984; Renger and Schulze 1985; Eckert and Renger 1988; Schatz et al. 1988; Leibl et al. 1989; Baake and Shloeder 1992; Roelofs et al. 1992; Bernarding et al. 1994; Renger et al. 1995; Vasil'ev et al. 1996; Stirbet et al. 1998; Bulychev and Vredenberg 1999; Schodel et al. 1999; Renger 2001; Lazar 2003; Renger and Holzwarth 2005; Steffen et al. 2005a; Zhu et al. 2005). Other parameters were used as free ones. Their values were evaluated by the fitting of the experimental data (Table 11.1). For instance, we took as free parameters the rate constants ($k_{21} \div k_{27}$) of the exchange of quinol at the Q_B site by quinone molecules of the pool.

Using values for rate constants that are consistent with the literature data, the best fit was achieved with an initial ($t = 10$ ns) population probability of less than 100 % for the sum of forms 4 and 5 ($x_4 + g_4 + y_4 + z_4 + x_5 + g_5 + y_5 + z_5$). This deviation from 100 % is ascribed to dissipative processes. The best simulation of the data was achieved with an initial (10 ns) state distribution of the total population probability of forms 4 ($x_4 + g_4 + y_4 + z_4$) and 5 ($x_5 + g_5 + y_5 + z_5$) of 82.1 % and 8.6 %, respectively. The population probability of forms 4 and 5 together is approximately 91 %.

The distribution of PSII state concentrations obtained in this way for $t = 10$ ns was taken as the initial one for the subsequent calculation of SFITFY that emerges under exposure to the measurement light ($k_L = 0.2\ s^{-1}$) within a time domain of 100 ns to 10 s after the cessation of the actinic saturating flash. The simulation of the effect due to the time-averaged measuring light using a value of $k_L = 0.2\ s^{-1}$ corresponds to 0.8 μmol photons $m^{-2}\ s^{-1}$ (see Goh et al. 1999 and the PSII model description).

The obtained results (black solid line) are presented in Fig. 11.5, together with the experimental data (diamonds). The parameter values used for the best fit of the simulation to the experimental data are presented in Table 11.1.

This study shows that on the basis of the scheme of the PSII reaction pattern depicted in Fig. 11.2, a perfect simulation of the single-turnover, flash-induced transients of the normalized fluorescence yield (SFITFY) can be achieved. The simulations also reveal that in the time range of 100 ns to 10 s the measuring light does not produce any significant actinic effect on the control sample. The SFITFY curves can be successfully simulated by assuming that the pH of the lumen and stroma remains unaffected by the low-intensity measuring light because the processes of ΔpH formation are much slower.

The simulation of the SFITFY curve provides information on the time courses of the population probabilities of different PSII states, as shown in Fig. 11.5.

An analysis of these time courses shows that the maximum (F_m) and minimum (F_0) of the normalized Fl yield critically depend on the rate of the recombination processes (radiative and dissipative nonradiative), which are included in the current model version.

Table 11.1 Values of parameters used for quantitative fits by PSII model (scheme, Fig. 11.2) simulations (solid lines in Figs. 11.4 and 11.5) of fluorescence induction after short saturating laser flash for thermophilic algae *Chlorella pyrenoidosa Chick*

Figure 11.2, reaction number (*n*)	k_n (s^{-1}) References	K_{eq}	k_{-n} (s^{-1})	Processes
1,8,15,28 5,12,19,32	$k_L = 0.2$ Goh et al. (1999)			Excited state ^{1}Chl* formation with light rate constant k_L
			$k_F = 6.7 \times 10^7$	
			$k_{P680+} = P{\cdot}8 \times 10^9$	
			$P = 0.175$	Decay of excited states by fluorescence emission (k_F)
			$k_{3Car} = a{\cdot}2 \times 10^9$	Quenching with $P680^+$(k_{P680+})
			τ_{3Car} =3 μs	Quenching with ^{3}Car(k_{Car})
			$a = 0.14$	
			Steffen et al. (2005a) 3.2×10^7	
2,9,16,29	$3.2 \times 10^{11}/100$ Schatz et al. (1988), Roelofs et al. (1992), Renger et al. (1995)	100		Charge separation (open RC)
6,13,20,33	$3.2 \times 10^9/2$ Schatz et al. (1988), Roelofs et al. (1992)	100/2.5 Schatz et al. (1988), Roelofs et al. (1992)	4×10^7 Renger et al. (1995)	Charge separation (closed reaction centers)

(continued)

Table 11.1 (continued)

Figure 11.2, reaction number (n)	k_n (s^{-1}) References	K_{eq}	k_{-n} (s^{-1})	Processes
3, 10, 17, 30	3×10^9 Schatz et al. (1988), Roelofs et al. (1992), Renger et al. (1995)	10^8Renger and Holzwarth (2005)	30	Charge stabilization on Q_A^-
4, 11, 18, 31	$(3.3 \div 1.5) \times 10^7$ Renger (2001)	200 Renger (2001)		Electron donation from WOC to $P680^+$
7	3,500 Renger and Schulze (1985)	14 Crofts and Wraight (1983)	350 Crofts and Wraight (1983), Renger and Schulze (1985)	ET from Q_A^- to Q_B
14	1,600 Renger and Schulze (1985)	1 Crofts and Wraight (1983)	1,600	ET from Q_A^- to Q_B^-
42 – 45	5×10^8 Roelofs et al. (1992), Renger and Holzwarth (2005), Steffen et al. (2005a)			Nonradiative recombination: Phe^- with $P680^+$
46 – 49	5,000 ÷ 6,000 Steffen et al. (2005a)			Nonradiative recombination: Q_A^- with $P680^+$
41	3 ÷ 5 [rev. in Lazar (2003)]	40 ÷ 60		Second oxidation of mobile carrier PQH_2

$pH_{Lumen} = 6.4 \div 6.8$; $H_{Stroma} = 7.3 \div 7.7$ [free] $(PQH_2 + PQ):\Sigma(x_i + y_i + z_i + g_i) = 10:1$
$\Delta\Psi_0 \sim 40 \div 50$ mV, $\tau_\Psi \sim 1 \div 2$ s

The developed model of isolated PSII can be used for theoretical comparative analyses of time-dependent fluorescence signals observed in the photosynthetic samples after a short flash and in other conditions (in the presence of uncouplers), when the processes in the remaining electron transport chain and coupled processes of ΔpH formation and transmembrane ion fluxes can be neglected.

The model of isolated PSII is not able to describe the kinetics of the fluorescence induction curve at moderate and low light intensities, nor can it describe the slow phase of the Fl induction curve. To analyze the slow phase, it is necessary to consider the processes responsible for the outflow of electrons from PSII, as well as processes affecting electron movements inside PSII. These processes include electron transfer by PQ molecules from PSII to cytochrome b_6f complexes, coupled to proton transport, electron transport from Cyt b_6f to PSI, and finally electron flow to the CO_2 fixation cycle through ferredoxin (Fd) and ferredoxin:$NADP^+$-reductase (FNR). In these processes the influence of the electrochemical transmembrane potential is very important. However, until recently only these experimental situations, where transmembrane potential effects can be neglected, were successfully simulated. In the next chapter, we extend the model to describe the regulation of photosynthetic electron transport by transmembrane electrochemical potential.

Chapter 12
Generalized Kinetic Model of Primary Photosynthetic Processes

The developed here describes photosynthetic processes according to the classical Z-scheme, where PSII and PSI operate in turn (Hall and Rao 1999; Nelson and Yocum 2006). The model was developed on the basis of the simulation of electron transport processes in isolated fragments of PSI, PSII, and bacterial reaction centers (Riznichenko et al. 1990; Bukhov et al. 1988; Chrabrova et al. 1989). The distinctive feature of the model (similar to the simplified model in Chap. 11) is that it simulates the processes inside the photoreaction center complexes in more detail, taking into account also the role of electric and electrochemical potentials.

Model Structure

The processes simulated in the model are presented in Fig. 12.1. The general model comprises submodels of separate parts of the electron transport chain: photosystem II complex (Lebedeva et al. 2000; Belyaeva et al. 2008), cytochrome b_6f complex (Kamali et al. 2004), and photosystem I. Along with the processes occurring in the photosynthetic reaction centers of PSI and PSII and in the Cyt b_6f complex, the model also describes transmembrane proton fluxes directed toward the intrathylakoid luminal space, the buildup of electric and electrochemical potentials, ion fluxes across the membrane, ATP–synthase activity, and the role of buffer groups in luminal and stromal compartments of the thylakoid.

The model described below simulates the changes in the redox states of electron carriers as well as changes in electric and electrochemical potential values in the photosynthetic membrane.

Full electron transport chain (Fig. 12.1) contains PSII, Cyt b_6f, and PSI complexes with a fixed structure. Interactions between these complexes and with the environment proceed via mobile carriers like PQ, Pc, and Fd.

Simulation of the electron transfer inside PSII, Cyt b_6f, and PSI complexes is based on the concept that a catalytic cycle for each such complex includes a

A. Rubin and G. Riznichenko, *Mathematical Biophysics*, Biological and Medical Physics, Biomedical Engineering, DOI 10.1007/978-1-4614-8702-9_12,

© Springer Science+Business Media New York 2014

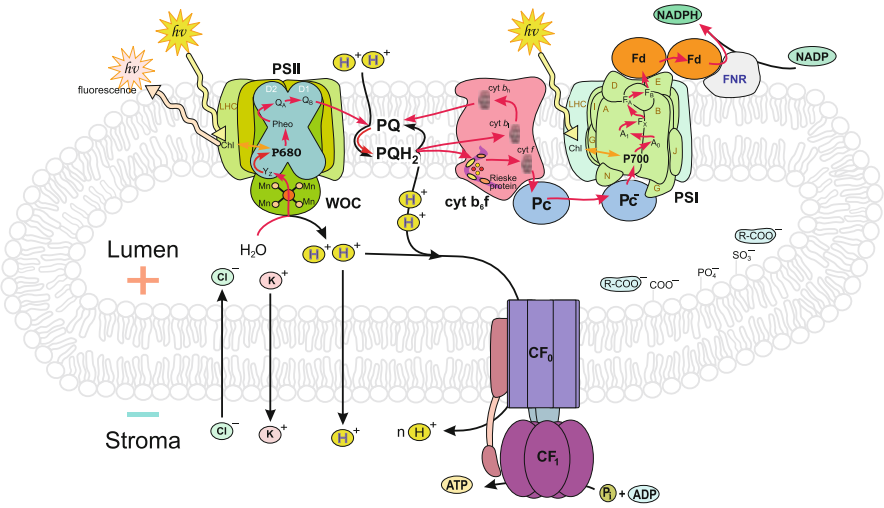


Fig. 12.1 Flowchart for generalized model of primary photosynthetic processes. PSI, PSII: photosystems I and II; LHC: light-harvesting complex; WOC: water-oxidizing complex; Chl: antenna chlorophyll; P680 and P700: pigments of PSII and PSI reaction centers; Q_A: primary quinone acceptor of PSII; Q_B: secondary quinone acceptor of PSII; A_0, A_1, F_x, F_A, F_B: acceptor complex of PSI; Fd: ferredoxin; FNR: ferredoxin:$NADP^+$-reductase; Pc: plastocyanin; cyt b_6f: cytochrome b_6f complex; cyt b_h and cyt b_L: high and low potential hemes; PQ: plastoquinone, PQH_2: plastoquinol; $R–COO^-$: buffer groups. Signs (+) and (−) on membrane indicate that the thylakoid lumen is charged positively and the chloroplast stroma is charged negatively during photosynthetic processes. *Zigzag arrows*: quanta of incident light and fluorescence; *black arrows*: direction of electron transfer along chain and ion fluxes across thylakoid membrane upon onset of illumination

sequence (or network) of states, their number being determined by the number of electron carriers included in the model and by the number of their redox states (e.g., excited, oxidized, reduced, protonized). For a detailed description of the method see Chap. 9.

Any photosynthetic complex contains several components, each of which can be presented in oxidized and reduced forms. Some carriers can exist in more than two forms; for example, Chl can be in oxidized, reduced, or excited form. Thus schemes of the states and their transitions for a photosynthetic complex usually include dozens of states. The complexity of the scheme depends on the actual goals of the simulation.

Photosystem II Complex

Our submodel of the PSII complex was discussed in detail in Chap. 11. In the literature there are several PSII models describing OJIP fluorescence transients, which consider detailed schemes of electron transport and energy transformation in PSII, especially the donor side of PSII: oxygen evolving complex, and the

interaction of the PSII complex with Chl antenna molecules (Stirbet and Strasser, 1995, 1996; Stirbet and Strasser, 1998; Vredenberg 2000, 2005; Lazar 2003; Zhu et al. 2005). A comparative study of the different fluorescence quenchers was carried out by Strasser and Stirbet (2001), who considered fluorescence (FL) yield to be dependent on the redox state of either [Q_A^-] or [Phe^-] or on both of them. Since these three models were equally satisfactory in fitting experimental data with an accuracy of approximately 2 % over the time span from 20 μs to 2 s, it was not possible to choose the model that best described reality [see discussion in Strasser et al. (2004)].

We used another scheme, discussed in Chap. 11 (Fig. 11.2), where we suppose the FL yield to be proportional to the concentration of PSII complexes with the excited Chl* as a source of FL emission. Such a scheme proved to contain the necessary details to simulate experimental data.

In Chap. 11 we discussed the processes in PSII initiated by a short laser flash. Here we shall simulate the processes initiated by continuous light.

When a light is switched on, Chl goes into the excited state (steps 1 and 28), which may be accompanied by primary (steps 2 and 29) and secondary (steps 3 and 30) charge separation. In the dark without illumination (dark adaptation) the PSII complex acquires states x_1 and g_1, which reach equilibrium (step 34).

The oxygen evolving complex reduces the oxidized reaction center pigment (steps 4 and 31). Here we did not consider the molecular mechanism of the WOC functioning but assumed that for every electron transferred from the WOC to the oxidized P680, one proton is released into the intrathylakoid space. Thus, the sequence of steps 1–4 or 28–31 leads to the formation of a closed reaction center with reduced Q_A (states x_5 and g_5).

Further illumination of the closed reaction center may result in the repeated excitations of the pigment (steps 5 and 32) and in the primary charge separation (steps 6 and 33). Thus, states with oxidized pigment and reduced Phe and Q_A (states x_7 and g_7) appear in the PSII description.

In any state g_i ($i = 1, 2, \ldots, 7$), PQ can be bound at the Q_B site (steps 34–40) to give the corresponding states x_i ($i = 1, \ldots, 7$). The bound Q_B is a two-electron carrier and can consequently accept two electrons from Q_A^-. Steps 7 and 14 (dashed lines in Fig. 12.5) describe the transfer of the first and second electrons to Q_B with the formation of states y_1 (Chl Phe Q_A Q_B^-) and g_1 (Chl Phe Q_A). Under light, these states can undergo the sequence of conversions described for x_1 and g_1, including pigment excitation (steps 8 and 15), primary (steps 9 and 16) and secondary (steps 10 and 17) charge separation, reduction of oxidized P680 by the WOC (steps 11 and 18), and excitation of the closed reaction center (steps 12 and 19) attained by primary charge separation (steps 13 and 20).

At any state z_i ($i = 1, \ldots, 7$), plastoquinol (PQH_2) may be released (following uptake of two H^+_s protons) from the chloroplast stroma, giving states g_i ($i = 1, \ldots, 7$) with a vacant Q_B site (steps 21–27). Steps 1, 5, 8, 12, 15, 19, 28, and 32, marked by bold arrows in the scheme, are the light-activated steps describing the transition of Chl into the excited state Chl*, and the reverse process resulting in fluorescence emission.

Excitation of Chl and generation of the state Chl* are described in the model by the corresponding light rate constants $k_L = k_i$, $i = 1, 5, 8, 12, 15, 19, 28, 32$, which are proportional to the light intensity. FL emission is determined by the rate constant $k_F = k_{-i}$. The FL yield (F) is calculated as the product of the sum of the excited states and the ratio between the rate constants k_F and k_L:

$$F = \frac{k_F}{k_L} \cdot (x_2 + y_2 + z_2 + g_2 + x_6 + y_6 + z_6 + g_6). \tag{12.1}$$

We use FL yield $F = \mathrm{FL}/k_L$ (instead of FL intensity) to compare the energy efficiency of photosynthetic processes under different conditions.

Cytochrome b_6f Complex

The cytochrome b_6f complex is one of the major photosynthetic protein units of the thylakoid membrane, positioned between the two photosystems PSII and PSI in the electron transport chain. This dimeric complex mediates electron transfer between the PSII and PSI reaction center complexes by oxidizing lipophilic plastoquinon and reducing soluble plastocyanin (O'Keefe 1988).

An essential function of the Cyt b_6f complex is to couple electron transport to electrochemical proton potential $\Delta\mu_{H^+}$ across the thylakoid membrane, supporting ATP synthesis. The main elements of the Cyt b_6f complex are the Rieske iron-sulfur center (FeS_R), cytochrome f, two hemes of cytochrome b (high-potential b_H and low-potential b_L), and two binding sites denoted here as l, luminal, and s, stromal, for plastoquinol oxidation and plastoquinone reduction.

In our model (Fig. 12.2) we used the most popular scheme of the Q-cycle, where the second electron from plastoquinol reduces b_l (Hope et al. 1992; Hope 2000). Electrons are fed into the Q-cycle at the luminal (l) side of the membrane (step 41, dotted arrow in the left-hand part of Fig. 12.2). Upon binding with the l center of the Cyt b_6f complex, plastoquinol passes one electron to the Rieske iron-sulfur center (FeS_R) and releases one proton into the thylakoid lumen, a complex between protonated PQ with reduced FeS_R forms (steps 43, 44, 45,46 depending on the redox states of FeS_R and Cyt b hemes). If the low-potential heme b_l is reduced, the semiquinone remains bound at the Rieske center until b_l is oxidized (in steps 49, 55, and 61). Then the second proton is released, and the semiquinone of the FeS^r_R–$QH^\bullet$ complex gives an electron to the b_l heme, thus converting into free PQ (steps 47 and 48), and this form diffuses back to the stromal side (step 42, dotted arrow in upper part of scheme in Fig. 12.2). Further, an electron is transferred across the membrane from the low-potential to the high-potential heme (steps 61–63). Thereupon the reduced b_h heme reduces PQ in the s center to produce semiquinone $PQ_s^\bullet$ (steps 49–54). This semiquinone takes the second electron from b_h, consuming two protons from the stroma, and becomes plastoquinol (steps 55–60). Simultaneously, one electron accepted by the FeS_R center is transferred to Cyt f and then to Pc (steps

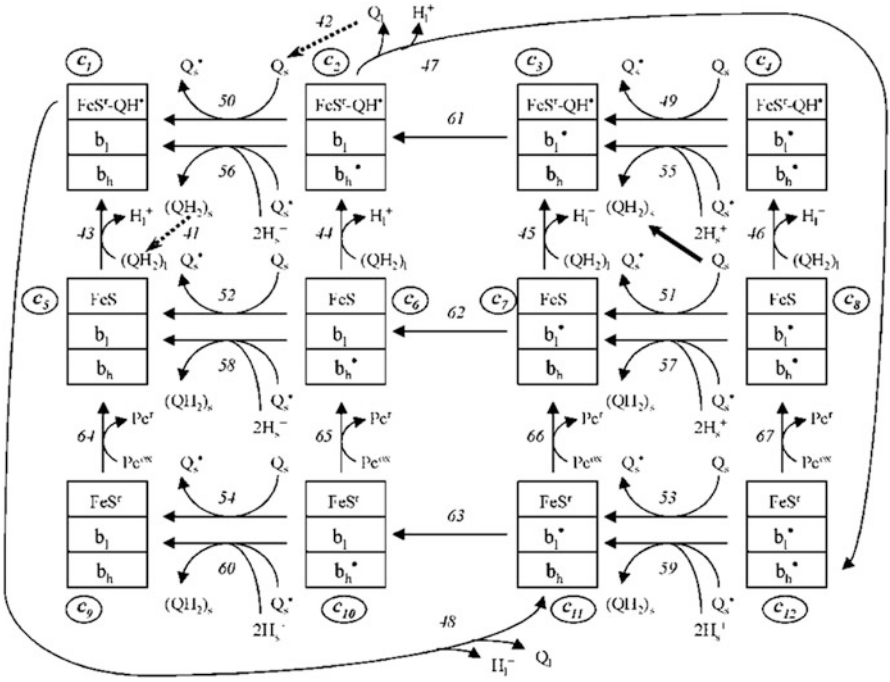


Fig. 12.2 Scheme of catalytic cycle of cytochrome b_6f complex. Each *box* represents one of the possible kinetic states of the complex, determined by the states of its components. b_h and b_l: high- and low-potential hemes; FeSR and FeS^rR: Rieske iron-sulfur center in neutral and reduced forms; Pc^r and Pc^{ox}: reduced and oxidized plastocyanin. The letters c_i ($i = 1, \ldots, 12$) designate the variables in the model. H_l^+: protons released into lumen; H_s^+: protons absorbed from stroma; PQ: plastoquinone; PQH_2: plastoquinol. Subscripts l and s indicate the luminal and stromal sites of the cytochrome complex; ($^\bullet$) means the presence of an electron on the corresponding molecule (Kamali et al. 2004)

64–67). The scheme does not show the step corresponding to the electron transfer between FeS and Cyt f, but these carriers are in fast equilibrium (both rate constants $>10^5\ s^{-1}$, and the equilibrium constant is approximately 3) (Hope, 1993). That is why we combine Cyt f—as the compound actually interacting with Pc—with FeS^r in one component.

Kamali et al. (2004) developed a submodel of the Cyt b_6f complex assuming Q-cycle and a dependence of the electron transfer rates on the electric potential. The model was presented as a set of ODEs for two types of variables. The first type was represented by the probabilities of different states of the cytochrome b_6f complex, (c_1–c_{12}); the concentration of each state of the complex was calculated as the product of the given state population and the total concentration of all complexes in the membrane.

The other type of variable was related to concentrations of mobile electron carriers: plastocyanin (Pc^r, Pc^{ox}), plasoquinone in the twice protonized form, at

the stromal and luminal sites of the Cyt b_6f complex (QH_2, Q_s, Q_l), and proton concentrations in lumina and stromata. The interaction of the complex with mobile carriers was described by the mass action law equations.

In the Cyt b_6f complex submodel, the dependence of the rate constants on $\Delta\Psi$ (similar to the PSII model) was taken into account. We assumed that the Q-cycle has four electrogenic steps: the first one corresponds to the transmembrane electron transport from b_l to b_h (steps 61–63), while the three others correspond to proton transport coupled to the plastoquinone reduction (steps 55–60) and plastoquinol oxidation (steps 43–48). The interheme electron transport was assumed to be responsible for 80 % of the overall electrogenesis, and the remaining 20 % were shared equally among the proton-transport steps, which is in accord with the data (Drachev et al. 1989) obtained for the cytochrome bc_1 complex in purple bacteria.

The model parameters were fitted with experimental data on redox conversions of Cyt b and Pc, as well as on the proton pumping into the thylakoid lumen upon a 15 ns saturating light flash (Hope et al. 1992). The concentration of the reduced Cyt b was described as the sum of concentration of the states containing b_h^r, in accordance with its main contribution to the measured signal (Hope et al. 1992):

$$b_h^r = c_2 + c_4 + c_6 + c_8 + c_{10} + c_{12}.$$

The rate constants of the model were taken from the literature and refined by fitting.

Photosystem I Complex

The version of the model we are discussing is focused on the simulation of Chl a fluorescence transients. There is general agreement that at room temperatures, Chl a fluorescence in plants, algae, and cyanobacteria, in the 680- to 740-nm spectral region is emitted mainly by PSII (Dau 1994; Strasser et al. 2004; Golbeck 2006). For this reason we present the PSI complex by a rather simplified scheme (Fig. 12.3), though PSI may significantly influence the shape of the fluorescence induction curve by its effect on the electron outflow from PSII.

The PSI submodel (Fig. 12.3) includes five kinetic states that are determined by the state of the P700 reaction center pigment and the A acceptor complex. Note that A here designates the entire complex of acceptors: primary and secondary A_0 and A_1 and iron clusters F_x, F_A, and F_B. We do not go into detail of electron transport within the acceptor complex A but assume that it can generally exist in oxidized and reduced states as a single carrier. This simplification appears to be reasonable because electron transfer along the A_0–A_1–F_x chain is very rapid (from 10^{-12} to 10^{-9} s) (Malkin and Niyogi 2000).

Under illumination, P700 becomes excited (P700*, step 68) with the subsequent charge separation (step 69) and formation of the state $P700^+A^r$. This state

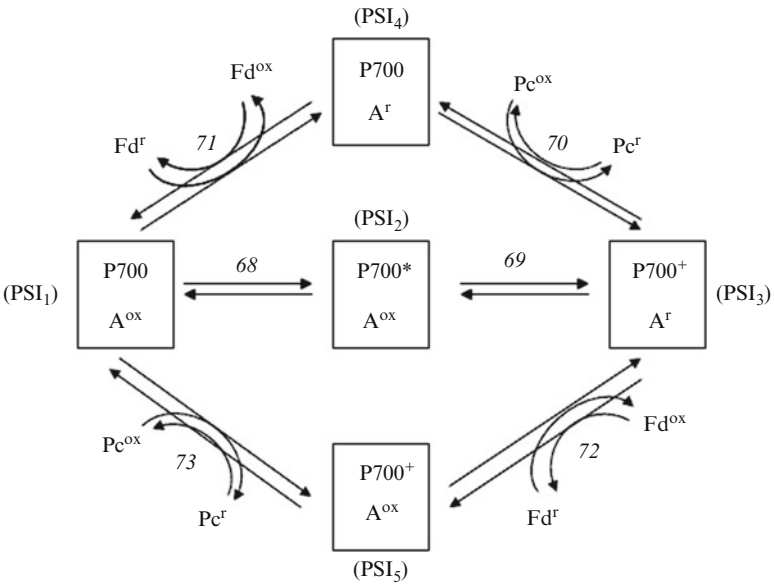


Fig. 12.3 Simplified scheme of electron transfer in PSI. P700 is the reaction center chlorophyll, A here means the entire acceptor complex; Fd, ferredoxin; Pc, plastocyanin; superscripts mark the reduced (r) and oxidized (ox) states. PSI_i is the number of the model variables

can be further utilized in two ways. The oxidized $P700^+$ may first accept an electron from Pc (step 70), after which the acceptor complex will reduce Fd (step 71) or vice versa; first the A^r complex may give its electron to Fd (step 72), and after that Pc will reduce the oxidized P700 (step 73). Most of the equilibrium and rate constant values were taken from the literature. At the same time, some parameters were optimized so as to attain satisfactory theoretical results fitting the experimental data.

Mobile Carriers in Kinetic Model

Electron transport between the complexes is carried out by mobile carriers (Fig. 12.1). Molecules of the protein plastocyanin (Pc) move in the inner luminal part of a thylakoid. Molecules of ferredoxin (Fd) diffuse in the external stromal space, and molecules of plastoquinone in neutral and double-protonized form (PQ, PQH_2) move inside the lipid bilayer of the membrane. In the general kinetic model, we describe interactions between the mobile carriers and the multienzyme complexes by means of the mass action law, similar to the interactions described in Chap. 10.

Role of Transmembrane Electric Potential

Transmembrane electron and ion transport is accompanied by the formation of the transmembrane electric potential $\Delta\Psi$. We assume that $\Delta\Psi$ is a variable in the model that is determined by the overall changes in the electrical charge in the lumen and stroma as a result of the transmembrane transfer of electrons and ions (Krab et al. 1985):

$$\frac{c_{\mathrm{m}}}{F} \times \frac{d(\Delta\Psi)}{dt} = \upsilon(q_{\mathrm{lumen}}) - \upsilon(q_{\mathrm{stroma}}).$$

Here c_{m} is the capacity, F is Faraday's constant, $\upsilon(q_{\mathrm{lumen}})$ and $\upsilon(q_{\mathrm{stroma}})$ are bulk charge densities in the lumen and stroma, and q_{lumen} and q_{stroma} are functions of the concentrations of H^+, K^+, and Cl^- ions in the relevant thylakoid compartments. Concentrations of H^+, other positive ions (K^+, Mg^{2+}), and negative ions (Cl^-) in the lumen and stroma are the model variables.

We assume that the rates of electron transport in PSII, cytochrome complexes, PSI, and at the transfer steps directed normally to the membrane surface depend on $\Delta\Psi$, as was discussed in detail in Chap. 11. The dependence of the reaction rate constants on the transmembrane electric potential is an important characteristic of the model that allows us to simulate experimental data when $\Delta\Psi$ varies.

Transmembrane Ion Transfer and $\Delta\mu_{H^+}$ Generation

The transmembrane proton gradient ΔpH is a model variable since at any time moment it is determined by the proton concentration difference in the stroma $[H_n]$ and lumen $[H_p]$:

$$\Delta\mathrm{pH} = \ln\left[\mathrm{H}_p\right] - \ln\left[\mathrm{H}_n\right].$$

Transmembrane proton transfer in the direction opposite that of the concentration gradient is coupled to the electron transport and occurs at several steps of the photosynthetic chain. The main contribution is brought about by PQ reduction/oxidation and the Q-cycle. A mobile PQ molecule in the membrane binds to the acceptor side of PSII, accepts two electrons, and takes up $2H^+$ from the stromal space. A double-protonized neutral molecule of PQH_2 detaches from the PSII complex and diffuses inside the membrane until it contacts the luminal binding site of Cyt b_6f. As a result of this contact, two electrons in series enter the chain of the Cyt b_6f complex, and two protons are released into the luminal space, taking part in the generation of the electrochemical membrane potential. Protons are also liberated into the luminal space as a result of water splitting at the donor side of PSII. These processes are considered in the scheme of transitions between the PSII

states (Fig. 11.2), which takes into account the formation of the transmembrane proton gradient. Proton transport inside the thylakoid can occur also during cyclic electron transport around PSI.

$\Delta\mu_{H^+}$ is consumed in the ATP–synthase reaction. The formation of ATP from ADP and P_i is accompanied by proton transfer from lumen to stroma. The proton gradient could also decrease due to the passive proton leakage. The capture and release of protons at the stromal and luminal sites of PSII and Cyt b_6f, coupled to the photoinduced electron transport, lead to a redistribution of the charges in the stroma and lumen. The electric potential $\Delta\Psi$ thus generated induces passive ion fluxes across the thylakoid membrane.

We used the model of ion transport through a three-barrier channel (Nicholls 1974; Brown and Brand 1986; Kholodenko 1988; Tester and Blatt 1989; Potossin and Schönknecht 1996) for the description of the transmembrane movement of protons and positive (K^+, Mg^{2+}) and negative ions (Cl^-).

The effect of the transmembrane electric potential $\Delta\Psi$ on the rate of ion flux was described using the following formula (Rubin 2013):

$$\nu_I = \frac{V_I \cdot e^{\delta_I \psi} \cdot \left(I_p - e^{-\psi} \cdot I_n\right)}{\left(1 + \frac{I_p \cdot e^{\delta_K \psi}}{K_p}\right) \cdot \left(1 + \frac{I_n \cdot e^{\delta_I \psi}}{K_n}\right)}.$$

Here v_I is the rate of ion flux and V_I the rate of ion flux in the absence of an electric potential on the membrane.

Buffer groups taking part in proton-gradient formation are localized in luminal and stromal spaces. In the model, we take into account association–dissociation reactions of these groups.

The rate equation for the ATP–synthase reaction was based on the minimal kinetic scheme of ATP synthesis/hydrolysis (Boork and Wennerström 1984).

Buffer Properties of Lumen and Stroma

The chloroplast stroma and the thylakoid lumen are known to exhibit buffer properties due to the presence of various proton-binding groups in their volume. In our model, we approximate the buffering in each compartment by three proton-binding groups (B_1, B_2, B_3), and their pK_s for protons vary from 6.7 to 8.7:

$$B_j + H_l^+ = B_j H, K_B^j = \frac{B_j H_l^+}{B_j H},$$
$$K_B^1 = 10^{-6.7}\,\mathrm{M}, K_B^2 = 10^{-7.7}, K_B^3 = 10^{-8.7}\,\mathrm{M}.$$

The dissociation constants and the concentrations of buffering groups were chosen so as to fit the experimental data on the buffer capacity of the thylakoid lumen (Van Kooten et al. 1986).

Parameter Values

Estimation of the parameters is a peculiar problem. Some values can be determined accurately, e.g., the rate constants for the charge separation in PSII (Schatz et al. 1988; Renger 2001; Strasser et al. 2004, Golbeck 2006). Other processes are less studied. This is particularly true for the slower processes such as PQ diffusion in a photosynthetic membrane and transmembrane ion transport and the buffer properties of the lumen and stroma. A wide range of these rate values is connected with the variability of the geometry, pH, ion strength, and other parameters in different cells under different environmental conditions. We shall discuss this problem when we formulate the direct multiparticle model of photosynthetic electron transport in Part IV.

In our model, most of the equilibrium and rate constants for the reactions were taken from the literature. For each reaction (n is the number of the reaction) we take into account the ratio between the rate constant of the forward k_n and reverse k_{-n} reactions using the equilibrium constant $K_{n,\mathrm{eq}}$:

$$k_n = k_{-n} \cdot K_{n,\mathrm{eq}},$$

where k_n and k_{-n} are the rate constants for the reactions shown in schemes in Figs. 11.2, 12.2, and 12.3.

The equilibrium constants of the redox reactions were determined from the experimental data on the midpoint redox potential:

$$K_{\mathrm{eq}} = \exp\left(-\frac{\Delta E_{\mathrm{m}}}{RT/n \cdot F}\right).$$

Here ΔE_{m} is the difference between the midpoint redox potentials of the electron carriers (Schatz et al. 1988; Laisk et al. 1989; Renger 2001; Roelofs et al. 1992) measured with respect to a standard hydrogen electrode and n is the number of electrons transferred in the redox reaction. ΔE_{m}, k_n, and k_{-n} values were taken from the literature and used as preliminary estimates. These values were changed to improve the fit to the experimental data. The detailed tables for the model parameter values are available in the original papers (Lebedeva et al. 2000, 2002; Kamali et al. 2004; Belyaeva et al. 2008).

Classical experimental fluorescence induction curves at different light intensities (Strasser et al. 1995) are presented in Fig. 11.1. Our model, including the description of the whole electron-transport chain, allows us to simulate the shape of fluorescence induction curves at low, intermediate, and high light intensities. The low, middle, and high intensities correspond to 15, 150, and 1,500 quanta s^{-1} for PSI and PSII. The light intensities were set with the appropriate values of the light-dependent rate constants k_i (i = 1, 5, 8, 12, 15, 19, 28, 32, 68) (schemes of PSII and PS I complexes, Figs. 11.2 and 12.1). The time-dependent relative fluorescence yield after the onset of illumination (Fig. 12.4) was calculated according to Eq. (12.1).

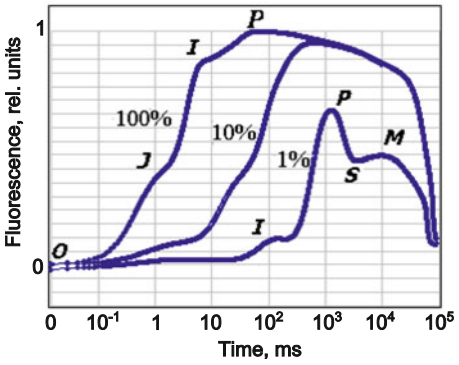


Fig. 12.4 Simulated chlorophyll fluorescence yield induction curves at different light intensities: 600 (100 %), 60 (10 %), and 6 (1 %) W m^{-2} (Lebedeva et al. 2002). See Fig. 11.1 for corresponding experimental data

To simulate changes in the state of the photosynthetic system after the start of illumination, we had to establish the initial values of the variables that would correspond to the dark state of the system. The stationary solution was obtained in the case where all the light-dependent rate constants were zero and the average chloroplast volume was 40 μm^3; P700 content was 2 mmol/mol chlorophyll; the chloroplast stroma, thylakoid lumen, and thylakoid membrane volume ratio was 10:1:1. The stoichiometry of PSII, Cyt b_6f, PSI, PQ, and Pc in the thylakoid membrane was taken to be 1:1:1:6:2.

Simulation of Fluorescence Transients at Different Light Intensities

For the simulation we used the general model, including the processes presented in Fig. 12.1. The schemes of the submodels of individual photosynthetic complexes are presented in Figs. 11.2, 12.2, and 12.3 and were described earlier.

The model provides a rather good fit of simulations and experimental fluorescence transients, not only for high light intensities as published earlier (Stirbet et al. 1998; Strasser et al. 2004; Zhu et al. 2005; Lazar 2003; Lazar et al. 2005) but also for low and middle light intensities. At low values of the light-dependent constants corresponding to low illumination (1 % or 6 W m^{-2}), fluorescence reaches its maximum in approximately 1–2 s, and the induction curve exhibits one intermediate phase (200 ms). A tenfold increase in the light constants corresponding to medium illumination (10 %, 60 W m^{-2}) causes a rise in the signal and shortens the time it takes to reach the maximum (approximately 50 ms), while the intermediate phase becomes less pronounced. At high light intensity (100 %, 600 W m^{-2}) fluorescence transient acquires its classical OJIP shape, reaching its peak in 100–200 ms, with two intermediate phases (J approximately 2 ms and I approximately 20 ms).

Role of Different States of Photosystem II in Fluorescence Induction

Analysis of the model showed that to simulate a fluorescence induction curve at low light intensity and over time intervals longer than 1 s (the slow phase of fluorescence induction), it is necessary to include in the model electric and electrochemical potentials, as well as the processes occurring in Cyt b_6f and PSI.

In Fig. 12.5, transformations of the system components in response to illumination are presented. Chlorophyll fluorescence yield (curve F) and electric potential (curve $\Delta\Psi$) transients are presented in Fig. 12.5a. In Fig. 12.5b, we plotted the time dependencies of the concentrations of PSII states capable of emitting fluorescence

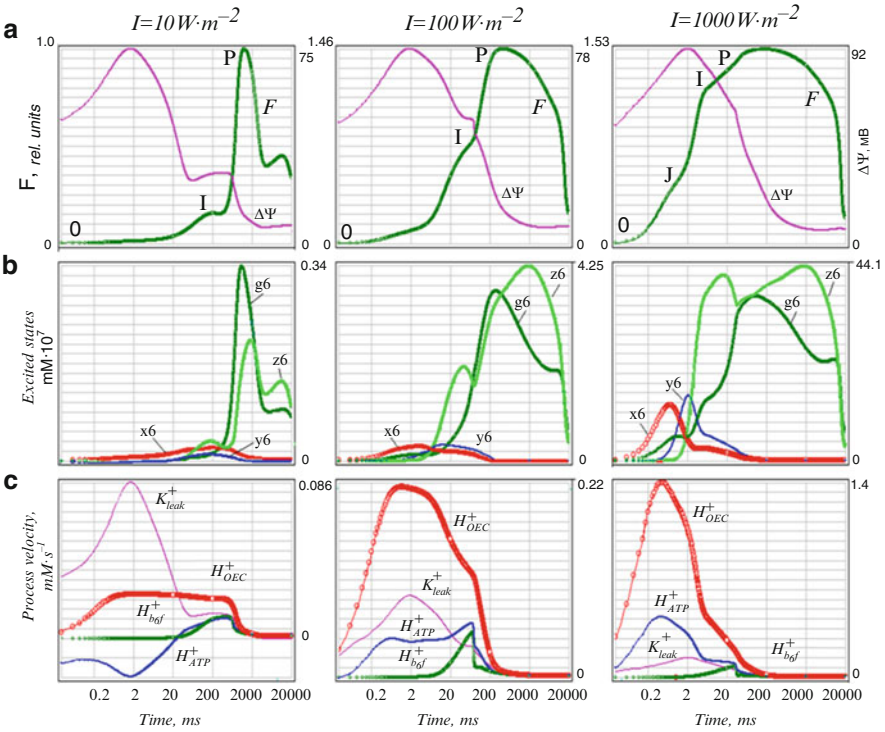


Fig. 12.5 Simulated induction curves for three different intensities of illumination: 1,000 (100 %), 100 (10 %), and 10 (1 %) W m^{-2}. The *pictures* in each column correspond to the same intensity of illumination. Results are presented on a logarithmic time scale. (**a**) Fluorescence yield (F) and transmembrane electric potential ($\Delta\Psi$). (**b**) Concentration of different excited states of photosystem II (see Fig. 11.2 for details). (**c**) Rates of processes generating and consuming electric charge in thylakoid lumen. H^+_{bf}: proton flux directed into lumen by plastoquinone reduction at lumen site of Cyt b_6f complex; H^+_{OEC}: proton flux directed into lumen from oxygen evolving (i.e., water-oxidizing) complex (WOC) of photosystem II; H^+_{ATP}: rate of proton consumption in ATP–synthase reaction; H^+_{leak}: rate of leakage of H^+ ions from lumen of thylakoid (Rubin and Riznichenko 2009)

(shaded in Fig. 11.2). Simulation experiments revealed that at all light intensities the contribution of the states with oxidized Q_A to the fluorescence transients was at least one order of magnitude lower than the contribution of the states with reduced Q_A. This is in accordance with the existing idea that variable fluorescence is approximately proportional to the concentration of the closed (Q_A^--containing) reaction centers of PSII (Stirbet et al. 1998; Strasser et al. 2004). For this reason only PSII fluorescing states z_6 (Chl*Phe$Q_A^-Q_B^{2-}$), g_6 (Chl*PheQ_A^-), x_6 (Chl*Phe$Q_A^-Q_B$), and y_6 (Chl*Phe$Q_A^-Q_B^-$) with reduced Q_A are presented in Fig. 12.5b.

The relative concentration of each of the fluorescing forms depends on the light intensity. Under low intensity, fluorescence is emitted mostly by the states g_6 (Chl*PheQ_A^-, quinone acceptor with reduced Q_A and vacant Q_B) and z_6 (Chl*Phe$Q_A^-Q_B^{2-}$). Indeed, these states are generated due to light absorption from g_5 (ChlPheQ_A^-) and z_5 (ChlPhe$Q_A^-Q_B^{2-}$), where electron transfer cannot proceed from Q_A since the secondary acceptor is either absent or fully reduced. Since the PQ binding to the Q_B site and PQH_2 dissociation are relatively slow processes, the states g_5 (Chl PheQ_A^-) and z_5 (Chl Phe$Q_A^-Q_B^{2-}$), and hence g_6 (Chl*PheQ_A^-) and z_6 (Chl*Phe$Q_A^-Q_B^{2-}$), can accumulate at greater concentrations than the corresponding x and y, where the secondary acceptor is not fully reduced and the Q_A^- electron can be transferred further to Q_B to produce y_1 (ChlPhe$Q_AQ_B^-$) and z_1 (ChlPhe$Q_AQ_B^{2-}$) states. At low light intensities the rate of this process exceeds the rate of formation of the excited states, so that fluorescing forms x_6 (Chl*Phe$Q_A^-Q_B$) and y_6 (Chl*Phe$Q_A^-Q_B^-$) are minor. Under moderate illumination, the fluorescence of the system is also mostly determined by the sum of g_6 and z_6, though the populations of x_6 (Chl*Phe$Q_A^-Q_B$) and y_6 (Chl*Phe$Q_A^-Q_B^-$) increase slightly, too.

Under intense illumination, the contribution of x_6 (Chl*Phe$Q_A^-Q_B$) and y_6 (Chl*Phe$Q_A^-Q_B^-$) to fluorescence becomes comparable to that of g_6 (Chl*PheQ_A^-) and z_6 (Chl*Phe$Q_A^-Q_B^{2-}$) because the time between the successive photon hits becomes close to the time of the electron transfer from Q_A to Q_B. The fluorescence induction curve (Fig. 12.5, upper row) exhibits two distinct intermediate phases, J and I, the J phase provided by x_6 and y_6 and the I phase largely by z_6, while g_6 contributes to both of them.

From Fig. 12.5a, b we can draw some conclusions concerning the origins of the phases J, I, and P for different light intensities. The peak P corresponds to the maximum value of the sum of concentrations of PSII fluorescing states with closed quinone acceptor complexes g_6 (Chl*PheQ_A^-) and z_6 (Chl*Phe$Q_A^-Q_B^{2-}$). Phase I is distinctly pronounced at any illumination intensity, and the time to reach this phase shortens with increasing light intensity. The onset of this phase roughly corresponds to the appearance of an intermediate maximum on the curve for the z_6 state content. Phase J is clearly discernible only under sufficiently intensive light and is associated with the accumulation of fluorescing states in which the acceptor is not fully reduced (not more than one electron on Q_B).

In this model, we do not consider the role of nonphotochemical FL quenching, known to contribute to FL decay after the maximum P after 1–2 s but demonstrating the role of electron fluxes between the two photosystems responsible for the Fl decay in the time range 1–10 s.

Simulation of $\Delta\Psi$ Kinetics

The analysis of data in Fig. 12.5 reveals explicitly the kinetics of $\Delta\Psi$ and the generation of different redox states, taking part in fluorescence induction and ion fluxes. We suggest that at any moment $\Delta\Psi$ is determined by the electric charge difference between lumen and stroma. Figure 12.5 depicts the time changes in the rates of processes involved in the generation and utilization of electric charge differences in the lumen. In the left-hand panel one can see that the emergence of the $\Delta\Psi$ slow phase coincides with the establishment of the quasi-steady phase I on the Fl induction curves. This means that over the period of time from 50 to 300 ms processes proceeding in the opposite direction largely counterbalance each other. From 50 to 200 ms the proton influx to the lumen increases due to plastoquinol oxidation at the luminal side of the Cyt b_6f complex (Fig. 17c, $H^+_{b/f}$). The system accumulates states with Q_B^{2-}, which upon protonation dissociates from PSII. The presence of plastoquinol at the stromal side of the thylakoid membrane triggers Cyt b_6f complex operation. Proton influx from the oxygen evolving complex (H^+_{OEC}) is balanced by the K^+ and Mg^{2+} outflow and proton consumption in the ATP–synthase reaction (H^+_{ATP}). In addition, a fraction of protons is bound by the buffer. As a result, the evolving slow phase in the transmembrane potential kinetics leads to the inhibition of the electron transfer in potential-dependent reactions of PSII: electron transfer at the donor side from the oxygen evolving complex (OEC) to $P680^+$ and the electron transfers Phe $\rightarrow Q_A$ and $Q_A \rightarrow Q_B$ at the acceptor side. Such inhibition, in turn, hinders the rise of the z_6 (Chl*Phe$Q_A^-Q_B^{2-}$) population and produces the intermediate minimum (Fig. 12.4b), resulting in the appearance of the I phase on the FL induction curve (Fig. 12.4a).

The breakdown of the quasi-steady state over 300–600 ms described earlier (Fig. 12.4c) is caused by the activation of PSI processes, with the enhancement of the cyclic electron transfer resulting in competition for PQ between PSII and the Cyt b_6f complex. As a consequence, the elevated concentrations of the fluorescing forms g_6 (Chl*PheQ_A^-) and z_6 (Chl*Phe$Q_A^-Q_B^{2-}$) result in enhanced fluorescence.

Thus, analysis of the model shows the dynamics of the separate states of the PSII complex, ion fluxes, and electric potential generation kinetics. It explains the main characteristics of the fluorescence induction curves. The model also allows us to obtain information on $\Delta\Psi$ generation under different experimental conditions.

The described general kinetic model can accurately simulate the main features of fluorescence induction curves. Such modeling can be used as a tool to study specific features of the photosynthetic machinery and its differences in, for example, various species, ecological niches, and growth conditions. Different stress effects (inhibitors, starvation) modify the patterns of fluorescence induction curves, resulting in sharp differences after 1–2 s from the onset of illumination. These distinctions are often related to the oxygen stress effects, damage in the protein synthesis system, and other processes. The mechanisms of the latter are not known in detail, but we should include them in the models as a tool for quantitative analysis in biotechnological and ecological monitoring.

The classic kinetic approach proved to be productive in evaluating the rate constants of individual reactions of electron transport and the ratios of energy fluxes at different steps of the electron transport chain. However, using only differential equations it is difficult to take into account the spatial heterogeneity and complex geometry of interacting macromolecules, as well as the interior of the photosynthetic membrane where these interactions occur. To solve this problem we have developed direct multiparticle models, which mimic processes at the molecular level.

Part IV
Direct Multiparticle Models of Processes in Subcellular Systems

Chapter 13
Method of Direct Multiparticle Simulation of Protein Interactions

Electron transport processes in the photosynthetic and mitochondrial membranes of a cell are mediated by protein–protein complexes and mobile carriers. For a general kinetic description of these reactions mathematical models have been developed where some modifications of the mass action law are used. The rate constants of biochemical reactions of protein–protein association and concentrations of donor and acceptor protein molecules serve as parameters in these kinetic models. Rate constant values are determined under various conditions (e.g., different pH, ionic strength) and evaluated according to experimental data; therefore, the corresponding kinetic models are essentially phenomenological since their rate constants have effective values.

In recent papers, models based on modern structural and kinetic data have been presented simulating separate stages of electron transport processes. The most advanced are kinetic models of photosynthetic electron transfer between components within multienzyme complexes (Stirbet, et al. 1998; Riznichenko et al. 2009; Rubin and Riznichenko 2009; Lazar 2003, 2006; Strasser et al. 2004; Zhu et al. 2005; Belyaeva, et al. 2008, 2011) and models of complex formation between two mobile proteins based on a Brownian dynamics (BD) approach (Ullmann et al. 1997; Pearson and Gross 1998; Rienzo et al. 2001; Gross and Pearson 2003; Gross and Rosenberg 2006).

In subcellular energy-transforming systems—chloroplasts and mitochondria—redox reactions occur in the limited space between membranes of complex geometry. To simulate the behavior of such subcellular systems in vivo, it is necessary to consider individual pairs of interacting molecules and their ensembles in confined reaction volumes with real geometrical characteristics. We developed a new direct multiparticle simulation method (DMSM) where dynamic behavior is considered in the molecular surroundings representing the real intracellular interior of protein complexes (Kovalenko et al. 2003, 2006, 2007, 2008, 2009; 2011a, b, c; Riznichenko et al. 2009, 2010; Rubin and Riznichenko 2009).

A. Rubin and G. Riznichenko, *Mathematical Biophysics*, Biological and Medical Physics, Biomedical Engineering, DOI 10.1007/978-1-4614-8702-9_13,

© Springer Science+Business Media New York 2014

As an object for the simulation we considered a system of photosynthetic electron transport investigated thoroughly in the literature (Malkin and Niyogi 2000). For this system the structural data on the composition of protein components in the photosynthetic chain, rate constants of protein interactions in solution at different ionic strength values, rate constants of electron transfer in chloroplast thylakoids are well known (Part III).

Restricted Diffusion of Mobile Electron Carriers in Photosynthetic Membrane

Kinetic models of photosynthetic processes, described in Chap. 15 and based on ODEs, assume a homogeneous distribution of the interacting components in the reaction volume at each moment. However, there are data showing that multienzyme complexes are distributed heterogeneously in a membrane. For example, PSI complexes are concentrated in the stroma-exposed part, while PSII complexes are located in granal (appressed) parts of the thylakoid membrane (Albertsson 2000, 2001; Nelson and Yocum 2006). Electron microscopy data show the existence of membrane areas where multienzyme complexes form small local microdomains, and their concentration may be high enough to prevent free diffusion of plastoquinone (PQ) (Joliot et al. 1992; Kirchhoff et al. 2000, 2002). Within each domain PQ diffuses rapidly, but long-distance migration of PQ is restricted. As a result, plastocyanin (Pc) is assumed to play the main role in electron transport over long distances.

The small copper protein Pc diffuses in the lumen and transfers electrons from cytochrome f (Cyt f)—a subunit of the cytochrome b_6f complex—to P700, a reaction center of PSI (Hope 2000; Nelson and Yocum 2006). The difference in the Pc concentrations in granal and stromal areas of the membrane during light–dark transitions was interpreted as evidence for long-distance transport between these compartments (Haehnel et al. 1989).

The mobility of Pc molecules is restricted by the membrane complexes protruding into the lumen space. The mechanism of Pc mobility in a lumen is of special interest. In native chloroplasts the luminal space is narrow (40–100 Å) and contains proteins protruding from the thylakoid membrane. Since the size of the Pc molecule ($40 \times 28 \times 30$ Å) is close to the thickness of a lumen, the diffusion of Pc in a lumen is obviously hindered by the membrane protein complexes located there (Hope 2000; Kirchhoff et al. 2000; Dekker and Boekema 2005; Shimoni et al. 2005). It is not clear how Pc can rapidly diffuse over a distance of hundreds of nanometers between grana stacks and stroma lamellae. The 30–50 μs lag phase of Cyt f oxidation, after a saturating light pulse, shows that it takes some time for the oxidized Pc to diffuse from P700 to the nearest Cyt b_6f complex (Haehnel et al. 1980). This lag is followed by the multicomponent relaxation kinetics that

may correspond to different Pc diffusion distances. In addition, it is not clear whether the diffusion of Fd in the stromal space is free as well.

Electron flux rates at the diffusional stages are strongly regulated by cellular factors, such as pH, temperature, endogenous inhibitors, and metabolites. Changes in the geometry of the system can even block electron transport, as happens during hyperosmotic stress (Cruz et al. 2001), and conversely, illumination as an external factor influences the geometry of a system in a way that promotes electron transfer (Kruger et al. 1997).

Thus the basic assumption of kinetic modeling by differential equations—free random diffusion of mobile carriers and a homogenous structure of the reaction system—is far from reality. Therefore, interaction of individual protein molecules started to be simulated using a BD approach (Pearson et al. 1996; Pearson and Gross 1998; Ullmann et al. 1997; Gross and Pearson 2003; Gross 2004; Haddadian and Gross 2005, 2006; Gross and Rosenberg 2006). BD models are used to investigate processes of complex formation, to predict the structure of complexes, and to estimate the rate constants of protein association. Following this approach proteins are treated as rigid or semirigid bodies, their geometric shape is considered at an atomic resolution, and electrostatic interactions are described in great detail. However, the BD approach does not consider interactions of ensembles of molecules like those proceeding in the interior of photosynthetic membranes.

Direct Model Environment

The structural features of heterogeneous photosynthetic membranes can be described by direct multiparticle computer models. Such modeling allows us to design a 3D visual dynamic image of processes proceeding simultaneously and to trace the individual behavior of separate components.

The direct multiparticle 3D model is represented by a 3D environment comprised of a thylakoid membrane and luminal and stromal spaces. Visualization of the 3D environment for a model of cyclic electron transport around PSI (described in detail below) is presented in Fig. 13.1. The inner volume of the thylakoid is restricted by two membrane planes. Membranes contain PSI, Cyt b_6f complexes, and hypothetical complexes of Fd-PQ-reductase (FQR), designated as R. The question as to whether FQR is a separate complex or a subunit of PSI or Cyt b_6f is still a subject of discussion (Chow and Hope 2004; Yamashita et al. 2007). In the version presented in Fig. 13.1, these complexes are fixed in the membrane. The concentrations and sizes of the complexes were chosen based on data presented in the literature (Albertsson 2000, 2001; Dekker and Boekema 2005; Nelson and Yocum 2006; Shimoni et al. 2005). Inside the thylakoid lumen mobile molecules of Pc carry charges; similarly, mobile molecules of Fd carry charges in the stroma. PQ (PQH_2) molecules move inside the membranes.

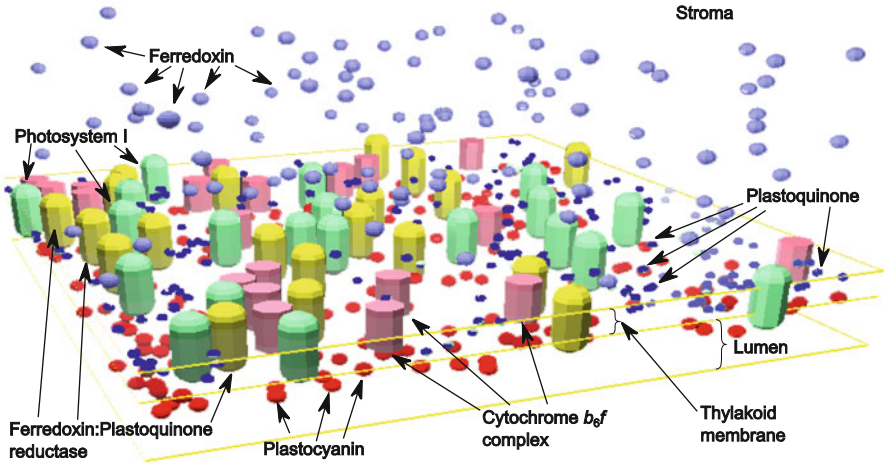


Fig. 13.1 Visualization of 3D environment for direct multiparticle 3D model of cyclic electron transport around PSI. Segments of thylakoid membrane, luminal space, and stromal space are shown (Kovalenko et al. 2007)

Brownian Dynamics of Mobile Carriers

To simulate the movement of Pc, PQ, and Fd in corresponding compartments we use the formalism of BD, taking into account the geometrical restrictions of the created model scene. We assume that particles move in a viscous medium under the influence of random forces:

$$\xi \frac{dx}{dt} = f(t). \tag{13.1}$$

According to the fluctuation-dissipation theorem (Kubo 1966) $f(t)$, a random force, is normally distributed with zero mean value and a standard deviation of $2kT\xi$ (k is Bolzmann's constant and T is temperature). The friction coefficient for a spherical particle is $\xi = 6\pi\eta a$, where η is the viscosity of the medium and a is the radius of the particle.

The mechanism of the electron transfer is considered as follows. If a mobile carrier via chaotic Brownian diffusion approaches a protein complex at a distance shorter than a given effective radius of interaction, the carrier docks to the complex with some probability. The docking probability and the effective radius of interaction are parameters of the model, which are different for different types of complexes and mobile carriers (Fig. 13.2).

To estimate the effective radii and probabilities of interactions between the participants of photosynthetic electron transport we analyzed kinetic data for interactions of proteins in solution (Kovalenko et al. 2006, 2007). The results of direct computer experiments show that the observed rate constant of interaction

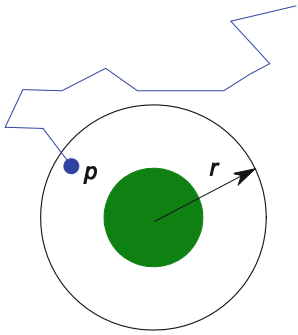


Fig. 13.2 Radius and probability of interaction

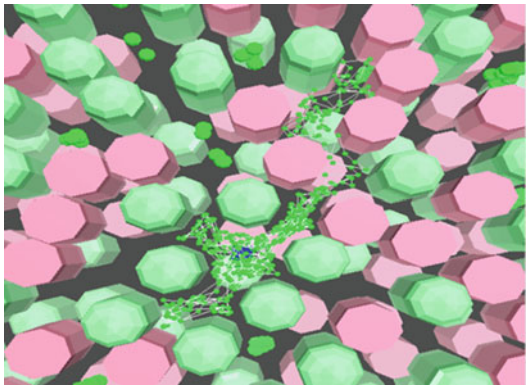


Fig. 13.3 Model trajectory of a PQ particle in a membrane with PSI and Cyt b_6f complexes. One can see that closely packed complexes limit the diffusion of PQ molecules (Kovalenko et al. 2007)

between two proteins in solution strongly depends on the shape of the volume where these interactions occur. Thus the rate of interaction between Pc and Cyt f molecules is much lower in a narrow luminal space than in a wide one, provided that concentrations are equal (Kovalenko et al. 2007).

Equation (13.1) was solved numerically for every electron carrier. The states of the complexes, the mechanisms of their interactions with mobile carriers, and the physical laws of carrier movements were determined by rules described in (Ustinin et al. 2009, 2013).

In Fig. 13.3, the model trajectory of a PQ molecule in a membrane containing PSI, PSII, and Cyt b_6f complexes is presented. Values of the concentrations and sizes of protein complexes were taken from the literature (Staehelin and Van der Staay 1996; Albertsson 2001). The PSI particle density in the membrane was taken to be 8.47×10^{-4}, that of Cyt b_6f was 3.5×10^{-4}, and that of PSII was 2.2×10^{-4} particles nm^{-2} (Albertsson 2001). The number of FQR complexes was assumed to be equal to the number of PSI complexes. The size of PSI in the lateral plane was 13 nm, that of Cyt b_6f 9 nm, and of PSII 13 nm. PSII complexes are not included in Fig. 13.3 for the sake of intelligibility of the picture.

Simulation of Cyclic Electron Transport Around Photosystem I

The method of direct simulation was applied to a description of cyclic electron transport around PSI (Kovalenko et al. 2003, 2007). Computer simulations adequately describe the experimental kinetics of the EPR signal, registered in thylakoids from pea leaves (*Pisum sativum*) in anaerobic conditions (Krendeleva et al. 2001; Kovalenko et al. 2003). In these experiments, DCMU [(3-3,4-dichlorophenil)-1,1 dimethylurea], trade name - Diuron, was added to the reaction mixture to block electron transport from PSII. Recently, similar kinetics of P700 redox transformations due to cyclic electron flow around PSI in spinach leaves were published (Fan et al. 2007).

Figure 13.4 presents a kinetic scheme of cyclic electron transport around PSI in chloroplasts. It includes the docking of molecules of the mobile carrier Fd on the acceptor site of PSI and participation of the Cyt b_6f complex in redox transformations of PQ. We assume that electron transfer from Fd to PQ occurs through the hypothetical ferredoxin–quinone–reductase (FQR) complex, which has a Fd docking site exposed to the stromal space and a PQ docking site exposed inward (Bendall and Manasse 1995).

The kinetic model simulates experimental data on the P700 reduction kinetics with fast and slow components at different Fd concentrations. As in the experiments, the amplitude and contribution of the fast phase of the P700 reduction

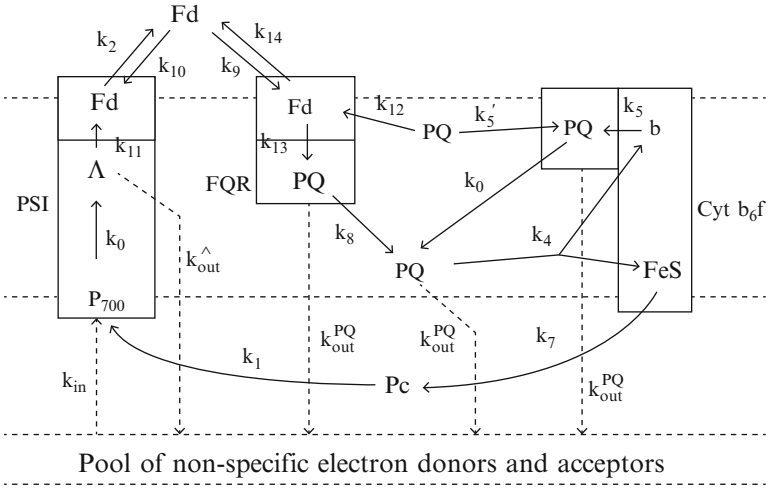


Fig. 13.4 Scheme of kinetic model of cyclic electron transport around PSI. *Boxes*: PSI, FQR, and Cyt b_6f complexes; P700: pigment of PSI reaction center; A: generalized acceptor; FeS: Rieske iron–sulfur center; b: high-potential cytochrome b_h; Fd: ferredoxin; Pc: plastocyanin; PQ: plastoquinone; PQ^{2-}: plastoquinol; $PQ^{-}{}_n$: semiquinone at *n* site of Cyt b_6f (at stromal side of membrane). *Arrows*: electron transport pathways; k_{in}, k_{out}, k_1, …, k_{14}: rate constants for respective reactions of electron transfer. *Dashed lines*: thylakoid membrane and hypothetical pool of nonspecific electron donors and acceptors (Kovalenko et al. 2003)

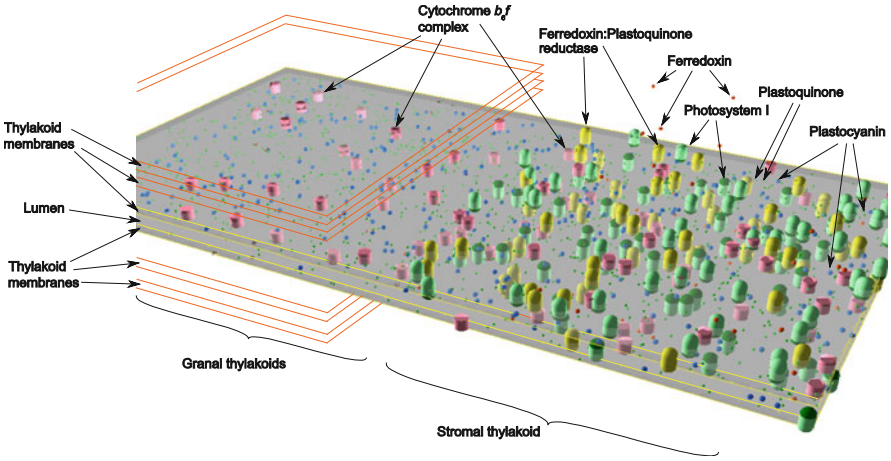


Fig. 13.5 Visualization of 3D scene of granal and stromal parts of thylakoid membrane in multiparticle model of cyclic electron transport. PSII complexes are not shown, although they were simulated (Kovalenko et al. 2007)

increase with Fd concentration, while its characteristic time barely changes, being determined by the rate of PQ interactions with Cyt b_6f.

However, to correctly simulate the slow phase, we needed to introduce a space heterogeneity of the system (Cleland and Bendall 1992; Bendall and Manasse 1995; Scheller 1996), which probably is the real reason for the existence of the slow phase in P700 reduction. As assumed by Albertsson (2001), cyclic transport takes place in the intergranular stromal lamellae, whereas linear transport occurs in granular terminal areas of thylakoid membranes. Accordingly, the 3D scene of the direct model (Fig. 13.5) has two different adjoining areas—granal and stromal.

In the computer simulation the system was illuminated for 1.5 min, as was done in the real experiments. During this time, PQH_2 molecules, reduced by Fd via FQR, were uniformly distributed in granal and stromal areas. After switching off the light, electrons from the PQH_2 pool continued to transfer to Pc via the Cyt b_6f complex. This process occurs in the granal as well as in the stromal area because Cyt b_6f complexes are distributed uniformly in the membrane. In the stromal area, reduced Pc molecules quickly transfer electrons to PSI reaction centers with a characteristic time of 200 ms. The process corresponds to the fast phase of $P700^+$ reduction. As in the experiments, the fast reduction of $P700^+$ is not complete, but a fraction of $P700^+$ remains in oxidized form (Fig. 13.6a). The direct model demonstrates that this effect is due to the fact that a certain number of electrons is still bound to molecules of PQ and Pc in the granal parts of the membrane, where PSI is absent.

Later diffusion of PQ inside the membrane and diffusion of Pc in the luminal space occur: electrons gradually return to the stromal area, where an additional $P700^+$ reduction takes place. The characteristic time of this reduction phase is approximately 10 s, and it is determined by the size of the system. This result explains why the time course of the reduction of photo-oxidized $P700^+$ can be

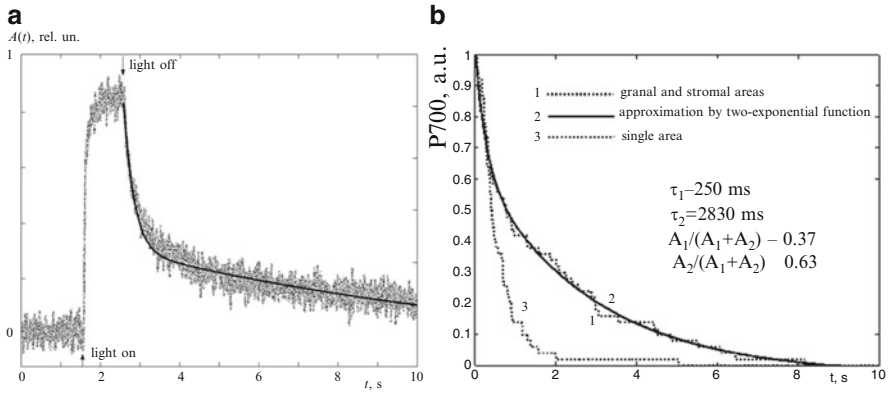


Fig. 13.6 Two kinetic phases (fast and slow) of postillumination reduction of PSI photoactive pigment P700. (**a**) Experimental EPRsignal. (**b**) Kinetics of $P700^+$ reduction obtained by direct model simulation (Kovalenko et al. 2007). τ_1, τ_2, A_1, A_2—characteristic times and amplitudes of fast and slow phases

approximated by the sum of two exponents (Fig. 13.6). Thus the direct multiparticle model naturally explains the existence of two phases of the dark reduction in a heterogeneous system without additional artificial assumptions on the existence of an external pool of nonspecific donors and acceptors.

The direct modeling of the cyclic electron transport around PSI demonstrates that the experimentally observed redox kinetics of the electron carriers are determined not only by concentrations, redox states, and conformations of the proteins, but also by the spatial distribution of the mobile carriers and the configuration of the reaction volume (lumen, stroma). It is known that changes in the physiological state of a cell leading to different pH and salt concentrations results in changes in the distances between thylakoid grana and in the geometry of the system. The direct model approach allows us to see how these changes affect the kinetic characteristics of photosynthesis.

Chapter 14
Modeling of Protein Complex Formation in Solution with Diffusion and Electrostatic Interactions

In the first versions of the direct multiparticle simulation method, protein interactions were treated as simple collisions, as described in Chap. 13. However, electron-carrying proteins have rather complicated shapes. To perform electron transfer, donor and acceptor carriers should form a complex in which the distance between the active sites must be small enough to support electron tunneling from the donor molecule to the acceptor molecule. Therefore, their proper mutual orientation in a complex stabilized by means of van der Waals and hydrophobic interactions, hydrogen bonds, and other biochemical interactions is necessary.

Steps of Redox Protein Interactions

Electron transfer between proteins proceeds via the following steps (Fig. 14.1):

1. Protein diffusion to the docking point (or diffusion of the mobile protein to another protein embedded in the membrane multienzyme complex);
2. Mutual orientation of proteins under the effect of electrostatic interactions;
3. Formation of preliminary complex;
4. Conformational changes and final complex formation, where active sites come close to each other;
5. Charge transfer (tunneling) from one protein carrier to another;
6. Dissociation of complex.

Both donor and acceptor proteins may be mobile in solution or, as occurs in photosynthetic electron transport, only one of the proteins may be mobile (as Pc in thylakoid lumen) while the other is an element of a multienzyme complex embedded in the membrane. An example is the supercomplex of Cyt and Pc as shown in Fig. 15.2.

In the process of complex formation between donor and acceptor proteins or anchoring of the mobile carrier in the multienzyme membrane complex, electrostatic forces play a significant role.

A. Rubin and G. Riznichenko, *Mathematical Biophysics*, Biological and Medical Physics, Biomedical Engineering, DOI 10.1007/978-1-4614-8702-9_14,
© Springer Science+Business Media New York 2014

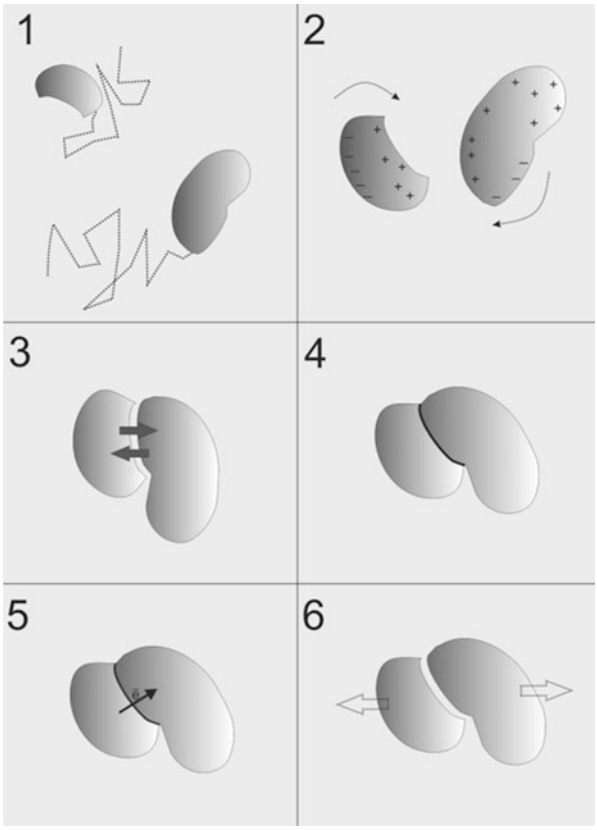


Fig. 14.1 Electron transfer steps between proteins in solution. *1* Diffusional movement (translational and rotational). *2* Relative orientation of interacting proteins under influence of Brownian and electrostatic forces. *3* Proper mutual localization (preliminary complex). *4* Transition from preliminary complex to final complex. *5* Electron transfer between active sites of donor and acceptor proteins. *6* Dissociation of complex and formation of a pair of proteins

In recent years, the Brownian dynamics (BD) approach (Pearson and Gross 1998; Ullmann et al. 1997; Gross and Pearson 2003; Gross 2004; Haddadian and Gross 2005, 2006; Gross and Rosenberg 2006) has been used to simulate interactions of two individual protein molecules. Following the BD approach it is possible to predict the structures of complexes and estimate the rate constant values of complex formation using the probability of protein binding obtained in computer experiments (Gabdoulline and Wade 1997, 1998). However, in such BD models, interactions of ensembles of molecules like those in the interior of photosynthetic membranes are not considered.

Model of Protein–Protein Interaction in Solution

Before the actual simulation of protein interactions in the subcellular interior, it is necessary to construct an adequate model of protein interactions in solution in order to estimate the parameters of the direct multiparticle simulation method (DMSM). To investigate the effects of protein shape, the geometry of the reaction volume, and

the electrostatic interactions on the observed kinetic characteristics, in particular on the rate constant values, we first simulate protein interactions in solution. On the basis of experimental data on the kinetics of processes in solution, we evaluate the parameters introduced in the multiparticle model, i.e., probabilities and distances characterizing protein interactions. These models were developed by us to simulate individual interactions in solution of cytochrome f with plastocyanin, a small protein molecule shuttling electrons between the cytochrome b_6f complex and PSI (Kovalenko et al. 2006), ferredoxin (Fd), and ferredoxin:$NADP^+$-reductase (FNR) (Kovalenko et al. 2010), and interactions of multienzyme complex PSI with mobile stromal proteins ferredoxin and flavodoxin (Abaturova et al. 2008).

Interacting molecules are considered Brownian particles that make translational and rotational motions in viscous media due to the collisions of proteins with surrounding molecules. Electrostatic forces are considered only at a distance between molecules under 35 Å (the distance of electrostatic interactions), whereas at greater distances electrostatic interactions were negligible (Finkelstein and Ptitsyn 2002).

Protein Diffusion. Approximation with Ellipsoids of Revolution

To simplify the calculation of viscous friction coefficients, protein molecules are represented as ellipsoids of revolution with axes $2a$, $2b$, and $2c$ ($2a$ is the axis of revolution, $b = c$; Fig. 14.2).

The Langevin equation for translational motion is similar to (13.1), but on the right-hand side we have a sum of projections of the random and electrostatic forces:

$$\xi_{\mathrm{tr}}^{x}\frac{dx}{dt} = f_x(t) + F_x, \quad \langle f_x(t)\rangle = 0, \left\langle f_x(t)^2 \right\rangle = \frac{2kT\xi_{\mathrm{tr}}^{x}}{\Delta t}. \tag{14.1}$$

Here k is the Boltzmann constant, T is temperature, x is a coordinate, ξ_{tr}^{x} is the viscous friction coefficient for the x-axis, and $f_x(t)$ and F_x are projections of the random Brownian force and electrostatic force onto the x-axis, respectively. $F_x = -\,q \cdot (d\varphi/dx)$, q is the charge, φ is the electrostatic potential.

The Langevin equation for the rotational motion is

$$\xi_{\mathrm{rot}}^{x}\frac{d\alpha}{dt} = m_x(t) + M_x, \tag{14.2}$$

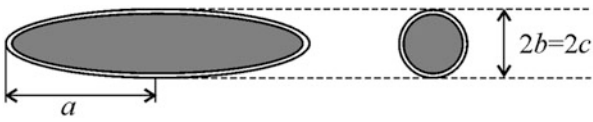


Fig. 14.2 Ellipsoid of revolution

where α is the angle of rotation, ξ^x_{rot} is the viscous friction coefficient for the rotational motion around the x-axis, and $m_x(t)$ and M_x are moments of the random Brownian force and electrostatic force with respect to the x-axis, respectively. The random Brownian force has a normal distribution with zero mean value and dispersion $2kT\xi^x_{\text{tr}}/\Delta t$.

The 3D molecular models are constructed based on Protein Data Bank (PDB) data. The axes and sizes of the ellipsoids are chosen in such a way that the moment of inertia relative to the axis of revolution (axis a) is minimal and equal to the moment of inertia of the protein molecule.

The translational and rotational viscous friction coefficients of the ellipsoid are calculated according to the formulae of Perrin from 1936 (Bloomfield 2000):

$$\begin{aligned}
\xi^a_{\text{tr}} &= \frac{8\pi\eta R\cdot(p^2-1)^{3/2}}{\sqrt[3]{p}\cdot\left[(2p^2-1)\cdot\ln\left(p+\sqrt{p^2-1}\right)-p\cdot\sqrt{p^2-1}\right]},\\
\xi^b_{\text{tr}} &= \frac{16\pi\eta R\cdot(p^2-1)^{3/2}}{\sqrt[3]{p}\cdot\left[(2p^2-3)\cdot\ln\left(p+\sqrt{p^2-1}\right)+p\cdot\sqrt{p^2-1}\right]},\\
\xi^a_{\text{rot}} &= \frac{16\pi\eta R^3\cdot(p^2-1)^{3/2}}{3p\cdot\left[p\cdot\sqrt{p^2-1}-\ln\left(p+\sqrt{p^2-1}\right)\right]},\\
\xi^b_{\text{rot}} &= \frac{16\pi\eta R^3\cdot(p^2-1)^{3/2}(p^2+1)}{3p\cdot\left[(2p^2-1)\cdot\ln\left(p+\sqrt{p^2-1}\right)-p\cdot\sqrt{p^2-1}\right]}.
\end{aligned} \tag{14.3}$$

Here ξ^a_{tr}, ξ^b_{tr} and ξ^a_{rot}, ξ^b_{rot} are friction coefficients for the a and b axes for translational and rotational motion, η is the viscosity of the medium, $2a$ is the axis of rotation, $b = c$, $p = a/b$, and $R = \sqrt[3]{a\cdot b\cdot b}$.

Ellipsoids of revolution for Pc and Cyt f are presented in Fig. 14.3.

For a description of the position of each object in the model scene we chose a Cartesian coordinate system with mirror boundary conditions (the scene coordinate system). To each object a local Cartesian coordinate system is assigned, which coincides with the axes of the respective ellipsoids. Such a choice of local coordinate system is very convenient because the friction coefficients for the ellipsoids in this system are known (formulae 14.3). The Langevin equation is solved numerically in the local coordinate system: at each time step, the displacement of the ellipsoid along its axes and rotations around its axes are calculated. The displacement and rotation values found in the local coordinate system for each object are then recalculated in the scene coordinate system. The position of every object in the model is specified by the displacement and rotation of the local coordinate system of the object with respect to the scene coordinate system.

A visualization of the interactions of proteins Pc and Cyt f is presented in Fig. 14.4.

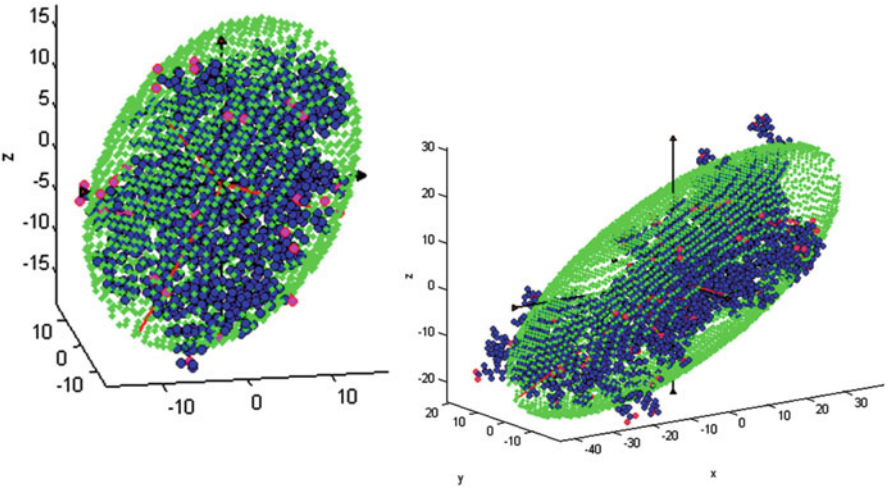


Fig. 14.3 Approximation of plastocyanin and cytochrome f by ellipsoids of revolution for calculation of viscous friction coefficients of molecules (Kovalenko et al. 2006)

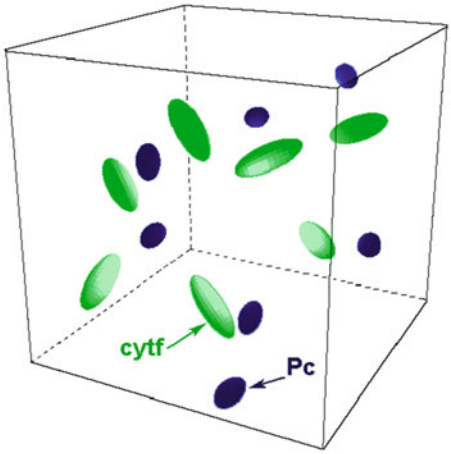


Fig. 14.4 Visualization of model scene of direct multiparticle simulation of interactions between proteins Pc and Cyt f in solution. Proteins are presented as ellipsoids of revolution

Simulation of Geometric Shape of Proteins and Their Collisions

In the model, proteins are considered rigid bodies. They diffuse in the simulated reaction volume and can come close to each other without overlapping. The 3D geometrical surfaces of many proteins (including Pc and Cyt f) are known at an atomic resolution based on the crystal structure of these proteins. The data are from the PDB. In the model, we approximated the surfaces of the molecules by a set of

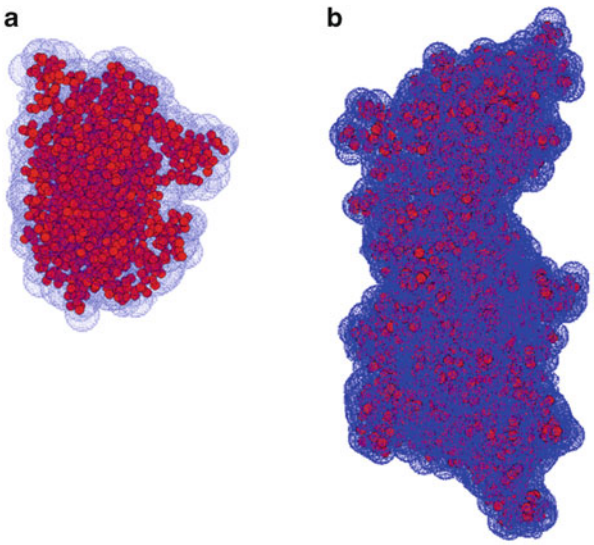


Fig. 14.5 Approximation of surfaces of molecules Pc (**a**) and Cyt f (**b**) with sets of spheres (Kovalenko et al. 2006)

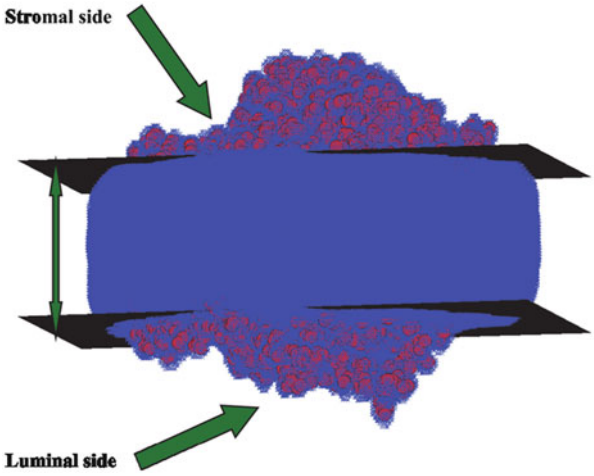


Fig. 14.6 Approximation of surface of PSI complex with set of spheres. The approximation of parts of the molecule protruding from the membrane is more detailed than the approximation of the intramembrane part (Abaturova et al. 2008)

spheres. With this approximation, two molecules overlap if the respective sets of spheres overlap. The geometric interpretation of the surface by a rather small number of spheres (several dozen) is less time consuming than the calculation of each atom overlap. To verify the overlapping of two spheres, it is enough to know the radii and coordinates of their centers.

The radii and coordinates of the spheres are selected in such a way that the deviation in shape from the real protein surface did not exceed 2 Å (in other computer experiments it was no greater than 1 Å). Examples of approximation of protein surfaces with the sets of sphere are presented in Figs. 14.5 and 14.6.

Electrostatic Interactions

The charges of amino acid residues form a heterogeneous electrostatic field around proteins. This field is screened by polar water molecules, which is why the electrostatic potential rapidly decreases with the distance from the protein surface. If a protein is far from another protein, then its motion is determined only by Brownian diffusion. As the protein comes closer to another protein, both move in their common electrical field, so that a mutually favorable position for the formation of a predocking complex may be achieved. It was confirmed by the results of computer experiments that in the presence of electrostatic forces, the proper orientation of proteins is achieved faster and that the rate constant of a reaction increases considerably (by 1–3 orders) compared to the case where proteins collide randomly.

In simulation, protein molecules are presented as a low dielectric area ($\varepsilon = 2$) with spatially distributed fixed partial charges. The surrounding solution has a high dielectric constant ($\varepsilon = 80$). The dielectric constant on the border between protein surface and solution equals 40. As a result of the screening of protein charges by water molecules at a distance of 35 Å in a solution with an ionic strength of 100 mM, the electrostatic potential becomes 80 times smaller than in a solution without ions (Finkelstein and Ptitsyn 2002). Based on these data, we consider electrostatic interactions between proteins only if the distance between them becomes less than 35 Å.

To simulate the effect of the electrostatic force, it is necessary to calculate the value of electrostatic force and its moment and to take into account the influence of other proteins located closer than the electrostatic interaction distance. For this reason we chose a 3D rectangular region around each protein, set up a rectangular grid in the region, and mapped on it charges, dielectric constants, and ionic strength. The step of the grid is a model parameter and determines the accuracy of the potential calculations. If we decrease the grid step at a fixed distance of interaction, then the number of grid cells increases and considerably increases the volume of PC memory used and time of calculation.

Then we calculate the electrostatic potential around all types of objects in the model scene (e.g., for oxidized and reduced forms of both Pc and Cyt f). Formal charges on the proteins are calculated as described in Durell et al. (1990). The value of the ionic strength inside the protein is 0. For other cells the value of the ionic strength is equal to that of the solution. The procedure is illustrated by Fig. 14.7.

To calculate the electrostatic potential grid, the Poisson–Boltzmann approach (Ullmann et al. 1997; Ullmann and Knapp 1999) is used. In the finite difference representation, the electrostatic potential of a given cell on the grid in the nth iteration is calculated by iteration formula (14.4), which takes into account potential values in the neighboring cells from the previous step and the entire charge of the cell. In the nth iteration the electrostatic potential value in the cell is

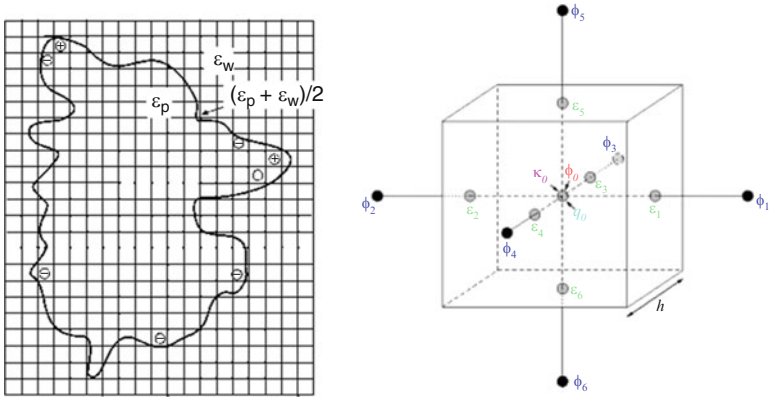


Fig. 14.7 Grid for calculation of electric potential around protein (*left*) and an individual cell (*right*)

$$\varphi_0 = \frac{\left(\sum_{i=1}^{6} h\varepsilon_i\varphi_i\right) + 4\pi q_0}{\left(\sum_{i=1}^{6} h\varepsilon_i\right) + h^3\kappa_0^2}, \tag{14.4}$$

$$\kappa^2 = \frac{8\pi N_A e^2 I}{k_B T}, \quad I = \frac{1}{2}\sum_{i=1}^{K} c_i^{\text{bulk}} Z_i^2,$$

where φ is the electrostatic potential, ε the dielectric constant, q_0 the charge density, c_i^{bulk} the concentration of the ith ion in solution, Z_i the charge of the ith ion, e the electron charge, T the temperature (K), N_A Avogadro's number, I the ionic strength of the solution, and h the step of the grid.

Thus, for each type of object (proteins in reduced and oxidized states) we know the value of the electrostatic potential in the fixed area around it. Now to calculate the force and its moment affecting an individual charge on the protein, it is necessary to calculate the potential gradient created by other charges at the point where the charge is situated. To calculate the electrostatic force and its moment applied to an entire protein molecule, we geometrically sum the forces and their moments applied to every charge of the molecule.

Figure 14.8 represents the proteins Pc and Cyt f and the calculated equipotential surfaces around them (Kovalenko et al. 2006). Figure 14.9 shows the proteins Fd and FNR (Diakonova et al. 2008), and Fig. 14.10 shows PSI with a light-harvesting complex and the corresponding equipotential surfaces (Abaturova et al. 2008).

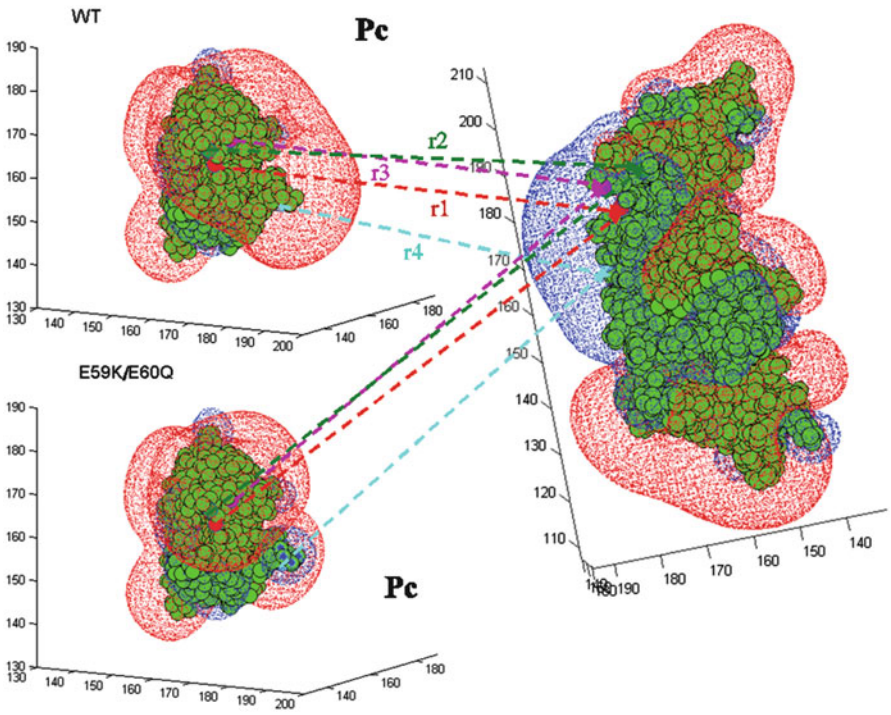


Fig. 14.8 Equipotential surfaces −6.5 mV (*red*) and +6.5 mV (*blue*) for reduced Cyt f (*right*) and oxidized Pc (wild type and mutant E59K/E60Q), calculated by Poisson–Boltzmann equation; ionic strength = 100 mM, pH = 7, $\varepsilon_{sol} = 80$, $\varepsilon_{prot} = 2$. The *lines* connect amino acid residues on Pc and Cyt f used in the simulation for calculation of the distance between the proteins. For mutant Pc the *black points* represent atoms with changed charges relative to the wild type (Kovalenko et al. 2006)

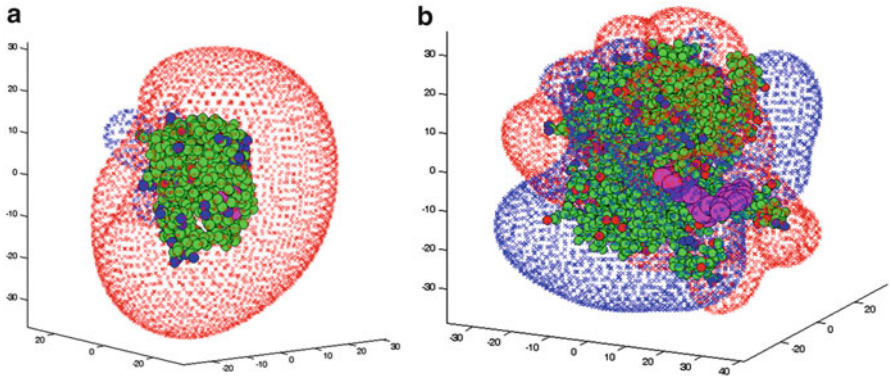


Fig. 14.9 Equipotential surfaces −6.5 mV (*red*) and +6.5 mV (*blue*) for reduced wild-type Fd (**a**) and oxidized wild type FNR (**b**) calculated using Poisson–Boltzmann equation; ionic strength = 100 mM, pH = 7, $\varepsilon_{sol} = 80$, $\varepsilon_{prot} = 2$. *Green spheres*: atoms of molecule, *pink spheres*: cofactors [2Fe–2S]-cluster and FAD of ferredoxin and FNR, respectively (Diakonova et al. 2008)

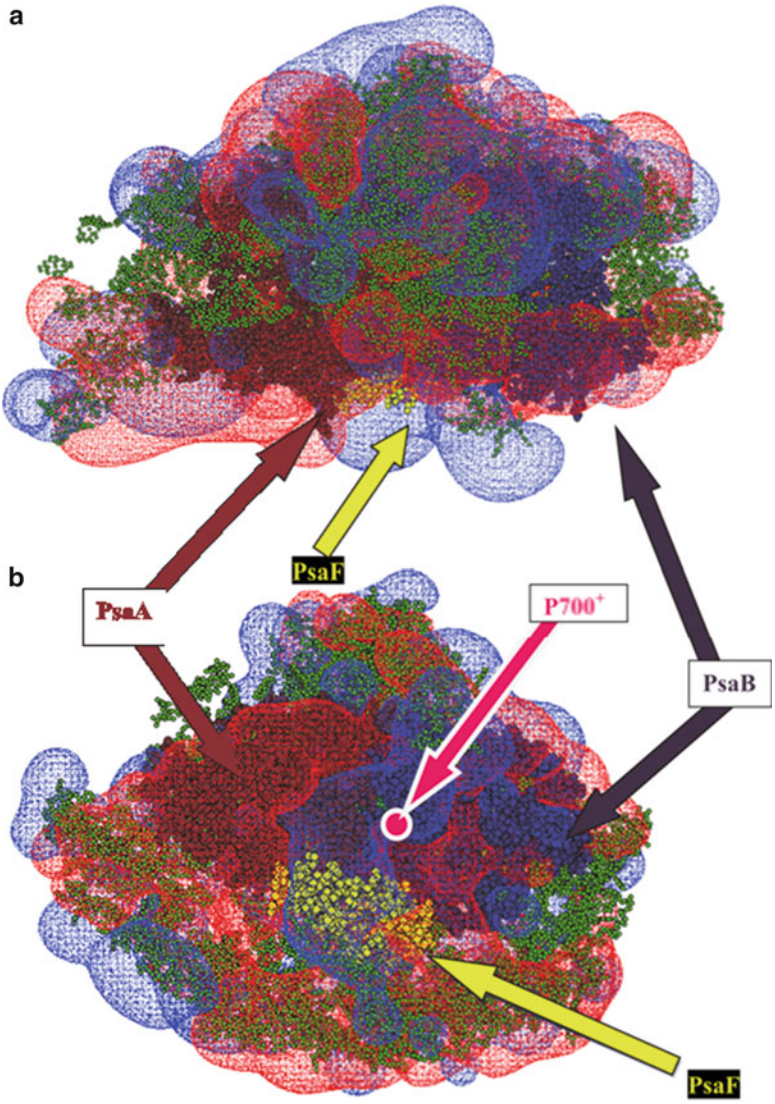


Fig. 14.10 Equipotential surfaces −6.5 mV (*red*) and +6.5 mV (*blue*) for reduced PSI multienzyme complex calculated using Poisson–Boltzmann equation; ionic strength = 100 mM, pH = 7, $\varepsilon_{sol} = 80$, $\varepsilon_{prot} = 2$. View from side (**a**) and from thylakoid lumen (**b**). Psa, Psb, Psf: subunits of PSI (Abaturova et al. 2008)

Simulation of Complex Formation

In the model, proteins of different types move randomly in the solution guided by Brownian and electrostatic forces. As they come closer to each other, under the electrostatic field effect they may achieve a position that is favorable for docking. This means that the distances between certain amino acid residues become less than the docking distances (model parameters). For some proteins these distances are known from X-ray and nuclear magnetic resonance (NMR) studies. Thus, the structure of the Pc–Cyt f encounter complex is described in Ubbink et al. (1998), and the PDB ID is 2PCF.

In the model, distances between the chosen amino acid residues at every step in the process of diffusion are monitored. If the distances are less than the docking distance, then the molecules can form a complex with probability p, which is a model parameter.

We do not explicitly consider the process of protein–protein complex formation, stages 4 and 5 of the reaction, as described at the beginning of this chapter. We also do not consider hydrophobic interactions, possible complex rearrangements, and conformational changes necessary for electron transfer. Instead we simulate the event of reaction implicitly by introducing a parameter of probability p of final complex formation.

In simulation, when two proteins approach each other at the docking distance, the algorithm generates a random number uniformly distributed in the interval [0, 1]. If the generated number is less than the given probability p, than the probability of the choice of this random number is taken as the probability of complex formation. If the generated number is greater than the parameter of docking probability p, the program proceeds to the next step. If at the next step the proteins still satisfy the docking conditions, then the described procedure is repeated. If two molecules form a complex, then immediately electron transfer occurs, and the molecules change their redox states.

To estimate the model parameters, we compare the results of simulations with experimental data for wild and mutant forms of proteins, which differ from each other in their local electric charges and, as a consequence, in the shape of their potential surfaces. Equipotential surfaces for Pc of the wild type and one of the mutants are presented in Fig. 14.8. Using the model we calculated the dependencies of the electron transfer reaction rate constant on the ionic strength for the interaction of Cyt f with Pc (Kovalenko et al. 2006), Fd with FNR (Diakonova et al. 2008; Kovalenko et al. 2010), and PSI with donor (Pc) and acceptors (Fd and Fld). Figure 14.11 presents experimental and model data for Cyt f and Pc reactions.

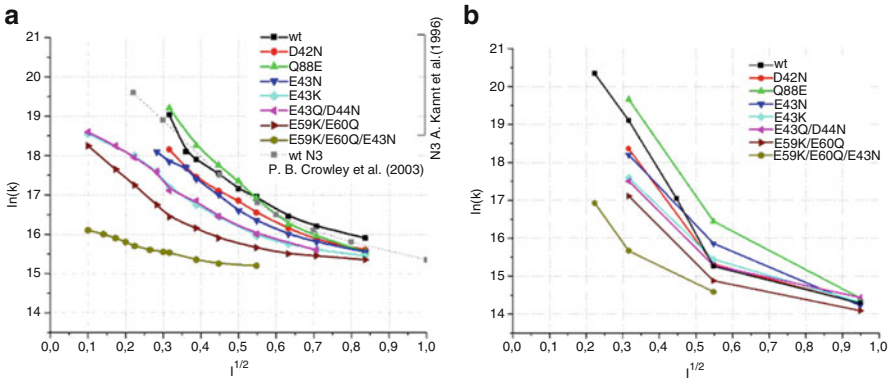


Fig. 14.11 Logarithm of second-order rate constant k dependence on root square ionic strength I for wild-type and mutant Pc and Cyt f (**a**). Experimental data from Kaant et al. (1996) and from Crowley et al. (2003). (**b**) Simulation results; docking probability is $p = 0.01$; k is in (Moles s-1), the ionic strength I is in Moles (Kovalenko et al. 2006)

Docking Rate Constant Dependence on Ionic Strength of Solution

The contribution of electrical interactions to the total rate of reaction depends on the presence of ions in the water solution screening the surface charges of the interacting proteins. The model is able to describe the experimentally observed nonmonotonous pattern of the docking rate constant dependence on the ionic strength. This type of pattern is obviously a result of different shapes of proteins' electric potential surfaces at different ionic strength values. Figure 14.12 presents equipotential surfaces at different values of ionic strength for the protein flavodoxin (Fld), an acceptor of electrons from PSI in cyanobacteria, and Fig. 14.13 does so for a PSI complex.

The PSI–Fld reaction rate constant's dependence on the ionic strength obtained using the DMSM model is presented in Fig. 14.14b. Qualitatively, the dependence character corresponds to the experimental data (Fig. 14.14a).

The decay portions of the curves presented in Fig. 14.14 at ionic strength values exceeding 40 mM are due to a decrease in the electrostatic attraction with the ionic strength. Similar decay dependencies are presented in Fig. 14.11. The nonmonotonous pattern of the dependencies is of special interest, namely, the decay of the rate constant value with the decrease in the ionic strength below 40 mM.

The main hypothesis explaining the nonmonotonous pattern observed in the experiments is based on the formation of tight but nonproductive complexes due to strong electrostatic interactions at low salt concentrations (Ubbink et al. 1998). At low ionic strengths the mutual orientations of PSI and Fld in the supercomplex are elecrostatically favorable but not optimal for electron transfer. Using the model

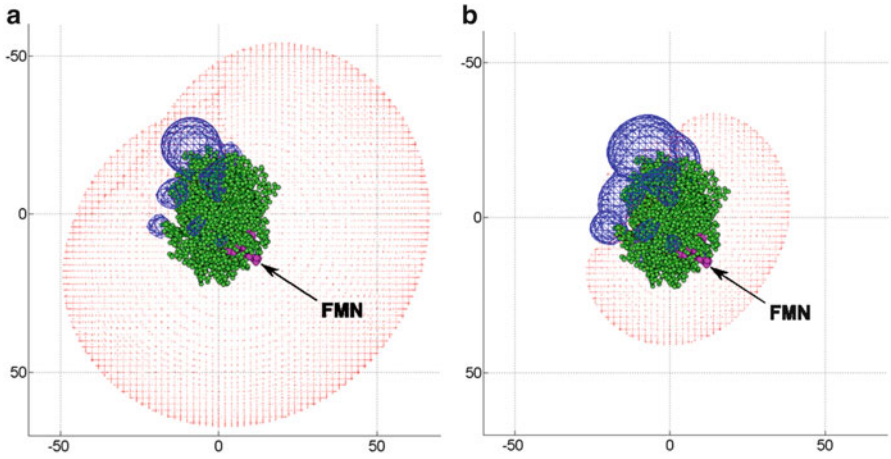


Fig. 14.12 Equipotential surfaces −6.5 mV (*red*) and +6.5 mV (*blue*) for flavodoxin. *Green circles*: atoms of molecule; *arrow*: location of cofactor FMN. (**a**) Ionic strength 0 mM. (**b**) Ionic strength 80 mM (Abaturova et al. 2008, 2009)

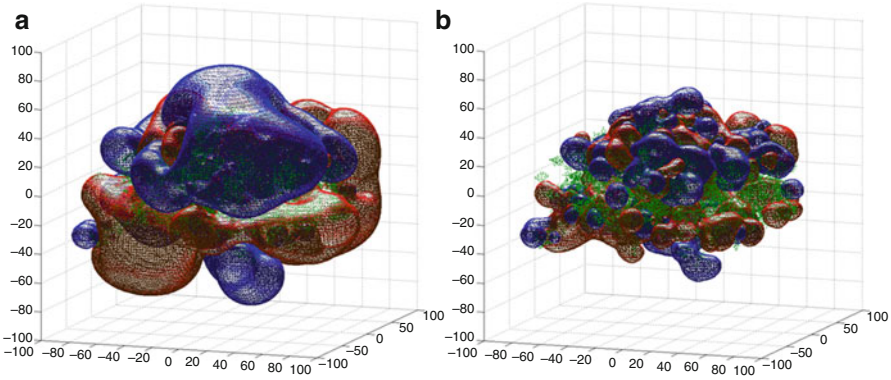


Fig. 14.13 Equipotential surfaces −6.5 mV (*red*) and +6.5 mV (*blue*) for PSI. *Above*: acceptor side of PSI; *beneath*: donor side. (**a**) Ionic strength 0 mM. (**b**) Ionic strength 80 mM (Abaturova et al. 2008, 2009)

we obtained a similar decrease in the rate constant at values of ionic strength that were less than optimal. Thus, to explain the nonmonotonous dependencies we have to take into account electrostatic interactions.

We also investigated the dependencies of the observed rate constant of the reaction on the geometrical size of the reaction volume. Changes in the geometrical size may change the reaction rate considerably and thus serve in photosynthetic organisms as an effective regulatory mechanism.

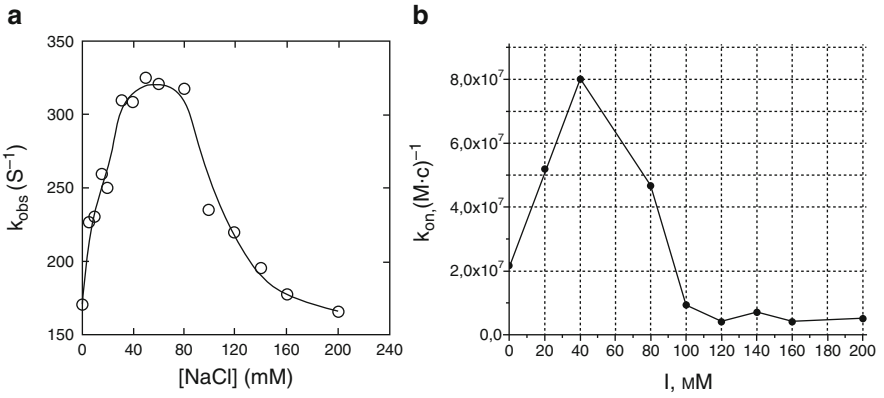


Fig. 14.14 (**a**) Experimental dependence of observed rate constant of PSI–Fld reaction on ionic strength (Medina et al. 1992). (**b**) Result of simulation: dependence of docking rate constant on ionic strength. Docking distance $r = 22$ Å, docking probability $p = 0.025$ (Abaturova 2008, 2009)

Comparative Analysis of Interaction of Pc with Cyt f and PSI Reaction Centers in Higher Plants and Cyanobacteria. Role of Electrostatics

The dependencies of the rate constants on the ionic strength for electron-transport protein Pc reactions with photosystem I and cytochrome b_6f complexes in cyanobacteria and higher plants are different. As discussed earlier, in higher plants and green algae, electron-transport proteins first form complexes via diffusion and electrostatic attraction, and then these preliminary complexes transform into final complexes through hydrophobic and other interactions.

The mechanisms of interaction of proteins in cyanobacteria were suggested based on an analysis of the experimental curves of the observed reaction rate dependencies on the ionic strength. Thus De la Cerda et al. (1997) found that the rate of reduction of photosystem I by plastocyanin in the cyanobacterium *Synechocystis* sp. PCC 6803 did not depend on the ionic strength. It is therefore concluded that in this case the reaction proceeds by random collisions. At the same time, the reaction rate of Cyt f oxidation by plastocyanin in cyanobacteria *Phormidium laminosum* only slightly decreases with increasing ionic strength (Schlarb-Ridley et al. 2002). It is concluded that the reaction proceeds through the formation of a transition complex of a electrostatic or hydrophobic nature.

Multiparticle models reveal the role of electrostatic interactions in the mechanism of donor–acceptor complex formation and observed kinetic curves.

The rate of Pc $\rightarrow$ PSI electron transfer in plants is two orders of magnitude higher than in cyanobacteria (Jolley et al. 2005). Obviously, this can be attributed to the differences in the structure and electrostatic properties of these organisms' photosystems. In higher plants, Pc binds to the luminal portions of PsaA, PsaB,

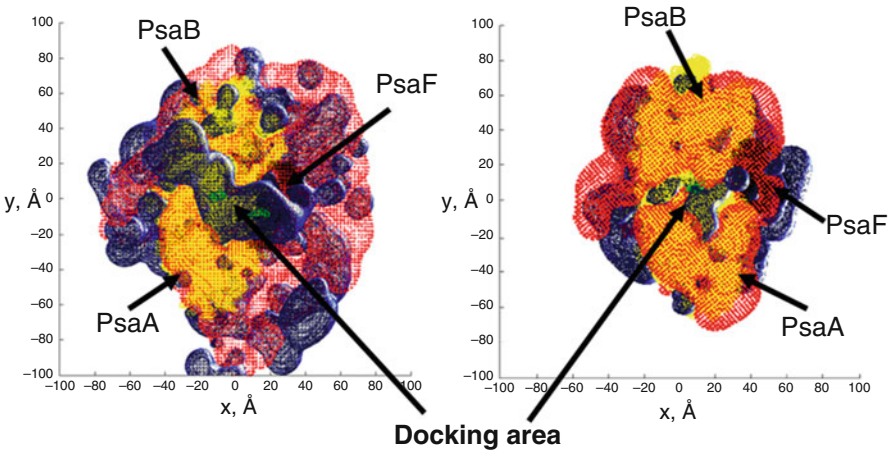


Fig. 14.15 Electrostatic surface of PSI calculated using Poisson–Boltzmann equation. *Left*: higher plants; *right*: *Thermosynechococcus elongatus*. *Red*: negative electrostatic surface potential (−6.5 mV); *blue*: positive (+6.5 mV)

and PsaF subunits of PSI, wherein the higher plants N-terminal domain PsaF is quite long and has positively charged amino acid residues that provide effective Pc binding.

For comparison, as an object of modeling we selected a transmembrane protein complex of PSI obtained from *Thermosynechococcus elongatus* (PDB ID: 1JB0), Pc derived from *Synechocystis* sp. PCC 6803 (PDB ID: 1J5D), and Pc mutants (D44A, K33A, D44K).

Figure 14.15 shows the electrostatic surfaces of the photosystems of higher plants and cyanobacteria. As can be seen from the figure, PSI of higher plants has a large area of positive charge in the Pc binding site, which is a negatively charged protein, while the region of positive charge on cyanobacterial PSI is much smaller and therefore cannot provide equally effective protein binding.

The model assumptions were used on a Pc–PSI complex produced by computer modeling with the software GRAMM, FTDOCK, DOT, and AUTODOCK (Myshkin and Bullerjahn 2002). Distances between atoms of magnesium in chlorophyll P700 dimer and copper atoms in Pc, and the midpoint between tryptophan residues on PsaA (Trp 655) and PsaB (Trp 631) on the PSI and nitrogen atoms on amino acid residue His86 of Pc were taken as docking distances.

In all numerical experiments on multiparticle models, the size of the reaction volume was 160 × 160 × 160 nm, the amount of protein was 100 molecules of each type, and the pH was 7.5. The resulting dependence of the number of formed complexes on time was approximated by a hyperbolic function, and for each such dependence a bimolecular rate constant was calculated.

Figure 14.16 shows the second-order rate constants of the complex formation of Pc with Cyt f (Fig. 14.16a) and PSI (Fig. 14.16b) for different values of ionic strength of the solution. For comparison, the dependence of the rate constant of

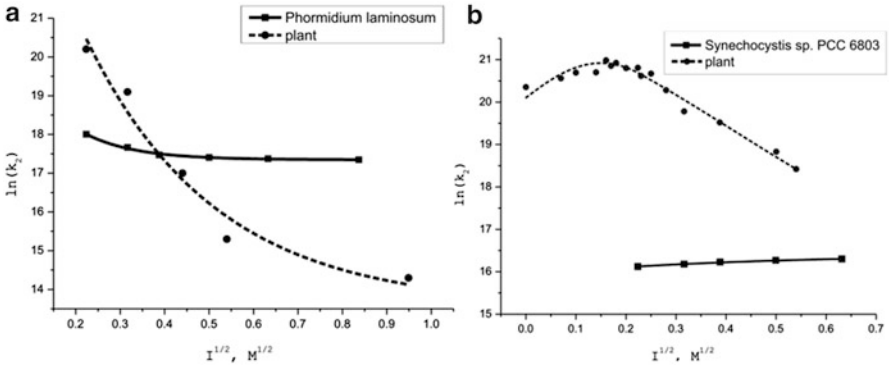


Fig. 14.16 Dependence of rate of complex formation in reactions Pc–Cyt f (**a**) and Pc–PSI (**b**) on ionic strength in cyanobacteria and higher plants obtained in computer simulations (Kovalenko et al. 2011)

complex formation between similar proteins of higher plants calculated in Kovalenko et al. (2006, 2011a, b, c) is presented. From Fig. 14.16 we can see that the reaction rate constant of the complex formation in cyanobacteria is almost independent of ionic strength.

Unlike in plants, in which electrostatic interactions play a major role, in cyanobacteria their role is less pronounced. In Fig. 14.16 we can see that the rate of Pc–PSI binding reaction in cyanobacteria is one order of magnitude smaller than in higher plants. At the same time, for the formation of Pc–Cyt f complexes the kinetic curves of the second-order rate constants of protein binding dependence on ionic strength intersect in the region of $I = 200$ mM (Fig. 14.16a). The ionic strength in the chloroplast stroma of cyanobacteria is 130–200 mM (Hall 1976). Therefore, at the physiological ionic strength, the formation of Pc–Cyt f complexes in cyanobacteria proceeds approximately at the same rate as in higher plants. At high ionic strengths, the rate of formation of P–Cyt f complexes in cyanobacteria is one order of magnitude greater than in higher plants. Conversely, at lower ionic strengths, the rate of the reaction in higher plants is greater than in cyanobacteria.

In living cells, oxidation of Cyt f and reduction of PSI by Pc occur sequentially. At the physiological ionic strength values, the first reaction proceeds at approximately the same rate in higher plants and cyanobacteria, whereas the second reaction rate is significantly lower in cyanobacteria, i.e., PSI reduction in cyanobacteria may limit the overall rate of electron transport. In higher plants, the rate of the reaction is considerably higher, resulting in acceleration of the PSI recovery in higher plants.

A study using a computer model clearly shows that the difference between cyanobacteria and higher plants in terms of the absolute reaction rates is due to the different electrostatic potentials created by charged amino acid residues on the protein surface (Fig. 14.15). In cyanobacteria, electrostatic interactions play a less important role than in higher plants; the rate of formation of complexes Pc–PSI and

Pc–Cyt f in cyanobacteria depends weakly on the ionic strength. In contrast to cyanobacteria, in higher plants and green algae, electrostatic interactions can significantly speed up the formation of the complex: the reaction rate of binding of plastocyanin with photosystem I in higher plants is several orders of magnitude higher than in cyanobacteria.

Chapter 15
Modeling of Protein Interactions in Photosynthetic Membrane

Electron transfer between PSII and PSI is performed via a cytochrome (Cyt) complex, and the step Cyt → PSI is executed by a mobile electron carrier Pc. This small (10.5 kDa) protein diffuses in a lumen, a relatively narrow closed space between the thylakoid membranes, oxidizes Cyt f, a subunit of the Cyt complex, and reduces the PSI reaction center, anchoring at the lumen site of PSI and creating a Pc–PSI supercomplex (Fig. 15.1).

According to a review by Dekker and Boekema (2005), the average distance between two membranes in granal stacks, obtained by analysis of electron micrographs, ranges from 4 to 14 nm, with values between 6 and 11 nm being the most common. The luminal volume in granal stacks was reported to decrease by one-third upon illumination (Murakami and Packer 1970), so these values may correspond to the states of light and dark adaptation.

Electron microscopy tomography data allowed researchers to reconstruct the 3D organization of thylakoid membranes of higher plant chloroplasts. The mean thickness of the granal layer, i.e., of the two membranes and the luminal space between them, has been estimated at 20 ± 2 nm, which corresponds to a luminal span of 10 nm. Thus the span of the lumen is comparable with the Pc dimensions ($40 \times 28 \times 30$ Å). Therefore, Pc diffusion in the lumen is hindered by the protruding parts of transmembrane multienzyme complexes and by other mobile molecules.

The lateral distribution of Pc was examined by immunocytochemical localization and redox kinetics of $P700^+$. Upon dark adaptation, Pc concentration in the stromal region of the lumen proved to be approximately twice that of the granal region. Illumination caused a rise in Pc concentration in the granal region and a decline in the stromal region, and it was concluded that light induces Pc migration. Thus, Pc travels quite large distances (hundreds of nanometers) shuttling between the granal and stromal regions of the thylakoid (Fig. 15.1).

By means of direct multiparticle models we simulated the process of Pc diffusion in the thylakoid and its interaction with Cyt complexes and PSI (Abaturova, 2008; Kovalenko et al. 2008; Kniazeva et al. 2010).

A. Rubin and G. Riznichenko, *Mathematical Biophysics*, Biological and Medical Physics, Biomedical Engineering, DOI 10.1007/978-1-4614-8702-9_15,

© Springer Science+Business Media New York 2014

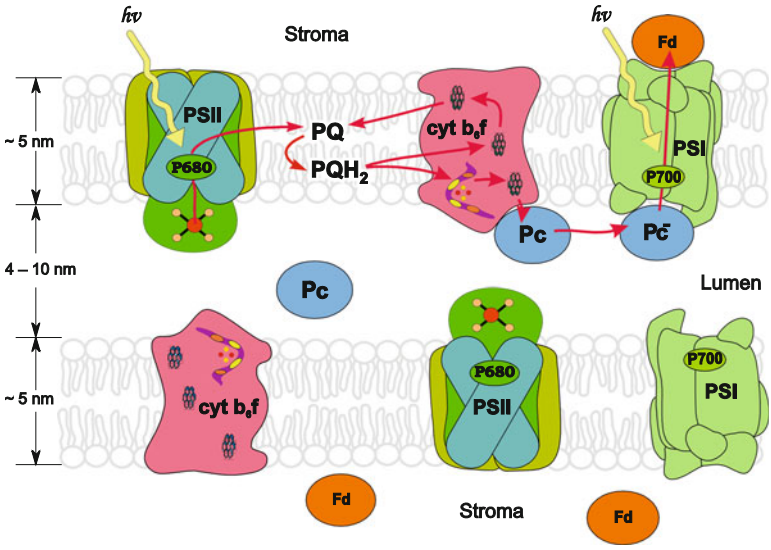


Fig. 15.1 Schematic view of photosynthetic electron transport. Two thylakoid membranes and the luminal space between them are shown. Multiprotein complexes photosystem I, photosystem II, and cytochrome b_6f are embedded in the membrane. The mobile electron carrier protein plastocyanin (Pc) diffuses in the lumen. *Arrows*: electron transport. The connection with the Calvin cycle is carried out by mobile small protein ferredoxin Fd (or flavodoxin Fld in cyanobacteria)

Interaction of Pc with Cyt f in Thylakoid Lumen

The values of parameters obtained by the DMSM analysis of protein interactions in solution (Chap. 14), taking account electrostatic interactions, were used to simulate interactions of mobile carrier Pc and Cyt f as part of the cytochrome complex protruding into the lumen space (Fig. 15.2) (Kovalenko et al. 2008). The Cyt b_6f complex of *Chlamydomonas reinhardtii* is comprised of four large subunits—Cyf f, Cyt b, Rieske iron-sulfur protein, and subunit IV—and four small hydrophobic subunits (Stroebel et al. 2003). The Rieske protein and Cyt f extend into the lumen. Pc diffusing in the lumen can form a supercomplex with Cyt f and oxidize it. The NMR structure of the complex between spinach Pc and turnip Cyt f was obtained by Ubbink et al. (1998), and the PDB ID was 2PCF. In 2003, an X-ray structure was established for *Chlamydomonas reinhardtii* Cyt b_6f (1Q90). Combination of these structures allowed us to predict the possible mutual orientation of Pc and Cyt f relative to the membrane to be used in modeling (Kovalenko et al. 2008). It was assumed that Pc molecules could form a complex with immobile Cyt f partners only in the appropriate orientation.

The model scene of the luminal space was presented as a parallelepiped bounded by membranes at the top and bottom, while at the ends mirror boundary conditions were assumed (Fig. 15.3).

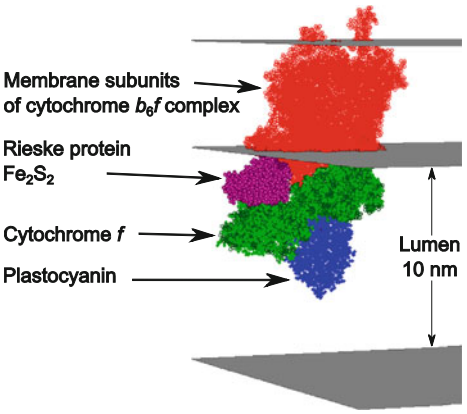


Fig. 15.2 Cytochrome b_6 f–Pc supercomplex. The picture was constructed by superposition of PDB structures 2PCF and 1Q90 (Kovalenko et al. 2006)

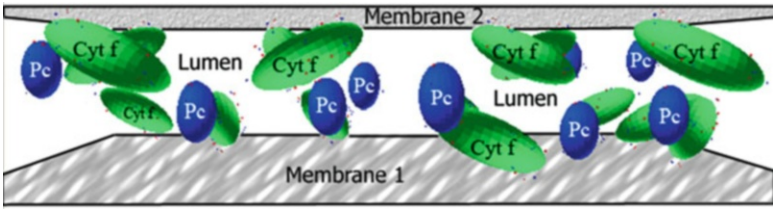


Fig. 15.3 Model visualization (thylakoid lumen bounded by thylakoid membranes) with proteins Pc and Cyt f

The space occupied by the membranes, the distance between the membranes, the density of the cytochrome complexes, and the mobile Pc concentrations were evaluated based on data from the literature: the diameter of the granal membrane varies from 300 to 600 nm (Staehelin and van der Staay 1996), the density of Cyt b_6f complexes in the membrane is approximately 2.55 per 1,000 nm^2 (Albertsson 2001), the number of Pc molecules is considered to be equal to the number of Cyt b_6f complexes (at a luminal span of 100 Å it corresponds to a Pc concentration of 430 μM).

Modeling of Pc–PSI Interaction Considering Membrane Surface Charge and Multienzyme Complexes Embedded in Membrane

We studied the dependence of the reaction rate constant on the distance between membranes (the width of a lumen) by varying the latter from 2 to 40 nm but keeping constant the number of molecules (270 each) and the membrane area (322×322 nm^2). We considered two cases (Fig. 15.4) with Cyt f molecules (Fig. 15.4a) membrane-bound and exposed in the lumen and (Fig. 15.4b) diffusing

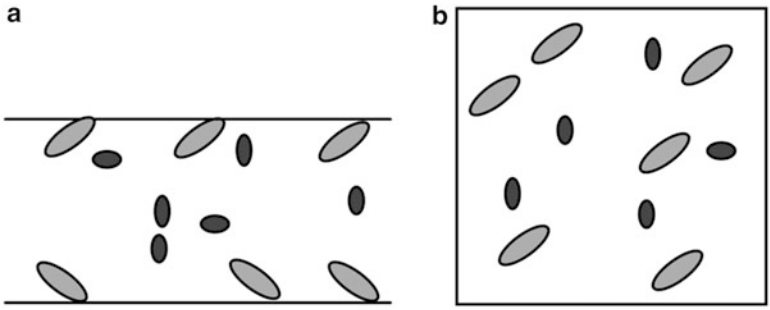


Fig. 15.4 Two versions for numerical experiments: (**a**) Cyt f molecules are membrane-bound in accordance with structural data; (**b**) all molecules diffuse in cubic space of same volume as in (**a**)

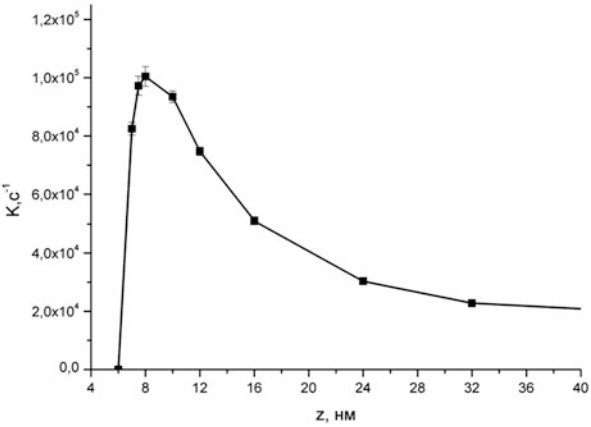


Fig. 15.5 Dependence of rate constant of Pc–Cyt f reaction, divided by Cyt f concentration, in thylakoid lumen at distance z between membranes at constant number of molecules (Kovalenko et al. 2008)

together with Pc in a cubic space of the same volume. The case shown in Fig. 15.4a reflects the experimental data on the Cyt f disposition in thylakoid, whereas Fig. 15.4b corresponds to experiments with isolated particles in solution.

The results of numerical simulation are displayed in Fig. 15.5. The rate constant value has a maximum at a distance of 8 nm, which is in agreement with the experimental photosynthetic data (Dekker and Boekema 2005). Further increase in the distance leads to a decrease in the rate because of the decrease in Pc molecule concentration. A decrease in the distance below the optimal value also leads to a rate constant decrease because Pc diffusion in the luminal space becomes difficult and even impossible at small lumen widths. At $z < 7$ nm the rate constant abruptly drops to zero. Indeed, Cyt f with attached Pc protrudes from the membrane at 7 nm (Fig. 15.2), so if the opposite membrane is closer than this, the complex cannot form.

This conclusion corresponds to the known effect of hyperosmotic stress, which leads to a change in the luminal volume and inhibition of the Pc–Cyt reaction (Cruz et al. 2001).

The interaction between Pc and the Cyt b_6f complex in the photosynthetic membrane is an example of a biochemical reaction that can be modulated by changes in the physical characteristics of the surroundings, in this case the luminal span. We suppose that such events are physiologically relevant and expedient: control of the electron transport at the Pc level by narrowing the lumen while checking the proton release into the lumen, including PQ interaction with the Cyt complex and other mechanisms, would prevent photoinduced damage under intense illumination and attenuate the linear electron transport. This is very much in agreement with the data on light constriction of lumina (Murakami and Packer 1970). Notably, this mechanism is operative in granal regions and affects the linear electron transport, while the stromal lamellae where the cyclic electron transport takes place exhibit no changes in luminal width or rate of electron transfer from Cyt f to Pc.

Modeling of Pc Interaction with Cyt f and PSI in Lumen

The interaction of a Pc protein with subunit f of cytochrome complex (an electron uptake from Cyt f) and PSI (an electron transfer to P700) occurs in the luminal space of thylakoid membranes. The surface charge of the membrane generates an electric field that influences the movement of charged proteins in the lumen.

Membranes contain glycolipids—sulfolipids and galactolipids, as well as built-in multienzyme complexes. Approximately 15–20 % of the total lipids are charged lipids—the sulfolipid sulfoquinovosyldiacylglycerol (SQDG) and phospholipid phosphatidylglycerol (PG) are negatively charged at neutral pH. Negatively charged amino acid residues Glu and Asp of transmembrane protein complexes also contribute to the membrane field (Prochaska and Gross 1977; Barber 1982). Thus, the thylakoid membrane has a negative surface charge at neutral pH with values varying from 8.4 to 74 mC/m^2 (Barber 1982).

By lowering the pH the value of the surface charge is reduced, and at a pH of approximately 4.1 the membrane becomes electrically neutral. Thus, due to the acidification of lumina under illumination, the surface charge of the membrane decreases. According to Dahlin (2003), for the thylakoid membrane of wheat grown under different illumination conditions, the surface charge lies between 23 and 34 mC/m^2.

The luminal space between two thylakoid membranes is where reactions take place. Each model membrane is represented by two charged planes confining the lipid bilayer from two sides. On the surfaces of the membranes, negative point charges, the number of which is determined from experimental data based on the concentration of the charged lipids, are uniformly distributed.

The model considers processes in a time range on the order of milliseconds, and the movements of lipids and other components of the membrane within such a short

period of time can be neglected. Therefore, lipids embedded in the membrane and Cyt f representing subunits of cytochrome complex in the model are treated as static objects.

Pc molecules move forward and rotate in the luminal space in accordance with formulas (14.2) and (14.3). The operative external electrostatic force F^i_{el} acting on the Pc molecules and the interaction force acting between mobile Pc molecules were calculated separately:

$$F^i_{\text{el}} = \sum_{j,\, i \neq j} F_{ij} + F^i_s, \tag{15.1}$$

where F_{ij} is the force of interaction between the moving proteins i and j and F^i_s is the electrostatic force acting on the ith mobile protein due to the electrostatic field created by charges of the membrane, cytochrome f, and ions of the solution. For calculation of the forces, the Poisson−Boltzmann equation was used, which describes the electric field around fixed charges in the presence of free ions (Derjaguin et al. 1985):

$$\nabla\left(\varepsilon\left(\vec{r}\right)\nabla\varphi\left(\vec{r}\right)\right) = -\frac{1}{\varepsilon_0}\left(-2Ie_0^2\frac{\varphi\left(\vec{r}\right)}{kT} + \rho_{\text{prot}} + p_{\text{membr}}\right). \tag{15.2}$$

Equation (15.2) is an approximation of the classic Boltzmann equation

$$\nabla\left(\varepsilon\left(\vec{r}\right)\nabla\varphi\left(\vec{r}\right)\right) = -\frac{1}{\varepsilon_0}\rho\left(\vec{r}\right),$$

where ε_0 is the dielectric constant, $\rho\left(\vec{r}\right), \varepsilon\left(\vec{r}\right), \varphi\left(\vec{r}\right)$ are local values of the bulk charge density, dielectric constant of the medium, and electrostatic potential, respectively.

The charge density is a sum of the charge density of charged lipids, proteins embedded in the membrane, and free ions of the solution:

$$\rho = \rho_{\text{memb}} + \rho_{\text{prot}} + \rho_{\text{ion}}.$$

The bulk density of the ions is calculated using the formula

$$\rho_i\left(\vec{r}\right) = \sum c_i z_i e_0,$$

where c_i is the local concentration of ions, z_i the atomic number, and e_0 the charge of an electron. Free ions are uniformly distributed in the solution, but in the vicinity of the proteins embedded in the membrane they are distributed heterogeneously.

Assuming that free ions do not interact with each other, their distribution in the field of fixed charges with potential $\varphi\left(\vec{r}\right)$ obeys the Boltzmann law:

$$c_i = c^i_{\text{bulk}} \exp\left(-\frac{W_i}{kT}\right),$$

where c^i_{bulk} is the bulk concentration of ions, $W_i = z_i e_0 \varphi\left(\vec{r}\right)$ the action on the movement of ions in the neighborhood of the point $\vec{r} = (x, y, z)$. Thus:

$$\rho_{\text{ions}}\left(\vec{r}\right) = \sum c_i z_i e_0 = \sum_i c_i^{\text{bulk}} z_i e_0 \exp\left(-z_i e_0 \varphi\left(\vec{r}\right)/kT\right).$$

For small values of the potential, we can restrict the linear term in the expansion of the exponential equation and obtain (15.6), where

$$I = \frac{1}{2}\sum_i c_i^{\text{bulk}} z_i^2$$

is the ionic strength.

A detailed derivation of formulae and a description of the algorithm for its iteration are given in Kniazeva et al. (2010). The equipotential surfaces of the electrostatic potential in the luminal space of the thylakoid for the granal area of the thylakoid membrane were calculated using the Poisson–Boltzmann equation (Fig. 15.6a–c). Red designates a negative equipotential surface (−6.5 mV), while blue indicates a positive equipotential surface (+6.5 mV).

By means of multiparticle models of the interactions of Pc and f subunits of the cytochrome complex in the thylakoid lumen, the binding kinetic curves of Pc and cytochrome f for different values of the surface charge of the membrane were calculated. It was shown that at real values of ionic strength in the luminal space ($I \sim 100$ mM), the membrane does not affect the reaction rate of Pc–Cyt f complex formation when the surface charge density is less than 30 mC/m^2. At higher densities of negative surface charge, the rate constant is reduced because the strong negative field in this case prevents the approach of negatively charged Pc molecules to the binding site of Cyt f exposed to the lumen.

The dependence of the reaction rate constant on the ionic strength at different values of the surface charge produced on the model is shown in Fig. 15.7. From a family of these curves we can see that the reaction rate depends on the ionic strength in a nonmonotonic manner with k increasing from 0 to 40 mM, reaching its maximum value at $I = 20$–40 mM and then decreasing with further increases in ionic strength. For large values of the surface charge the nonmonotonic shape of the curves is more pronounced. At low ionic strengths the rate of the reaction is low due to weak screening, and therefore the negatively charged membrane prevents the approach of negatively charged Pc molecules. Note that in experiments in solution,

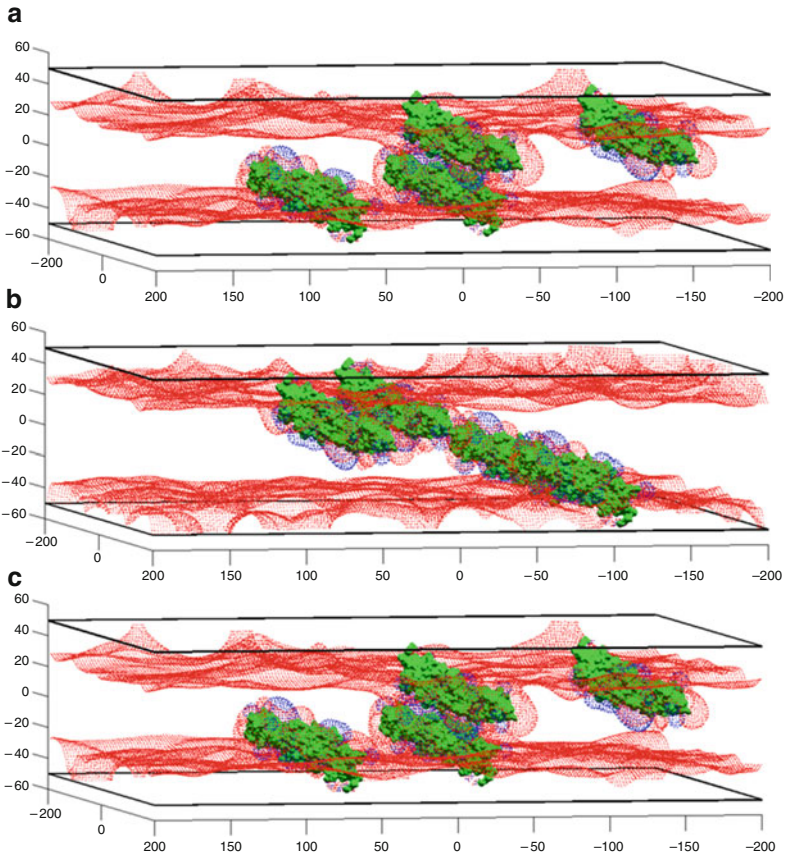


Fig. 15.6 Equipotential surfaces (+6.5 mV, 6.5 mV) for thylakoid membrane and Cyt f. (**a**) pH $= 7, I = 100$ mM, $\sigma = -46.7$ mC/m^2. (**b**) pH $= 7, I = 150$ mM, $\sigma = -46.7$ mC/m^2. (**c**) pH $= 7$, $I = 100$ mM, $\sigma = -18.6$ mC/m^2 (Kniazeva et al. 2010)

both real and computer, the rate constant dependencies on the ionic strength were monotonic (Fig. 14.12).

A review by Barber (1982) presented experimental data on the charge of the thylakoid membrane: in stromal areas of the membrane, the surface charge density varies from 8.4 to 10.8 mC/m^2, while in granal areas it is much higher, ranging from 20 to 74 mC/m^2. The results of modeling show that in the stromal areas the surface charge does not prevent interaction of Pc with the cytochrome complex. At the same time in the granal areas the surface charge can inhibit this interaction. Thus, the effect of the surface charge can contribute to the directed motion of the molecules of Pc from the granal area to the stromal area in linear electron transport.

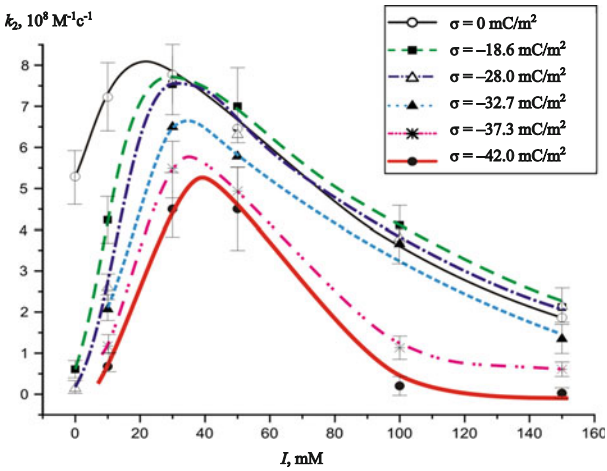


Fig. 15.7 Dependence of binding rate constants of Cyt f–Pc complex formation on ionic strength for various values of the of charge density of the membrane (mC/m^2). Size of simulation volume: 100 × 100 × 10 nm, pH = 7.0, amount of protein = 25 molecules of each type (Kniazeva et al. 2010)

Chapter 16
Spatiotemporal Evolution of Electrochemical Potential $\Delta\mu_{H+}$ in Photosynthetic Membrane

An important stage of energy transformation in the primary processes of photosynthesis is the formation of an electrochemical potential, which is generated due to transmembrane proton transfer into the thylakoid and transmembrane transfer of other ions: K^+, Ca^{2+}, Cl^-. Protons accumulating in the lumen are used by a molecular machine ATP–synthase for the production of ATP molecules from ADP and inorganic phosphate (Fig. 16.1).

Exit of protons into the lumen occurs at two sites in the electron-transport chain. One proton is released into the lumen at the donor site of PSII as a result of water splitting for each electron transferred across the membrane during photoinduced charge separation. The other point is transmembrane proton transfer, associated with the plastoquinone pool performing electron transfer from the acceptor side of PSII (exposed to stroma) to the luminal side to the cytochrome complex. At this stage, the transfer of two electrons is accompanied by a transfer of two protons from the stromal to the luminal space of the photosynthetic membrane. The transfer of protons, coupled to the cyclic electron transport around photosystem I, is also possible, with PQ molecules also being involved.

Modeling of Proton Transfer

Considering the process of proton transport in a photosynthetic system, we take into account the following processes: release of protons into lumina, lateral diffusion, and passive leakage of protons. It is impractical to include protons as particles in the model of mobile carriers because of significantly different moving speeds. The diffusion coefficient of protons in water is approximately 10^{-4} cm^2/s, which is two orders of magnitude larger than the diffusion coefficient of the protein carriers. Therefore, the apparatus of differential equations was used, as suggested in Dubinsky and Tikhonov (1994, 1995), Vershubskii and Tikhonov (2013), and

A. Rubin and G. Riznichenko, *Mathematical Biophysics*, Biological and Medical Physics, Biomedical Engineering, DOI 10.1007/978-1-4614-8702-9_16,

© Springer Science+Business Media New York 2014

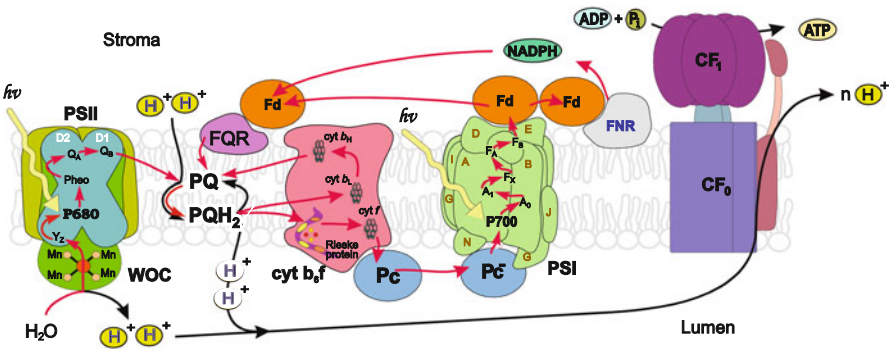


Fig. 16.1 Scheme of primary processes of photosynthesis. Path of linear electron transfer (from H_2O to $NADPH^+$, *red line*) and protons (*black lines*)

Vershubskii et al. (2007). In this case, the variables in the equations are concentrations of protons in lumina and stromata, they depend on the coordinates and time.

However, under real conditions the total number of protons in a thylakoid lumen is small—it may be dozens or even less than ten units per a single granal compartment. Therefore, a question arises: can the notion of concentration be used for such a small number of particles? An acceptable interpretation was suggested in Tikhonov and Blumenfeld (1985), according to which we do not consider the concentration but rather the probability density of the proton distribution. That is, the variable in the equation is interpreted as the probability density of finding a proton at a given point.

A combination of a discrete model of electron transport in photoreaction centers and a multiparticle model for mobile electron carriers with a diffusion model of proton transfer was constructed in the following manner (Ustinin et al. 2010, 2013). Let us consider a 3D grid covering the area of the modeling—a scene where we consider the transfer of protons. The width of grid cells corresponds to the diameter of the protein complexes, and it is on the order of 10 nm. In this case, each cell contains no more than one protein complex—a potential source of protons. For each proton, a grid function is given that determines the probability of finding it in the cell. At the end of each step of the calculation, the model analyzes all transitions between states of the complexes that have occurred in this step. Some of these transitions are accompanied by release of protons into the lumen. If such a transition is identified in any of the complexes, a new proton is added to the corresponding lumen cell.

The probability distribution functions specified are as follows: the probability equals 1 in the cell corresponding to the complex where the proton was allocated and zero in all other cells. Then, at each step of the multiparticle simulation we recalculate the probability distribution of all protons, solving for each of them a system of finite-difference equations describing diffusion and interaction with the buffer system.

Fusion of the discrete multiparticle model with a finite-difference model of the proton diffusion is also needed for the modeling of proton transfer through

ATP–synthase. It is performed as follows: for each ATP–synthase complex its coordinates are known, and consequently we know the cell in which it resides. We know the probability of finding each proton in the cell. At the end of each step of the multiparticle model for every ATP–synthase complex and every proton we choose a random number from a uniform distribution in the interval [0, 1]. If that number is less than the probability of the proton will be in a cell near the ATP–synthase complex, a proton transfer occurs. The proton is excluded from consideration in the lumina and is added for consideration in the stromata, and the rotation of the mobile ATP–synthase subunit γ by 120° is simulated. After three such rotations have occurred, a new ATP molecule is synthesized.

Model of Proton Release into Lumen

The probability density for each free proton in the lumen, defined by the variable H, is specified on a rectangular grid with dimension $N_X \cdot N_Y \cdot N_Z$, and the cell size is chosen according to the average diameter of protein complexes (10 nm). Since the thickness of the lumen is also approximately 10 nm, in the simulation of the proton transfer in a lumen, only one cell along the z-axis (perpendicular to the plane of the membrane) may be considered. In fact, the diffusion of protons inside the lumen is modeled by a 2D grid.

The release of protons is the result of light-induced decomposition of water with a PSII water-splitting complex, as well as oxidation of plastoquinol (QH_2) with a cytochrome b_6 f complex. In the multiparticle model, these events are described by changing the states of the complexes at the end of each time step of the simulation. Knowing the light intensity, we can calculate a probability of absorption of a photon by photosystem II during a time equal to the duration of the model step. This probability can be calculated as

$$p = \frac{I \cdot \sigma \cdot t}{h\nu},$$

where I is the light intensity (approximately 1,000 W/m^2), σ the effective absorption cross section, t the duration of the multiparticle model step, h Planck's constant, and ν the frequency of the absorbed light.

When the specified PSII complex consumes a quantum of light, we know the coordinates of this complex, and we also know the grid cell where the probability density of a proton should be recalculated to include new protons in the equation. Now we add new a proton to this cell, so the probability density of this proton in this cell should be increased by the value

$$\Delta H = \frac{1}{dV \cdot (1 + K \cdot B)}. \tag{16.1}$$

Here dV is the volume of the cell, K the equilibrium constant for a proton binding to a buffer group, and B the concentration of the buffer groups. In all other cells the probability of finding this proton is equal to zero.

In this formula, the interaction of hydrogen ions with buffer groups fixed on the interior and exterior surfaces of the thylakoid membrane is taken into account. Buffering groups are charged amino acid residues of the protein chains of numerous complexes embedded in the membrane, which protrude into the lumen. Protons may temporarily bind to these residues, and this process slows their diffusion in the lumen and reduces the concentration of free protons in the aqueous phase of the lumen by approximately 1,000 times. Therefore, it is necessary to consider the presence of buffer groups in proton diffusion modeling.

Model of Lateral Diffusion of Protons

Proton diffusion is considered in lumina (intermembrane space). Geometrically, the environment of simulation is a cuboid region, where the upper and lower sides are photosynthetic membranes through which protons flow.

Hydrogen ions diffuse in the aqueous phase of the thylakoid volume, and the pH in the stroma (pH_s) in this version of the model is taken to be constant. To simulate the process of lateral transfer of protons in the interthylakoid space, a system of differential equations was used that takes into account the binding buffer groups:

$$\begin{aligned} \frac{\partial H}{\partial t} &= D_H \nabla^2 H - k_1 H(B_0 - c) + k_2 c + J, \\ \frac{\partial c}{\partial t} &= k_1 H(B_0 - c) - k_2 c, \end{aligned} \tag{16.2}$$

where $H(r, t)$ is the probability density of finding a proton at that point of the lumen; c (r, t) is the density of proton–buffer group complexes; B_0 is the maximal concentration of buffer groups (in this version of the model it is assumed to be independent of the coordinates and time); k_1 and k_2 are the rate constants of binding and decay; D_H is the diffusion coefficient of free protons in water; and J is the total inflow of protons into the lumen due to the operation of photosystem II and cytochrome b_6f complexes and outflow through the ATP–synthase complex and due to passive proton outflow.

The boundary conditions are given as impenetrable walls on the upper and lower planes of the lumen and are periodic on the lateral boundaries. The numerical solution of the problem was found using the method of finite differences. When implementing the algorithm for the GPU (Graphyc Processor Utility), the method of particles is more convenient (Hockney and Eastwood 1981). This method allows efficient use of high parallelism of GPUs to accelerate calculations by a factor of 10–15 compared to the finite-difference version.

Proton Flow Through ATP–Synthase and ATP Synthesis

Each ATP–synthase complex is modeled as a single 3D object located in the thylakoid membrane. At each step of the multiparticle simulation we consider the probability of finding a proton in a cell adjacent to the selected ATP–synthase complex. If at this step the random number is less than that probability, then we believe that a proton is present in that cell of the lumen and, with some probability p_f (which is a model parameter), may go through this ATP–synthase complex. This process corresponds to the rotation of the mobile subunit γ (rotor) for 120° within the stationary subunit α (stator). When three protons go through the ATP–synthase complex, one ATP molecule is synthesized. At this stage we do not consider whether the system has enough free ADP and phosphate molecules, assuming ATP synthesis is limited only by the presence of protons.

Computer Simulation of Proton Gradient Evolution and ATP Creation

Proton transfer in the plane of the membrane produced by photosynthesis was simulated in the following numerical experiment. The computer simulation includes the granal area of the membrane (bottom right in Fig. 16.2) where photosystems II are located (green dots in figure) and the stromal area (top left in Fig. 16.2) where ATP–synthases and photosystems I are located. Cytochrome complexes (red dots) are spaced randomly in the plane of the membrane.

First, the system was kept for some time in the dark. When a light is turned on, photosystems II begin to absorb photons, and water decomposition and release

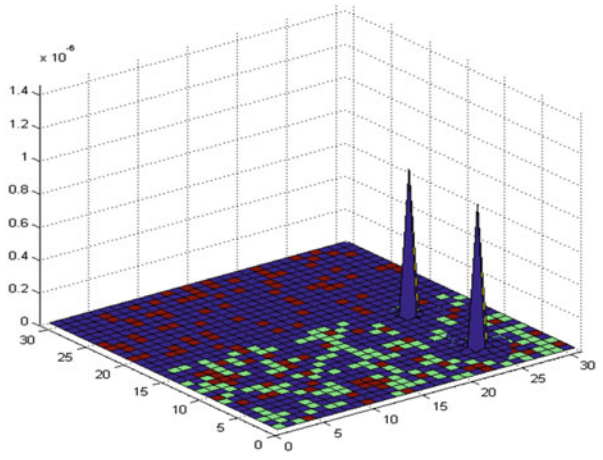


Fig. 16.2 Probability density distribution of protons in plane of membrane at beginning of illumination. *Green dots*: location of photosystems II in plane of membrane; *red dots*: location of cytochrome complexes. Peaks correspond to the position of the photosystem and cytochrome complexes after the release of protons at the current step of the model (Ustinin et al. 2013)

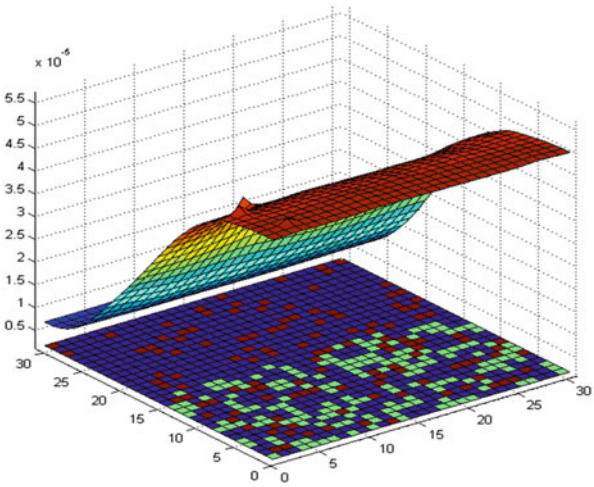


Fig. 16.3 Distribution of protons in membrane plane 50 ms after onset of illumination. The concentration gradient between the granal area (*bottom right*) containing photosystems II and the stromal area (*top left*) is shown (Ustinin et al. 2013)

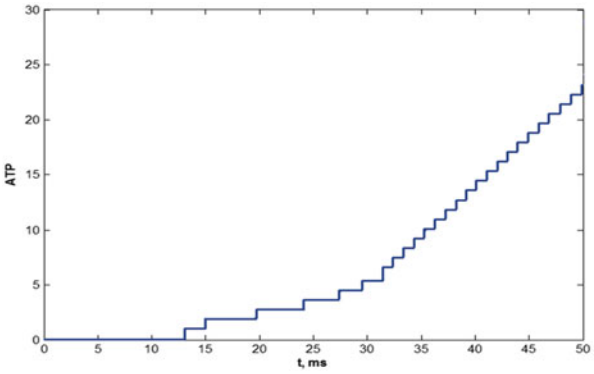


Fig. 16.4 Dependence of number of produced ATP molecules on time. Following a lag, at first the synthesis rate is limited by the number of available protons, and then by the time of subunit rotation (Ustinin et al. 2013)

of protons into the lumen occur. When a new proton is released into a lumen by means of the water splitting complex of the PSII or cytochrome complex, its probability density is a delta function, localized in the space near the PSII complex that produced the proton. In Fig. 16.2 it can be seen as peaks on the right side of the graph.

Over time, protons start to diffuse in space, and the shape of their probability density becomes flatter and resembles a Gaussian bell. The number of protons increases in lumina of the granal area, and protons begin to diffuse into the stromal area. With the accumulation of protons, a proton gradient between the stromal and granal parts is created (Fig. 16.3).

When the probability of finding protons in the stromal area becomes considerable, the synthesis of ATP begins, which is associated with the flow of protons through the ATP–synthase complex. The dependence of the number of synthesized ATP molecules on time is illustrated in Fig. 16.4. One can observe a lag period

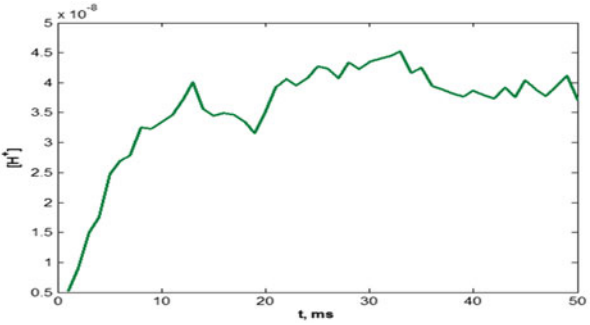


Fig. 16.5 Total number of protons in lumen (Ustinin et al. 2013)

when the probability of finding a proton in the stromal region is small. After proton concentration in the vicinity of the ATP–synthase complex increases, the rate of ATP synthesis becomes constant and the curve becomes linear.

Figure 16.5 shows the dynamics of the total number of protons in a lumen. At first it increases, then the inflow of protons due to PSII and cytochrome complexes becomes equal to the leakage through the ATP–synthase complex, and the distribution of protons in the lumen is stabilized.

Taking into account the nonuniform distribution of protein complexes in the membrane and modeling the diffusion of electron carriers and protons, we can simulate the effect of a delay between switching on the light and the start of ATP synthesis. The delay in this case is due to several factors—the ultimate rates of diffusion of electron carriers in the stromal and granal parts, the slow time scales of electron transfer in cytochrome complexes that are coupled to proton transport, and the finite rate of diffusion of protons in lumen. As a result, accumulation of protons in stromata with an ATP–synthase complexes is delayed, which results in delay of the onset of ATP synthesis. The model allows for consideration of these factors on a single spatiotemporal scale.

Conclusion

Kinetic models consisting of ODEs proved to be very useful in the modeling of the processes of photosynthetic electron transport. They describe the kinetic curves of fluorescence induction at different light excitation protocols (flashes of different intensities and durations, continuous illumination). A kinetic approach is also effective in studying the relationships between the primary processes of photosynthesis and the dark metabolism of plant cells, in particular the Calvin cycle of carbon fixation, nitrogen and sulfur cycles, the glycolytic cycle, and other metabolic pathways (Karavaev and Kukushkin 1993; Kuznetsova and Kukushkin 1996; Zhu et al. 2007; references in the book "Photosynthesis *in silico*", 2009). The state of metabolism controls the degree of quinone pool reduction, the efficiency of the acceptor side of PSI, and the ratio between linear and cyclic electron transport pathways around PSI.

In the models that take into account the relationship of primary processes to metabolism, it is not always necessary to use detailed submodels of multienzyme complexes. One can use reduced models, provided they retain the main kinetic characteristics of the full versions. Such models can be used to analyze not only the growth part of the fluorescence induction curve (which is traditional for modeling) but also the induction curve portion recorded at longer time intervals. In fact, various types of stresses (e.g., inhibitors, starvation) cause a significant change in the shape of the induction fluorescence curve at times longer than 1–2 s following onset of illumination. These changes are often associated with the effects of oxygen stress, imbalance in protein synthesis, and other alterations, the details of which are not currently well understood. But these processes need to be included in the model, at least in the form of parameters, if we want to use the model for quantitative analysis in biotechnology and environmental monitoring.

The kinetic approach proved effective for the evaluation of the values of reaction rate constants and the relationship between energy flow in the electron transport chain and a large number of light-induced processes occurring simultaneously in a cell population. However, systems of differential equations are hardly suitable for

A. Rubin and G. Riznichenko, *Mathematical Biophysics*, Biological and Medical Physics, Biomedical Engineering, DOI 10.1007/978-1-4614-8702-9,

© Springer Science+Business Media New York 2014

detailed descriptions of these processes in terms of the spatial heterogeneity and complex geometry of interacting macromolecules in the confined interior of the photosynthetic membrane. In fact, separate compartments of the thylakoid involve a relatively small number (tens or hundreds) of macromolecules. Thus the use of a traditional kinetic approach based on the concepts of statistical physics and the kinetics of chemical reactions in solution is not quite correct.

To simulate the interaction of assemblies of macromolecules with limited mobility in a heterogeneous interior of complex shape, we have been developing an approach of direct multiparticle modeling. In our models, the simulated molecules that move in accordance with the laws of Brownian dynamics are oriented relative to each other in the electrostatic field created by the molecules themselves and by the medium. They form a 3D computer environment, constructed according to the contemporary data about the spatial organization of the photosynthetic membrane. The adequacy of the model is proved by comparing the kinetic characteristics of the simulated processes with the observed experimental data.

Due to the direct multiparticle modeling approach, it becomes possible to take explicitly into account the shape and size of the molecules and elements of the reaction volume. We study the effect of the geometry of the reaction volume, the number and location of interacting molecules, and other characteristics on the rate of the reaction. Using data from the PDB we can directly calculate the electric potential distribution around each of the interacting molecules and evaluate the role of electrostatic interactions in the process of docking and complex formation in the oxidation–reduction reaction.

This can be done on the basis of an implicit analysis of the kinetic model by introducing additional "effective" parameters, although the physical nature of such parameters usually cannot be interpreted unambiguously. At the same time, multiparticle modeling helps to understand how the real physical mechanisms of molecular interactions (e.g., diffusion, electrostatics) determine the overall dynamics of the processes in a cell.

Currently we are working on modeling the processes of interaction of PSI in the membrane with a donor component Pc in lumina and the acceptor component (Fd or Fld) in stromata. The study of these processes in the framework of a combined model will reveal the mechanisms of regulation of a photosynthetic reaction center. The next important step is to combine the kinetic modeling approach with direct multiparticle modeling to simulate electron transfer by mobile carriers and with partial differential equations to describe the evolution of the trasmembrane potential.

In general, the application of kinetic modeling and a direct multiparticle approach and their combination in the study of photosynthesis appears to be promising for understanding the fundamental mechanisms of processes in living cells and for the practical purpose of diagnosing plant and algal cell states in biotechnology and environmental monitoring.

References

Abaturova AM (2008) Investigation of mechanisms of component interactions in the photosynthetic electron transport chain by means of computer simulation methods. PhD Thesis. Lomonosov Moscow State University, Moscow

Abaturova AV, Kovalenko IB Riznichenko GY et al (2008) Direct computer modeling of the ionic strength effect on the rate constant of interaction of flavodocsin with Photosystem 1. In: Riznichenko G. (ed) Mathematics, computer, education, vol 15(3). ICS-RCD, Moscow-Izhevsk, p 71 (Rus)

Abaturova AV, Kovalenko IB, Riznichenko GY et al (2009) Investigation of complex formation of flavodoxin and Photosystem I by means of direct multiparticle computer simulation. Comput Res Model 1(1):85–91 (Rus)

Albertsson P-A (2000) The domain structure and function of the thylakoid membrane. Recent Res Dev Bioener 1:143–171

Albertsson P-A (2001) A quantitative model of the domain structure of the photosynthetic membrane. Trends Plant Sci 6:349–354

Alekseev VV, Loskutov AY (1987) Control of the system with strange attractor by periodic parametric action. Doclady AS USSR 293:1346–1348 (Rus)

Aliev RR (2008) Computer modeling of hart activity. In: Belozerkovsky OM and Cholodov AS (eds) Medicine in the mirror of informatics. Nauka, Moscow

Aliev RR, Chailakhyan LM (2005) Study of the effect of acetylcholine on intracellular homeostasis of true pacemaker cells of rabbit sinus node using computer simulation. Dokl Biochem Biophys 402(1):236–239

Aliev RR, Panfilov AV (1996) A simple two-variable model of cardiac excitation. Chaos Solitons Fractals 7(3):293–301

Allen JF (2004) Cytochrome b6f: structure for signalling and vectorial metabolism. Trends Plant Sci 9(3):130–137

Aponina EA, Aponin YM, Bazykin AD (1982) Analysis of the complex dynamic behavior in the predator-two prays model. In: Izrael YA (ed) Problems of environment monitoring and ecosystem modeling, vol 5. Hydrometeoizdat, Leningrad

Awrejcewich J (1996) Crystals. Their role in nature and in science. Academic, New York

Baake E, Shloeder JP (1992) Modelling the fast fluorescence rise of photosynthesis. Bull Math Biol 54:999–1021

Baake E, Strasser RJ (1990) A differential equation model for the description of the fast fluorescence rise (O-I-D-P transient) in leaves. In: Baltscheffsky M (ed) Current research in photosynthesis, vol 1. Kluwer Academic, Dordrecht, pp 567–570

Balakhovskii IS (1965) Some regimes of exitation movement in ideal excitable tissue. Biofizika 10(6):1063–1067 (Rus)

Bann C (1964) Crystals. Their role in nature and in science. Academic, New York

A. Rubin and G. Riznichenko, *Mathematical Biophysics*, Biological and Medical Physics, Biomedical Engineering, DOI 10.1007/978-1-4614-8702-9,

© Springer Science+Business Media New York 2014

Barber J (1982) Influence of surface charges on thylakoid structure and function. Annu Rev Plant Physiol 33:261–295
Bard JB (1981) A model for generating aspects of zebra and other mammalian coat patterns. J Theor Biol 93(2):363–385
Bazykin AD (1985) Mathematical biophysics of interacting populations. Nauka, Moscow
Bazykin AD (1998) Nonlinear dynamics of interacting populations. World Scientific, Singapore
Belintsev BN, Belousov LB, Zaraisky AG (1985) Model of epithelial morphogenesis based on elastic forces and the contact cell polarization. Ontogenesis 16:5–14 (Rus)
Belousov BP (1959) Periodic reaction and its mechanisms. In: The collection of essays in radiation medicine in 1958. Medgiz, Moscow (Rus)
Belyaeva NE (2004) Generalized model of primary photosynthetic processes in thylakoid. Dissertation, Lomonosov Moscow State University (Rus)
Belyaeva NE, Lebedeva GV, Riznichenko GYu (2003) Kinetic model of primary photosynthetic processes in chloroplasts. Modeling of electric potential on thylakoid membrane. In: Riznichenko G. (ed) Mathematics, computer, education, vol 10. Progress-Traditsiya, Moscow, pp 263–276 (Rus)
Belyaeva NE, Schmitt F-J, Paschenko VZ et al (2008) PSII model-based simulations of single turnover flash-induced transients of fluorescence yield monitored within the time domain of 100ns-10 s on dark-adapted Chlorella pyrenoidosa cells. Photosynth Res 98:105–119
Belyaeva NE, Schmitt F-J, Paschenko VZ et al (2011) PS II model based analysis of transient fluorescence yield measured on whole leaves of Arabidopsis thaliana after excitation with light flashes of different energies. Biosystems 103(2):188–195
Bendall DS, Manasse RS (1995) Cyclic photophosphorylation and electron transport. Biochim Biophys Acta 1229:23–38
Bergmann A, Eckert H-J, Renger G (1998) Picosecond laser-fluorometer with simultaneous time- and wavelength resolution for monitoring decay spectra of photoinhibited Photosystem II particles at 277 K and 10 K. Photosynth Res 58:305–312
Bernarding J, Eckert H-J, Eichler HJ et al (1994) Kinetic studies on the stabilization of the primary radical pair $P680^{+}Phe^{-}$ in different photosystem II preparations from higher plants. Photochem Photobiol 59(5):566–573
Bernhardt K, Trissl H-W (1999) Theories for kinetics and yield of fluorescence and photochemistry: how, if at all, can different models of antenna organization be distinguished experimentally? Biochim Biophys Acta 1409:125–142
Bloomfield P (2000) Fourier analysis of time series. An introduction. Wiley, New York
Boels HD, Hansen UP (1982) Light and electrical current stimulate the same feed-back system in Nitella. Plant Cell Physiol 23:343–346
Boork J, Wennerström H (1984) The influence of membrane potentials on reaction rates. Control in free-energy transducing systems. Biochim Biophys Acta 767(2):314–320
Boyland PL (1986) Bifurcations of circle maps: Arnol'd tongues, bistability and rotation intervals. Comm Math Phys 106(3): 353–381 http://euclid./euclid.cmp/1104115779
Brettel K, Schlodder E, Witt HT (1984) Nanosecond reduction kinetics of photooxidized chlorophyll-aí(P-680) in single flashes as a probe for the electron pathway, H +-release and charge accumulation in the O2-evolving complex. Biochim Biophys Acta 766:403–415
Briggs GE, Haldane JB (1925) A note on the kinetics of enzyme action. Biochem J 19:338–339
Brown AJ (1902) Enzyme action. J Chem Soc Trans 81:373–388
Brown GC, Brand MD (1986) Changes in permeability to protons and other cations at high proton motive force in rat liver mitochondria. Biochem J 234:75–81
Bukchov NG, Egorova EA, Govindachary S, Carpentier R (2004) Changes in polyphasic chlorophyll a fluorescence induction curve upon inhibition of donor or acceptor side of photosystem II in isolated thylakoids. Biochim Biophys Acta 1657:121–130
Bukhov NG, Damirov HG, Dzhibladze HB et al (1988) Kinetic analysis of variable and delayed fluorescence induction transitions in the presence of diuron and carbonylcyanidephenylhydroson. Biol Sci (Rus) 4:28–37

Bulychev AA, Vredenberg WJ (1999) Light-triggered electrical events in the thylakoid membrane of plant chloroplast. Physiol Plantarum 105:577–584

Bulychev AA, Vredenberg WJ (2001) Modulation of photosystem II chlorophyll fluorescence by electrogenic events generated by photosystem I. Bioelectrochemistry 54:157–168

Bulychev AA, Niyazova MM, Rubin AB (1987) Fluorescence changes of chloroplasts caused by the shifts of membrane-potential and their dependence on the redox state of the acceptor of photosystem II. Biol Membr 4:262–269 (Rus)

Bulychev AA, Polezhaev AA, Zykov SV et al (2001) Light-triggered pH banding profile in *Chara* revealed with a scanning pH microprobe and its relation to self-organization phenomena. J Theor Biol 212(3):275–294

Bulychev AA, Cherkashin AA, Rubin AB et al (2002) Distribution of acidic and alkaline bands on the surface of *Chara corallina* cells under stationary and local illumination. Fiziol Rast 49:805–813 (Rus)

Bulychev AA, Zykov VS, Rubin AB et al (2003) Transitions from alkaline spots to regular bands during pH pattern formation at the plasmalemma of *Chara* cells. Eur Biophys J 32:144–153

Cadoni M, De Leo R, Demelio S et al (2008) Nonlinear torsional dynamics of macromolecules: from DNA to polyethylene. Int J Non Lin Mech 43:1094–1107

Cadoni M, Demelio R, De Leo S et al (2010) Propagation of twist solitons in real DNA chains. J Nonlin Math Phys 17:557–569

Chance B (1943) The kinetics of the enzyme-substrate compound of peroxidase. J Biol Chem 151:553–577

Chemeris YK, Korol'kov NS, Seifullina NK et al (2004) PSII complexes with destabilized primary quinone acceptor of electrons in dark-adapted chlorella. J Plant Physiol 51(1):9–14

Chernavskii DS (1986) Biology and information. Znanie, Moscow

Chernavskii DS (2000) The origin of life and thinking from the viewpoint of modern physics. Phys Usp 43:151–176

Chow WS, Hope AB (2004) Electron fluxes through photosystem I in cucumber leaf discs probed by far-red light. Photosynth Res 81:77–89

Chow PL, Tam WC (1976) Periodic and traveling wave solutions to Volterra-Lotka equations with diffusion. Bull Math Biol 38(6):643–658

Chrabrova EN, Vorobjeva TN, Riznichenko GY et al (1989) Identification of electrostatic parameters of plastocyanin interaction with PSI complex in higher plants. Biophysika 34(3):429–433

Christen G, Seeliger A, Renger G (1999) $P680^{\bullet+}$ reduction kinetics and redox transition probability of the water oxidizing complex as a function of pH and H/D isotope exchange in spinach thylakoids. Biochemistry 38:6082–6092

Christen G, Steffen R, Renger G (2000) Delayed fluorescence emitted from light harvesting complex II and photosystem II of higher plants in the 100 ns-5μs time domain. FEBS Lett 475:103–106

Cleland RE, Bendall DS (1992) Photosystem I cyclic electron transport: measurement of ferredoxin-plastoquinone reductase activity. Photosynth Res 34:409–418

Crick FHS, Watson JD (1954) The complementary structure of deoxyribonucleic acid. Proc R Soc (London) A-223:80–96

Crofts AR, Wraight CA (1983) Tha lelctrochemical domain of photosynthesis. BBA 726: 149–185

Crowley P, Hunter D, Sato K et al (2003) The parsley plastocyanin -turnip cytochrome f: a structurally distorted but kinetically functional acidic patch. Biochem J 378(1): 45–57

Cruz JA, Salbilla BA, Kanazawa A et al (2001) Inhibition of plastocyanin to P_{700}^{+} electron transfer in Chlamydomonas reinhardtii by hyperosmotic stress. Plant Physiol 127:1167–1179

Cuenda S, Sánchez A (2004) Disorder and fluctuations in nonlinear excitations in DNA. Fluct Noise Lett 4:L491–L504

Dahlin C (2003) Surface charge densities and membrane fluidities in thylakoids with different degrees of thylakoid appression after Norflurazon treatment. Photosynthetica 41(4):635–639

Dau H (1994) Short-term adaptation of plants to changing light intensities and its relation to Photosystem II photochemistry and fluorescence emission. J Photochem Photobiol B Biol 26:3–27

Dau H, Sauer K (1992) Electric field effect on the picosecond fluorescence of photosystem II and its relation to the energetics and kinetics of primary charge separation. Biochim Biophys Acta 1102:91–106

de la Cerda B, Navarro JA, Hervas M et al (1997) Changes in the reaction mechanism of electron transfer from plastocyanin to photosystem I in the *Cyanobacterium Synechocystis* sp. PCC 6803 as induced by site-directed mutagenesis of the copper protein. Biochemistry 36:10125–10130

De Leo R, Demelio S (2008) Numerical analysis of solitons profiles in a composite model for DNA torsion dynamics. Int J Non Lin Mech 43:1029–1039

Dekker JP, Boekema EJ (2005) Supramolecular organization of thylakoid membrane proteins in green plants. Biochim Biophys Acta 1706:12–39

Derjaguin BV, Churaev NV, Muller VM (1985) Surface forces. Nauka, Moscow (Rus)

Derks G, Gaeta G (2011) A minimal model of DNA dynamics in interaction with RNA-Polymerase. Phys D 240:1805–1817

Diakonova AN, Abaturova AV, Kovalenko IB et al (2008) Direct computer modeling of ferredocsin-FNR complex formation. In: Riznichenko G. (ed) Mathematics, computer, education, vol 15(3). ICR-RCD, Moscow-Izhevsk, p 263 (Rus)

Doi M, Edwards SF (1986) The theory of polymer dynamics. Oxford University Press, New York

Drachev LA, Kaurov BS, Mamedov MD et al (1989) Fkash induced electrogenic events in the photosynthetic reaction center and BC1 complexes of *Phodobacter sphaeroides* chromatophores. Biophys. Biochem Acta 973(2): 189–197

Driesch H (1905) Der Vitalismus als Geschichte und als Lehre. Barth, Leipzig, in English (2010) Kessinger

Driesch H (1914) The history and theory of vitalism. Macmillan, London

Dubinsky AY, Tikhonov AN (1994) Regulation of electron and proton transport in the chloroplasts. Kinetic model and comparison of it with the experiment. Biophysics 39:657–670

Dubinsky AY, Tikhonov AN (1995) Mathematical simulation of the light-induced uptake of protons by chloroplasts upon various mechanisms of proton leak through thylakoid membrane. Biophysics 40:365–371

Dupont G, Goldbeter A (1989) Theoretical insights into the origin of signal-induced calcium oscillations. In: Goldbeter A (ed) Cell to cell signalling: from experiments to theoretical models. Academic, London

Dupont G, Goldbeter A (1992) Oscillations and waves of cytosolic calcium: insights from theoretical models. Bioessays 14:485–493

Dupont G, Goldbeter A (1994) Properties of intracellular Ca2+ waves generated by a model based on Ca^{2+} induced Ca^{2+} release. Biophys J 67:2191–2204

Durell SR, Labanowski JK, Gross EL (1990) Modeling of the electrostatic potential field of plastocyanin. Arch Biochem Biophys 277: 241–54

Dynnik VV, Sel'kov EE (1975) Oscillator generator in the lower portion of the glycolytic system. Biofizika 20(2):288–292

Eckert H-J, Renger G (1988) Temperature dependence of P680+ reduction in O2-evolving PS II membrane fragments at different redox states Si of the water oxidizing system. FEBS Lett 236:425–431

Edwards GE, Baker NR (1993) Can CO_2 assimilation be predicted accurately from chlorophyll fluorescence analysis? Photosynth Res 37:89–102

Endo M, Tanaka M, Ogawa Y (1970) Calcium induced release of calcium from the sarcoplasmic reticulum of skinned skeletal muscle fibres. Nature 228(5266):34–36

Englander SW, Kallenbach NR, Heeger AJ et al (1980) Nature of the open state in long polynucleotide double helices: possibility of solution excitations. Proc Natl Acad Sci USA 77:7222–7226

Fabiato A, Fabiato F (1975) Effects of magnesium on contractile activation of skinned cardiac cells. J Physiol 249:497–517
Fan D-Y, Nie Q, Hope AB et al (2007) Quantification of cyclic electron flow around Photosystem I in spinach leaves during photosynthetic induction. Photosynth Res 94:347–357
Feijo JA, Sainhas J, Hackett GR et al (1999) Growing pollen tubes possess a constitutive alkaline band in the clear zone and a growth-dependent acidic tip. J Cell Biol 144:483–496
Field RJ, Burger M (eds) (1985) Oscillations and travelling waves in chemical systems. Wiley-Interscience, New York
Field RJ, Noyes RM (1974) Oscillations in chemical systems. IV. Limit cycle behavior in a model of a real chemical reaction. J Chem Phys 60:1877–1884
Field RJ, Körös E, Noyes RM (1972) Oscillations in chemical systems. II. Thorough analysis of temporal oscillations in the bromate-cerium-malonic acid system. J Am Chem Soc 94:8649–8664
Finkelstein AV, Ptitsyn OB (2002) Protein physics. A course of lectures. Academic, Amsterdam
Fisahn J, Mikschl E, Hansen U-P (1986) Separate oscillations of the electrogenic pump and of a K^+-channel in Nitella as revealed by simultaneous measurement of membrane potential and of resistance. J Exp Bot 37(1): 34–47
Fisahn J, Lucas WJ (1992) Direct measurement of the reversal potential and the current–voltage characteristics in the acid and alkaline regions of *Chara coralline*. Planta 186:506–512
Fisahn J, Lucas WJ (1995) Spatial organization of transport domains and subdomain formation in the plasma membrane of *Chara coralline*. J Membr Biol 147:275–281
Fisahn J, McConnaughey T, Lucas WJ (1989) Oscillations in extracellular current, external pH and membrane potential and conductance in the alkaline bands of *Nitella* and *Chara*. J Exp Bot 40:1185–1189
Fisher RA (1937) The wave of advance of advantageous genes. Ann Eugen 7:353–369
FitzHugh R (1961) Impulses and physiological states in theoretical model of nerve membrane. Biophys J 1(6):445–466
FitzHugh R (1969) Mathematical models of excitation and propagation in nerve. In: Schwan HP (ed) Biological engineering. McGraw-Hill, New York
Franklin RE, Ghosting RG (1953) Molecular structure of nucleic acid. Molecular configuration of sodium thymonucleateb. Nature 171:740–741
Freidlin MI, Sivak SA (1976) Small parameter method in multidimensional reaction–diffusion problem. Stud Biophys 76:129–136
Gabdoulline RR, Wade RC (1997) Simulation of the diffusional association of barnase and barstar. Biophys J 72(5):1917–1929
Gabdoulline RR, Wade RC (1998) Brownian dynamics simulation of protein-protein diffusional encounter. Methods 14:329–341
Gause GF (1932) Experimental studies on the struggle for existence. 1. Mixed population of two species of yeast. J Exp Biol (British) 9:389–402
Gause GF (1934a) Experimental analysis of Vito Volterra's mathematical theory of struggle for existence. Science 79:16
Gause GF (1934b) The struggle for existence. Williams and Wilkins, Baltimore, MD
Gelfand IM, Gurfinkel VS, Kots IM, Tsetlin ML, Shik ML (1963) On synchronization of motor units and its connection with the model representation. Biofizika 8:475–487 (Rus)
Gelfand IM, Gurfincel VC, Tsetlin ML et al (1966) Some aspects of movement research. In: Gelfand IM (ed) Models of structural and functional organization of some biological systems. Nauka, Moscow (Rus)
Gibasiewicz K, Dobek A, Breton J, Leibl W (2001) Modulation of primary radical pair kinetics and energetics in photosystem II by the redox state of the quinone electron acceptor Q_A. Biophys J 80:1617–1630
Gibbon BC, Kropf DL (1991) pH gradients and cell polarity in Pelvetia embryos. Protoplasma 163:43–50
Gierer A (1981) Generation of biological patterns and form: some physical, mathematical and logical aspects. Prog Biophys Mol Biol 37:1–47
Gierer A, Meinhardt H (1972) A theory of biological pattern formation. Kybernetik 12(1):30–39

Ginzbourg LR, Colivan M (2004) How planets move and populations grow. Oxford University Press, Oxford
Giudice E, Várnai P, Lavery R (2003) Base pair opening within B-DNA: free energy pathways for GC and AT pairs from umbrella sampling simulations. Nucleic Acids Res 31:1434–1443
Gizzatkulov NM, Goryanin II, Metelkin EA et al (2010) DBSolve Optimum: a software package for kinetic modeling which allows dynamic visualization of simulation results. BMC Syst Biol 4:109
Glansdorff P, Prigogine I (1971) Thermodynamics theory of structure, stability and fluctuations. Wiley-Interscience, London
Goh C-H, Schreiber U, Hedrich R (1999) New approach of monitoring changes in chlorophyll a fluorescence of single guard cells and protoplasts in response to physiological stimuli. Plant Cell Environ 22:1057–1070
Golbeck J (ed) (2006) Photosystem I: the light-driven plastocyanin: ferredoxin oxidoreductase. Springer, Dordrecht
Goldbeter A (1996) Biochemical oscillations and cellular rhythms: the molecular bases of periodic and chaotic behaviour. Cambridge University Press, Cambridge
Goodwin BC (1984) Changing from an evolutionary to a generative paradigm in biology. In: Pollard JW (ed) Evolutionary theory: paths into the future. Wiley, Chichester
Govindjee (ed) (1982) Photosynthesis, vol 2. Academic, New York
Govindjee (1995) Sixty-three years since Kautsky: chlorophyll a fluorescence. Aust J Plant Physiol 22:131–160
Gradmann D (2001) Impact of apoplastic volume on ionic relations in plant cells. J Membr Biol 184:61–69
Gradmann D, Hoffstadt J (1998) Electrocoupling of ion transporters in plants: interaction with internal ion concentrations. J Membr Biol 166:51–59
Gradmann D, Blatt MR, Thiel G (1993) Electrocoupling of transporters in plants. J Membr Biol 136:327–332
Gray P, Scott SK (1994) Chemical oscillations and instabilities. Oxford Science, Oxford
Grill S, Zykov VS, Muller SC (1995) Feedback controlled dynamics of meandering spiral waves. Phys Rev Lett 75(18):3368–3371
Gross EL (1996) Plastocyan: structure, location, diffusion and electron transfer mechanisms. In: Ort DR, Yocum CF (eds) Oxygenic photosynthesis: the light reactions. Kluwer Academic, Dordrecht
Gross EL, Pearson DC (2003) Brownian dynamics simulations of the interaction of Chlamydomonas cytochrome f with plastocyanin and cytochrome c6. Biophys J 85:2055–2068
Gross EL (2004) A Brownian dynamics study of the interaction of *Phormidium laminosum* plastocyanin with *Phormidium laminosum* cytochrome *f*. Biophys J 87:2043–2059
Gross EL, Rosenberg I (2006) A Brownian dynamics study of the interaction of Phormidium cytochrome f with various cyanobacterial plastocyanins. Biophys J 90:366–380
Guéron M, Kochoyan M, Leroy J-L (1987) A single mode of DNA base-pair opening drives imino proton exchange. Nature 328:89–92
Gurvich AG (1944) The theory of biological field. Sov Nauka, Moscow (Rus)
Haddadian EJ, Gross EL (2005) Brownian dynamics study of cytochrome f interactions with cytochrome c6 and plastocyanin in Chlamydomonas reinhardtii plastocyanin, and cytochrome c6 mutants. Biophys J 88:2323–2339
Haddadian EJ, Gross EL (2006) A Brownian dynamics study of the interactions of the luminal domains of the cytochrome b_6f complex with plastocyanin and cytochrome c_6: the effects of the Rieske FeS protein on the interactions. Biophys J 91:2589–2600
Haehnel W, Propper A, Krause H (1980) Evidence for complexed plastocyanin as the immediate electron donor of P-700. Biochim Biophys Acta 593:384–399
Haehnel W, Ratajczak R, Robenek H (1989) Lateral distribution and diffusion of plastocyanin in chloroplast thylakoids. J Cell Biol 108:1397–1405
Haehnel W, Jansen T, Gause K et al (1994) Electron transfer from plastocyanin to photosystem I. EMBO J 13:1028–1038
Haldane JB (1930) Enzymes. In: Plimmer RHA, Sir FG, Hopkins MA (eds) Monographs on biochemistry. Longmans, Green & Co, London, MIT Press 1965 edition with new preface

Hall DO (1976) The coupling of photophosphorylation to electron transport in isolated chloroplasts. In: Barber J (ed) The intact chloroplast. Elsevier North-Holland Biomedical, Amsterdam, p 135
Hall DO, Rao KK (1999) Photosynthesis, 6th edn. Cambridge University Press, Cambridge
Hansen UP (1978) Do the light-induced changes in the membrane potential of Nitella reflect the feed-back regulation of a cytoplasmic parameter? J Membr Biol 41:197–224
Helmholtz H (1850) Messungen über den zeitlichen Verlauf der Zuckung animalischer Muskeln und die Fortpflanzungsgeschwindigkeit der Reizung in den Nerven. Archiv für Anatomie, Physiologie und wissenschaftliche Medicin 17:176–364
Henri V (1902) Theorie generale de l'action de quelques diastases. C R Acad Sci 135:916–930
Henri V (1903) Lois generals de l'action des diastases. Hermann et Ci, Paris.
Herbert D (1958) Some principles of continuous culture. In: Tunesall G (ed) Recent progress in microbiology. VII International congress for microbiology. Almqvist & Wiksell, Stockholm
Herbert D, Elswerth R, Telling RC (1956) The continuous culture of bacteria: a theoretical and experimental study. J Gen Microbiol 14:601–622
Hess B, Markus M (1985) The diversity of biochemical time patterns. Ber Bunsenges Phys Chem 89:642–651
Higgins JA (1954) A chemical mechanism for oscillations in glycolytic intermediates in yeast cells. Proc Natl Acad Sci USA 51:989–994
Higgins JA (1964) A chemical mechanism for oscillations in glycolytic intermediates in yeast cells. Proc Natl Acad Sci USA 51:989–994
Higgins JA (1967) The theory of oscillating reactions. Ind Eng Chem 59(5):18–62
Hill R, Bendall F (1960) Function of the two cytochrome components in chloroplasts: a working hypothesis. Nature 186:136–137
Hinshelwood CN (1946) The chemical kinetics of the bacterial cell. Oxford University Press, Oxford
Hockney RW, Eastwood JW (1981) Computer simulation using particles. McGraw-Hill, New York
Hodgkin AL, Huxley AF (1952) A quantitative description of membrane current and its application to conduction and excitation in nerve. J Physiol 117(4):500–544
Holling CS (1959) Some characteristics of simple types of predation and parasitism. Can Entomol 91:385–398
Hope AB (2000) Electron transfers amongst cytochrome f, plastocyanin and photosystem I: kinetics and mechanisms. Biochim Biophys Acta 1456:5–26
Hope AB, Huilgol RR, Panizza M et al (1992) The flash-induced turnover of cytochrome b-563, cytochrome f and plastocyanin in chloroplasts. Model and estimation of kinetic parameters. Biochim Biophys Acta 1100:15–26
Hsu B-D (1992) A theoretical study on the fluorescence induction curve of spinach thylakoids in the absence of DCMU. Biochim Biophys Acta 1140:30–36
Hsu B-D (1993) Evidence for the contribution of the S-state transitions of oxygen evolution to the initial phase of fluorescence induction. Photosynth Res 36:81–88
Hunter PJ, Kohl P, Noble D (2001) Integrative models of heart: achievements and limitations. Phil Trans R Soc A 359:1049–1054
Ireland CR, Long SP, Baker NR (1984) The relationship between carbon dioxide fixation and chlorophyll a fluorescence during induction of photosynthesis in maize leaves at different temperatures and carbon dioxide concentration. Planta 160:550–558
Israel G (1988) On the contribution of Volterra and Lotka to the development of modern biomathematics. Hist Philos Life Sci 10(1):37–49
Ivanitskii GR, Krinskii VI, Celkov EE (1978) Mathematical biophysics of the cell. Nauka, Moscow (Rus)
Joliot P, Joliot A (2002) Cyclic electron transport in plant leaf. Proc Natl Acad Sci USA 99:10209–10214
Joliot P, Joliot A (2006) Cyclic electron flow in C3 plants. Biochim Biophys Acta 1757:362–368
Joliot P, Lavergne J, Beal D et al (1992) Plastoquinone compartmentation in chloroplasts. I. Evidence for domains with different rates of photo-reduction. Biochim Biophys Acta 1101:1–12

Jolley C, Ben-Shem A, Nelson N et al (2005) Structure of plant photosystem I revealed by theoretical modeling. J Biol Chem 280:33627–33636
Kaant A, Young S, Bendall DS (1996) The role of acidic residues of plastocyanin in its interaction with cytochrome f. Biochim Biophys Acta 1277:115–126
Kamali J, Lebedeva GV, Demin OV et al (2004) A kinetic model of cytochrome bf complex. The fitting of model parameters to experimental data. Biofizika 49(6):1061–1068
Karavaev VA, Kukushkin AK (1993) Theoretical model of light and dark processes of photosynthesis: the problem of regulation. Biophysics 38(6):987–1003
Kern J, Renger G (2007) Photosystem II: structure and mechanism of the water: plastoquinone oxidoreductase. Photosynth Res 94:183–202
Kholodenko BN (1988) Stabilizing regulation on multienzyme systems: modeling of bioenergetic processes. Doktoral (Phys.-Math.) Dissertation, Belozersky Institute of Physico-Chemical Biology
Kirchhoff H, Horstmann S, Weis E (2000) Control of the photosynthetic electron transport by PQ diffusion microdomains in thylakoids of higher plants. Biochim Biophys Acta 1459:148–168
Kirchhoff H, Mukherjee U, Galla H-J (2002) Molecular architecture of the thylakoid membrane: lipid diffusion space for plastoquinone. Biochemistry 41:4872–4882
Kniazeva OS, Kovalenko IB, Abaturova AM et al (2010) Multiparticle computer simulation of diffusion and interaction of plastocyanin with cytochrome f in the electrostatic field of the thylakoid membrane. Biophyzika 55(2):221–227
Kohl P, Ravens U (2003) Mechano-electric feedback and cardiac arrhythmias. Prog Biophys Mol Biol 82(1–3):1–266
Kolmogoroff AN, Petrovsky IG, Piscounoff NS (1937) Etude de equation de la diffusion avec croissance de la quantite de materie et son application a un problem biologique. Moscow Univ Bull Math 1:1–25
Kolmogorov AN (1972) Qualitative analysis of mathematical models of population dynamics. In: Problems of cybernetics, vol. 5. Nauka, Moscow, pp 100–106
Kolmogoroff AN, Petrovsky IG, and Piscounoff NS (1975) The study of the diffusion equation, coupled with an increase in substance and its application to a biological problem. In: Problems of cybernetics, vol 12 (Rus) 3–30
Kovalenko IB, Ustinin DM, Grachev NE et al (2003) Experimental and theoretical investigation of cyclic electron transport around photosystem I. Biofizika 48(4):656–665
Kovalenko IB, Abaturova AM, Gromov PA et al (2006) Direct simulation of plastocyanin and cytochrome f interactions in solution. Phys Biol 3:121–129
Kovalenko IB, Abaturova AM, Ustinin DM et al (2007) Multiparticle computer simulation of photosynthetic electron transport in a thylakoid membrane. Biofizika 52(3):492–502
Kovalenko IB, Abaturova AM, Gromov PA et al (2008) Computer simulation of plastocyanin–-cytochrome f complex formation in the thylakoid lumen. Biophysics 53:140–146
Kovalenko IB, Abaturova AM, Riznichenko GY et al (2009) A novel approach to computer simulation of protein–protein complex formation. Dokl Biochem Biophys 427:215–217
Kovalenko IB, Diakonova AN, Abaturova AM, Riznichenko GY, Rubin AB (2010) Direct computer simulation of ferredoxin and FNR complex formation in solution. Phys Biol 7:026001
Kovalenko IB, Knyazeva OS, Riznichenko GY et al (2011a) Mechanisms of interaction of electron transport proteins in photosynthetic membranes of cyanobacteria. Dokl Biochem Biophys 440:272–274
Kovalenko IB, Abaturova AM, Diakonova AN et al (2011b) Computer simulation of protein-protein association in photosynthesis. Math Model Nat Phenom 6:39–54
Kovalenko IB, Abaturova AM, Riznichenko GY et al (2011c) Computer simulation of interaction of photosystem 1 with plastocyanin and ferredoxin. Biosystems 103:180–187
Kovaleva NA, Loskutov AY (2004) Stabilization of chaotic processes induced by diffusion. Dokl RAS 396(1):68–70
Krab K, Van Walraven HS, Hoolts MJS et al (1985) Measurement of diffusion potential in liposomes. Biochim Biophys Acta 809:236–244

Krause GH, Weiss E (1991) Chlorophyll fluorescence and photosynthesis; the basics. Ann Rev Plant Mol Biol 42:313–349

Krendeleva TE, Kukarskikh GP, Timofeev KN et al (2001) Ferredoxin-dependent cyclic electron transport in isolated thylakoids occurs with the participation of ferredoxin-NADP-reductase. Dokl Ross Akad Nauk 379:1–4 (Rus)

Krinskii VI, Fomin SV, Kholopov AV (1967) Critical mass during fibrillation. Biofizika 12(5):908–914

Krueger A, Protozanova E, Frank-Kamenetskii M (2006) Sequence-dependent base pair opening in DNA double helix. Biophys J 90:3091–3099

Kruger GHJ, Tsimilli-Michael M, Strasser RJ (1997) Light stress provokes plastic and elastic modification in structure and function of Photosystem II in camellia leaves. Physiol Plantarum 101:265–287

Kubo R (1966) The fluctuation-dissipation theorem. Rep Prog Phys 29(I):255–284

Kühn P, Eckert H-J, Eichler H-J et al (2004) Analysis of the $P680^{+\cdot}$ reduction pattern and its temperature dependence in oxygen evolving PS II core complexes from thermophilic cyanobacteria and higher plants. Phys Chem Chem Phys 6:4838–4843

Kuznetsova SA, Kukushkin AK (1996) Slow fluorescence induction and pentose phosphate pathway: theoretical investigation. Biophysics 41:1247–1253

Laible PD, Zipfel W, Owens TG (1994) Excited state dynamics in chlorophyll-based antennae: the role of transfer equilibrium. Biophys J 66:844–860

Laisk A, Walker DA (1989) A mathematical model of electron transport. Thermodynamic necessity for photosystem II regulation. Proc R Soc Lond B237:417–444

Laisk A, Nedbal L, Govindjee (eds) (2009) Photosynthesis *in silico*: understanding complexity from molecules to ecosystems. Springer, Dordrecht

Lavergne J, Trissl HW (1995) Theory of fluorescence induction in photosystem II. Biophys J 68:2474–2492

Lavrova AI, Plusnina TY, Bulychev AA et al (2005) Modeling of hysteresis in pH pattern formation along the cell membrane of the algae *Chara corallina*. Biofizika 50:105–110

Lazar D (1999) Chlorophyll a fluorescence induction. Biochem Biophys Acta 1412:1–28

Lazar D (2003) Chlorophyll a fluorescence rise induced by high light illumination of dark-adapted plant tissue studied by means of a model of photosystem II and considering photosystem II heterogeneity. J Theor Biol 220:469–503

Lazar D, Ilik P, Kruk J, Strzalka K et al (2005) A theoretical study on effect of the initial redox state of cytochrome b-559 on maximal chlorophyll fluorescence level (F_m0 Implications for photoinhibition of photosystem II. J Theor Biol 233:287–300

Lazar D (2006) The polyphasic chlorophyll *a* fluorescence rise measured under high intensity of exciting light. Funct Plant Biol 33:9–30

Lebedeva GV, Belyaeva NE, Riznichenko GY et al (2000) Kinetic model of photosystem II of green plants. J Phys Chem 74(10):1874–1883 (Rus)

Lebedeva GV, Belyaeva NE, Demin OV et al (2002) Kinetic model of primary photosynthetic processes in chloroplasts. Description of the fast phase of chlorophyll fluorescence induction under different light intensities. Biophysics 47(6):968–980

Lebrun A, Lavery R (1998) Modeling the mechanics of a DNA oligomer. J Biomol Struct Dyn 16:593–604

Leibl W, Breton J, Deprez J et al (1989) Photoelectric study on the kinetics of trapping and charge stabilization in oriented PS II membranes. Photosynth Res 22:257–275

Leonetti M, Pelce P (1994) On the theory of pH bands in Characean algae. C R Acad Sci Paris, Science de la vie/Life Sciences 317:801–805

Leslie PH (1945) On the use of matrices in certain population mathematics. Biometrika 33(3):183–212

Leslie PH (1948) Some further notes on the use of matrices in population mathematics. Biometrica 35:213–245

Lorenz EN (1963) Deterministic non-periodic flow. J Atmos Sci 20:131–141

Loskutov AY, Mikchailov AS (1996) Foundations of synergetics: chaos and noise. Springer, Berlin
Loskutov AY, Mikchailov AS (2007) Bases of the complex systems theory. ICS-RCD, Moscow-Izhevsk (Rus)
Loskutov AY, Shishmarev IA (1994) Control of dynamical system behavior by parametric perturbations: an analytic approach. Chaos 4(2):391–395
Lotka AJ (1925) Elements of physical biology. Williams and Wilkins, Baltimore, MD
MacArthur RH (1970) Graphical analysis of ecological systems. In: Cowan JD (ed) Some mathematical questions in biology. American Mathematical Society, Providence, RI
MacKendrick AG (1925) Application of mathematics to medical problems. Proc Edin Math Soc 44:98–130
Malkin S (1971) Fluorescence induction studies in isolated chloroplast. On the electron-transfer equilibrium in the pool of electron acceptors of photosystem II. Biochim Biophys Acta 234(3):415–427
Malkin R, Niyogi K (2000) Photosynthesis. In: Buchanan BB, Gruissem W, Jones R (eds) Biochemistry and molecular biology of plants. American Society of Plant Physiologists, Rockville, MD
Malthus TR (1798) An essay on the principal of Population. Reprinted (2007) BiblioBazaar, Charleston, SC
Markus M, Müller SC, Hess B (1985a) Observation of entrainment, quasiperiodicity and chaos in glycolyzing yeast extracts under periodic glucose input. Ber Bunsenges Phys Chem 89:651–654
Markus M, Kuschmitz D, Hess B (1985b) Properties of strange attractors in yeast glycolysis. Biophys Chem 22:95–105
Martiel J-L, Goldbeter A (1987) A model based on receptor desensitization for cyclic AMP signalling in *Dictyostelium* cells. Biophys J 52:807–828
Mathews FS, Mauk AG, Moore GR (2000) Protein–protein complexes formed by electron transfer proteins. In: Kleanthous C (ed) Protein–protein recognition. Oxford University Press, Oxford
May RM (1986) When two and two make four: nonlinear phenomena in ecology. Proc R Soc Lond 228:241–268
Mazurov ME (2008) Identification of mathematical models of nonlinear dynamical systems. ICS-RCD, Moscow-Izhevsk (Rus)
McAllister RE, Noble D, Tsien RW (1975) Reconstruction of the electrical activity of cardiac Purkinje fibres. J Physiol 251(1):1–59
McCommon JA, Harvey SC (1987) Dynamics of proteins and nucleic acids. Cambridge University Press, Cambridge
Medina M, Hervas M, Navarro JA et al (1992) A laser flash absorption spectroscopy study of *Anabaena* sp. PCC 7119 flavodoxin photoreduction by photosystem I particles from spinach. FEBS Lett 313(3):239–242
Meinhardt H (1982) Models of biological pattern formation. Academic, London
Meinhardt H (1995) The algorithmic beauty of sea shells. Springer, Berlin
Meinhardt H (2000) Beyond spots and stripes: generation of more complex patterns and modifications and additions of the basic reaction. In: Maini PK, Othmer HG, Santosa F, Keel M (eds) Mathematical models for biological pattern formation. Springer, New York
Messinger J, Renger G (2007) Photosynthetic water splitting. In: Renger G (ed) Primary processes of photosynthesis: principles and apparatus. Part II Reaction centers/photosystems, electron transport chains, photophosphorylation and evolution. Royal Society Chemistry, Cambridge
Michaelis L, Menten MI (1913) Die Kinetic der Invertinwirkung. Biochem Zeitung 49:333–369
Mikhailov AS, Loskutov AYu (1996) Foundations of synergetics II. Chaos and noise, 2nd revised and enlarged edition (1st ed 1991). Springer series in synergetics. Springer, Berlin
Miller AL, Gow NAR (1989) Correlation between root-generated ionic currents, pH, fusicoccin, indoleacetic acid, and growth of the primary root of *Zea mays*. Plant Physiol 89:1198–1206
Monk A, Othmer HG (1989) Cyclic AMP oscillations in suspensions of *Dictyostelium discoideum*. Phil Trans R Soc Lond 323:185–224

Monod J (1942) Recherches sur la croissanse des cultures bacteriennes. Hermann, Paris
Monod J (1950) La technique de culture continue. Theorie et applications. Ann Inst Pasteur 79:390–410
Monod J (1971) Chance and necessity. Vintage, New York
Monod J, Jacob F (1961) General conclusions: teleonomic mechanisms in cellular metabolism, growth and differentiation. Cold Spring Harb Symp Quant Biol 26:389–401
Müller SC, Plesser T, Hess B (1986) Two-dimensional spectrophotometry and pseudo-color representation of chemical patterns. Naturwissenschaften 73(4):165–179
Müller SC, Markus M, Hess B (1988) Dynamic pattern formation in chemistry and mathematics: aesthetics in sciences. Max-Planck-Institut fur Ernährungsphysiologie, Dortmund
Munekage Y, Hashimoto M, Miyake C et al (2004) Cyclic electron flow around photosystem I is essential for photosynthesis. Nature 429:579–582
Murakami S, Packer L (1970) Protonation and chlorophyll membrane structure. Cell Biol 47(2):32–351
Murphy LF (1983) A nonlinear growth mechanism in size structured population dynamic. J Theor Biol 104(8):493–506
Murray JD (1981) A pre-pattern formation mechanism for animal coat marking. J Theor Biol 88(1):161–199
Murray JD (1993) Mathematical biology. Springer, Berlin
Murray JD (2002) Mathematical biology. I: Introduction. Springer, New York
Murray JD (2003) Mathematical biology. II: Spatial models and biomedical applications. Springer, Berlin
Myshkin E, Bullerjahn GS (2002) Computational simulation of the docking of Prochlorothrix hollandica plastocyanin to photosystem I: modeling the electron transfer complex. Biophys J 82:3305–3313
Nagumo J, Arimoto S, Yoshizawa S (1962) An active pulse transmission line simulating nerve axon. Proc IRE 50(10):2061–2071
Nelson N, Yocum CF (2006) Structure and function of photosystems I and II. Annu Rev Plant Biol 57:521–565
Neubauer C, Schreiber U (1987) The polyphasic rise of chlorophyll fluorescence upon onset of strong continuous illumination: I. Saturation characteristics and partial control by the photosystem II acceptor side. Z Naturforsch 42c:1246–1254
Nicholls DG (1974) The influence of respiration and ATP hydrolysis on the proton-electrochemical gradient across the inner membrane of rat-liver mitochondria as determined by ion distribution. Eur J Biochem 50:305–315
Nicolis G, Prigogine IR (1977) Self-organization in non-equilibrium systems. Wiley, New York, NY
Nisbet RM, Gurney WSC (1982) Modeling fluctuating populations. Wiley, New York
Noble D (1962) A modification of the Hodgkin-Huxley equations applicable to Purkinje fiber action and pacemaker potentials. J Physiol 160(2):317–352
Noble D (2002) Modeling the heart: from genes to cells to the whole organ. Science 295:1678–1682
Novak B, Tyson JJ (1993) Modeling the cell division cycle: M-phase trigger, oscillation and size control. J Theor Biol 165:101–104
O'Keefe DP (1988) Structure and function of the chloroplast cytochrome bf complex. Photosynth Res 17:189–216
Oppenheimer JM (1970) Hans Driesch and the theory and practice of embryonic transplantation. Bull Hist Med 44(4):378–382
Oster GF, Murray JD, Harris AK (1983) Mechanical aspects of mesenchymal morphogenesis. J Embryol Exp Morphol 78:83–125
Papageorgiou GC, Govindjee (ed) (2004) Chlorophyll a fluorescence: a signature of photosynthesis. Springer, Berlin
Papageorgiou GC, Tsimilli-Michael M, Stamatakis K (2007) The fast and slow kinetics of chlorophyll a fluorescence induction in plants, algae and cyanobacteria: a viewpoint. Photosynth Res 94:275–290

Parson WW, Chu ZT, Warshel A (1990) Electrostatic control of charge separation in bacterial photosynthesis. Biochim Biophys Acta 1017:251–272
Patrin M (2008) Modeling of regulatory mechanisms of primary photosynthetic processes. MS Thesis Lomonosov Moscow State University, Moscow
Pearson DC Jr, Gross EL (1998) Brownian dynamics study of the interaction between plastocyanin and cytochrome f. Biophys J 75:2698–2711
Pearson DC, Gross EL, David ES (1996) Electrostatic properties of cytochrome f: implications for docking with plastocyanin. Biophys J 71:64–76
Pertsov AM, Aliev RR, Krinsky VI (1990) Three-dimensional twisted vortices in an excitable chemical medium. Nature 345(6274):419–421
Petrovskii SV, Malchow H (1999) A minimal model of pattern formation in prey–predator system. Math Comput Model (Pergamon) 29:49–63
Pielou EC (1969) An introduction to mathematical ecology. Wiley-Interscience, New York
Pielou EC (1977) Mathematical ecology. Wiley, New York
Plant RE (1978) The effect of calcium++ on bursting neurons. A modeling study. Biophys J 21(3):217–237
Plant RE (1981) Bifurcation and resonance in a model for bursting nerve cells. J Math Biol 11(1):15–32
Plyusnina TY, Riznichenko GY, Aksenov SI et al (1994) Effect of a weak electrictrical action on the trigger system of transmembrane ionic transfer. Biofizika 39(2):321–326
Plyusnina TY, Riznichenko GY (1996) The types of nonlinear behaviour of the system of ion transfer across the membrane on exposure to a weak electric field. Biofizika 41(4):953–957
Plyusnina TY, Lavrova AI, Riznichenko GY et al (2005) Modelling of pattern formation and oscillations in pH and transmembrane potential near the cell membrane of *Chara coralline*. Biofizika 3:492–499
Plyusnina TY, Lavrova AI, Price CB et al (2008) Nonlinear dynamics near the cell membrane of *Chara corallina*. J Biol Syst 16(2):197–217
Poincare H (1914) Science and method. Thomas Nelson, London
Polezhaev AA (2010) Mechanisms of biological morphogenesis. In: Riznichenko G, Rubin A (eds) Dynamic models of processes in cells and subcellular nanostructures. RCD-ICS, Moscow-Izhevsk (Rus)
Polezhaev AA, Zykov VS, Müller SC (1998) Destabilization of cell aggregation under nonstationary conditions. Phys Rev E 58(5):6328–6332
Polezhaev AA, Hilgardt C, Mair T et al (2005) Transition from an excitable to an oscillatory state in *Dictyostelium discoideum*. Syst Biol 152(2):75–79
Polezhaev AA, Pashkov RA, Lobanov AI et al (2006) Spatial patterns formed by chemotactic bacteria *Escherichia coli*. Int J Dev Biol 50(2–3):309–314
Potossin II, Schönknecht G (1996) Ion channel permeable for divalent and monovalent cations in native spinach thylakoid membranes. J Membr Biol 152:223–233
Prévost C, Takahashi M, Lavery R (2009) Deforming DNA: from physics to biology. R Chem Phys Chem 13:1399–1404
Prigogine I (1997) End of certainty. Free Press, New York
Prigogine IR, Lefever R (1968) Symmetry breaking instabilities in dissipative systems. J Chem Phys 48:1665–1700
Prigogine I, Stengers I (1984) Order out of chaos: man's new dialogue with nature. Heinemann, London
Prochaska U, Gross EL (1977) Evidence for the location of divalent cation binding sites on the chloroplast membrane. J Membr Biol 36:13–32
Rappaport F, Cuni A, Xiong L, Sayre R, Lavergne J (2005) Charge recombination and thermoluminescence in photosystem II. Biophys J 88:1948–1958
Renger G (2001) Photosynthetic water oxidation to molecular oxygen: apparatus and mechanism. Biochim Biophys Acta 1503:210–228

Renger G, Holzwarth AR (2005) Primary electron transfer. In: Wydrzynski T, Satoh K (eds) Photosystem II: the light driven water-plastoquinone oxido-reductase in photosynthesis. Springer, Dordrecht
Renger G, Schulze A (1985) Quantitative analysis of fluorescence induction curves in isolated spinach chloroplasts. Photobiochem Photobiophys 9:79–87
Renger G, Eckert H-J, Bergmann A et al (1995) Fluorescence and spectroscopic studies on exciton trapping and electron transfer in photosystem II of higher plants. Aust J Plant Physiol 22:167–181
Reynolds IA, Johnson EA, Tanford C (1985) Incorporation of membrane potential into theoretical analysis of electrogenic ion pumps. Proc Natl Acad Sci USA 82:6869–6873
Richard G-F, Kerrest A, Dujon B (2008) Comparative genomics and molecular dynamics of DNA repeats in eukaryotes. Microbiol Mol Biol Rev 72(4):686–727
Rienzo FR, Gabdoulline M, Menziani P et al (2001) Electrostatic analysis and Brownian dynamics simulation of the association of plastocyanin and cytochrome f. Biophys J 81:3090–3104
Rinzel J (1981) Models in neurobiology. In: Enns RH, Jones BL, Miura RM, Rangnekar SS (eds) Nonlinear phenomena in physics and biology. Plenum, New York
Rinzel J, Troy WC (1982) A one-variable map analysis of bursting in the Belousov-Zhabotinsky reaction. In: Smoller J (Ed) Nonlinear partial differential equations. American Mathematical Society, Providence, RI
Riznichenko GYu (1991) Mathematical models of primary photosynthetic processes. Advances in science and techniques. Biophysics, vol 31. VINITI, Moscow (Rus)
Riznichenko GY (2011) Lectures on mathematical models in biology. RCD, Moscow-Izhevsk (Rus)
Riznichenko GY, Plyusnina TY (1996) Non-linear organization of subcellular system – the condition for response to weak electromagnetic factors. Biofizika 41(2):421–425
Riznichenko GY, Rubin AB (1998) Mathematical models of production processes. Moscow State University Press, Moscow
Riznichenko GY, Rubin AB (2004) Biophysical dynamics of production processes. ICS, Moscow-Izhevsk (Rus)
Riznichenko GY, Vorobjeva TN, Chrabrova EN et al (1990) Identification of kinetic parameters of plastocyanin and P700 interactions in chloroplasts and pigment-protein complexes of photosystem 1. Photosynthetica 24(3):37–51
Riznichenko GY, Plusnina TY, Vorobeva TN et al (1993) Model of the response of the membrane-transport system to the variable electric field. Biofizika 38(4):689–693
Riznichenko GY, Plusnina TY, Aksyonov SI (1994) Modeling of the effect of weak electric field on a nonlinear transmembrane ion transfer system. Bioelectrochem Bioenerg 35:39–47
Riznichenko GY, Lebedeva GV, Demin OV et al (1999) Kinetic mechanisms of biological regulation in photosynthetic organisms. J Biol Phys 25:177–192
Riznichenko GY, Belyaeva NE, Kovalenko IB et al (2009) Mathematical and computer modeling of primary photosynthetic processes. Biophysics 54:10–22
Riznichenko GY, Kovalenko IB, Abaturova AM et al (2010) New direct dynamic models of protein interactions coupled to photosynthetic electron transport reactions. Biophys Rev 2:101–110
Roelofs TA, Lee C-H, Holzwarth AR (1992) Global target analysis of picosecond chlorophyll fluorescence kinetic from pea chloroplasts. Biophys J 61:1147–1163
Romanovsky YM, Stepanova NV, Chernavskii DS (1975) Mathematical modeling in biophysics. Nauka, Moscow (Rus)
Romanovsky YM, Stepanova NV, Chernavskii DS (2004) Mathematical modeling in biophysics. Introduction to the theoretical biophysics. ICS-RCD, Moscow-Izhevsk (Rus)
Rosenzweig ML (1969) Why the prey curve has a hump. Am Nat 103:81–87
Rosenzweig A, MacArthur RH (1963) Graphical representation and stability conditions of predator–prey interactions. Am Nat 97:209–223
Rubin AB (2013) Biophysics, vol 1, 2, 3. Regular and Chaotic Dynamics, Moscow-Izhevsk (Rus)

Rubin A, Riznichenko G (2009) Modeling of the primary processes in a photosynthetic membrane. In: Laisk A, Nedbal L, Govindjee (eds) Photosynthesis *in silico*: understanding complexity from molecules to ecosystems. Springer, Dordrecht

Rubin AB, Shinkarev VP (1984) Electron transport in biological systems. Nauka, Moscow (Rus)

Saeger W (1984) Principles of nucleic acid structure. Springer, Berlin

Salerno M (1992) Dynamic properties of DNA promoters. Phys Lett A 167:49–53

Salerno M, Kivshar Yu S (1994) DNA promoters and nonlinear dynamics. Phys Lett A 193:263–266.

Sanders D, Hansen UP, Slayman CL (1981) Role of the plasma membrane proton pump in pH regulation in non-animal cells. Proc Natl Acad Sci USA 78:5903–5907

Schatz GH, Brock H, Holzwarth AR (1988) Kinetic and energetic model for the primary processes in photosystem II. Biophys J 54:397–405

Scheller HV (1996) *In vitro* cyclic electron transport in barley thylakoids follows two independent pathways. Plant Physiol 110:187–194

Schlarb-Ridley BG, Wagner MJ, Vijgenboom E et al (1999) Expression of plastocyanin and cytochrome f of the cyanobacterium *Phormidium laminosum* in *Escherichia coli* and *Paracoccus denitrificans* and the role of leader peptides. Gene 234:275–283

Schlarb-Ridley BG, Bendall DS, Howe CJ (2002) The role of electrostatics in the interaction between cytochrome f and plastocyanin of the cyanobacterium Phormidium laminosum. Biochemistry 21:3279–3285

Schlick T (2002) Molecular modeling and simulation. An interdisciplinary guide. Springer, New York, second edition 2010

Schodel R, Irrgang KD, Voigt J et al (1998) Rate of carotenoid triplet formation in solubilized light-harvesting complex II (LHCII) from spinach. Biophys J 75:3143–3153

Schodel R, Irrgang KD, Voigt J et al (1999) Quenching of chlorophyll fluorescence by triplets in solubilized light-harvesting complex II (LHCII). Biophys J 76:2238–2248

Schreiber U, Bulger W (1993) Progress in chlorophyll fluorescence research: major developments during the past years in retrospect. Prog Bot 54:151–173

Schreiber U, Krieger A (1996) Two fundamentally different types of variable chlorophyll fluorescence in vivo. FEBS Lett 397:131–135

Schreiber U, Schliwa U, Bulger W (1986) Continuous recording of photochemical and nonphotochemical fluorescence quenching with a new type of modulation fluorometer. Photosynth Res 10:51–62

Scudo FM (1971) Vito Volterra and theoretical ecology. Theor Popul Biol 2(1):1–23

Segel LA (1984) Modeling dynamic phenomena in molecular and cellular biology. Cambridge University Press, Cambridge

Sel'kov EE, Dynnik SN, Kirsta YB (1979) Qualitative study of a mathematical model of the open futile cycle fructose-6-P-fructose-1,6-P2. Biofizika 24(3):431–437

Sinai YaG (1963) On the foundations of the ergodic hypothesis for a dynamical system of statistical mechanics. *Sov Math Dokl* 4:1818–1822

Sinai YaG (1970) Dynamical Systems with Elastic Reflections. Russian Mathematical Surveys 25:137–191

Shannon RE (1975) Systems simulation: the art and science. Prentice Hall, Englewood Cliffs, NJ

Shartzer SA, Fisahn J, Lucas WJ (1992) Simultaneous measurements of extracellular current and membrane potential of *Chara corallina* internodal cells during light-dependent modulation of H^+ transport. C R Acad Sci Paris 315:247–254

Shimoni EO, Rav-Hon O, Ohad I et al (2005) Three-dimensional organization of higher-plant chloroplast thylakoid membranes revealed by electron tomography. Plant Cell 17:2580–2586

Shuvalov VA, Klimov VV, Dolan E et al (1980) Nanosecond fluorescence and absorbance changes in photosystem II at low redox potential. FEBS Lett 118:279–282

Soljanik GI, Chernavskii DS (1980) Mathematical model of morphogenesis. Preprint FIAN 8 (Rus)

Solovyova O, Vikulova N, Markhasin VS et al (2003) A novel method for qualifying the contribution of different intracellular mechanisms to mechanically induced changes in action

potential characteristics. In: Magnin IE, Montagnat J, Clarysse P et al (eds) Functional imaging and modeling of the heart (Conference proceedings). Springer, Lyon
Somogyi R, Stuckin JW (1991) Hormone-induced calcium oscillations in liver cells can be explained by a simple one pool model. J Biol Chem 266:11068–11077
Sorokin EM (1973) Non-cyclic electron transport and connected processes. Plant Physiol (Rus) 20:389–399
Staehelin AL, van der Staay GWM (1996) Structure, composition, functional organization and dynamic properties of thylakoid membranes. In: Govindjee (ed) Advances in photosynthesis and respiration, vol 4. Springer, Dordrecht, p 11
Steffen R, Christen G, Renger G (2001) Time-resolved monitoring of flash-induced changes of fluorescence quantum yield and decay of delayed light emission in oxygen-evolving photosynthetic organisms. Biochemistry 40:173–180
Steffen R, Eckert H-J, Kelly AA et al (2005a) Investigations on the reaction pattern of photosystem II in leaves from Arabidopsis thaliana by time-resolved fluorometric analysis. Biochemistry 44:3123–3133
Steffen R, Kelly AA, Huyer J et al (2005b) Investigations on the reaction pattern of photosystem II in leaves from Arabidopsis thaliana wild type plants and mutants with genetically modified lipid content. Biochemistry 44:3134–3142
Stirbet AD, Strasser RR (1995) Numerical simulation of the fluorescence induction in plants. Arch Sci 48(1):41–59
Stirbet AD, Strasser RJ (1996) Numerical simulation of the in vivo fluorescence induction in plants. Math Comput Simulat 42:245–253
Stirbet A, Govindjee, Strasser BJ et al (1998) Chlorophyll a fluorescence induction in higher plants: modeling and numerical simulation. J Theor Biol 193:131–151
Strasser RJ, Stirbet AD (2001) Estimation of the energetic connectivity of PSII centers in plants using the fluorescence rise (O-J-I-P) – fitting of experimental data with to three different PSII models. Math Comput Simulat 56:451–461
Strasser RJ, Srivastava A, Govindgee (1995) Polyphasic chlorophyll a fluorescence transient in plants and cyanobacteria. Photochem Photobiol 61(1):32–42
Strasser RJ, Tsimilli-Michael M, Srivastava A (2004) Analysis of the chlorophyll a fluorescence transient. In: Papageorgiou GC, Govindjee (eds) Chlorophyll fluorescence: a signature of photosynthesis. Springer, Dordrecht
Stroebel D, Choquet Y, Popot JL et al (2003) An atypical haem in the cytochrome b(6)f complex. Nature 426(6965):413–418
Taiz L, Zeiger E (2002) Plant physiology. Sinauer, Sunderland, MA
Takeuchi Y, Kishimoto U, Ohkawa T et al (1985) A kinetic analysis of the electrogenic pump of *Chara corallina*: II. Dependence of the pump activity on external pH. J Membr Biol 86:17–26
Tester M, Blatt MR (1989) Direct measurement of K+ channels in thylakoid membranes by incorporation of vesicles into planar lipid bilayers. Plant Physiol 91:249–252
Thomas D (1975) Artificial enzyme membranes, transport, memory, and oscillatory phenomena. In: Thomas D, Kernevez J-P (eds) Analysis and control of immobilized enzyme systems. Springer, Berlin
Tikhonov AN (1952) Ordinary Differential Equation systems with small parameters at the derivatives. Mat Cbornik 32(3):575–586
Tikhonov AN, Blumenfeld LA (1985) Concentration of hydrogen ions inside the subcellular particles – physical meanings and determination methods. Biofizika 30(3):527–537
Toko K, Chosa H, Yamafuji K (1985) Dissipative structure in the *Characeae*: spatial pattern of proton flux as a dissipative structure in characean cells. J Theor Biol 114:127–175
Toko K, Hayashi K, Yoshida T et al (1988) Oscillations of electric spatial patterns emerging from the homogeneous state in characean cells. Eur Biophys J 1:11–21
Turing AM (1952) The chemical basis of morphogenesis. Phil Trans R Soc Lond B 237:37–71
Ubbink M, Ejdebeck M, Karlsson BG et al (1998) The structure of the complex of plastocyanin and cytochrome *f*, determined by paramagnetic NMR and restrained rigid-body molecular dynamics. Structure 6:323–335
Ullman GM (2004) Macromolecular electrostatics. University of Heidelberg, Heidelberg

Ullmann GM, Knapp E-W, Kostic NM (1997) Computational simulation and analysis of dynamic association between plastocyanin and cytochrome f. Consequences for the electron-transfer reaction. J Am Chem Soc 119:42–52

Ullmann GM, Knapp E-W (1999) Electrostatic models for computing protonation and redox equilibria in proteins. Eur Biophys J 28:533–551

Ustinin DM, Kovalenko IB, Grachev EA et al (2010) Method of direct multiparticle computer simulation of photosynthetic electron-transport chain. In: Riznichenko G, Rubin A (eds) Dynamic models of processes in cells and subcellular nanostructures. RCD-ICS, Moscow-Izhevsk (Rus)

Ustinin DM, Kovalenko IB, Riznichenko GY, Rubin AB (2013) Combination of different simulation techniques in the complex model of photosynthetic membrane. Comput Res Model 5(1):65–81

Van Kooten O, Snel JFH, Vredenberg WJ (1986) Free energy transduction related to the electric potential changes across the thylakoid membrane. Photosynth Res 9:211–227

Varnai P, Lavery R (2006) Modeling DNA deformation. In: Lankas F, Sponer J (eds) Computational studies of DNA and RNA. Springer, Berlin

Vasil'ev S, Bergmann A, Redlin H et al (1996) On the role of exchangeable hydrogen bonds for the kinetics of $P680^{+}Q_{A}^{-}$ formation and $P680^{+}Phe^{-}$ recombination in photosystem II. Biochim Biophys Acta 1276:35–44

Vasiljev VA, Romanovsky YM (1976) About the role of diffusion in the autocatalytic systems. In: Theoretical and experimental biophysics, vol 6. Kaliningrad (Rus) p. 73–87

Verhulst PF (1838) Notice sur la loi que la population suit dans son accroissement. Corr Math Phys 10:113–121

Vershubskii AV, Tikhonov AN (2013) Electron transport and transmembrane proton transfer in photosynthetic systems of oxygenic type in Silico. Biophysics 58(1):60–71

Vershubskii AV, Priklonskii VI, Tikhonov AN (2007) Mathematical model of electron and proton transfer in oxygenic photosynthetic systems. Russ J Gen Chem 77(11):2027–2039

Vershubskii AV, Kuvykin IV, Priklonskii VI et al (2011) Functional and topological aspects of pH-dependent regulation of electron and proton transport in chloroplasts in silico. Biosystems 103:164–179

Volterra V (1924) Variozionie fluttuasionie del numero d'individui in specie animali conviventi. Mem Acad Lincei 2:31–113

Volterra V (1931) Lecóns sur la théorie mathematique de la lutte pour la vie. Gauthiers-Villars, Paris

von Foerster H (1959) Some remarks on changing population. In: Stolhman J Jr (ed) The kinetics of cellular proliferation. Grune and Stratton, New York

von Foerster H, Mora PM, Amiot LW (1961) Population density and growth. Science 133:1932–1937

Vredenberg WJ (2000) A three-state model for energy trapping and chlorophyll fluorescence in photosystem II incorporating radical pair recombination. Biophys J 79(1):26–38

Vredenberg WJ (2005) System analysis and photo-electrochemical control of chlorophyll fluorescence in terms trapping models of photosystem II: a challenging view. In: Papageorgiou GC, Govindjee (eds) Chlorophyll fluorescence: a signature of photosynthesis. Springer, Berlin

Vredenberg WJ, Bulychev AA (2003) Photoelectric effects on chlorophyll fluorescence of photosystem II in vivo. Kinetic in the absence and presence of valinomycin. Bioelectrochemistry 60:87–95

Webster G, Wolpert L (1966) Studies on pattern regulation in hydra. J Embryol Exp Morphol 16(1):91–104

Wiener N, Rosenblueth A (1946) The mathematical formulation of the problem of conduction of impulses in a network of connected excitable elements, specifically in cardiac muscle. Arch Inst Cardiol Mex 16:205–265

Wilkins MHF, Seeds WE, Stokes AR et al (1953) Helical structure of crystalline deoxypentose nucleic acid. Nature 172:759–762

Winer N (1948) Cybernetics: or control and communication in the animal and the machine. Hermann & Cie/MIT Press, Paris/Cambridge, MA, 2nd revised ed 1961
Winfree AT (2001) The geometry of biological time. Springer, Berlin
Wydrzynski TJ, Satoh K (eds) (2005) Photosystem II – the light-driven water: plastoquinone oxidoreductase. Springer, Dordrecht
Yakushevich LV (2004) Nonlinear physics of DNA. Wiley-VCH, Weinheim, first edition 1998
Yakushevich LV (2007) Theoretical physics of DNA: new ideas and tendencies in the modeling of the DNA nonlinear dynamics. EJTP 4:97–114
Yakushevich LV (2011) Biomechanics of DNA: rotational oscillations of bases. Comput Res Model 3(3):319–328 (Rus)
Yakushevich LV, Krasnobaeva LA, Shapovalov AV et al (2005) One- and two-soliton solutions for DNA. Biofizika 50(3):450–455
Yakushevich LV, Gapa S, Awrejcewicz J (2009) Mechanical analog of the DNA base pair oscillations. In: Awrejcewicz J, Kazmierczak M, Olejnik P, Mrozowski J (eds) Dynamical systems – theory and applications. Left Grupa, Lodz
Yamashita E, Zhang H, Cramer WA (2007) Structure of the cytochrome b6f complex: quinone analogue inhibitors as ligands of heme c_n. J Mol Biol 370:39–52
Young DA (1984) A local activator-inhibitor model of vertebrate skin patterns. Math Biosci 72:51–58
Zhabotinsky AM (1974) Concentration oscillations. Nauka, Moscow (Rus)
Zheng C, Davis ME, McCammon JA (1990) Electrofield distribution inside the bacterial photosynthetic reaction center of Rhodopseudomonas viridis. Chem Phys Lett 173:246–252
Zhu X-G, Govindjee, Baker NR, deSturler E et al (2005) Chlorophyll a fluorescence induction kinetics in leaves predicted from a model describing each discrete step of excitation energy and electron transfer associated with Photosystem II. Planta 223:114–133
Zhu X-G, de Shulter E., Long SP (2007) Optimizing the distribution of resources between enzymes of carbon metabolism can dramatically increase photosynthetic rate; A numerical simulation using an evolutionary algorithm. Plant Physiol 145: 513–526
Zykov VS, Steinbock O, Muller SC (1994) External forcing of spiral waves. Chaos 4(3):509–516

Index

A
Accommodation, 106
Active element, 103
Adenosine monophosphate (AMP), 100
Adenosine triphosphatase (ATPase), 79, 243, 245
Adenosine triphosphate (ATP) synthesis, 245
Age structure of population, 19–21
Amoeba aggregation, 99–101
AMP. *See* Adenosine monophosphate (AMP)
Andronov–Hopf bifurcation, 64
Arabidopsis thaliana, 167–169
Arnold, V.I., 53
Arnold tongues, 53
Arrhythmia, 111–115
ATPase. *See* Adenosine triphosphatase (ATPase)
Attractor, 25
  strange, 30
Autocatalysis, 46
Autowave process, 39, 103–115
Axiomatic model, 111–115
Axon, 104

B
Bakst, N.I., 103
Bazykin, A.D., 15, 31
Bazykin model, 15, 31
Belousov, B.P., 43
Belousov–Zhabotinsky reaction, 43–54
Bifurcation, 15
  Andronov–Hopf, 64
  point, 64, 78
  subcritical Hopf, 75
Biomass yield, 18
Bistable system, 10–11, 17, 60–63
Black hole, 75
Boltzmann equation, 236
Brown, A.J., 16
Brownian dynamics (BD), 208–209
Brusselator, 40–42, 89, 91

C
Calcium oscillations, 27–28
Calvin cycle, 144
cAMP. *See* Cyclic adenosine monophosphate (cAMP)
Cardiomyocytes, 111
Carotenoid, 178
Cellular membrane, 69
Chance, B., 16
Chaos, 25–34
  deterministic, 28–31
Chara corallina, 69
Chargaff rule, 117
Chemotaxis, 99–101
Chernavskii, D.S., 10, 91
Chlamidomonas reinhardtii, 232
Chlorella pyrenoidosa, 178
Chlorophyll fluorescence induction, 171, 197
Chloroplast, 142–146
Chromatophore, 142
Competition, 9, 31
Concentration wave, 38
Conformational wave, 136
Cyanobacteria, 166, 192, 224, 228
Cyclic adenosine monophosphate (cAMP), 100
Cyclic electron flow in photosynthesis, 210–212
Cytochrome. *See* Photosynthesis, cytochrome

A. Rubin and G. Riznichenko, *Mathematical Biophysics*, Biological and Medical Physics, Biomedical Engineering, DOI 10.1007/978-1-4614-8702-9,

© Springer Science+Business Media New York 2014

D
Damped oscillations, 12, 15, 27, 70, 75
Darwin, C., 4
Deterministic chaos, 28–31
Dictyostelium discoideum, 100
Diffusion, 84
  of protons, lateral, 245–246
  restricted, 206–207
Discrete model, 5
Dissipation processes, 178
Dissipative structure, 39, 43, 76, 87
DNA
  dynamics, 115, 117–138
  elastic bar, 121
  long-range interactions, 135–136
  mobility, 126–130
  nonlinear oscillations, 130–133
  unwinding, 120
Docking
  distance, 223, 226
  point (site), 210, 213
  probability, 208, 223
  radius, 208
  rate constant, 224–226
Driesch, H.A.E., 90
Dupont, G., 27

E
Eccles, J., 105
Elastic bar, 121, 167–169
Electric potential. *See* Potential, electric
Electron transport chain, 143–148, 153, 158, 159, 185, 187, 190, 201, 249
Electrostatic interactions, 213, 219–222, 226–229
Ellipsoid of revolution, 215–217
Englander model, 126
Englander, S.W., 126
Entropy, Kolmogorov, 33
Enzyme catalysis
  bistable system, 10
  enzyme–substrate complex, 16
  Michaelis–Menten kinetics, 7, 16, 26
Excitable element, 108

F
Ferredoxin. *See* Photosynthesis, ferredoxin
Fisher, R.A., 36
FitzHugh, R., 107
FitzHugh–Nagumo model, 107
Flavodoxin. *See* Photosynthesis, flavodoxin
Fluorescence induction, 170, 178, 197
Foerster, H., 23
Fucus, 69

G
Gause, G.F., 9
Gause's principle, 9
Gene regulation, 7, 137–138
Gierer, A., 97
Gierer–Meinhardt model, 97
Glycolysis, 25–27, 32–33
Goldbeter, A., 27
Govindjee, 144
Grana, 142
Gurvich, A.G., 90

H
Heart
  activity, 103–115
  arrhythmia, 113
  diseases, 54, 111–115
Helmholtz, H.L.F., 103
Hodgkin, A.L., 103, 105
Hodgkin and Huxley model, 105–107
Hopf bifurcation, 75
Hopf conditions, 63
Huxley, A., 103, 105
Hydra, 96
Hysteresis, 76–79

I
Ion flux, 55–68, 70, 79–81
  calcium, 27–28, 111
  chloride, 188
  manganese, 200–201
  potassium, 56–60, 104, 111, 188, 200–201
  proton, 56–60, 188, 200–201, 241, 245
  sodium, 104, 111
  transmembrane, 188, 200–201
Ionic strength, 219

J
Jacob, F., 7, 10, 91
Jacob and Monod trigger system, 10–11

K
Kolmogorov, A., 13, 36
Kolmogorov
  entropy, 33
  model, 13

L
Langevin equation, 215
Leslie, P.H., 22
Leslie matrices, 22–23
Light intensity, 76–79
Limit cycle, 25
Limited growth, 4–6
Lipid, 235
Lorenz, E., 29
Lotka, A.J., 11
Lotka model, 11
Lumen, 144, 232, 241
Lyapunov exponent, 33

M
MacKendrick, A.G., 23
Malthus, T.R., 4
Malthus law, 4
Mass action law, 146
Master equation, 148
Meinhardt, H., 97
Melanoblast, 95
Membrane
  cellular, 69
  photosynthetic, 142–146, 231–239
  surface charge, 235–239
  thylakoid, 143, 188, 194, 200–201, 209, 211, 231–239
Menten, M.L., 6–8, 16
Michaelis, L., 6–8, 16
Michaelis–Menten equation, 6–8, 16
Microbial populations, 17
Mitchell cycle, 144
Mobile electron carrier, 144, 152–153, 193, 208–209
Monod, J.L., 7, 10, 91
Monod–Jerusalemskii formula, 19
Monod model, 7, 18
Morphogenesis, 83–101
Morphogenetic field, 90–91
Müller, S., 50
Multienzyme complex, 141, 206, 213
Multiparticle simulations, 205–212
Murray, J., 95, 97, 98, 110

N
Nagumo, J.-I., 107
Nerve pulse propagation, 103–115
Nitella, 75
Nitellopsys abtusa, 69
Noble, D., 111
Noble model, 111

O
OJIP-shape, 171, 197
Operon, 7
Oregonator, 46, 53
Oscillations, 25–34, 63–66
  in chemical reactions, 44
  damped, 12, 15, 27, 70, 75
  doubling of the cycle, 32
  in glycolysis, 25–27, 32–33
  of intracellular calcium concentration, 27–29
  limit cycle, 25
  of the membrane potential and pH, 75
  and periodic space structures, 69–81

P
Pacemaker, 113
Passive leakage of protons, 196, 241
Pattern
  formation, 69
  pH, 69
  pigmentation, 90
Pelvetia, 69
Pendulum chain dynamics, 127
Periodic effect, 32–33
Perrin formulae, 216
Petrovskii, I.G., 36
pH
  generation, 194–195
  patterns, 69
Phormidium laminosum, 226
Photosynthesis, 79–81, 141
  cyclic electron flow, 210–212
  cytochrome, 221, 226–229
  cytochrome bf complex, 142, 190–192
  cytochrome f, 226–229, 232–233, 235–239
  electron transfer in multienzyme complex, 148
  electron transport by mobile carriers, 152–153, 165–166, 193, 206–207
  electron transport chain (*see* Electron transport chain)
  energy dissipation in photosystem II, 178
  ferredoxin, 143, 221
  ferredoxin-NADP reductase, 221
  flavodoxin, 225
  interaction of two photosystems, 157–169
  kinetic models, 146–148, 187–201
  lumen (*see* Lumen)
  photosystem I, 142, 163–165, 192–193, 210–212, 222, 225–229, 235–239
  photosystem II, 142, 159–160, 173–175, 188–190, 198–199

Photosynthesis (*cont.*)
plastocyanin, 143, 206–207, 221, 226–229, 232–233, 235–239
plastoquinone, 143, 162, 206–207, 209
regulation, 157–158
stroma (*see* Stroma)
thylakoid (*see* Thylakoid)
Photosynthetic membrane, 142–146, 231–239
Pigmentation pattern, 90
Pisum sativum, 210
Plastocyanin. *See* Photosynthesis, plastocyanin
Plastoquinone. *See* Photosynthesis, plastoquinone
Poincaré, H., 29
Poisson–Boltzmann equation, 219, 236
Polezhaev, A.A., 100
Population dynamics, 8–9
age structured populations, 19–21
discrete model, 5
exponential growth, 3
limited growth, 4–6
Malthus law, 3
microbial, 17
three species model, 31–32
Verhulst model, 4–6
Potential
electric, 55–68, 144, 177, 200–201
electrochemical, 144, 194–195, 241–250
propagation, 103–115
resting, 104
transmembrane, 55–68, 103, 144, 177, 194–195, 200–201, 241–250
Predator–prey model, 8, 12, 15, 31
Preliminary complex, 213
Prigogine, I.R., 40
Probability density distribution of protons, 246
Promotor, 7, 137
Protein interactions
complex formation, 213–229
mutation effects, 224
photosynthetic membrane, 231–239
solution ion strength impact, 224–226
Protons
flux, 71, 79
passive leakage, 197, 241
probability density distribution, 246

R
Reaction–diffusion, 39, 43, 84, 95–99
Reentry, 54
Refractory period, 106
Resonance, 53, 55
Resting potential, 104
Reverberator, 114–115
Romanovskii, Y.M., 89
Rotational motion, 120, 214
Rozenzweig, M.L., 14
Rozenzweig model, 14

S
Selection, 9
Self-organization, 35–54
SFITFY. *See* Single flash induced transient fluorescence yield (SFITFY)
Sine-Gordon equation, 126
Single flash induced transient fluorescence yield (SFITFY), 178
Species interaction, 9, 13–16
Spherical wave, 113
Spinning vortex, 54
State probability, 149, 152, 160, 162, 166
Stimulation threshold, 55, 106
Stochastic regime, 32–33
Strange attractor, 30
Stroma, 142, 195, 241
Substrate limitation, 6
Synchronization, 113–114
Synechocystis, 224

T
Thermosynechococcus elongatus, 227
Three species model, 31–33
Threshold of stimulation, 55, 106
Thylakoid, 79, 142–146
membrane, 158, 188, 190, 194, 197, 200–201, 209, 211, 231–239
Transcription regulation, 137–138
Transmembrane potential, 103
Trigger, 10–11
distributed, 91–94
Turing, A.M., 39, 83, 88, 90
Turing instability, 75, 83–90, 101
Two-age model of a cell population, 19

V
Vasiljev, V.A., 89
Verhulst, P.F., 4–6
Verhulst model, 4–6
Viscosity, 208, 215
Volterra, V., 8, 12
Volterra model, 12, 15
Vortex, 54

W
Wash-out velocity, 18
Water oxidizing complex (WOC), 144, 159, 173, 178, 196
Wave
  concentration, 19–21
  conformational, 136
  propagation, 36, 103–115, 136
  spherical, 113
  spiral, 49, 54, 113
  velocity, 38
Winfree, A.T., 75
WOC. *See* Water oxidizing complex (WOC)

Y
Yakushevich, L.V., 121

Z
Zhabotinsky, A.M., 43
Z-scheme of photosynthesis, 144